From Micro- to Nano-porous Cellular Materials with Layered 2D Microstructure

KENICHI NAKANISHI

Supervisor: Prof. S. Hofmann
Prof. N.A. Fleck

Department of Electrical Engineering
University of Cambridge

This dissertation is submitted for the degree of
Doctor of Philosophy

Clare College
September 2019

Kenichi Nakanishi: *From Micro- to Nano-porous Cellular Materials with Layered 2D Microstructure,* PhD Thesis, University of Cambridge, © September 2019

DECLARATION

This thesis is the result of my own work and includes nothing which is the outcome of work done in collaboration except as declared in the Preface and specified in the text. It is not substantially the same as any that I have submitted, or, is being concurrently submitted for a degree or diploma or other qualification at the University of Cambridge or any other University or similar institution except as declared in the Preface and specified in the text. I further state that no substantial part of my dissertation has already been submitted, or, is being concurrently submitted for any such degree, diploma or other qualification at the University of Cambridge or any other University or similar institution except as declared in the Preface and specified in the text. This dissertation contains fewer than 65,000 words including appendices, footnotes, tables and equations and has fewer than 150 figures.

Clare College, September 2019

Kenichi Nakanishi

ABSTRACT

From Micro- to Nano-porous Materials with Layered Microstructure

Kenichi Nakanishi

A large body of work has been committed to studying the unique properties of 2D materials such as graphene, with advancements in both the material quality and scale of mechanical exfoliation and chemical vapour deposition (CVD) methods. These emergent 2D materials have recently been engineered as the cell walls in three-dimensional structures, but their superb material properties are yet to be fully realized in this new form. This thesis investigates the CVD processing of a range of catalytic templates to open new routes towards the controlled fabrication of graphitic foams and lattices. As part of a full feedback loop, mechanical characterization of these unique cellular materials was undertaken in order to examine their deformation and failure mechanisms, including capturing their behaviour in a new hierarchical model framework. These novel structures have the potential to combine the properties of structured porous materials, i.e. low density, high geometric surface area, permeability and mechanical stability, with the intrinsic properties of 2D materials such as enhanced electrical and thermal conductivity, high mechanical strength and stiffness as well as resistance to damage from extreme temperatures and chemical attack. Such high quality 2D-material based cellular structures have manifold potential applications in electrochemistry, catalysis and filtration.

Herein, freestanding graphitic foams are fabricated across a range of relative densities, and their uniaxial compressive responses are measured to investigate the operative deformation and failure mechanisms that govern the mechanical response of such foams. For this purpose, a hierarchical micromechanical model is developed, which traces the deformation of the hollow cell struts to the axial stretching of the cell walls. The waviness of

the multilayered graphitic wall increases the axial compliance of each cell wall, and it is established that axial straining within the cell wall occurs by interlayer shearing. Crucially, this mechanism demonstrates that the continuum properties of such foams are dictated by the weak out-of-plane shear properties of the layered cell wall material, leading to a large knockdown in the macroscopic mechanical properties of the foam.

Ordered graphene gyroid lattices possessing nanoscale unit cell sizes are then fabricated and characterized through a combination of nanoindentation and a multi-scale finite element analysis (FEA) study. These structured nanolattices were found to be highly conductive and possessed a high degree of elastic recovery and strength owing to the structural efficiency afforded by the stretching-dominated cellular architecture. However, the nanoscale interlayer shearing deformation mechanism was again found to be active in the cell walls of these structures, attenuating the continuum response of the lattice. The hierarchical micromechanical model developed herein rationalizes why CVD-grown multilayer graphitic foams and lattices possess diminished continuum elastic moduli and yield strengths in comparison to the exemplary in-plane mechanical properties of 2D materials, presenting a first step towards the understanding of porous materials whose cell walls are comprised of emergent 2D materials.

In addition, the direct shrinkage of commercial polymer foams and 3D printed templates is used herein to offer a very simple and low-cost method for reaching identically-shaped structures with sub-200 µm unit cell sizes. The conformal addition of different thicknesses of alumina is shown to control the level of isotropic shrinkage, reducing the shrinkage ratio from 125x to 4x after addition of 25 nm of alumina, while inducing a surface stress mismatch that drastically increases the surface roughness of the material. Furthermore, efficient graphitization was demonstrated through the use of an electrolessly deposited Nickel film, resulting in the formation of a conductive multilayer graphenic coating at temperatures below 1100 °C. These processes present the flexible production of multifunctional cellular materials with sub-mm unit cells, tuneable size, roughness and conductivity.

A final study investigates the preparation of a nascent 2D material, WS_2, through the use of a deconstructed metal organic chemical vapour deposition (MOCVD) process which allowed insight into the role of each process step. The catalytic effect of an Au substrate is unambiguously demonstrated, which allowed for a reduction in the precursor partial pressures required to nucleate and grow WS_2 by over an order of magnitude in comparison to competing methods. This enabled the efficient low-pressure growth of WS_2 films with low levels of carbon contamination. Furthermore, the reaction process developed herein exhibited a self-limiting monolayer growth behaviour with exposure cycles lasting just 10 minutes, a significant improvement over prior MOCVD processes requiring growth times in excess of 1 hour. These insights foster our understanding of the key underlying mechanisms of WS_2 growth for future integrated manufacturing of transition metal dichalcogenides (TMDCs) and other 2D materials.

Dedicated to Viola, and my family.

PUBLICATIONS

1. Aria, A. I., **Nakanishi, K.**, Xiao, L., Braeuninger-Weimer, P., Sagade, A. A., Alexander-Webber, J. A. & Hofmann, S. Parameter Space of Atomic Layer Deposition of Ultrathin Oxides on Graphene. *ACS Applied Materials & Interfaces* **8,** 30564–30575 (Nov. 2016).
2. Cebo, T., Aria, A. I., Dolan, J. A., Weatherup, R. S., **Nakanishi, K.**, Kidambi, P. R., Divitini, G., Ducati, C., Steiner, U. & Hofmann, S. Chemical vapour deposition of freestanding sub-60 nm graphene gyroids. *Applied Physics Letters* **111** (2017).
3. Degl'Innocenti, R., Xiao, L., Kindness, S. J., Kamboj, V. S., Wei, B., Braeuninger-Weimer, P., **Nakanishi, K.**, Aria, A. I., Hofmann, S., Beere, H. E. & Ritchie, D. A. Bolometric detection of terahertz quantum cascade laser radiation with graphene-plasmonic antenna arrays. *Journal of Physics D: Applied Physics* **50** (2017).
4. **Nakanishi, K.**, Aria, A. I., Berwind, M. F., Weatherup, R. S., Eberl, C., Hofmann, S. & Fleck, N. A. Compressive behavior and failure mechanisms of freestanding and composite 3D graphitic foams. *Acta Materialia* **159,** 187–196 (Oct. 2018).
5. Nam, D. H., Zhang, J. Z., Andrei, V., Kornienko, N., Heidary, N., Wagner, A., **Nakanishi, K.**, Sokol, K. P., Slater, B., Zebger, I., Hofmann, S., Fontecilla-Camps, J. C., Park, C. B. & Reisner, E. Solar Water Splitting with a Hydrogenase Integrated in Photoelectrochemical Tandem Cells. *Angewandte Chemie - International Edition* **57,** 10595–10599 (2018).

PUBLICATIONS - IN PREPARATION

1. Di Nuzzo, D., Mizuta, R., **Nakanishi, K.**, Martin, M.-B., Aria, I., Weatherup, R., H. Friend, R., Hofmann, S. & Alexander-Webber, J. Graphene-passivated nickel as an efficient hole-injecting electrode for organic semiconductor devices (2019).
2. **Nakanishi, K.** & Hofmann, S. Ordered Graphitic Microfoams via Shrinkage and Catalytic Conversion of Polymer Scaffolds. *APL Materials* **Just Accepted** (Jan. 2020).
3. **Nakanishi, K.**, Labonte, D., Hofmann, S. & Fleck, N. A. The indentation response of the hollow graphene gyroid nanolattice (2019).
4. **Nakanishi*, K.**, Fan*, Y., Veigang-Radulescu, V. P., Alexander-Webber, J. A., Mizuta, R., Stewart, C., Brennan, B., Pollard, A. J. & Hofmann, S. Catalytically enhanced metal organic chemical vapour deposition of monolayer WS_2 (2019).

ACKNOWLEDGMENTS

I would like to thank my supervisor, Professor Stephan Hofmann, for providing support and the freedom to explore many different avenues during my PhD. I am also grateful to my second supervisor Professor Norman Fleck for his invaluable help and guidance throughout my PhD.

I would like to extend my gratitude to and all the Postdocs in the Hofmann group - Dr. Indrat Aria, Dr. Ye Fan, Dr. Jack Alexander-Webber and Dr. Vitaly Babenko who have all provided invaluable training, discussion and guidance in each of my projects. I would also like to thank my contemporaries at the Hofmann group - Ryo Mizuta, Oliver Burton, Callum Stewart, Vlad Radulescu, Zenas Van-Veldhoven, Dr. Philipp Braeuninger and Dr. Ruizhi Wang who all made the culture of the group an enjoyable place to work.

I also thank my collaborators, without whom these projects would not have been possible. Dr. Indrat Aria for his CVD and ALD training and discussion, Dr. Matthew Berwind and Prof. Chris Eberl at the Fraunhofer Institute for their mechanical testing facilities, Dr. David Labonte for his help with nanoindentation measurements, Tomasz Cebo for his help with the gyroid fabrication, Vlad-Petru Veigang-Radulescu for his detailed ToF-SIMS work and Dr. Ye Fan for MOCVD training and TMDC project development.

I greatly appreciate the support from the NanoDTC, and acknowledge the funding for my PhD studies from the Engineering and Physical Sciences Research Council (EPSRC) and the Cambridge Trust.

I am deeply thankful to my family for their support and above all, I am extremely grateful to Viola Chan. Thank you for always being there and for growing with me every day.

CONTENTS

LIST OF FIGURES

LIST OF TABLES

ABBREVIATIONS

2PL	Two Photon Lithography
AFM	Atomic Force Microscopy
Al_2O_3/G	Alumina-supported Graphitic Foam
ALD	Atomic Layer Deposition
BSE	Back-scattered Electrons
CN	Carbonized Network
CVD	Chemical Vapour Deposition
DMS	Dimethylsulfide
EBS	Electron Beam Sintering
EDX	Energy Dispersive X-ray Spectroscopy
FEA	Finite Element Analysis
FET	Field Effect Transistor
FG	Freestanding Graphitic Foam
FIB	Focused Ion Beam
FTO	Fluorine-doped Tin Oxide
FWHM	Full Width Half Maximum
G/Ni	Graphitic Foam on Nickel Template
GO	Graphene Oxide
hBN	Hexagonal Boron Nitride

HR-TEM	High-Resolution Transmission Electron Microscopy
ITO	Indium Tin Oxide
LMIS	Liquid Metal Ion Source
LP-CVD	Low-Pressure Chemical Vapour Deposition
MBE	Molecular Beam Epitaxy
MOCVD	Metal-Organic Chemical Vapour Deposition
PDE	Partial Differential Equation
PS	Polystyrene
PEO	Poly(ethylene oxide)
PL	Photoluminescence
PMMA	Poly(methyl methacrylate)
PMMA/G	PMMA-supported Graphitic Foam
RIE	Reactive Ion Etching
SAED	Selected Area Electron Diffraction
SE	Secondary Electrons
SEM	Scanning Electron Microscope
SLA	Stereolithography
SLS	Selective Laser Sintering
TGA	Thermogravimetric Analysis
THC	Tungsten Hexacarbonyl
TMDC	Transition Metal Dichalcogenides
ToF-SIMS	Time of Flight Secondary Ion Mass Spectroscopy
TPMS	Triply Periodic Minimal Surface
XPS	X-ray Photoelectron Spectroscopy

1

INTRODUCTION

Cellular materials appear widely in nature, existing in the microstructure of cork, wood, trabecular bone and many growing organisms [246]. Due to their repeating structure, cellular materials may possess novel properties ranging from high geometric surface areas, permeability to fluids and mechanical stability while still possessing considerable weight savings relative to bulk materials [77]. Pliable polymer foams have long been used to absorb vibration, noise and impact energy, whereas hard-wearing and thermally resistant ceramic foams have found use in filtration, pollutant absorption and as catalytic substrates. Metallic foams offer a large surface area and the ability to pass flow through the pores while simultaneously passing heat or current through the solid network, making them ideal for use in electrochemical devices and as heat exchangers, evaporators or thermally insulating devices [12]. The physical properties of each cellular material are determined by the material properties of the constituent solid of which they are made, their relative density $\bar{\rho}$ (the fraction of space occupied by the solid) and their cellular architecture (cell size, wall thickness, connectivity and regularity).

Understanding of the structure/property relationship of cellular materials is crucial for their design and use in future applications. Many prior studies have sought to establish a direct relationship between the foam microstructure and macro-level properties. A number of theoretical models and empirical observations have determined a set of scaling laws that attempt to express the relationship between the effective mechanical properties of a homogenized foam and its relative density. Thereby, a mechanical property such as the overall stiffness may be expressed in a power law relation such as $E = C\bar{\rho}^n E_s$ where E_s is the Young's modulus of the constituent solid material, C is a geometric parameter and n is an exponent that is strongly influenced by the deformation behaviour under loading [77]. The cellular topology will determine the load bearing and stress transfer behaviour, which will influence these geometric scaling parameters and hence the final mechanical behaviour of a cellular material. In order to understand these structure/property relationships, many theoretical approaches have examined foams constructed from idealized repetitive unit cells . Further refinements have improved the representation of the morphological structure of the cellular materials through the introduction of cellular irregularities or the use of directly imaged cellular topology.

Cellular materials can be prepared with distinct cell morphologies from a wide variety of parent materials. Disordered polymeric foams are most commonly prepared by bubble formation within a liquid melt, with foaming occurring via physical or chemical blowing agents. At this stage, the rheological behaviour of the foaming liquid is a key factor that will determine the cell size, structure, and relative number of open cells. Open-cell polymer foams can be subsequently converted to metallic (or otherwise) foams through investment casting, CVD or slurry casting. Alternative templating methods may utilize hollow spheres or a leachable solid around which liquid material is injected then solidified. However, stochastic systems produced in these ways will consistently demonstrate inferior structural performance, leading to interest in the development of porous structures with periodic order and controlled cell morphology. To achieve this, additive manufacturing techniques have been utilized as an open platform for the preparation of lattice structures with rationally designed structures, possessing unit cell sizes down to the micron scale. This has lead to the design of lattice materials that take full advantage of geometry-based scaling efficiencies, which possess higher stiffness, strengths, and energy absorption capacities than their foamed counterparts with random geometry.

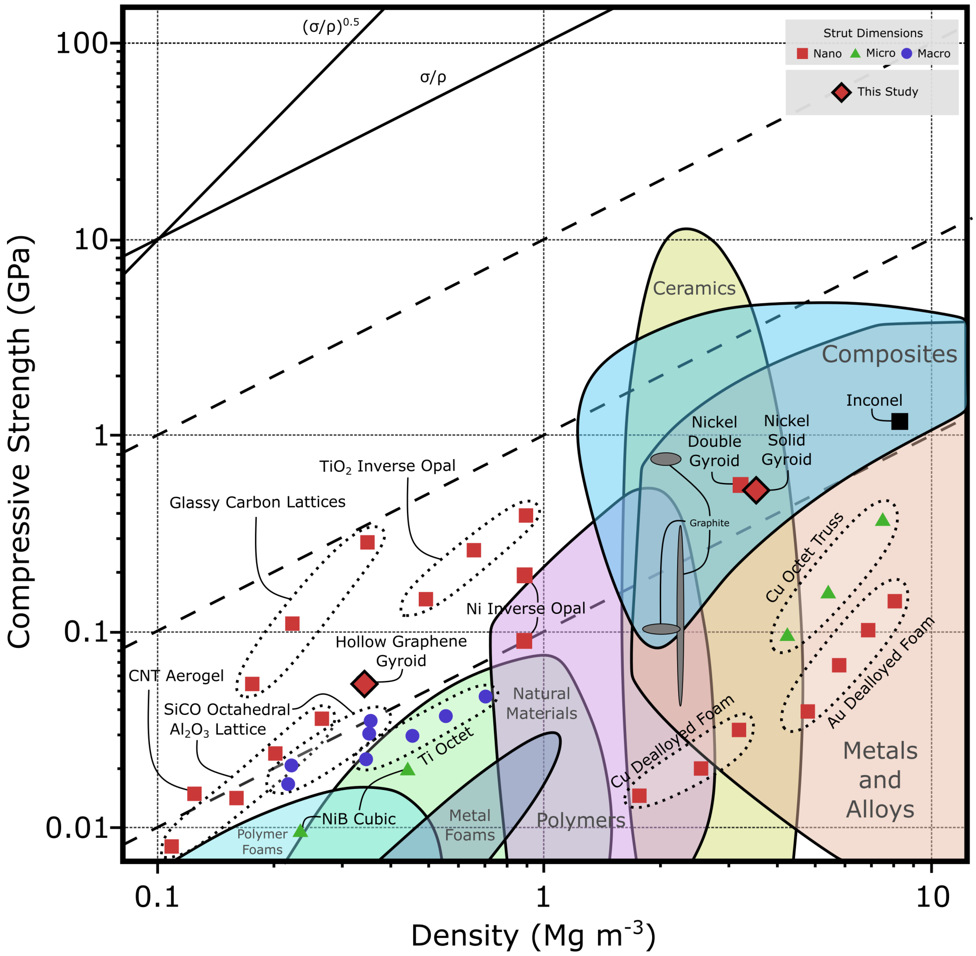

Figure 1.1: Compressive strength vs density Ashby chart showing state-of-the-art lattice materials, which are highlighted according to the length scale of their cellular architecture. Note for a given relative density, the increased strength that is present in cellular materials with increased structural order or reduced strut sizes.

Independently, advancements in material metrology and synthesis techniques have revealed that at the nanoscale, the mechanical, catalytic and electronic properties of a material can undergo significant changes [61, 116]. In one example, the typical bulk strength of metals and ceramics are orders of magnitudes smaller than their theoretical limit due to imperfections such as dislocations, grain boundaries and voids. The length scale of the microstructure within a material determines the size and distribution of these flaws, and hence the final strength of the material. For example, both the fracture strength σ_f of brittle materials and the yield strength σ_y of ductile metals are inversely proportional to a variable related to the material microstructure (i.e. the critical crack size a_c or the grain size/distance between dislocations, known as the characteristic length l). When the dimensions of a material are reduced, the distributions of flaw sizes decrease correspondingly, increasing strength towards their theoretical limit. This 'smaller is stronger' phenomenon has led to the development of nanolattices, in which the length scale of architecture is reduced to a scale small enough to exploit size-dependent strengthening. Pyrolytically derived ceramic nanolattices [16], atomic layer deposited hollow-beam ceramic nanolattices [96] and nickel double gyroid nanolattices [110] each possess nanoscale strut or nanoscale wall thickness, leading to extremely high relative compressive strength. These exemplify the potential outcomes of material strengthening size effects on the macroscopic strength of a cellular material, see Fig 1.1.

Size effects influence a wide range of physical properties, as demonstrated by the rise of 2D materials - an entire class of materials whose size has been reduced down to a dimensional limit. The isolation of graphene in 2004 demonstrated that 2D materials were not only thermodynamically stable, but possessed material properties that are present only in this atomically thin form of carbon. When individual flakes were examined, graphene has demonstrated conductivities of up to 200,000 $cm^2/V{\cdot}s$ [62] at $T = 20$ K, a tensile strength of 130 GPa and Young's modulus of 1 TPa [121]. Since the discovery and characterization of graphene, an extensive library of 2D materials have been found, possessing an broad spectrum of material properties. Transition metal dichalcogenides TMDC encompass an entire 2D material family in which transition metal atoms are sandwiched between two layers of close-packed chalcogenide elements (S, Se or Te). Depending on the coordination and oxidation state of the metal atoms, and doping of the lattice, TMDCs can be metallic, semimetallic or semiconducting [261]. Within this family, monolayer tungsten disulfide (WS_2) is particularly interesting as a prototypical semiconductor, possessing a wide direct band gap ($E_g \approx 2.0$ eV) [254] and bright room-temperature photoluminescence (PL) [83, 186].

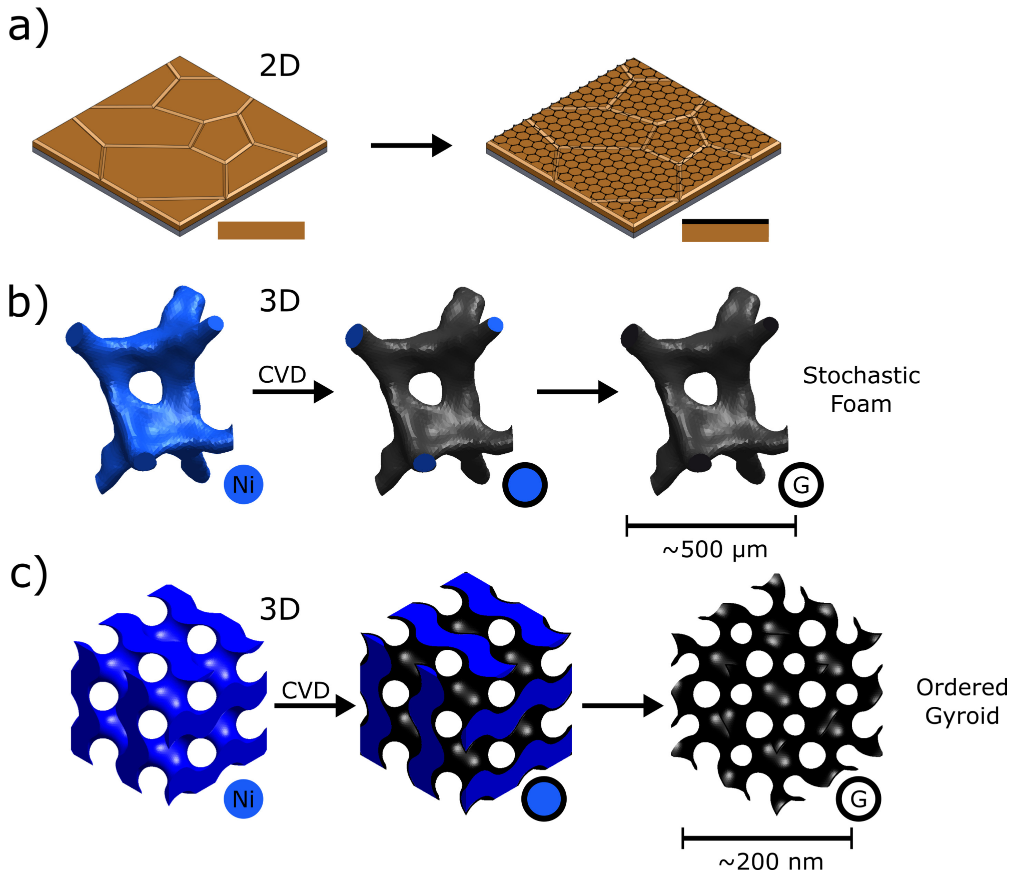

Figure 1.2: Schematics for the production of (a) 2D material on a flat catalyst, (b) 2D material grown on a disordered, macroscopic 3D template and (c) 2D material grown on an ordered nanoscale gyroidal template.

Combining an understanding of material growth and properties with the control over the 3D microstructure of 2D materials leads to exciting opportunities. Some examples which allow the exemplary properties of these materials to be highlighted in their respective applications include: the spinning of carbon nanotubes into fibers, [52], pressing of graphene flakes into flexible conductive papers [44], and the incorporation of exfoliated graphene sheets as a reinforcing additive [162] or blending into conductive inks [118]. Advances in manufacturing and characterization methods for 2D materials allow these layered solids to be engineered as the cell walls in a new class of 3D porous cellular materials [226, 252]. Grown as conformal layers of 2D materials, the cellular morphology of these 3D monoliths inherit the shape of their template independent of size and morphology see Fig 1.2. The utilization of the mechanical, thermal and electrical properties of 2D materials in low density and high surface area structures gives the opportunity for these 2D material based cellular materials to be used in applications ranging from energy storage [141], and electrochemistry [273] to thermal management [187], sorption [131] and filtration [14].

CVD-grown graphene foams have been examined as active electrode materials due to their large surface area (300-600 m^2g^{-1}), porosity (~99.7%, ~200 µm pore size), resistance to chemical corrosion, and high electrical conductivity (~10 S/cm) [36]. Electrodes based on graphene foams can operate at much higher charging and discharging rates compared to conventional battery electrodes due to the thinness of the active materials and close proximity to the porous conductive network [211]. Furthermore, the graphene scaffold is flexible, with the thinness of the active materials reducing stresses within the electrode, enabling bending radii as low as 5 mm [128]. Used as the scaffold for the fabrication of monolithic composite electrodes, these graphene foams have been demonstrated to possess a high specific capacitance of 800-1080 F/g when coupled with transition metal oxides [28, 54, 292] or 346 F/g with conductive polymers [59]. These values are significantly greater than those based on assembled chemically modified graphene (135 to 175 F/g) [228, 235], due to the use of a continuous and highly conductive graphene network that possesses less defects and intersheet junctions. Use of smaller catalytic templates have increased the available surface area (972-1509 m^2g^{-1}) but such systems possessed modest specific capacitances of 252-330 F/g [119, 275], owing to the relatively poor graphitic quality of the foams (conductivity 0.1 S/cm). Preparing foams with low density and high graphitic quality, conductivity, and surface area will be key in preparing electrode material for supercapacitors with high power and high energy density levels.

The production of high-performance electromagnetic interference (EMI) shielding materials have similar material requirements, with 3D graphene foams possessing low density, excellent flexibility, and extraordinary electrical conductivity having been used to produce EMI shields that exceed the target value needed for commercial applications (~20 decibels (dB)) [37, 279]. Use of CVD-grown graphene foams with large pore sizes (~200 µm, 5 mg/cm^3 density) have resulted in an EMI shielding effectiveness of 30 dB for a 1 mm thick sample [37]. Furthermore, CVD-grown graphene foams utilizing pressed powder templates (~200 µm pore size) have demonstrated an EMI shielding effectiveness of 60 dB at just 50 µm thickness [293], owing to the greater cross section of conductive material (810 mg/cm^3 density).

Graphene foams have also demonstrated enhanced biocompatibility, showing minimal toxic effects within the first 21 days of cell culture [51]. 3D graphene structures provide a high surface-to-volume ratio, 3D porous structure with favorable mechanical characteristics and rapid mass/electron transport kinetics (which are required for chemical/physical stimulation of differentiated cells) [2]. As such, mesenchymal stem cells (MSCs) have been successfully cultured within a graphene network, where the conductive graphene foam (0.5 S/cm) supported neuronal differentiation [146, 238]. Further application of surface coatings to graphene foams have allowed cultured MSCs to successfully undergo chondrogenic [170] or osteogenic [294] differentiation. Additionally, recent work by Ma et al. has reported that the morphology and mechanical properties of graphene foams will promote stem cell differentiation into various cell lineages. Soft graphene scaffolds (30 kPa elastic moduli) contributed to the differentiation of stem cells into neurons, whereby stiffer graphene scaffolds (64 kPa elastic moduli) encouraged differentiation into astrocytes [147]. Each of these studies utilized foams prepared from standard commercial nickel templates (~200 µm pore size), highlighting the opportunity for the investigation of the effect of architected porous graphene structures with the associated changes in stiffness, density and conductivity for use in tissue engineering and regenerative nanomedicine applications.

Hence, the potential outcome of these efforts is the development of a new class of multifunctional cellular materials which combine the size effects present in 2D materials with the superior mechanics and structural scaling available to architected lattices. Understanding of the structure/property relationships that exist within 2D material-based cellular solids is required to unlock the full potential of these emerging applications.

1.1 AIMS AND OBJECTIVES

The aim of this thesis is to investigate the preparation of CVD-enabled 3D cellular materials in order to fabricate and characterize porous structures whose cell walls are comprised of layers of high-quality graphene. The mechanical behaviour of such CVD-grown 3D cellular materials are then studied, with particular attention to the deformation response of the material across a range of length scales and cellular topology. Based on this, a hierarchical micromechanical model is developed to rationalize the continuum mechanical properties, furthering the understanding of these unique cellular materials. This also leads into an exploration of the preparation of alternative templates such as structured graphitic microfoams as well as the development of WS_2, a semiconducting TMDC material regarded as a promising candidate for the future generation of transistor in modern electronics.

This overall aim will be achieved through the following objectives:

1. Growth and characterization of CVD-based graphene foams utilizing a range of 3D catalytic templates.
    a) Developing CVD growth and processing methodologies to obtain disordered macroscopic free-standing graphitic foam samples across a range of relative densities.
    b) Developing CVD growth and processing methodologies to obtain ordered nanoscopic free-standing graphitic foam samples across a range of film thicknesses.
    c) Non-mechanical characterization of as-grown material using a suite of material characterization techniques.
2. Measure the mechanical response of CVD-based cellular materials.
    a) Developing both uniaxial compression and nanoindentation testing protocols for CVD-grown porous samples.
3. Use of hierarchical modelling and numerical simulation approaches towards interpreting experimental results.

    a) Developing an extension to the Gibson-Ashby model for open-cell cellular solids to describe the deformation behaviour of CVD-grown graphitic foams.
    b) Developing the use of FEA to explicitly model gyroid and hollow gyroid unit cells to determine the effective properties (Young's modulus, yield strength etc.) for an assumed set of parent material properties.
    c) Use of inverse FEA to determine the indentation response of the gyroid film.

4. Explore the parameter space of WS_2 for future incorporation as a cell wall material in a 3D lattice.
    a) Developing a growth recipe for the fabrication of high-quality WS_2 monolayers, with a focus on minimizing carbon by-product contamination in MOCVD.

1.2 SCOPE OF THIS THESIS

This thesis addresses the preparation of CVD-grown graphene across a range of catalytic templates as well as the definition of constitutive models that describe and predict the mechanical response of graphene-based cellular materials. However, both 2D materials and 3D cellular material mechanics are highly complex and thus it is necessary to consider several statements to bound the work of this thesis.

While the CVD graphene plays an important role in the motivation for this thesis, this work relies overall on an engineering approach to materials. This approach examines how the use of 2D materials influences mechanical behaviour, and material growth is developed with a focus on reproducible sample preparation. As both catalyst pre-treatment and process optimization are intimately linked to the type of template used, the CVD growth of graphene used herein utilizes simple, but consistent growth recipes. The development of these protocols have not included in-depth characterization of catalyst pre-treatment methods (for elemental contamination, roughness, domain size) or process optimization with respect to nucleation density and domain merging. As such, the effects of such optimization for the growth of 2D films as cell-wall materials remain outside the scope of this thesis.

The investigation of the mechanical properties of the tested graphitic foams in this work focuses on the use of uniaxial compression and nanoindentation, drawing conclusions within the limitations of each testing technique. In addition, the modelling approaches considered herein cover elastic and plastic behaviour, but do not extend into fracture mechanics, as compressed samples were found to deform without any observable brittle fracture or flake tearing. Furthermore, this thesis concentrates on yield criteria based on the principles of mechanical plasticity, and has not investigated the application of continuum damage models.

1.3 STRUCTURE OF THIS THESIS

Chapter 2 begins with an overview of cellular material mechanics, discussing the fundamental factors determining mechanical behaviour and the evolution of modelling techniques for open-cell foams, from classical representative unit cell models to modern numerical simulation methods. An in-depth look at the Gibson-Ashby model for open-cell foams is given in sub-section 2.1.2, which forms the framework for the analysis in Chapter 4. A review of state-of-the-art carbon-based cellular materials and template fabrication techniques across a range of length scales and degrees of order are investigated in Chapter 2.2, giving context to the fabrication space of CVD-based graphenic cellular materials. This is followed by a brief overview of 2D materials, with a particular focus on graphene and WS_2 in Chapter 2.3. Finally, an overview of the CVD method is covered in Chapter 2.4, discussing key parameters such as precursor and catalyst choice. This background guide the fabrication of freestanding graphenic foams in Chapters 4, 5, and 6, as well as the growth of monolayer WS_2 in Chapter 7.

Chapter 3 provides an understanding of the experimental methods used for the projects developed as part of this thesis, including systems, processes and characterization techniques. The subsequent mechanical characterization and modelling of freestanding macroscopic graphene foams is developed in Chapter 4. This research is extended to the use of a periodic gyroid lattice template to generate a freestanding graphene gyroid structure in Chapter 5. Therein, the mechanical properties of which are examined through the use of nanoindentation and finite element analysis (FEA). Chapter 6 investigates the preparation of alternative templates, utilizing the shrinkage and catalytic graphitization of polymer scaffolds to prepare structural graphitic microfoams. Finally, the CVD-based growth of an alternative 2D material (WS_2) is investigated in Chapter 7, whereby gold is used as a growth catalyst for the fast and efficient production of high quality WS_2 monolayers.

2

BACKGROUND

2.1 CELLULAR MATERIAL MECHANICS

Fundamentally, the mechanical behaviour of cellular materials depends on the matrix material, the pore structure and the relative density $\tilde{\rho}$, which is defined as

$$\tilde{\rho} = \frac{\rho}{\rho_s} \tag{2.1}$$

where ρ represents the apparent density[1] of the foam, and ρ_s is the density of the constituent solid. Though the overall mechanical behaviour has a strong dependency on the relative density of the foam, it is not the only factor that determines the mechanical behaviour of a cellular solid. Understand the structure/property relationship for cellular materials is crucial for the design of cellular solids. Previous studies on 3D foams have sought to establish a direct tie between the foam micro-structure and the macro-level foam properties.

A number of theoretical models and empirical studies support power law scaling relationships for 3D cellular solids such as $E = C\bar{\rho}nE_s$ where E_s is the Young's modulus of the cell wall material, C is a geometric parameter and the exponent n has a value of 1 for ideal stretching- and and a value of 2 for ideal bending-dominated behaviour of the cell edges [77]. While the vast majority of cellular solids are bending-dominated, stretching-dominated topologies

---

[1] This includes the pore spaces within the material in the volume measurement.

are significantly more weight-efficient due to improved load distribution and stress transfer throughout the structure. Generally, the geometric pre-factor C and scaling exponent n are determined by nodal connectivity (the number of struts connecting to a node), cell size and the shape of the cell struts or walls (e.g. curvature, and cross-sectional shape and uniformity). On a macroscopic scale, the periodicity of the cells will also impact the values of C and n.

While such relationships are useful, developing a constitutive model for cellular materials remains a substantial challenge. The mechanical response that cellular materials exhibit at the continuum scale are directly related to the deformation mechanisms that occur at the level of an individual foam cell. At this level, the structure of these materials is comprised of an interconnected network of cells. The edges of these cells are defined by struts, and possibly thin cell walls as well. Non-linear effects associated with large strain, evolving cellular geometry and cell wall contact lead to the characteristic physical behaviour exhibited by cellular materials. Hence, models that span multiple length scales are required. Models of the macroscopic response of cellular materials generally fall into one of two categories, which are outlined below.

2.1.0.1 *Representative Unit Cell Models*

This category of cellular-scale mechanical models are based on the simplified mechanics of a single, idealized unit cell or other representative structure [5, 78, 231]. The repetitive unit cell structure is not truly random but aims to represent a typical cross-section of a foam material. This chosen cell would reflect possible modes of failure and would allow for an understanding of failure locations and modes. The most widely referenced representative unit cell model was developed by Gibson and Ashby in 1982 [77], which used a representative regular cubic cell. Experimental and empirical evidence were used to determine formulae based on beam deformation mechanisms of cell structures under loading. Similar models have utilized more complex representative sub-structures for the modelling of high-strain reponses in foams, such as the tetrakaidecahedron [305], rhombic dodecahedron or rhombic-trapezoidal dodecahedron [230].

This approach has proven to be satisfactory for many applications, but relies on the simplifying assumption that the repeating unit fills the entire geometry of the foam. Due to this, representative unit cell models often struggle to form an accurate description of evolving non-linear properties, or to construct a full 3D constitutive model that is valid for large deformations. This has lead to many reports indicating that such models tend to over-estimate the bulk modulus and yield strength of real cellular materials [78, 181, 216]. To capture the true morphological structure of real foams and bring the predicted foam response in line with empirical measurements, refinements have added cellular irregularities such as defects and cell wall waviness [31, 231].

2.1.0.2 *Numerical Simulation Based Models*

These models are derived from detailed numerical simulations, most commonly those involving finite-element discretizations of realistic structures that contain a statistically significant number of cells. Finite element analysis (FEA) software is then used to simulate a range of mechanical tests and behaviours to numerically evaluate the response of the material. Sophisticated techniques utilizing computed tomography images as a basis for the geometrical discretisation of these foams are available today. The main advantage of this technique is that it allows for a truly accurate representation of the real geometry, captured using X-ray computed tomography or a serial sectioning method [157, 260].

The availability of 3D information such as pore shape, size distribution, orientation distribution, and connectivity, in addition to the relative density, are critical for many key aspects of microstructural characterization. Since the continuum properties are determined by local events within this cellular structure, to be able to predict these types of local events as well as visualize the distribution of stresses will allow for a more guided understanding of foam design. However, numerical analyses often suffer from issues related to large deformations and contact long before experimentally obtainable strains are reached [123], due to the complexity of the contact present in foam densification.

2.1.1 COMPRESSIVE BEHAVIOUR OF CELLULAR MATERIALS

The non-linear compressive behaviour of cellular materials can be simplified into a three part response: a linearly elastic regime, constant-stress load plateau and stiff densification regime, see Figure 2.1 [78].

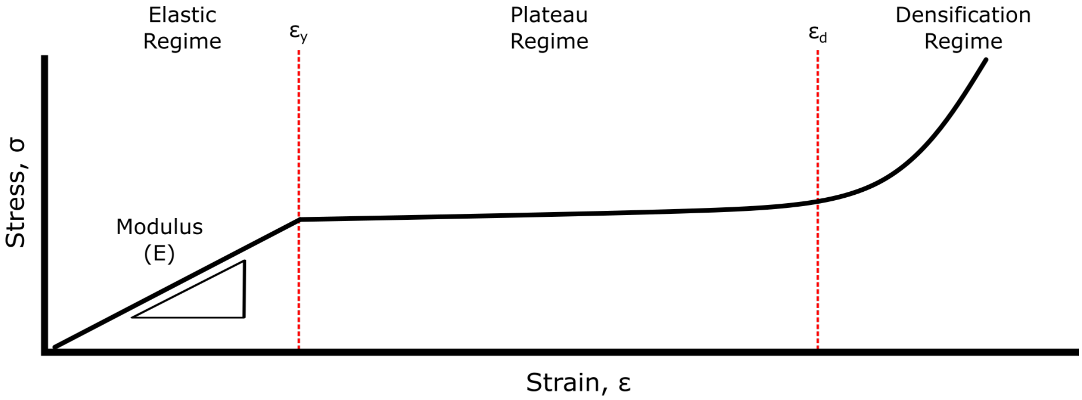

Figure 2.1: A characteristic compressive stress-strain curve for a cellular material [10].

2.1.1.1 *Elastic Region*

In this region of the stress-strain curve, the initial onset of load causes reversible cell bending in the foam micro-structure up to the yield strain ϵ_Y. The Young's modulus of the foam can be experimentally obtained from the linear relationship between stress and strain. Due to localized plastic deformation, this elastic portion of the stress-strain curve is often only partially reversible.

2.1.1.2 *Plateau Region*

In this region of the stress-strain curve, the stress-strain curve exceeds the yield strain ϵ_Y, and the measured stress remains approximately constant at the plateau stress σ_{pl}, as the structure continues to collapse. Cell collapse occurs by buckling, plastic yielding or crushing, depending on the micro-architecture of the unit cell as well as the nature of the constituent materials. The three possible collapse mechanisms compete and the one that requires the lowest stress dominates.

2.1.1.3 *Densification Region*

In this region of the stress-strain curve, following a large compressive strain, the cell walls of the material begin to make contact causing the measured stress to rise steeply. At the critical strain at the onset of densification ε_d, contact between cell walls will suppress the deformation modes that characterize the plateau region. For $\varepsilon > \varepsilon_d$, i.e. when the applied strain exceeds the densification strain, the compressive properties of a cellular solid will be dominated by the compressive properties of the cell wall material.

Based on experimental results, a linear function to determine the densification strain for both elastic and plastic foams was proposed by Gibson-Ashby in their 1997 work [78].

$$\varepsilon_d = 1 - \alpha\tilde{\rho} \tag{2.2}$$

where α varies between ~1.4 and 2.0 for currently available metal foams [12]. A weakness of this method is the reliance on being able to accurately identify the value of α, which is characteristic to each type of foam, which poses a particular challenge when working with a new class of material.

2.1.2 GIBSON-ASHBY MODEL FOR OPEN-CELL FOAMS

The Gibson-Ashby model for cellular materials is the most widely cited example of a representative unit cell model. In their approach, each macroscopic property is derived by correlation to a specific mechanism of deformation occurring in the representative unit cell when subjected to the appropriate loading condition. Simple beam theory is then applied to derive expressions for the scaling behaviour of each effective mechanical property. These expressions assume that the primary dependent variable for all foam mechanics is the relative density of the foam, with all other effects being expressed in various coefficients whose typical ranges are determined by careful experimental measurements.

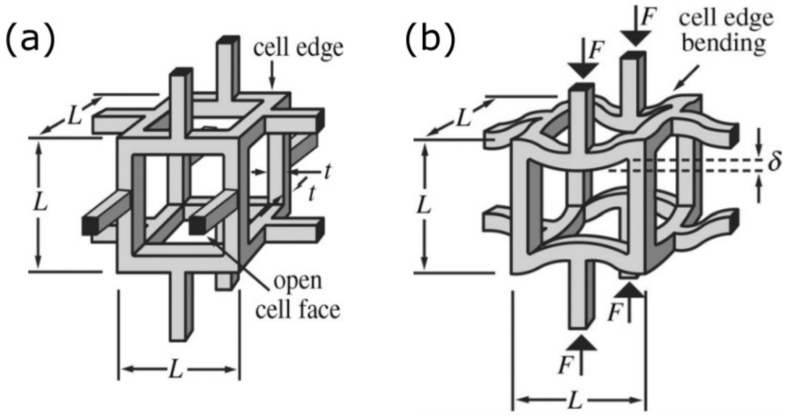

Figure 2.2: (a) The Gibson-Ashby idealized cell in an open-cell foam. (b) Beam deflection when a load is applied to the idealized unit cell. [10]

The Gibson-Ashby idealization of the unit cell in an open-cell foam can be seen in Figure 2.2. For this structure (in which $t << L$), the relative density is

$$\tilde{\rho} \propto \left(\frac{t}{L}\right)^2 \tag{2.3}$$

where L is the cell size and t is the thickness of the cell edges. Expressions for the elastic modulus and compressive yield strength for open-cell foams are summarized in Table 2.1.

PROPERTY	OPEN-CELL FOAM
Elastic Modulus	$E = C(\tilde{\rho})^n E_s$
Compressive Yield Strength	$\sigma_c = C(\tilde{\rho})^n \sigma_{c,s}$

Table 2.1: Typical scaling laws for the effective mechanical properties of open-cell foams as determined by Gibson-Ashby

The scaling variables C and n are of particular importance, and are closely linked to the microstructural details of the cellular material. Cellular solids can deform by either bending or stretching of the cell ligaments. The majority of cellular solids are bending-dominated, and possess scaling exponents of $n = 2$ and $3/2$ for stiffness and strength, respectively. Stretching-dominated cellular materials possess a scaling exponent of $n = 1$ for both stiffness and strength, and are hence much more weight efficient.

The topological criteria that dictates whether a foam will be bending or stretching-dominated behaviour has been shown to be linked to the Maxwell criterion and hence the nodal connectivity. The Maxwell criterion states that a mechanical truss is optimally constrained (rigid, but free of stress) when the number of constraints equals the number of degrees of freedom of the nodes. It has been shown though structural analysis that for a 2D pin-jointed structure, more than 5 nodal connections are required for structural rigidity. If the structure possesses a smaller connectivity than this critical value, it will collapse if pin-jointed, or behave as a compliant bending-dominated structure if it possesses rigid joints. Furthermore, the minimum nodal connectivity for a 3D lattice to be stretching-dominated is 12, regardless of the type of joint [55]. This has lead to the design of stretching-dominated lattice structures with high nodal connectivity, such as the octet-truss lattice.

The expressions for elastic modulus and compressive yield strength of open-cell foams are of particular interest for the analysis in the rest of the thesis, and hence their derivations are briefly outlined below.

2.1.2.1 *Elastic Modulus*

The elastic modulus of the idealised unit cell shown in Figure 2.2b, and therefore the entire open-cell foam, can be calculated by considering the linear-elastic deflection of a beam of length l loaded at the midpoint by a load F. The compressive stress σ experienced by the entire unit cell when a force F is applied, is $\sigma \propto F/A \propto F/L^2$ and hence the force felt by the cell edges is $F \propto \sigma L^2$. For the case of a simply supported beam of length L loaded at the midpoint by a force F, the beam will deflect by a distance δ proportional to $FL^3/E_s I$, where E_s is the modulus for the beam material and $I = t^4/12$ is the second moment of area of the beam with a square cross section, edge length t. The compressive strain experienced by the whole cell is therefore $\varepsilon \propto \frac{2\delta}{L}$, since the deflection is experienced on both sides of the cell.

Assembling these relations gives the modulus of the foam as

$$E = \frac{\sigma}{\varepsilon} \propto \frac{F/L^2}{2\delta/L} \propto \frac{F/L^2}{2FL^2/E_s I} \propto \frac{E_s I}{2L^4} \propto \frac{E_s t^4}{24L^4} \tag{2.4}$$

and substituting in Equation 2.3,

$$\frac{E}{E_s} \propto (\tilde{\rho})^2 \tag{2.5}$$

Since E/E_s tends to 1 as $\tilde{\rho}$ tends towards 1, it is expected that the constant C will be close to unity. This finding of $C = 1$ and $n = 2$ is typical of open-cell foams with low joint connectivity, and is supported by both experiment and numerical simulation [77].

As noted in Table 2.1, the variation of the elastic modulus with density is more generally modelled for open-cell foams with the following relation:

$$\frac{E}{E_s} = C(\tilde{\rho})^n \tag{2.6}$$

where E is the effective modulus, E_s is the modulus of the solid constituent material and C and n are scaling constants that depend on the microstructure of the cellular material.

2.1.2.2 *Compressive Yield Strength*

Similar analysis can be used to model the yield strength of the same idealized unit cell. It should be noted that elastoplastic, elastomeric, and brittle collapse mechanisms each compete, with the dominant mode being the one that requires the lowest stress. In each case, simple scaling laws have been shown to describe the strength scaling of the failure modes relatively well. Elastomeric foams collapse by elastic buckling whereas brittle foams collapse by cell fracture. Herein we focus on elastoplastic foam behaviour, in which collapse proceeds by plastic yielding of the cell struts.

Plastic yielding of the loaded struts will occur when the force exceeds their fully plastic moment,

$$M_p = \sigma_{ys} Z_p \propto \sigma_{ys} t^3 \tag{2.7}$$

where Z_p is the plastic section modulus of the beam. The plastic collapse stress of the foam $\tilde{\sigma}_{pl}$ can then be found by equating the applied moment M on a strut from a transverse force F, to the plastic moment M_p required to form plastic hinges.

$$M \propto Fl \propto \tilde{\sigma}_{pl} L^3 \tag{2.8}$$

Combining equations 2.7 and 2.8 gives the expression:

$$\frac{\tilde{\sigma}_{pl}}{\sigma_{ys}} \propto \left(\frac{t}{L}\right)^3 \propto \left(\frac{\rho}{\rho_s}\right)^{3/2} \tag{2.9}$$

For open-cell foams with plastic yielding behaviour, experiment and numerical simulation [77] gives the following relation:

$$\frac{\sigma_y}{\sigma_{ys}} \approx 0.3 \left(\frac{\rho}{\rho_s}\right)^{3/2} \tag{2.10}$$

where σ_y is the plastic collapse stress of the foam, and σ_{ys} is the yield stress of the solid material, respectively.

2.2 CARBON-BASED CELLULAR MATERIALS

Ongoing developments in the preparation of multifunctional cellular materials have not only leveraged improvements in three dimensional lattice manufacturing techniques, but also in material discovery and synthesis. Stochastic polymeric foams are prepared on a large scale from polymers by bubble formation within a liquid melt, with foaming occurring via physical or chemical blowing agents. Such polymeric foams can be converted to metallic foams through investment casting, chemical vapour deposition or slurry casting. Studies of the effect of lattice structure on material property were driven by macroscale fabrication techniques such as injection moulding of metals into ceramic casts of wax truss core panels, and later millimeter scale lithographic techniques involving the sintering of metallic powders with lasers or electron beams. Recent development of high-resolution fabrication techniques such as two photon lithography (2-PL) or the self-assembly of structured films have allowed for the fabrication of polymeric nano- and

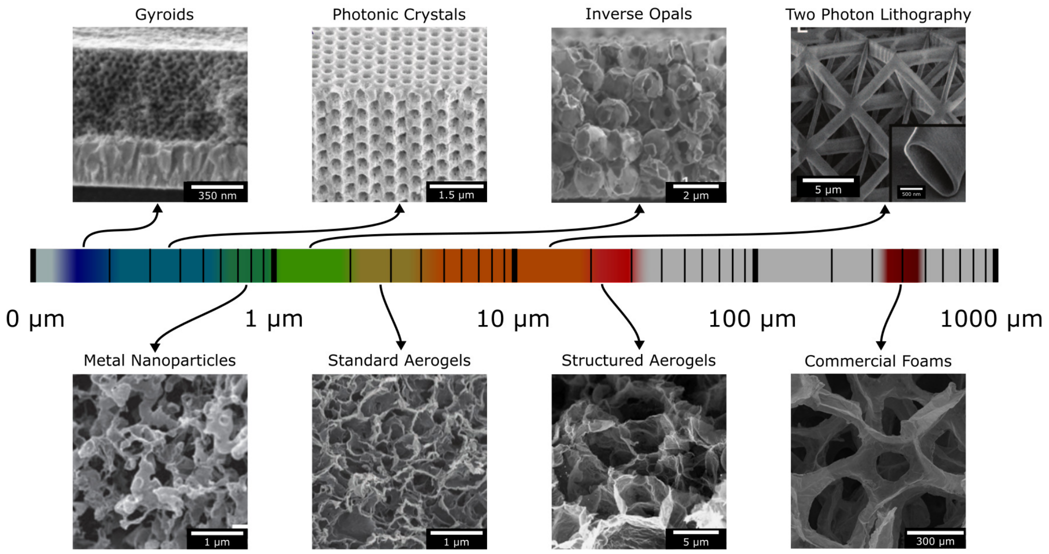

Figure 2.3: Images of the unit cell scales that current state-of-the-art fabrication techniques can reach in the preparation of 3D cellular materials.

micro-lattices. These polymeric lattices have been used as templates for the preparation of hollow metallic [158] and hollow ceramic [156] nanolattices through the addition of an overlayer and subsequent removal of the internal structure.

Carbon foams are a distinct class of foams that are chemically inert, with a low coefficient of thermal expansion, high stiffness and tailorable thermal and electrical conductivities, making them attractive for both structural and device applications. Currently, a range of fabrication methods exist in the fabrication of carbon-based foams, each with different physical properties that depend on the nature of the constituent carbon as well as the 3D structure. For example, glassy carbon microlattices can be prepared through pyrolysis of a polymer lattice, exhibiting extremely strong mechanical properties but are non-conductive and cannot yet be fabricated on a large scale [16, 219]. Graphene aerogels are moderately conductive, compressible and scalable in production but remain mechanically compliant with measured conductivities that are significantly lower than continuous networks of graphene [33, 223, 276]. Such continuous 3D graphene networks can be only obtained by templated CVD growth of graphene onto a networked catalytic template, which is discussed further in Chapter 2.4. Figures 2.3 and 2.4 respectively display and compare the length scales accessible to state-of-the-art cellular materials. To give context to the work presented in Chapters 4, 5 and 6, a review of the various methods by which a carbon-based cellular material may be prepared and a description of their mechanical properties (if measured) can be found below, grouped by degree of control over the final cellular architecture.

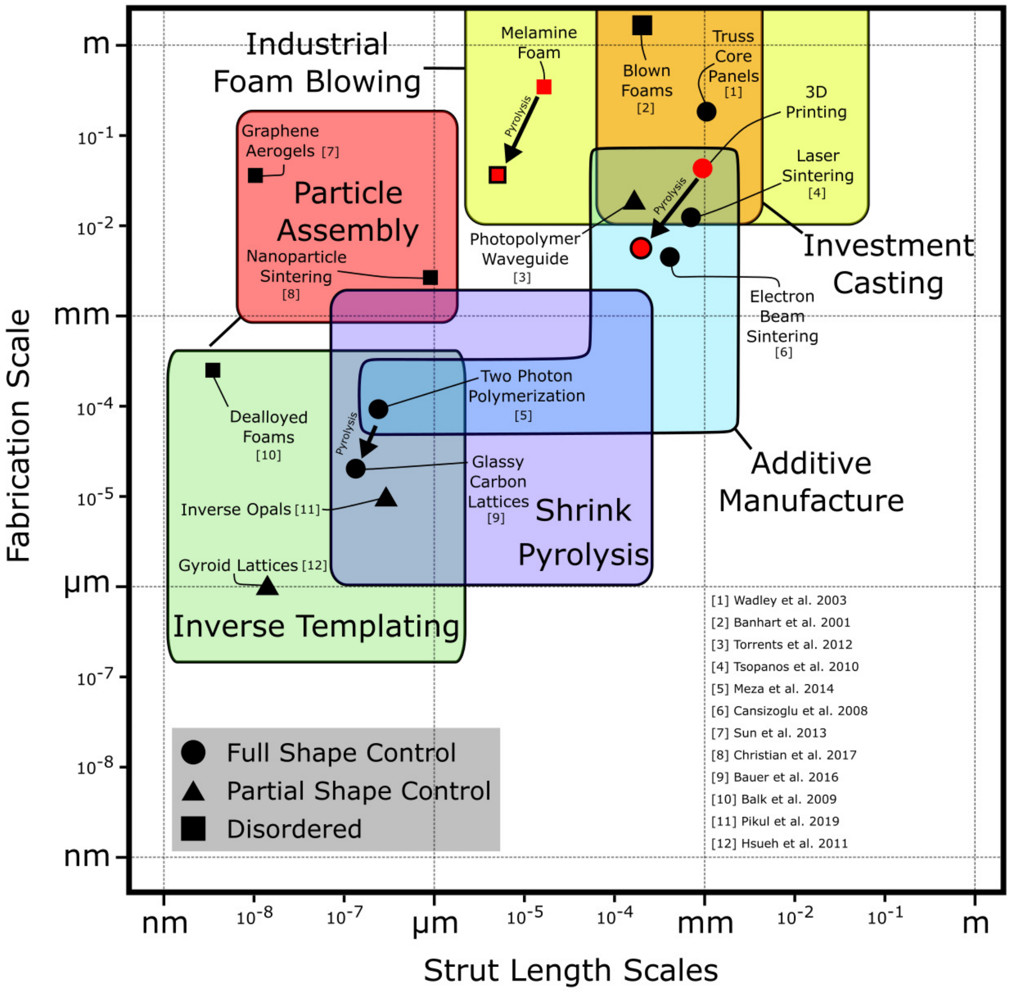

Figure 2.4: Comparison of fabricated cellular materials with a range of material strut length scales and demonstrated fabrication scales. A range of state-of-the-art and industrial methods are highlighted, comparing industrial methods such as foam blowing and investment casting to recently developed high-resolution fabrication methods such as two photon lithography and gyroid film self-assembly.

2.2.1 DISORDERED CELLULAR MATERIALS

2.2.1.1 *Commercial Metal Foams*

The commercially available macroscopic catalytic templates used for the growth of 3D CVD graphene are commonly high-purity nickel foams, formed by CVD of nickel tetracarbonyl onto open-cell polyurethane substrates [194]. Such foams possess a unit cell size of ~500 µm and strut sizes of ~75µm, see Fig. 2.5a. The nickel CVD process allows for a uniform deposition of nickel with a very high chemical purity (>99.8%), over the 3D polymer substrate. A sintering process afterwards removes the polymer substrate in a controlled atmosphere at high temperature. The open-cell polyurethane template that gives the nickel foam its ultimate shape is formed by blowing of a polymer melt through use of a physical or chemical blowing agent.

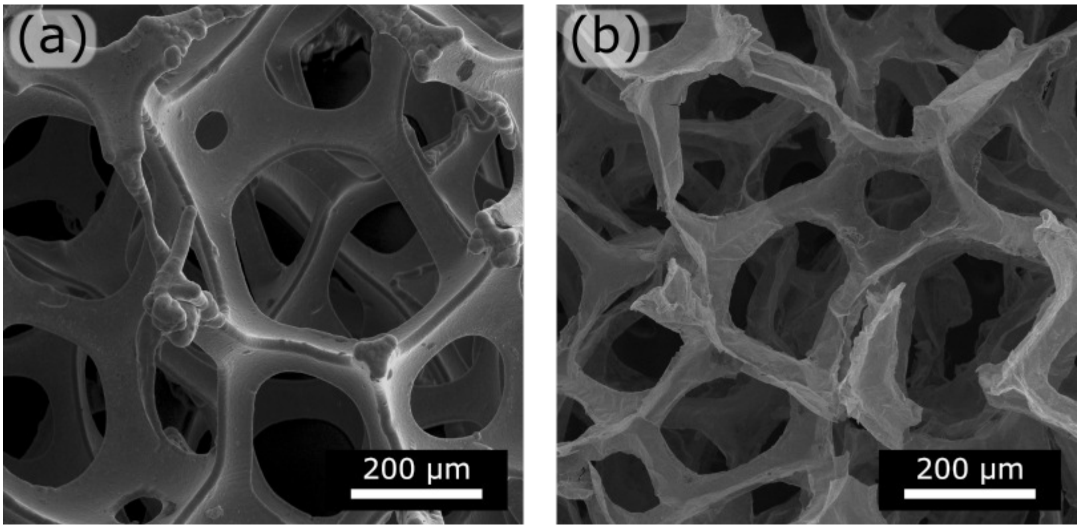

Figure 2.5: SEM images of macroscopic graphene foams grown on commercial nickel foam templates. (a) Commercial nickel foam. (b) Freestanding multilayered graphene foam grown from a commercial nickel foam template.

The bottom-up growth of CVD graphene on a 3D metal catalytic support was first demonstrated by Chen et al. in 2011 [36], who utilized CVD to grow graphene on a commercial nickel foam template. Raman spectroscopy was used to determine the presence of only a few layers of high quality graphene. After removal of the Ni foam core, a high surface area graphene monolith remained (850 m^2 g^{-1}, 10 S/cm), see Fig. 2.5b. Chen et al. also reported that uniformly monolayer graphene coatings could be achieved through the use of copper sponges. However, the collapse of the graphene sponges could not be prevented after the template removal [36].

Though some efforts have been made to characterize the mechanical properties of CVD-grown graphene foams, it must be noted that all studies noted below used samples of graphene foam purchased from the Graphene Supermarket (Calverton, NY, USA), motivating the growth, and subsequent mechanical investigation of the CVD graphene foams in Chapter 4. One such prior study by Nieto et al.[169] utilized in-situ tensile testing inside an SEM, and reported a macroscopic Young's modulus of 340 kPa at a relative density of 0.002. This low value was attributed to a high defect density and bending of the cell walls of the foam. A second study by Yocham et al. [282] compressed foam samples between platens, measuring a modulus of 12.5 kPa. In addition, Nautiyal et al. [166, 167] found that such graphene foams possessed extraordinary damping capabilities due to energy dissipation through three multiscale dampening mechanisms: ripple formation in sheets, weak interlayer van der Waals interactions and structural branch bending.

2.2.1.2 *Powder Metallurgy/Hot-Pressing*

Powder metallurgy has also been used to prepare porous metallic templates through the hot-pressing of micro or nanoparticles, which causes sintering and coagulation of the particles into a networked solid. Subsequent CVD of graphene and etching of the porous metallic templates afforded 3D graphene networks that inherited the key length scales (pore sizes, strut diameters) of the sintered foam. Porous Cu-graphene heterostructures with pores of about 30 µm and a porosity of 35% have been prepared and demonstrate improved thermal conductivity (approximately 40% at 1173 K) when compared to porous Cu [206]. Similarly, Ni particles of 1 µm diameter were used to prepare a freestanding multilayered graphene foam with high specific surface area (1080 m^2 g^{-1}) electrical conductivity (13.8 S cm^{-1}) [222], see Fig. 2.6a.

Nickel nanowires with a diameter of 500 nm were similarly assembled by Min et al. [160] into a nickel nanowire foam prior to 3D CVD graphene growth, forming a monolithic porous foam that retained the wire shapes, Fig. 2.6b. Growth was carried out at 670°C to avoid agglomeration of the nanowires into larger clusters. The 3D graphene foam possessed a high electrical conductivity (17.5 S/cm) and large specific surface area (145 m^2/g), with a density of 0.073 g/cm^3.

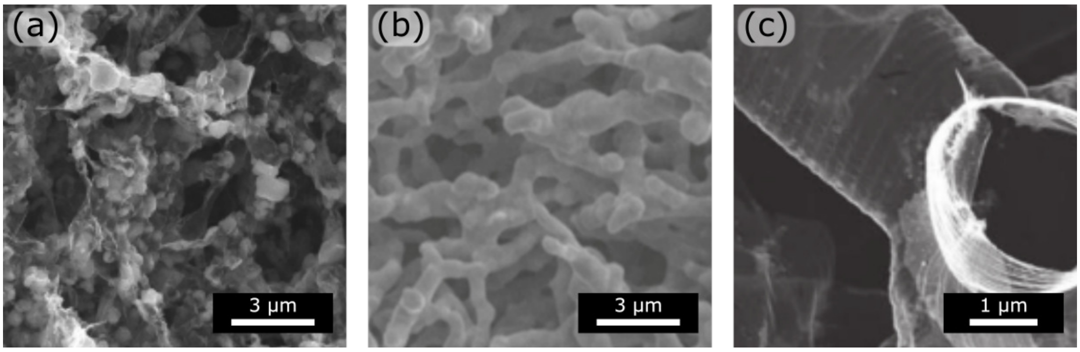

Figure 2.6: SEM images of porous cellular materials formed by hot-pressing. (a) Foam formed of nickel particles of 1 µm diameter [222]. (b) Hot-pressed nickel nanowire foam [160]. (c) Hollow corrugated pipe of Aerographite [154].

The available catalysts for this approach are not limited to just nickel and copper. Mecklenburg et al. [154] demonstrated the use of ZnO networks as a template for CVD growth of graphene. Macroscopic ZnO networks were formed by hot pressing powders of ZnO with tetrapod morphology to form connective junctions. During the graphene CVD process, the intake of hydrogen gas can reduce the ZnO to form metallic Zn, which is precipitated out of the exhaust system, but not before the deposition of a thin 15 nm hollow graphitic coating in a 3D structure dubbed 'Aerographite', see Fig. 2.6c. This Aerographite possessed a Young's modulus of 15 kPa and a conductivity of 0.2 S/cm at a density of 0.18 mg cm^{-3}.

2.2.1.3 *De-alloying*

De-alloying of one component in a solid solution alloy can allow for the production of metals with pore sizes down to 10 nm. Such nanoporous metals possess a highly disordered architecture with pore and ligament sizes that are dependent on the dealloying potential and alloy composition. Nanoporous Au prepared from selective dealloying of a Ag-Au alloy was examined mechanically by Hakamada et al. [85]. A power-law dependence of the yield stress on the ligament diameter was observed, suggesting that the deformation is dominated by the reduction of defect concentration and dislocations due to size effects. Selective de-alloying of manganese from a Ni/Mn alloy by Ito et al. [95] produced a nanoporous Ni foam with a 10 nm pore size. Again, a CVD graphene process (900°C, H_2:Ar:Benzene, 5-30 mins) was used to prepare a nanoporous graphene foam. Note that after graphene growth, the average nanopore size grew from 10 nm to between 100 nm and 2000 nm, depending on CVD time and temperature, due to coarsening of the nanoporous structure, see Fig. 2.7a. The freestanding nanoporous graphene foam was isolated via etching of the nickel, and subsequently subjected to a range of electronic and electrochemical characterization.

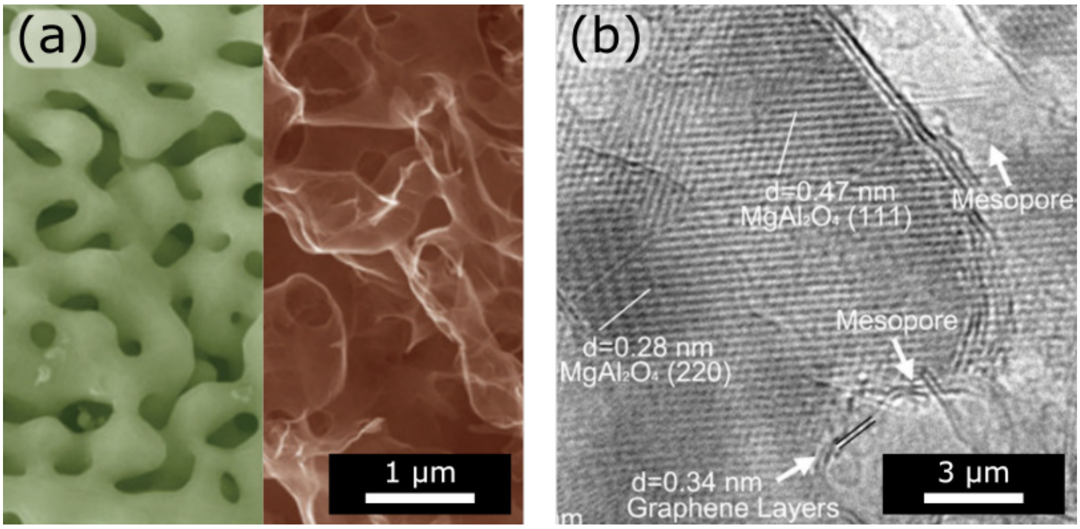

Figure 2.7: (a) De-alloying of a Ni/Mn alloy to form a nanoporous nickel template, subsequently used for the CVD growth of a graphene foam [95]. (b) TEM image of the hierarchical porous graphene network formed upon a Zn-Mg-Al template subjected to Kirkendall diffusion then graphene CVD [227].

2.2.1.4 *Kirkendall diffusion*

The Kirkendall effect is a result of differences in the vacancy diffusion rate between two different metals. As the flux of atoms from the material with a higher diffusion coefficient will be larger, this can result in the motion of the interface between two metals or the development of voids in one metal. This effect has been used to prepare hierarchically mesoporous oxide templates with small pores to prepare porous graphene networks. Shi et al. [227] used a Zn-Mg-Al system to fabricate a hierarchical oxide template with small pores induced by Kirkendall diffusion and large pores attributed to the evaporation of a volatile fraction, see Fig. 2.7b. 3D porous graphene was then grown via CVD (H_2:Ar:CH_4 at 70:200:600 sccm, 10 min) and isolated via chemical etching of the templates. The prepared porous graphene networks possessed mesopores with diameters between 3-25 nm, and a specific surface area of 1448 $m^2\ g^{-1}$.

2.2.1.5 *Gelation of Chemically Modified Graphene*

Graphene oxide (GO) flakes in suspension can be directly gelled and self assemble to form a monolithic reduced GO aerogel [276]. Reduction and gelation of GO occurs in solution through mild heating or the addition of reducing agents [172, 202]. This leads to the removal of oxygen functionalities on the surface of the sheets, leading to coagulation due to inter-flake interactions such as van der Waals forces and hydrogen bonding. Careful removal of the liquid fraction of the gel results in a freestanding microporous monolith with cell walls formed of layered graphene sheets, see Fig. 2.8a. In the literature, slight differences in methodology exist, which utilize a range of reducing species, temperature, flake sizes and additives to tailor the pore size, conductivity or cell structure of the final aerogel product [137, 268, 302].

For instance, complementary solution based templating techniques have been used to offer a degree of control over the final aerogel cell structure. Unidirectional freeze casting of GO suspensions have yielded structures with well-defined lamellar networks with rough control over wall thickness, channel width and shape [202], see Fig. 2.8b. Emulsion templating enables the

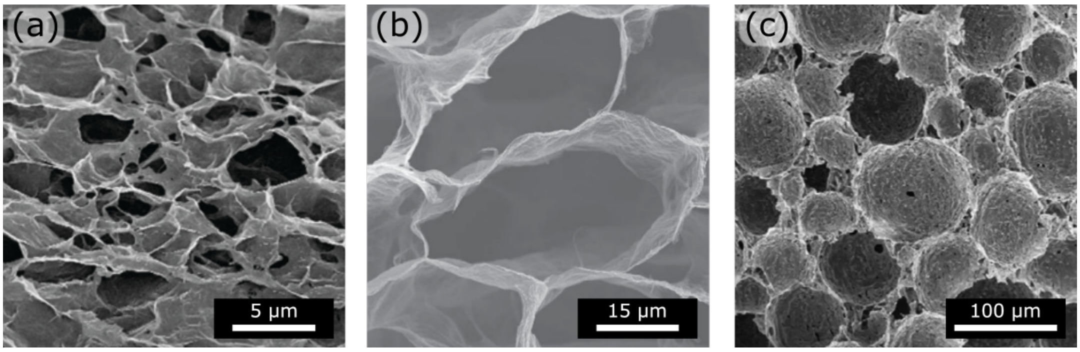

Figure 2.8: Various unstructured and structured graphene aerogels. (a) Unstructured graphene aerogel [276]. (b) Honeycomb-like cellular structure of aerogel that has undergone freeze casting. [202]. (c) Spherical microstructure of graphene aerogel that has undergone emulsion templating [14].

formation of open or closed-cell spherical pores through the self-assembly of flakes at the emulsion interface [14], see Fig. 2.8c.

The unstructured reduced GO aerogels largely demonstrate an elastic-plastic [276] or elastic-brittle mechanical response under compression. However, superelastic behaviour can be obtained through the use of GO flakes of large lateral size [267], or the addition of cellular structure [202]. Furthermore, structured reduced GO aerogels afford a superior Young's modulus compared to randomly gelled structures at comparable densities, due to the increased periodicity of the cellular pores. The density of reduced GO aerogels have ranged between 0.16 mg/cm^3 and 1600 mg/cm^3, with Young's moduli in the range of 0.1 to 6.2 MPa and yield stress values ranging from 3 to 28 kPa. Additionally, the conductivities of the produced sponges were notably poor (0.008-0.37 S cm^{-1}) across a density range of 0.2-100 mg cm^{-3}, see Figure 4.13.

2.2.2 CELLULAR MATERIALS - PARTIAL SHAPE CONTROL

2.2.2.1 *Interference Lithography*

Interference lithography is a technique for patterning regular arrays of fine features through the use of interference patterns in coherent light waves.

Xiao et al. reported graphene sponges created through the use of interference lithography to generate three dimensional patterns of amorphous carbon from a photoresist (NR7). This amorphous carbon structure was coated in a thin layer of sputtered nickel and then annealed in N_2/H_2, see Fig. 2.9a. The amorphous carbon core was able to diffuse through the nickel layer and form sp^2 hybridized graphene layers. Similar to before, the nickel template could be etched away to leave behind a templated hollow graphene network. [272]

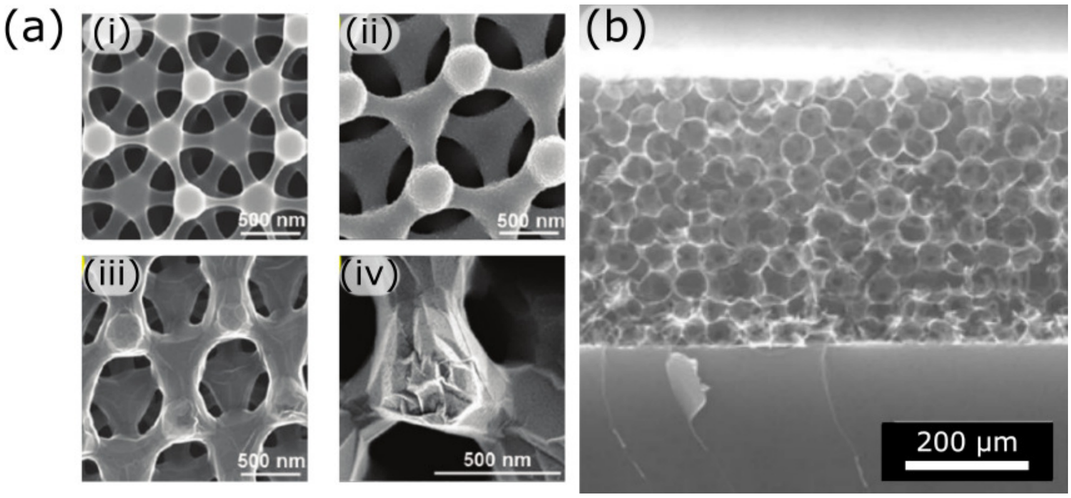

Figure 2.9: (a) SEM images of porous carbon lattice formed from interference lithography (i,ii) coated with nickel, and (iii,iv) converted to 3D graphene. [272] (b) Inverse opal 3D graphenic structure, with 220 nm pore size. [283].

2.2.2.2 *Inverse Opals*

Inverse opal processing uses a regular stack of micro or nano-beads, which are typically silica [283] or polymeric [101, 262]. The spheres are allowed to deposit into a cubic close-packed lattice, whereupon the interstitial spaces are filled with a catalytic template such as nickel or iron. Subsequent removal of the spheres affords a freestanding inverse opal catalyst for the CVD growth of 3D graphene. The pore size of the final freestanding inverse opal 3D graphene structure is intrinsically linked to the size of sphere used, and can range from 100 μm down to 220 nm, see Fig. 2.9b.

2.2.2.3 *Polymer Phase Separation*

Mixtures of chemically distinct polymers possess the ability to self assemble into one-, two- and three-dimensional periodic structures. Known as polymer phase separation, this process is driven by unfavorable interactions between chemical species. During separation, polymer chain reorganization (minimization of reaction enthalpy) is resisted by entropic elasticity (maximization of conformational entropy). This enthalpy-entropy balance governs the phase separation process. Semi-ordered porous polymer templates were prepared by Liu et al. [135] with pore sizes on the order of 20-50 µm, through the phase separation of a simple blend of polystyrene (PS) and polyethylene oxide (PEO), see Fig. 2.10a. Removal of the PEO phase afforded a PS template which could then be coated with Ni by electroless deposition. Subsequent dissolution of the PS fraction results in a freestanding Ni template. CVD growth of graphene (H_2:C_2H_2 64:4 sccm, 26.66 Pa, 700 °C, 3-5 mins) and etching of the Ni template afforded freestanding, bi-continuous 3D graphene monoliths.

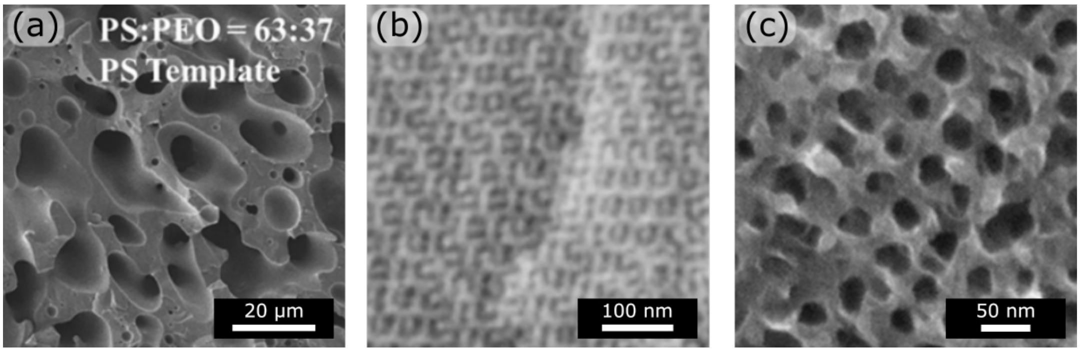

Figure 2.10: Cellular solids formed from polymer phase separation. (a)Semi-ordered microporous polymer templates prepared from phase separation of a simple PS/PEO blend [135]. (b) Bicontinuous inorganic semiconducting gyroid array with 10 nm channels formed by phase separation and in-filling of a block copolymer [49]. (c) Freestanding graphene gyroid with a 60 nm unit cell, formed using a nickel single gyroid template [29].

Block copolymers, in which the chemically distinct homopolymers are covalently linked, can also phase separate in a similar fashion but limited to the nanometer scale. In block copolymers, the microphase separation behaviour can be finely controlled by the composition, architecture and degree of polymerization [15]. As such, a range of block copolymer structures are achievable, ranging from classical lamellar, cylindrical and spherical morphology to the complex gyroid or bicontinuous double diamond. The selective removal of the sacrifical polymer block, followed by backfilling of the porous structure and removal of the remaining polymer template affords a freestanding structure that retains the chosen nanoscale ordering of the block copolymer. Using this method, gyroid structures have been prepared from metal oxides [49, 93, 148], gold [58], platinum [38] and nickel [92], see Fig. 2.10b. Recently, conversion of nickel gyroid structures with 35 and 60 nm unit cell sizes to freestanding graphene gyroids has been demonstrated by Cebo et al. [29] (see Fig. 2.10c), motivating their characterization in Chapter 5.

2.2.3 CELLULAR MATERIALS - FULL SHAPE CONTROL

2.2.3.1 *Additive Manufacturing Techniques*

Direct 3D printing provides a versatile platform for the fabrication of metal templates for the production of graphenic networks. Such additive manufacturing technologies present unparalleled structural control from the physical realization of nearly any unit cell shape. Control over thin feature generation in metals is typically achieved through layer-by-layer powder bed fusion by a focused beam. Selective laser sintering (SLS) and electron beam sintering (EBS) respectively utilize a laser and electron beam as energy sources, printing structures with strut diameters down to the order of 125 microns and with final lateral dimensions on the centimeter scale [241]. Yang et al. [280] utilized a SLS printed square lattice with 1 mm strut length as the template in a CVD graphene process (1000°C, $C_6H_5CH{=}CH_2{:}H_2{:}Ar$ at 4:200:180 sccm, 60 mins) to prepare a monolithic graphene foam. However, the surface of the struts remain extremely rough due to agglomerated particles and partial structural collapse is observed due to the high aspect ratio between the thin walls and thick struts, see Fig. 2.11a.

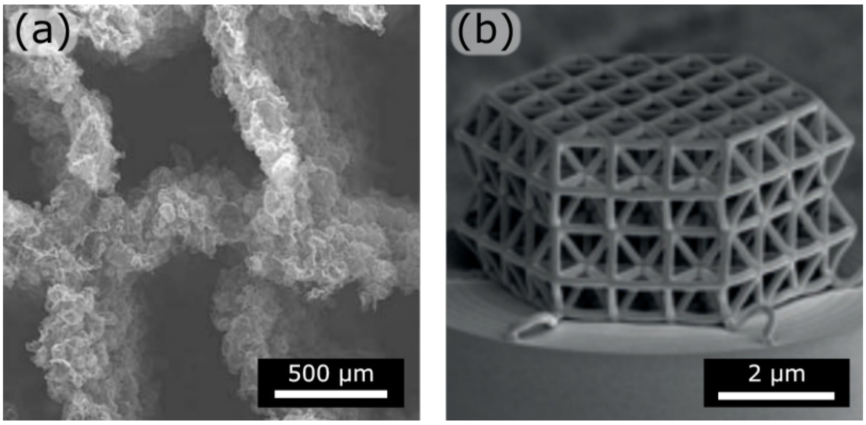

Figure 2.11: Ordered lattice structures prepared using additive manufacturing techniques. (a) Graphenic foam prepared from a SLS printed nickel square lattice [280]. (b) Pyrolysis of 2PL-printed polymeric microlattices creates glassy carbon nanolattices [16].

Ordered polymeric nanolattices can be created out of photo-sensitive polymer resin through the use of three dimensional direct laser writing, a two-photon lithography (2PL) process [248]. 2PL printed cellular materials can possess strut lengths of the order of 5-10μm and strut diameters down to 1 μm. [96, 156] Furthermore, these polymer resin ligaments, when subjected to carefully controlled pyrolysis, will be converted into considerably smaller (up to 80% shrinkage) glassy carbon structures with significantly enhanced mechanical properties. [219] A recent paper by J. Bauer et al. has shown that glassy carbon nanolattices with single struts shorter than 1 μm and diameters as small as 200 nm (see Figure 2.11b) can exhibit material strengths of up to 3 GPa. [16] However, the glassy carbon phase is a disordered carbon allotrope, primarily consisting of non-graphitic sp^2-bonded carbon, requiring surface functionalization to achieve achieve electrical conductivity [134]. Additionally, the 2PL process is extremely laborious and time consuming, and as of yet the final lateral sizes of such 2P-DLW structures are limited to just a few hundred microns, due to the need for fine accuracy over the entire raster range of the beams.

2.3 2D MATERIALS

Two-dimensional (2D) materials are a broad class of atomically thin crystalline materials. Since the isolation of graphene in 2004 [174], the family of 2D materials has grown rapidly to include hundreds of members [309]. Each of these ultra-flat materials have varying electronic, photonic and thermal properties that differ from their bulk material counterparts. These properties arise from their crystalline structures and the reduced dimensionality of the system. Quantum confinement of charge carriers and changes in the interlayer coupling and symmetry elements lead to dramatic changes in the electronic structure and thereby the properties of single- and few-layer TMDCs relative to their bulk counterparts [41, 75]. The same reduced dimensionality can have a large impact on the mechanical strength of a material [18]. As the dimensions of a material shrink to the nanoscale, the size of intrinsic microstructural flaws can be assumed to be reduced to the same length scale, leading to the well-known 'smaller is stronger' phenomenon.

2.3.1 GRAPHENE

Graphene is a 2D sheet of covalently bonded sp^2 hybridized carbon atoms that are each connected to three other carbon atoms in the plane, leaving one electron free in the perpendicular p_z orbital. Within a plane, the unit cell comprises two carbon atoms and the lattice vector has a length of 0.246 nm [123]. The strong covalent bonds between carbon atoms possess a bonding energy of 4.93 eV, and are responsible for the extraordinary mechanical properties of graphene. The additional electron within each p_z orbital are highly mobile, interacting with one another to form additional π bonds. As a result of this bonding scheme, pristine single layered graphene is extremely conductive, with freestanding samples having yielded electron mobilities of 200,000 $cm^2V^{-1}s^{-1}$ at a temperature of 20K [62]. Pristine graphene is also strong, possessing a Young's modulus of 1 TPa and a tensile strength of 130 GPa, as well as being able to be folded and deformed without breaking [121]. However, it should be noted that the exemplary mechanical and electrical properties of graphene are based on measurements of flawless single crystals.

The presence of material defects such as Stone-Wales type defects, single and multiple vacancies, dislocation-like defects, carbon adatoms, domain edges and other imperfections in large samples will introduce points of mechanical weakness and electrical resistance due to inhomogeneities in the bonding and structure at those points.

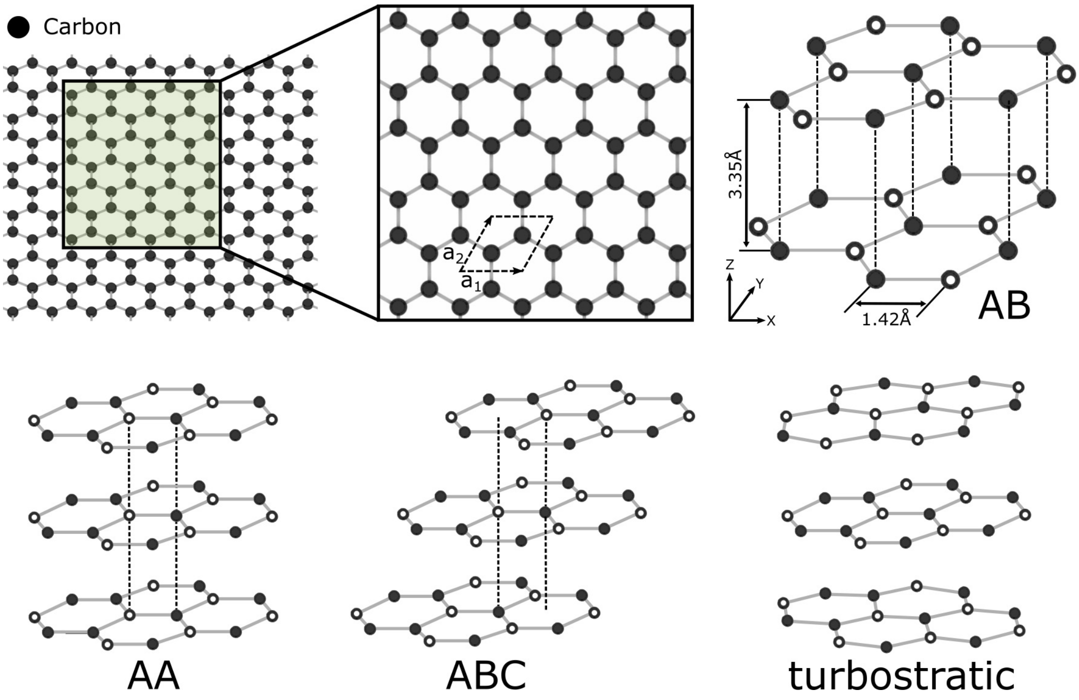

Figure 2.12: Structure of the graphene lattice. The unit cell and lattice vectors are highlighted. The crystal structure of AB, AA, ABC-stacked and turbostratic graphite are also highlighted.

Furthermore, graphitic multilayers can be stacked in a variety of configurations, see Fig. 2.12. The most stable these is AB or Bernal stacking, in which the layers of graphene are structurally commensurate with half the atoms lying directly over the centre of a hexagon in the lower sheet. Turbostratic stacking is the least ordered structure, whereupon each layer is randomly oriented with respect to one another. Layers interact with each other through weak long-range van der Waals interactions, and consequently graphitic multilayers possess a very low out-of-plane shear stiffness and strength compared to their exceptional in-plane modulus. Regardless, the stacking configuration can have a significant impact on the mechanical properties of a multilayer sheet of graphene. For both natural and grown graphitic materials, an increase in layer number leads to increasing amounts of rotational misalignment from perfect ABA symmetry (hex-g) to turbostratic stacking (turbo-g). These differences in stacking lead to differences in the stacking fault energy and consequently significantly decreased interlayer friction for turbostratic graphite [21].

A number of studies have examined the mechanical properties of graphene through to ultrathin graphite and have found that their mechanical properties are highly dependent upon the nature (e.g. stacking order, polycrystallinity) and quality of the material examined. Free-standing, monolayer graphene membranes possess an ultra-high elastic modulus of ~1.0 TPa, as determined by atomistic simulation, ultrasonic, sonic resonance, and static test methods [21, 301]. Multilayered stacks give a modest reduction in this elastic modulus [63]. Additionally, the elastic modulus of CVD-graphene has been shown to be identical to that of pristine graphene if post-processing steps avoid damage or rippling [122]. However, this value can be decreased to ~500 GPa for mechanically exfoliated kish graphite, down to ~250 GPa in the case of chemically derived graphene oxide flakes [70, 79]. Similarly, the intrinsic strength of graphene has been reported to be dependent on the quality of the graphene examined. CVD grown graphene has grain sizes on the micrometer scale, whose boundaries can degrade the strength of graphene depending on whether the grains consist of well-stitched boundaries, or are comprised of overlapping adjacent graphene boundaries (~50 nm in width) without covalently bonding. Covalently stitched graphene leaves the strength of graphene largely intact, remaining at 90 GPa [122].

In the case of shear modulus and shear strength, experiments and simulations have shown that superlubricity on the microscale can be observed in graphite mesas, occurring between atomically smooth surfaces that are structurally incommensurate [139]. If sliding surfaces are unconstrained, spontaneous sheet twisting can occur to move to a more stable commensurate configuration (AB-stacked), leading to lock-in to a higher friction state [68]. Graphene layer orientation and hence structural commensurability between adjacent layers

PROPERTY (IN-PLANE)	UNIT	GRAPHENE LAYERS
DENSITY	kg/m^3	2.27×10^3
ELASTIC MODULUS	GPa	1060[21,301] 500[70] 250[79]
TENSILE STRENGTH	GPa	130[121] 90[122]
SHEAR MODULUS	GPa	2-5 (Hex-g)[21,217] 0.16-0.35 (Turbo-g)[21,217]
SHEAR STRENGTH	GPa	0.1-0.14 (Hex-g)[139,140] 0.0009 - 0.0025 (Turbo-g)[21]

Table 2.2: Summary of the mechanical properties of graphene and graphitic multilayers.

of graphene have a large impact on the measured magnitudes of G_S and τ_{ys}. Nanotribological measurements of AB-stacked single crystal graphite has yielded $G_S \approx$ 2-5 GPa [21, 217] and $\tau_{ys} \approx$ 0.1-0.14 GPa [139, 140]. Measurements of structurally incommensurate stacking configurations (turbostratic stacking) yield significantly lower values of $G_S \approx$ 160-350 MPa [21, 217] and $\tau_{ys} \approx$ 0.9-2.5 MPa [21]. In a superlubric state, the magnitude of the interlayer shear strength can be as low as $\tau_{ys} \approx$ 0.04-0.06 MPa [139].

A table of the experimentally measured mechanical properties of graphene through to graphitic multilayers, as discussed, is shown in Table 2.2.

2.3.2 TMDC - WS_2

Transition metal dichalcogenides (TMDCs) are a family of materials in which transition metal atoms are sandwiched between two layers of close-packed chalcogenide elements (S, Se or Te). About 40 types of TMDCs are known

[41]. Depending on the coordination and oxidation state of the metal atoms, or doping of the lattice, Transition Metal Dichalcogenidess (TMDCs) can be metallic, semimetallic or semiconducting [261]. Among this family, monolayer tungsten disulfide (WS_2) is a particularly interesting representative due to its wide direct band gap (E_g ~2.0 eV) [254], strong spin-orbit coupling [271, 307] and bright room-temperature photoluminescence (PL) [83, 186]. 2H-WS_2 possesses a lattice vector length of 0.315 nm[220], and a thickness of ~0.9 nm[19], see Fig. 2.13. In multilayered WS_2, the indirect band gap luminescence is found to be a phonon-mediated process whose energy follows a two-dimensional confinement model, dependent on the layer number[163].

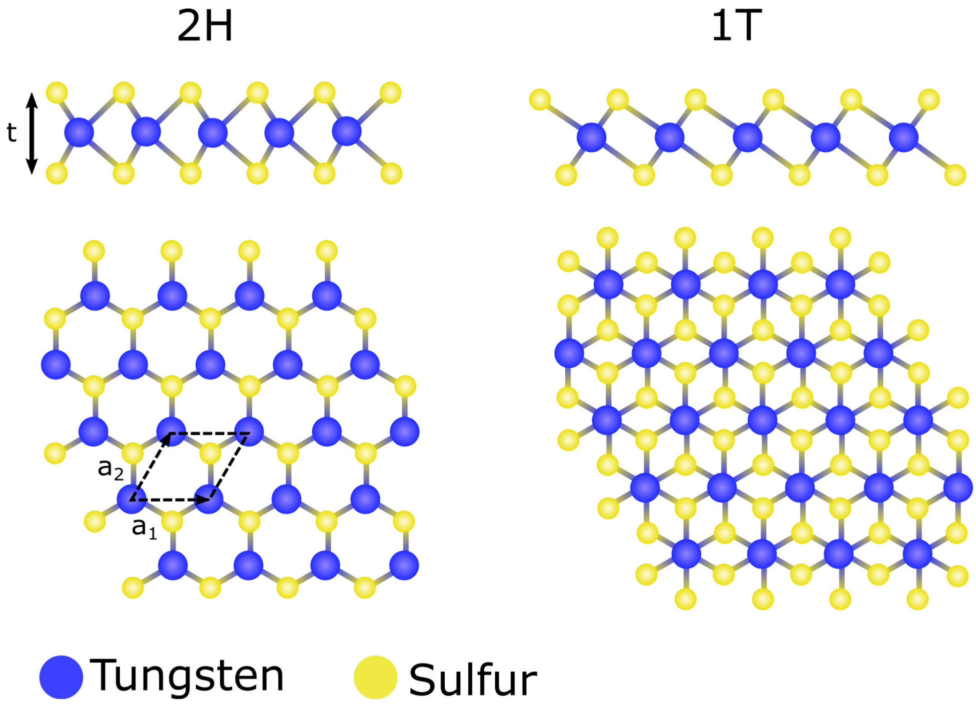

Figure 2.13: Structure of the disulfide (WS_2) lattice. The unit cell and lattice vectors are highlighted for the 2H polytype.

WS_2 has promise as a photoelectrochemical catalyst [233] and electrocatalyst [90] for the hydrogen evolution reaction. As such, nanostructured WS_2 is a particular topic of interest [247] due to the large number of active sites that can originate from the topology of a material. Nanostructures such as fullerene-like nanoparticles [150], nanotubes [32] and nanoflowers [130] each promote the density of active sites. Future use of a 3D nanostructured template for the growth of monolayer WS_2 could allow for the fabrication of structured catalysts with extremely high surface area, motivating the research in Chapter 6.

2.4 CVD GROWTH OF 2D MATERIALS

Chemical vapour deposition (CVD) has emerged as the major industrial method for the scalable, controlled growth of graphene and related 2D materials. The CVD process is able to grow large-area films of 2D materials with precise layer control using catalysts of nearly any shape or size, limited only by the size of the reactor [192]. This versatility in catalyst shape and size has allowed CVD to be used to grow continuous graphitic networks on 3D catalysts. In this section, an overview of the CVD growth process is discussed in the context of graphene growth to form a basis for the studies in Chapters 4, 5 and 6.

2.4.1 GENERAL OVERVIEW

CVD involves the deposition of a solid material onto a heated surface originating from a chemical reaction in the vapor phase. The majority of 2D material CVD processes utilize a catalytically active substrate to promote the dissociation of the precursor gas upon contact. By heating up the substrate in a specific environment, the initiation of precursor dissociation can be finely controlled. Under continued precursor exposure, a surface carbon supersaturation is reached. This leads to nucleation and island growth, which eventually merge to form a polycrystalline film. Detailed in-situ XPS studies have established that the kinetics of the CVD process have a large impact on the growth behaviour of graphene [256, 258]. This view of the CVD process examines the overall flux of active carbon species at the surface (see Fig. 2.14), controlled by a range of simultaneous processes which are outlined below.

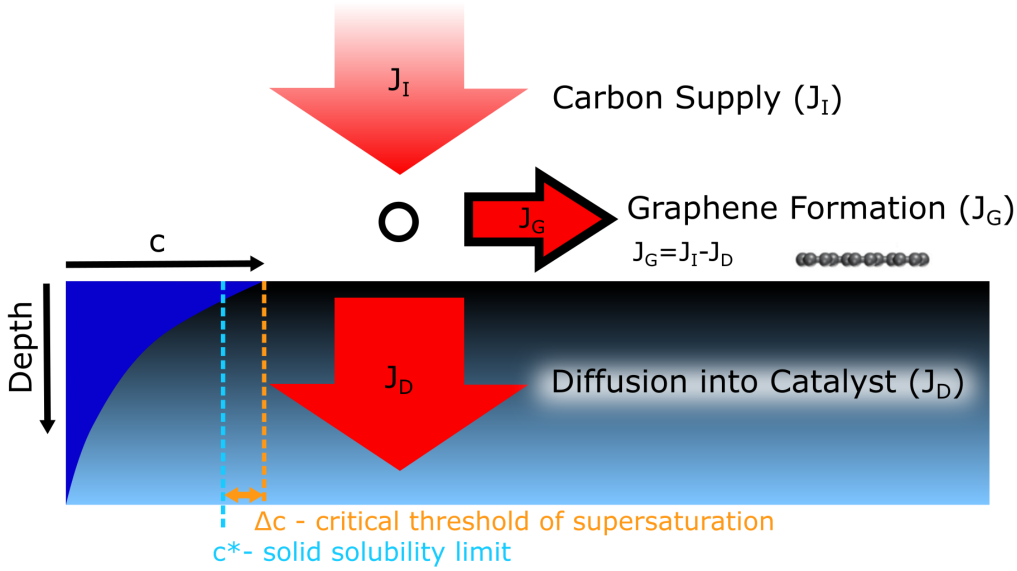

Figure 2.14: Carbon flux resulting from precursor dissociation (J_I) increases the carbon concentration (c) at the surface, which diffuses into the catalyst (J_D). Graphene formation (J_G) occurs when the carbon concentration c exceeds the carbon solvus c*. Figure adapted from Cabrero-Vilatela et al. [26]

Precursors are transported through the main gas flow into the chamber, whereupon species diffuse through a boundary layer (if present) to reach the substrate. This leads to precursor adsorption and breakdown which release active species, which is denoted as J_I in Figure 2.14 and 2.15. A portion of adsorbed precursor will naturally desorb without any reaction taking place. Importantly, based on the permeability (a product of solubility and diffusivity) of the substrate, a portion of active elemental species will also be absorbed into the bulk, which is denoted as J_D in Figure 2.14 and 2.15. Graphene nucleation and formation will remove active surface carbon species, denoted as J_G in Figure 2.14 and 2.15. Carbon species will also be eliminated due to reactive etching by H_2, H_2O or O_2 present in the reaction atmosphere. A final consideration is that upon cooling, absorbed precursor may precipitate out of the bulk.

A generalized growth schematic for the catalytic deposition of graphene is outlined in Figure 2.16. Graphene formation will occur when the surface

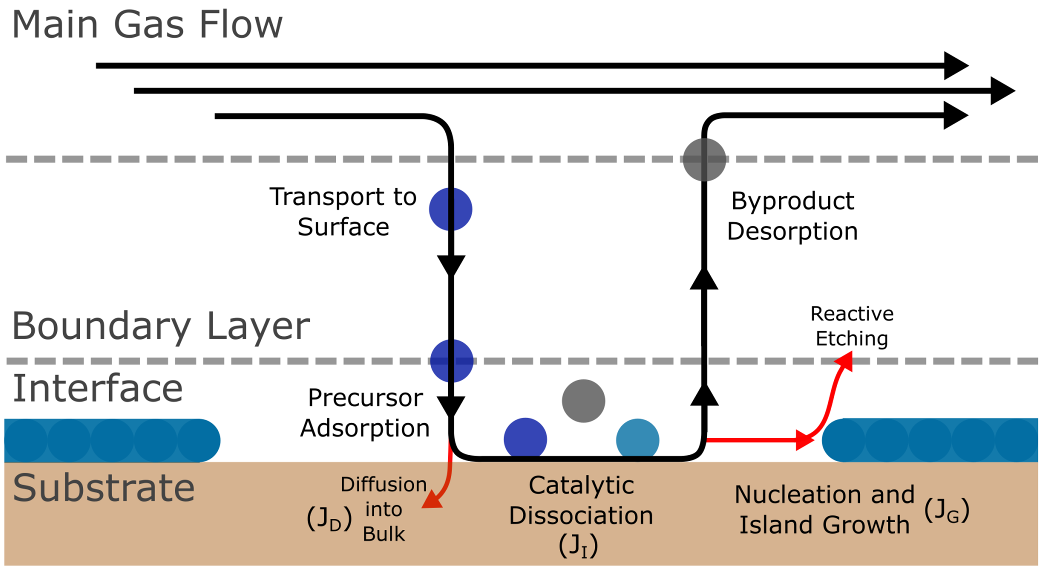

Figure 2.15: More detailed view of the relation between factors that affect the addition and removal of active dissociated carbon at the catalyst surface during a CVD process.

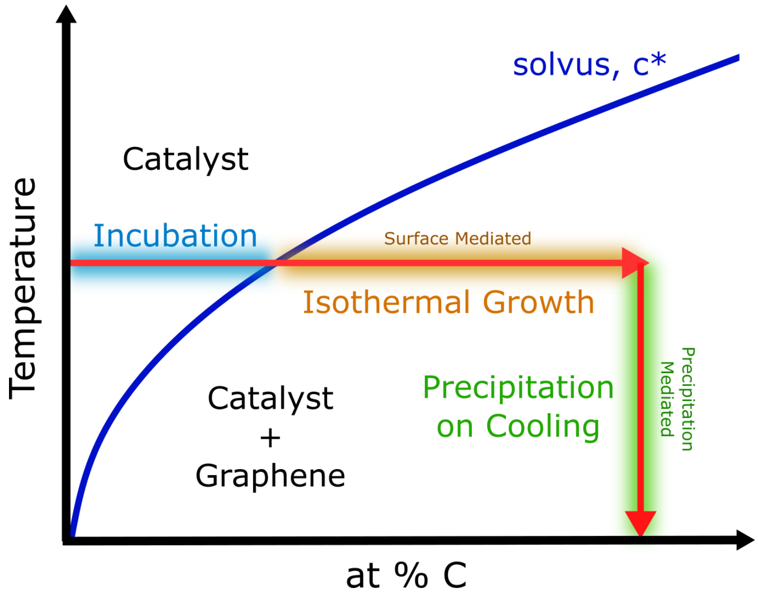

Figure 2.16: Simple carbon-metal solid solution phase diagram of the catalyst surface showing two possible routes for graphene growth: isothermal (orange) and precipitation (green). Figure adapted from Cabrero-Vilatela et al. [26]

carbon concentration c exceeds the carbon solvus c^*. As indicated in the phase diagram of Figure 2.16, this situation can occur from two different mechanisms which are not mutually exclusive,

1. Surface mediated growth, an isothermal process that occurs via solvus crossing due to continued hydrocarbon exposure and dissociation at the catalyst surface at constant temperature. Carbon adatoms that do not diffuse into the bulk but remain on the surface combine to form nuclei and eventually grow and merge to form the 2D material film.

2. Precipitation mediated growth, whereupon solvus crossing occurs due to elemental species that have diffused into the bulk, becoming supersaturated upon cooling at the end of the process due to a reduction in carbon solubility. These species will then precipitate onto the surface upon cooling to form a 2D material film.

However, it should be noted that the flux balance model outlined in Figure 2.14 informs these growth mechanisms throughout the different stages of the CVD process, see Figure 2.16. During the incubation process, incoming flux is balanced by diffusion into the bulk ($J_I = J_D$) with nucleation occurring when the local carbon concentration exceeds the critical threshold for supersaturation (Δc). If the incoming flux is very high ($J_I >> J_D$), ΔC may be reached quickly, leading to high nucleation densities or immediate few-layer growth. Similarly, during the isothermal growth period, graphene grows at a rate ($J_G = J_I - J_D$), where J_I will decrease as graphene coverage increases. When full single-layer coverage is reached, carbon will continue to be supplied through defects and grain boundaries, triggering further nucleation as the local concentration reaches Δc. This can be mediated if J_I is balanced against J_D, allowing the catalyst bulk to act as a carbon sink to avoid local supersaturation. Finally, the reversal of J_D on precursor cooling due to solubility changes can be controlled via the rate of cooling. Hence, in order to create homogeneous high quality films, each of these processes must be carefully controlled via the deposition conditions such as the precursor details, catalyst details, reaction atmosphere, exposure time and cooling rate.

2.4.2 CATALYST

In catalytic CVD, the choice of substrate plays a key role in the reaction dynamics that take place during the growth of 2D materials. The catalytic surface serves to provide a low activation energy pathway for precursor dissociation, graphene nucleation, domain growth and merging. On the nanoscale, the effects of solubility and diffusion become less relevant and hence graphene growth can be viewed as a heterogeneous catalytic surface reaction where the product is a solid rather than gas. In this model, absorbate bond strength becomes a major consideration as good catalysts must readily dissociate the adsorbed species without binding too strongly so that the product is also released [208]. Kinetic analysis of the heterogeneous catalysis of hydrocarbons on transition metal surfaces examined trends in the the activation energy E_a of precursor dissociation and the product binding energy ΔE across the transition metal elements. The balance of these lead to the 'volcano plot' or Bronsted–Evans–Polanyi (BEP) relation of catalyst efficiency against metal orbital energy, see Figure 2.17 [173].

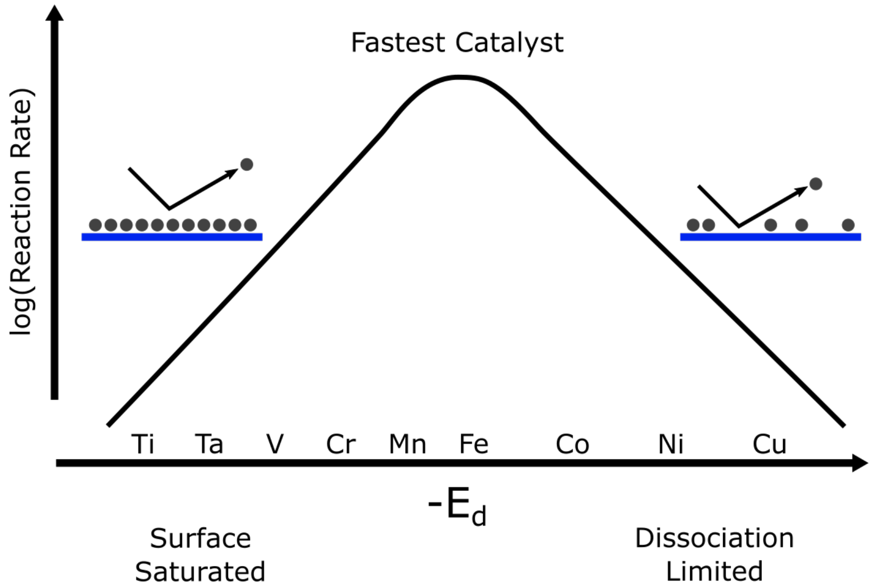

Figure 2.17: Reaction rate (turnover frequency) vs. metal d orbital energy E_d. A schematic of carbon atoms on the metal surfaces across the TM series shows the impact of excessive binding vs dissociation. Adapted from reference [208].

Some key considerations for the choice of CVD catalyst are summarized below,

1. Catalytically active: enhances precursor dissociation at a given temperature. This is linked to E_a and ΔE: the catalyst must readily bind the adsorbed species and dissociate the products.
2. Elemental solubility: lower solubility of the active elemental species in the CVD process will serve to limit any precipitation on cooling, favoring the production of uniform monolayers.
3. Stability at growth conditions: this includes limiting side reactions that can create alternative by-products as well as substrate stability over time, resisting sublimation or roughening.

The choice of catalyst has a strong influence on the growth mechanism(s) that are active during a CVD process. For graphene, a wide range of transition metals have been shown to be catalytically active in the breakdown of hydrocarbon precursors. However, different growth modes can be promoted due to differences in solubility. As can be determined from Fig. 2.16, precursors with low carbon solubility (such as copper) will favor surface mediated, isothermal growth due to a more accessible solvus crossing via hydrocarbon exposure. Alternatively, precipitation mediated growth occurs more typically in catalysts with a higher carbon solubility (such as nickel), due to solvus crossing via carbon precipitation on cooling. However, as always, the complexity of process kinetics as discussed in the flux balance model in Chapter 2.4.1 will inform this process, and careful control over process conditions has demonstrated monolayer isothermal growth of graphene on nickel [257].

The carbon flux balance may also become inhomogeneously distributed across the face of the catalyst, due to the roughness and polycrystallinity of the catalyst [259] as well as the presence of surface and bulk contaminants [22]. These factors will have a strong influence on the nucleation density of graphene, which will preferentially occur at sites of highest local carbon concentration [22, 185, 259]. Furthermore, while a large body of literature exists on the behaviour of carbon due to its importance in metallurgical processes, much less exists for W and S, which need to be considered in conjunction for the growth of WS_2 on a given catalyst. This is explored further in Chapter 7.

2.4.3 PRECURSOR

The role of each precursor is to transport the desired elemental species to the substrate, whereupon precursor breakdown occurs and the elemental species are released along with a by-product. Each precursor compound must be sufficiently stable under the environmental conditions present in the chamber to limit any gas-phase side reactions. Precursors should also catalytically react with the heated substrate at a chosen temperature (typically between 600-1000°C). Typically, methane (CH_4) is utilized as the carbon precursor for the growth of graphene. This choice is motivated by the low carbon fraction, which enables better control of the active carbon flux balance, and H_2 decomposition byproduct which serves as an activator for surface bound carbon [198] and is typically already present in the reaction atmosphere. Precursors with higher carbon fraction and chemical potential such as acetylene (C_2H_2) or benzene (C_2H_6) come with increased likelihood of film inhomogeneity and primary and secondary multilayer graphene nucleation [112].

However, coarsening of fine metallic features at high temperature is a major challenge in the growth of 3D nanostructured CVD graphene, due to self-diffusion at high temperatures such as 1000°C. Processing of a nanoporous Ni foam at 900°C results in severe coarsening of the nanoporous structure, increasing average pore sizes from 10 nm to between 100 and 2000 nm [95]. Similarly, templated nickel gyroid structure with 35 nm unit cell sizes are observed to coarsen at temperatures as low as 500°C, resulting in a loss of regularity [29]. Use of more reactive carbon sources that possess lower decomposition temperatures are crucial in preserving the structure of nanoscale metallic features.

The dissocation of ethylene (C_2H_4) at temperatures as low as 400°C has been observed through in-situ atomistic characterization via XPS of Ni catalysed graphene growth. In the context of the heterogeneous catalyst model, see Figure 2.17, this is related to the activation energy of precursor dissociation ΔE, which declines monotonically across the transition metal series as the the d orbital energy of the transition metal E_d becomes increasingly negative. Use of carbon sources such as acetylene (C_2H_2) has enabled the growth of 3D graphene networks at 500-550°C [29, 262]. Furthermore, carbon precursor pre-dosing schemes in which C_2H_2 is present in the reaction environment prior to heating have been shown to stabilize nanostructured nickel templates, preventing the formation of nickel clusters at growth temperatures of 650°C [29]. This is attributed to an increased uptake of carbon into the nickel template at low temperatures, leading to catalyst saturation and the formation of stabilizing surface graphitic deposits and nickel surface carbides prior to reaching the growth temperature.

3

EXPERIMENTAL METHODOLOGY

This chapter presents the systems, processes and characterization techniques used in this thesis. Firstly, material synthesis techniques used for the preparation of 3D CVD graphene-based cellular materials and planar growth of WS_2 are discussed. The associated material and mechanical characterization techniques are then introduced. This chapter provides an overview of the experimental methods and processes used for the work described in Chapters 4, 5, 6 and 7.

3.1 MATERIAL SYNTHESIS

3.1.1 3D CATALYTIC TEMPLATE PREPARATION

3.1.1.1 *Nickel Foam Preparation*

The nickel foam samples used herein were purchased from MTIXTL, with a purity of >99.99%, 95% porosity, 1.6 mm thickness, 80-110 pores per inch and a bulk density of 450 kg/m^3. Such foams are manufactured by chemical vapour deposition of nickel onto a polymeric scaffold, and possess hollow triangular struts with a low nodal connectivity, see Figure 3.1. Nickel foams were used as disordered macroscopic templates for the production of freestanding 3D graphene foams and their subsequent mechanical characterization, as discussed in Chapter 4. Prior to graphene growth, foam samples were cut to size and cleaned via sonication in acetone (5 min), isopropyl alcohol (5 min) before being blown dry with nitrogen.

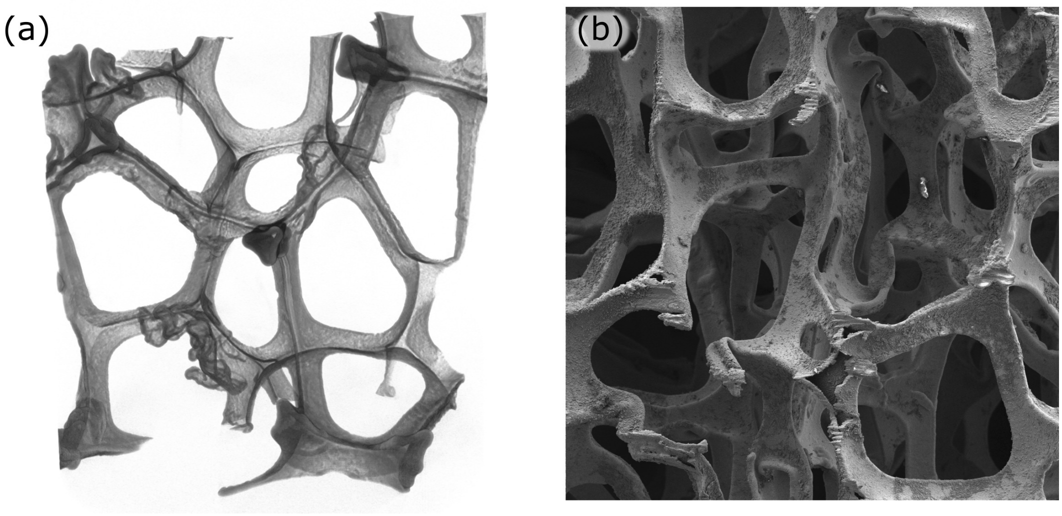

Figure 3.1: Morphology of commercial nickel foam templates. (a) X-ray micro computed tomography image of the nickel foam template, displaying the triangular struts with low nodal connectivity. (b) SEM image of laser-cut cross section of the nickel foam template showing the hollow struts which arise from the CVD of nickel onto a polymer scaffold followed by template removal. Roughness of the strut surfaces are caused by sputtering during the laser sectioning process.

3.1.1.2 *Gyroid Preparation*

The nickel double gyroid thin film coatings of various thicknesses were manufactured by block co-polymer self-assembly, in collaboration with Tomasz Cebo (see Fig. 3.2), as described in detail elsewhere [245]. Nickel gyroid films were used as a nanoscale ordered template for the production of freestanding hollow graphene gyroids, as discussed in Chapter 4. The salient points of their production are described in brief below.

A polymeric gyroidal layer was prepared through the self-assembly of polyisoprene-block-polystyrene-block-poly(ethylene oxide) triblock copolymer, which consists of linearly connected polyisoprene, poly(ethylene oxide), and polystyrene blocks. This triblock terpolymer was synthesised using anionic polymerization by members of the Steiner research group, and is described in detail in reference [13]. Samples are fabricated on a glass slide of thickness 2.2 mm with a 350 nm thick layer of fluorine-doped tin oxide (FTO) coating (Solarinox). Substrates were cleaned with a brief piranha etch then immersed for 15 s in a 0.2% (v/v) of octyltrichlorosilane (Sigma-Aldrich) in anhydrous cyclohexane (Sigma-Aldrich). An 80 kg/mol form with block volume fractions of 30%, 53%, and 17% was spun-coat onto the cleaned and functionalized substrates from a 10% (w/w) anhydrous anisole (Sigma-Aldrich) solution at 1200 rpm. The thickness of this film was slightly varied by altering the weight ratio of polymer in solvent, resulting in film thicknesses of 300, 500 and 700 nm ± 25 nm, as measured by cross-sectional SEM images.

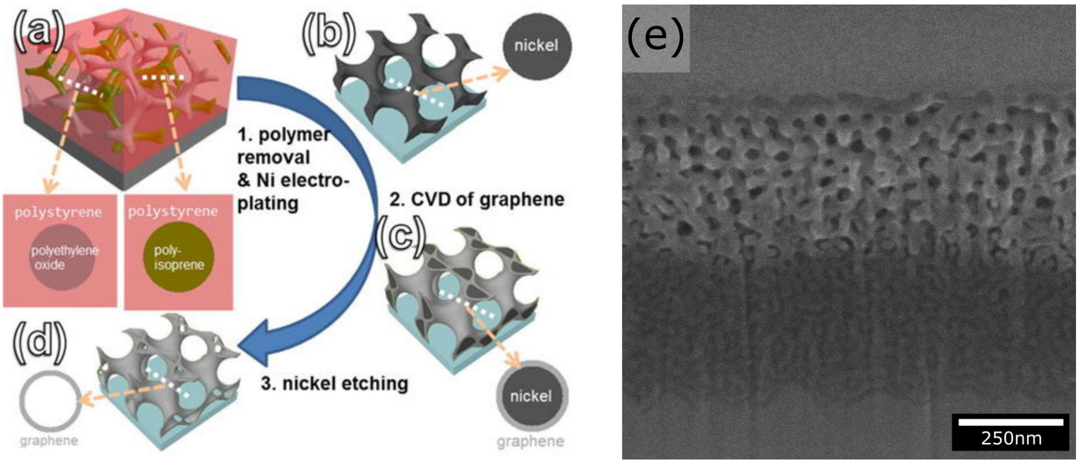

Figure 3.2: (a) Schematic geometry and composition of the alternating gyroid (gyroidal) phase of the ISO triblock copolymer (b) Nickel gyroid prepared by electroplating into the empty space left after polyisoprene removal. (c) Nickel gyroid covered in graphene after CVD with the acetylene precursor. (d) Self-standing graphene gyroid after nickel removal with ferric chloride solution. The insets show cross-sections of the respective gyroid along the indicated white lines. Figure reproduced from Cebo et al. [29] (e) Freestanding nickel gyroid prior to hydrogen annealing. The extremely small channel network inhibits the release of deep polymeric residues through the use of solvents.

Samples were then annealed for 30 minutes at 180 °C in a vacuum oven (ramp rate 150 °C/h), and allowed to cool over a period of 12h. The polyisoprene block was then degraded with UV exposure (VWR International, 254 nm, 50mW/cm^2) for 2 hours and removed by dissolution in ethanol. Nickel was introduced into the empty template left after polyisoprene removal using commercially available nickel electroplating solution (Alfa Aesar Bright Finish

Ni plating solution) at a constant potential of -1.05 V. Nickel is deposited within and on top of the polymer template, and excess nickel is cleaved at the interface between structured and bulk gold using Kapton tape, ensuring an interface with low surface roughness. Some of the remaining polymers were removed by oxygen plasma etching (Diener MRC 100 at 100% power) for 20 minutes, though not all could be removed this way, see Fig. 3.2. A hydrogen annealing process (250°C, 100:100 sccm H_2:Ar, 50 mBar) was carried out to remove polymeric residues and provide a clean and freestanding nickel gyroidal template prior to graphene growth. The resulting nickel single gyroid has a unit cell size of 60 nm and a fill fraction of 40%, as determined by SEM image analysis in Figure 3.3.

3.1.2 GRAPHENE CVD SYNTHESIS

A hot-wall tube furnace and low-pressure (LP-CVD) cold-wall reactor was used for the CVD growth of graphene. A cold-wall laser reactor was used for the MOCVD growth of WS_2. Each system were used due to the differences in the required growth conditions, precursors and catalysts for each project, which are discussed below for each respective system.

3.1.2.1 *Tube Furnace*

The hot-wall tube furnace possesses a large homogeneous hot-zone, enabling the use of catalysts with large lateral sizes. The commercial nickel foam templates, such as those discussed in Chapter 3.1.1.1 and used in Chapter 4, were processed with dimensions of 2.5×8 cm. Such sizes were used to both demonstrate large-area growth of CVD graphitic foams and allow for the preparation of samples for mechanical testing with relatively large lateral size, and equal relative densities. Use of a secondary internal quartz tube additionally allows for the isolation of contaminants that are released during the carbonization of materials, such as is performed in Chapter 6.

The tube-furnace system consists of a custom-built vacuum chamber with central quartz tube (external diameter 100 mm) coupled to stainless steel water-cooled flanges with gas inlets, see Fig. 3.4. A dual pumping system composed of a rotary roughing pump that reaches base pressures of 10^{-3}mbar

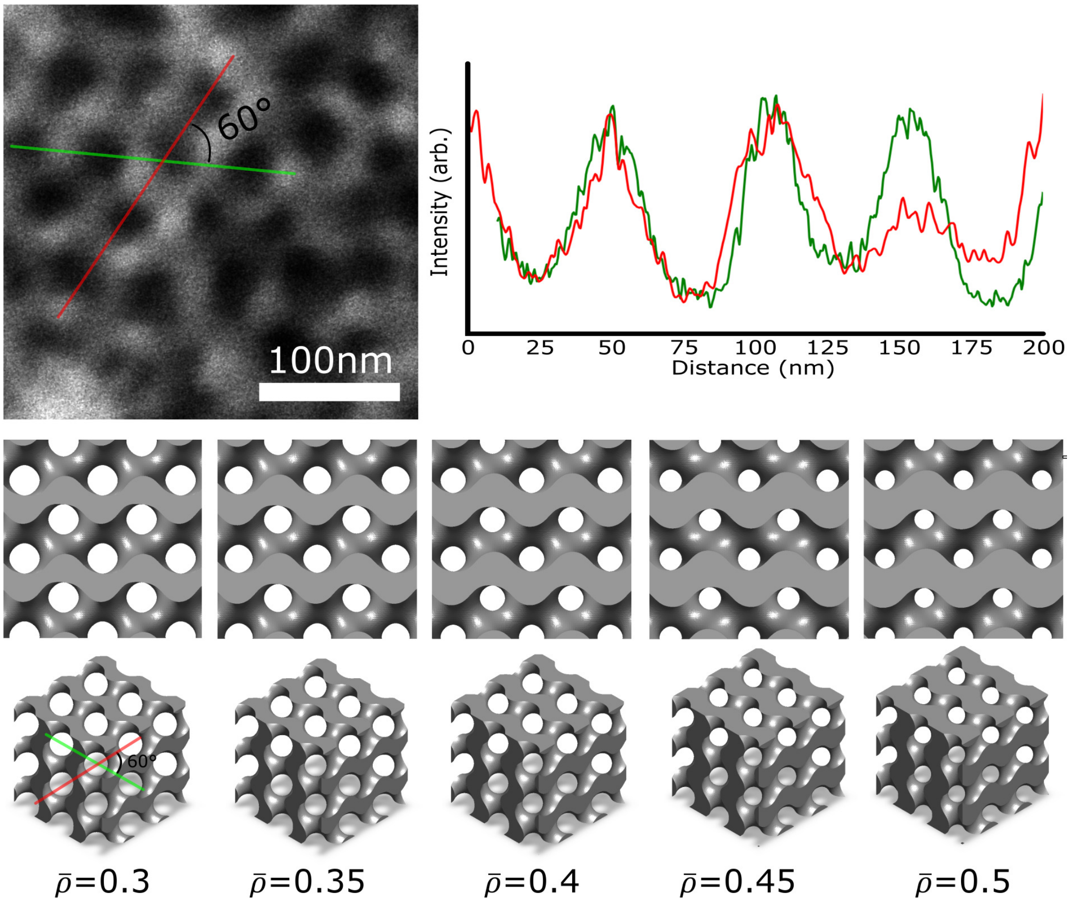

Figure 3.3: SEM image determination of volume fill fraction for the nickel solid gyroid lattice. Line profiles are taken from a high-magnification SEM image of the gyroid cross-section. The FWHM of the peaks are compared to those of modelled solid gyroids across a range of relative densities, and were found to most closely match those of the 40% solid gyroid.

and a turbomolecular pump that can achieve base pressures 10^{-7}mbar are used. Process gases are fed into the tube furnace upstream through the use of electronic mass flow controllers (MFCs). C_2H_4 (>99.95%, 5% in Ar, BOC Gases), H_2 (>99.999%, BOC Gases) and Ar are used. The samples are placed within a smaller quartz tube (external diameter 30mm), which is loaded into the furnace and held at the centre with quartz spacers. Temperatures are monitored with a thermocouple attached to the furnace, entering vertically through the top and contacting the top of the external quartz tube at the centre of the hot zone. Furnace temperatures (up to 1065 °C) are controlled

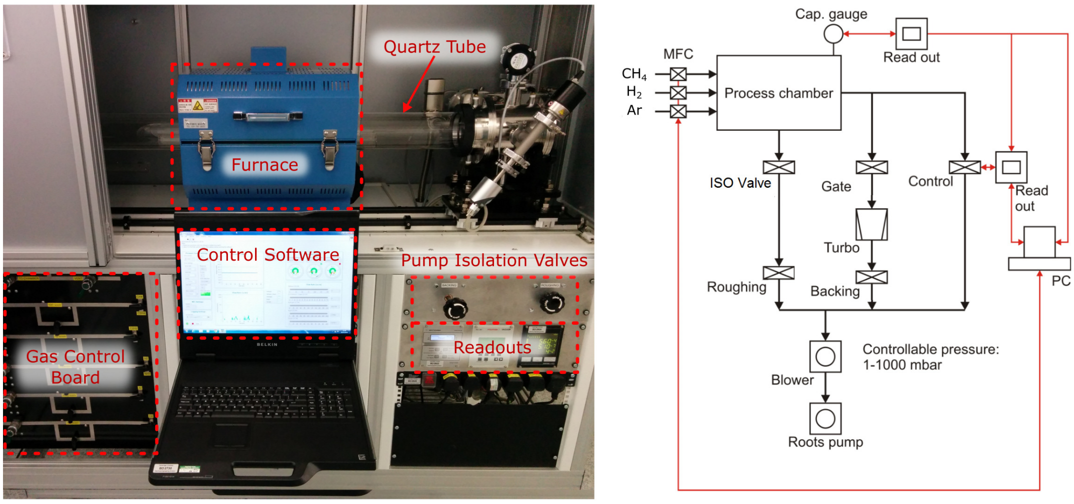

Figure 3.4: Image of the tube furnace, with associated systems labelled. Schematic of the CVD gas handling system on the right.

with external LabView software, with desired ramp rates and hold times programmed in advance.

CVD GROWTH OF GRAPHITIC FOAMS: Commercial nickel foams (see Chapter 3.1.1.1) were used as templates for the growth of freestanding graphitic foams in Chapter 4. Polycrystalline graphitic layers grow in parallel to the Ni surface for all grain orientations, resulting in continuous sheets that envelop the catalytic template [103]. This templating effect is well established, with graphitic lattice-metal interactions at the nanoscale dictate the nucleation and growth dynamics and thus the final lattice morphology [89, 257]. However, the gas flow within a porous network is expected to be impeded by the internal structure. These conditions can lead to local differences in deposition rate, material quality, and layer number. Such an effect has been observed by Rho et al. [206] in the preparation of 3D porous Cu-graphene composites, prepared by CVD of graphene upon sintered Cu microparticles. The structures possessed pore sizes of 30 µm, a porosity of ~35% and lateral sizes of 1×1×0.5 cm, and the CVD of graphene was carried out under 1.3 mBar of CH_4, at 1000°C for 30 minutes. Through the use of Raman spectroscopy and TEM at points along the sample cross-section, it was shown that the carbon layers far from the external template faces (i.e.

within the pores of the structure) were significantly more defective, whereas the faces and a separate planar Cu substrate were shown to possess high quality graphitic layers (5-10 nm thick). This difference was attributed to the stagnation of flow within the micropores of the structure, leading to bulk gas-phase reactions and the deposition of graphitic layers with a high defect density.

With this in mind, various growth conditions were tested to optimize the properties of the graphitic foams for homogeneity, handling and measurement. 3D graphitic foams (GF) were prepared in this thesis by CVD on sacrificial open-cell Ni foam templates, with a purity of >99.99%, ~150 µm pore size, 95% porosity, 1.6 mm thickness. Ni foam templates were cut to dimensions of 25 mm × 80 mm × 1.6 mm and cleaned before being loaded within the centre of a quartz tube, ensuring that the wide faces of the substrates were not held close to any adjacent surfaces in order to maximize gas flow in and around the porous substrate. The CVD process was carried out at a total pressure of 50 mBar throughout, placing the process in the mass-transport limited regime, where diffusion through the boundary layer is the rate-limiting step [20].

In all cases, the temperature was ramped up to 950 °C over a period of 30 minutes, before a 60 minute annealing step was performed. These steps were done in a H_2 environment with a flow rate of 200 sccm, in order to reduce oxide species, remove surface contaminants and increase grain size. A mixture of diluted 5% CH_4 in Ar with H_2 was used during growth (180 minutes), with a flow ratio ranging between 1:1 to 3:1 respectively. A richer hydrocarbon atmosphere resulted in a higher average number of graphene layers and thus a higher relative density. Samples were cooled at a maximum rate of 20°C/min after growth in Ar with a flow rate of 200 sccm, over a period of 120 minutes. CVD grown samples were stored in ambient conditions prior to further processing and characterization. A schematic of this growth process is shown in Figure 3.5.

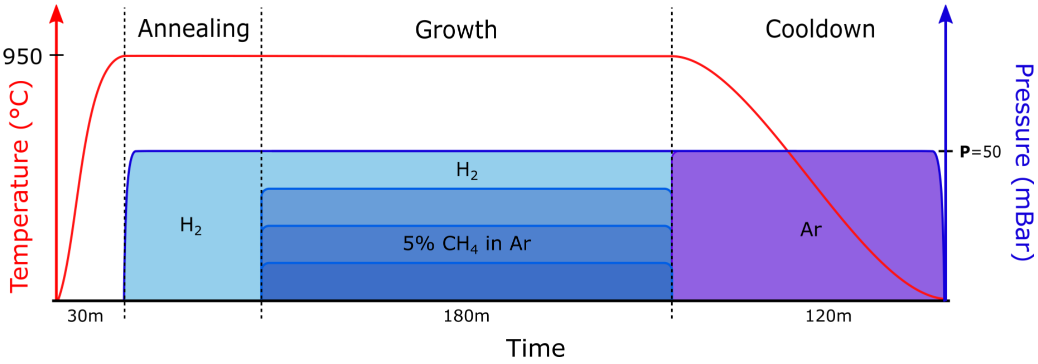

Figure 3.5: Schematic of the tube furnace CVD process conditions used herein to grow graphitic foams of differing relative densities.

Sample homogeneity was confirmed via Raman spectroscopy (Chapter 3.2.6 across the long lateral dimension of the samples, as well as within the porous internal structure as compared to the surface. No significant variation was observed for the process conditions detailed above. This is likely due to the significantly larger pore size, greater porosity and low thickness (spanning ~10 unit cells) of the Ni foam template used herein, resulting in less obstruction of gas transport through the porous network.

PYROLYTIC SHRINKAGE AND GRAPHITIZATION: Polymeric templates were subjected to a slow pyrolytic carbonization process in an inert Argon atmosphere (250 mBar, 200 sccm) that converted the samples to a carbonized network (CN). Samples were ramped to 350°C at a rate of 3°C/min, held 30 minutes then further ramped to 450°C at a rate of 5°C/min and held for an additional 60 minutes. Samples were returned to room temperature over a period of 120 minutes, then removed and stored in ambient conditions. This process, as shown in Figure 3.6a, allowed for the polymeric templates to degass and decompose at a slow rate, preventing severe structural breakdown.

Further increases in carbonization temperature up to 850°C produced no changes in overall mass loss and shrinkage for either the melamine foam or resin lattices. After coating with a thin film of nickel, the samples were placed again in the hot-wall reactor for pyrolytic graphitization, see Figure 3.6b. Samples were raised to a temperature of 1065°C at a rate of 30°C/min

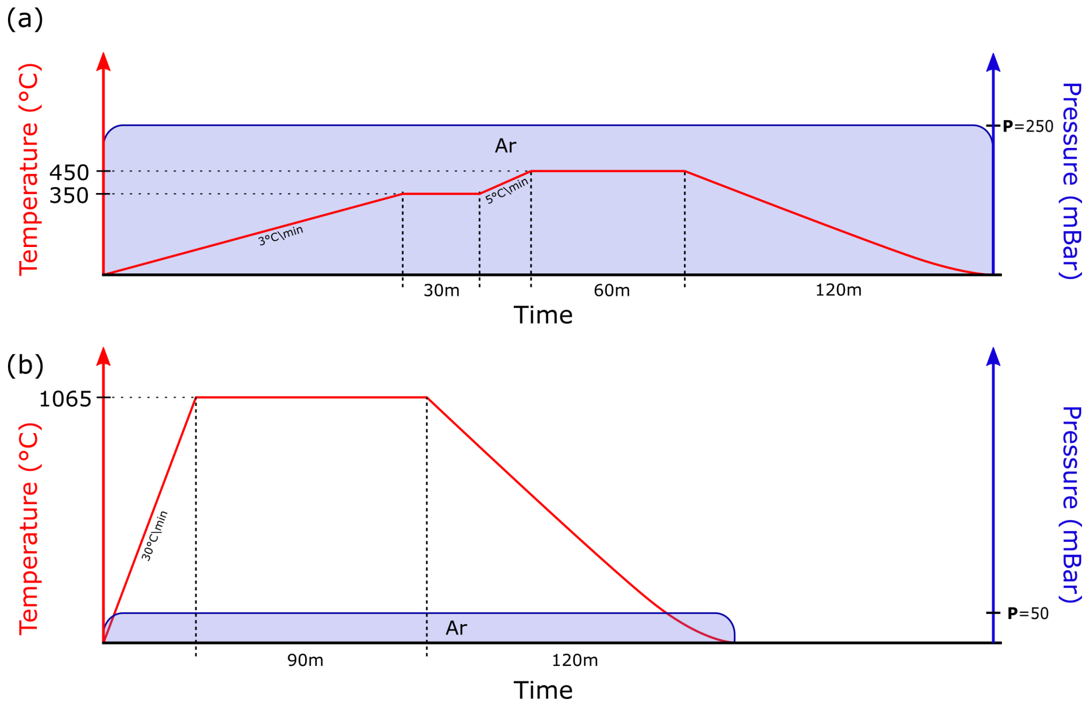

Figure 3.6: Schematic of the tube furnace CVD process conditions used herein to prepare pyrolytically shrunken graphitic foams. (a) Pyrolytic shrinkage process (b) pyrolytic graphitization process.

and held for 90 minutes. The graphitization process was carried out at a total pressure of 50 mBar, under a 250 sccm flow of argon in a hot-walled tube furnace. Samples were returned to room temperature over a period of 120 minutes then removed and stored in ambient conditions. This method results in a complete coverage of the Ni thin film in a thin multilayer graphitic film.

3.1.2.2 *Low-Pressure CVD Furnace*

The low pressure chemical vapour deposition (LP-CVD) system was used in this thesis to prepare freestanding graphene gyroids from nickel gyroid nanolattices, which possessed a unit cell size of 60 nm and strut sizes with a ~15 nm diameter. In the CVD of graphene on delicate polycrystalline structures, the growth temperature must be taken into account. Coarsening of nanoscale features in Ni due to thermal reflow can occur as low as 550 °C [29], necessitating the use of more reactive precursors. As discussed in Chapter 2.4.3, methane requires a temperature of ~760 °C to decompose and act as a carbon precursor. Acetylene possesses a low dissociation energy [144] and has been shown to be a much more reactive precursor that is able to decompose to form graphene of a high quality at relatively low temperatures (500-550°C) [29, 262]. The LP-CVD system, see Figure 3.7, used herein both enables the use of acetylene at low working pressure and the fine and responsive control of temperature through the use of a small heating stage in direct contact with the sample.

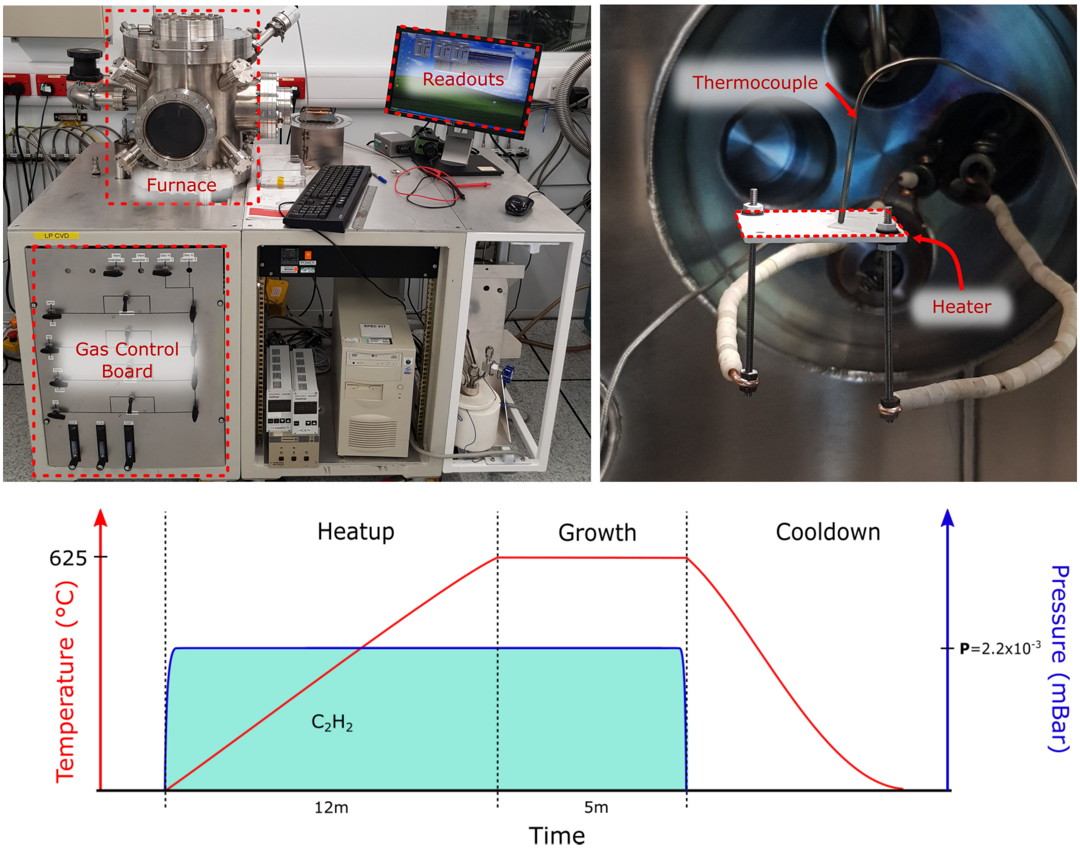

Figure 3.7: Image of the LP-CVD furnace, with associated systems labelled. Image of the sample heating stage on the right. Schematic of the LP-CVD process conditions used herein to prepare freestanding graphene gyroids is shown below.

The LP-CVD system consists of a custom-built stainless steel vacuum chamber with gas inlets, electrical feed-throughs and view windows. A two-stage pumping system is used, composed of a rotary roughing pump (base pressure of 10^{-3}mbar) and a turbomolecular pump (base pressure 10^{-7}mbar). Electronic MFCs are used to control the flow of gas into the system, which enter through a showerhead positioned vertically above the sample. C_2H_2 (>99.95%, BOC Gases), H_2 (>99.999%, BOC Gases) and Ar (>99.99%, BOC Gases) are used. Samples are heated with a Boralectric HTR1001 stage, which consists of pyrolytic graphite coated with an insulating layer of pyrolytic boron nitride. Desired temperatures reached by controlling the electric current passing through the stage. The temperature is monitored with a thermocouple gently contacting the surface of the sample.

Graphene multilayers were synthesised on Ni gyroid films for the studies described in Chapter 5. Growth of graphene gyroids were carried out in the LP-CVD based on the method developed by Cebo et al [29], see Figure 3.7. Ni gyroid films are loaded onto the centre of the heating stage, and the thermocouple is placed on the corner of the sample. The process chamber is then evacuated to 5×10^{-6} mbar. Acetylene is then pre-dosed into the chamber at 5 sccm, and the working pressure adjusted to 2.2×10^{-3} mbar. The samples are then ramped to 625°C at 50°C per minute, then held at temperature for 5 minutes. The gas flow was then stopped and the system evacuated, and the samples allowed to cool in vacuum.

3.1.3 WS_2 CVD SYNTHESIS

3.1.3.1 *Laser CVD Furnace*

A specialized laser CVD system was used in this thesis for the preparation of monolayer WS_2 films as detailed in Chapter 7. Carbon contamination introduced by organic precursors is major challenge for MOCVD [45], which motivated the examination of possible catalytic enhancement of growth by an Au substrate. Consequently, the growth of WS_2 herein was developed using a deconstructed MOCVD process in order to allow for a process-resolved understanding. Use of a laser system allows for the rapid and direct heating and cooling of a catalyst film with a laser source. When utilized within a low pressure, cold-wall system, this allows for a minimal heating profile which suppresses the pre-reaction of precursors in the gas phase. This encourages reaction pathways to be limited to the substrate surface, enabling each process step to be isolated. This was done by using a simple pattern of sequential exposure to low-cost, least-toxic precursors (tungsten hexacarbonyl [THC; $W(CO)_6$] and dimethylsulfide [DMS; $S(CH_3)_2$]). Gaining insight into the role of each process step was deemed necessary to build an understanding of the underlying reaction mechanisms that underpin the growth of 2D WS_2.

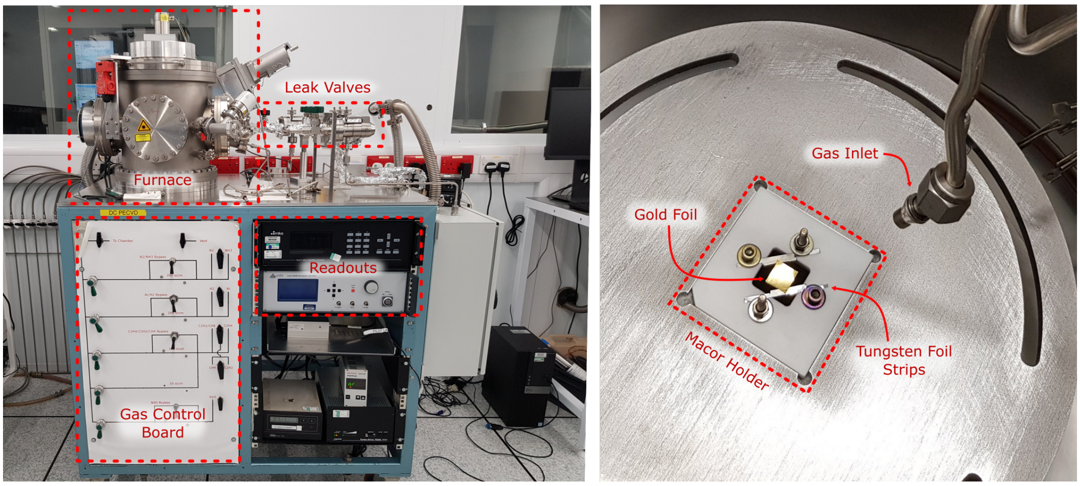

Figure 3.8: Image of the laser furnace, with associated systems labelled. Image of the sample loading configuration on the right.

The laser CVD system consists of a custom-built stainless steel vacuum chamber with gas inlets and feed-throughs for both gases and heating laser. A two-stage pumping system is again used, composed of a rotary roughing pump (base pressure of 10^{-3}mbar) and a turbomolecular pump (base pressure 10^{-7}mbar). A 808 nm continuous wave diode laser is used as the heating source, which is mounted below the chamber and equipped with a beam shaper to achieve a 5×5 mm square profile at the sample plane. Standard processing gases such as H_2 and Ar are introduced to the system through electronic MFCs. THC (whose source and line heated to 90°C) and DMS both possess limited vapour pressure, and hence flow is regulated manually through variable leak valves, which allow a pressure control precision better than 5×10^{-7} mbar. Substrates are mounted in a Macor holder, suspended across a central cutout (1.5×1.5 cm) on thin strips of W foil (purity >99.95%, Alpha Aesar, 1 mm wide, 10 µm thick), allowing the laser beam to directly interact with the underside of the foil, see 3.8. Sample temperature is monitored with a pyrometer, positioned vertically above the sample outside of the chamber, with a measurement error estimated around 50°C. For gold, transmission and emissivity values of 0.9 and 0.2 were assumed respectively.

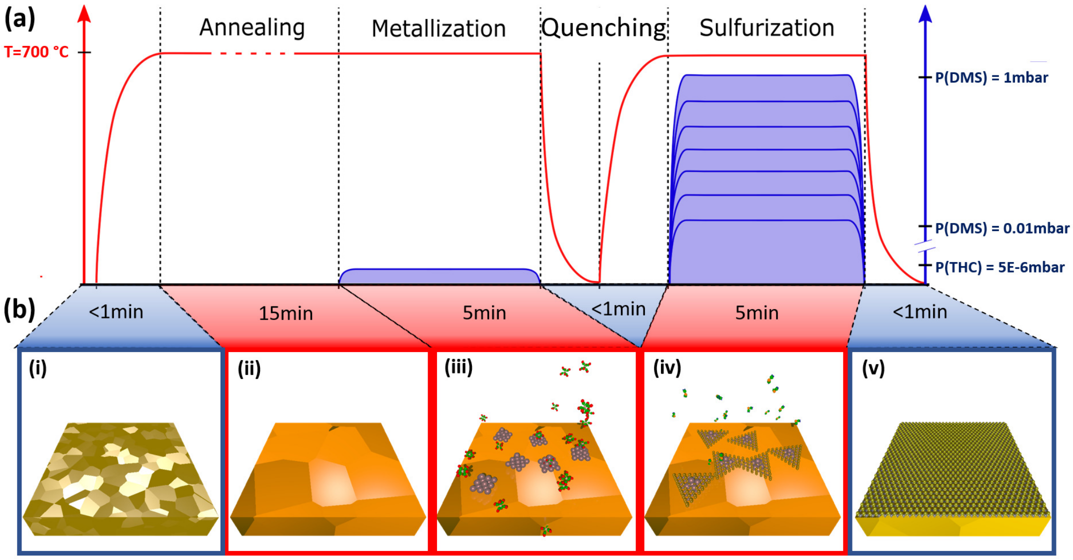

Figure 3.9: Schematic of the 2-step MOCVD procedure for WS_2 on Au foil. (a) Process step precursor timing and pressure. (b) Visualization of key growth processes (i) Poly-crystalline Au foil exhibits grain growth upon annealing (ii). (iii) Deposition of W during metallization. (iv) Sulfurization of W seeds. (v) WS2 covered Au after MOCVD.

WS_2 monolayers are grown on Au foil for the detailed process analysis in Chapter 7. A schematic of the growth process is shown in Figure 3.9. Au foil (purity >99.985%, Alpha Aesar, 25 µm thick, 8×8 mm) is heated to and kept at 700°C under base pressure better than 3×10^{-6} mbar for a 15 minute annealing and stabilization phase in vacuum. $W(CO)_6$ (purity >99.9%, Strem Chemicals) was then sublimated at 120°C and introduced for 5 minutes to deposit W seeds, in what is termed the metallization step. The partial pressure of $W(CO)_6$ was set to 5×10^{-6} mbar. The sample temperature is then lowered and chamber vented to prevent potential undesired pre-reactions between the two precursors. An Ar partial pressure of 5.5×10^{-3} mbar is introduced to stabilize the base pressure before the sample is then heated back to 700°C. $S(CH_3)_2$ (purity >99%, Sigma Aldrich) is introduced in the sulfurization step. The partial pressure of $S(CH_3)_2$ is again controlled by a leak valve and held between 0.1 to 1 mbar for 5 minutes to study its influence on carbon contamination, in what is termed the sulfurization step. The sample is then cooled down rapidly for further characterization.

3.1.4 ATOMIC LAYER DEPOSITION

This subsection is based on the publication "Parameter Space of Atomic Layer Deposition of Ultrathin Oxides on Graphene" [8]. The general approach and model development was performed by A.I. Aria. Experimentation, parameter search and AFM characterization was assisted by the author of the thesis.

Atomic layer deposition (ALD, Savannah System, Cambridge Nanotech S100 G1) was employed in this thesis to deposit thin conformal films of alumina onto 3D cellular materials comprised of graphene or resin, see Fig. 3.10. Alumina films were used as a strengthening and stiffening scaffold for freestanding 3D graphene foams, as discussed in Chapter 4. Alumina films deposited on 3D printed resin lattices mediated the amount of shrinkage experienced during carbonization and increased surface roughness as discussed in Chapter 6.

The key parameters that govern the ALD process are temperature (T_{dep}), oxidant and precursor doses (P_{dos} and t_{dos}) and purge time (t_{pur}). The deposition temperature must be sufficient to both drive the necessary surface reactions and avoid reactant condensation. However, excessively high temperatures will lead to desorption of precursor or thermal decomposition of a reactant. Precursor and oxidant doses are expressed herein as the product of dose pressure and dose time (approximation of maximum and FWHM of the pulse pressure) for consistency. Purging serves to remove all gas-phase precursors remaining from previous reactions and thus depend on both deposition temperature and purge time since unreacted gas-phase and surface-physisorbed precursors require more time to be removed at lower temperatures.

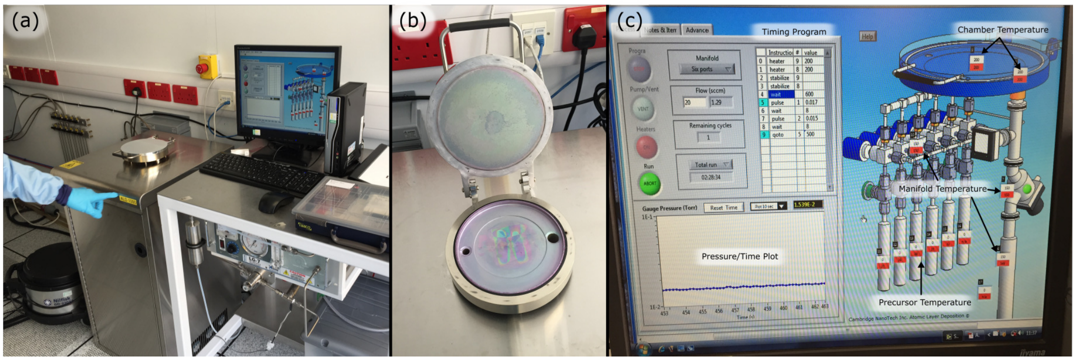

Figure 3.10: Photographs of (a) ALD system, (b) process chamber and (c) software interface.

Deposition temperature, flow rates and pulse timings were controlled by varying said parameters using the associated software. Trimethylaluminum (TMA, purity >98%, Strem Chemicals) was used as the alumina precursor, with deionized H_2O serving as the oxidant. Both precursors were volatilized at 40°C. Before ALD deposition, the chamber was purged with 20 sccm of N_2 and simultaneously pumped to a base pressure of 3.8×10^{-1} Torr for 10 min to clear the ALD system of residual precursors. Oxidant and precursors were introduced alternately to the chamber, carried with a 20 sccm flow of N_2. All samples were then loaded and unloaded while the chamber was at deposition temperature.

2D materials such as graphene possess strong covalent intralayer bonding, contrasted by a weak out-of-plane interaction dominated by van der Waals forces. Due to the weak out-of-plane interactions and hence low surface energy of 2D materials such as graphene [7] it is challenging to fabricate ultrathin continuous films atop the surface of such 2D materials. Recipes were optimized to provide a continuous film on graphene via a systematic study on the effect of precursor residence time [8]. The same approach was utilized to achieve the growth of continuous films atop the surface of 3D networked substrates, where precursor diffusion into a narrow network of pores must occur for each precursor pulse to achieve a uniform coating [80]. Previously, the most common approaches to enhancing wetting on graphene and achieving a more conformal coverage employed either lower deposition

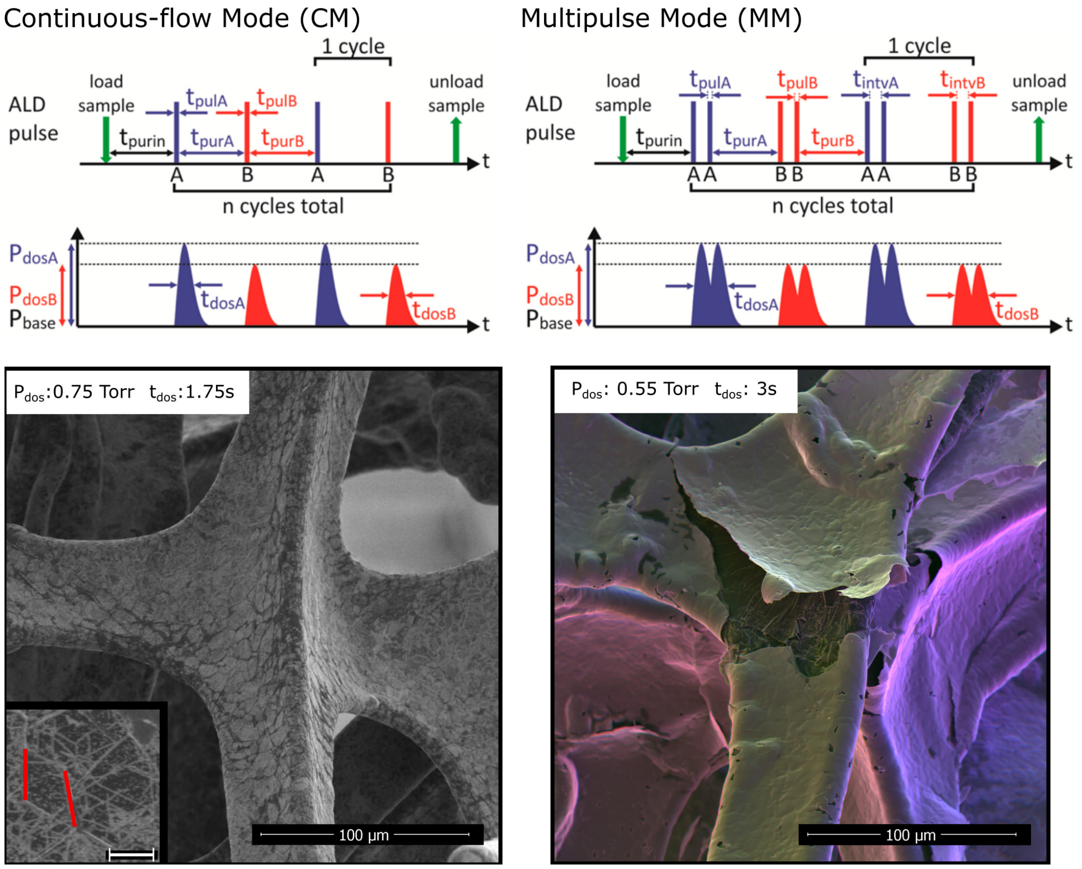

Figure 3.11: AlO_x nucleation by ALD in CM at a T_{dep} of 200 °C using varying doses of H_2O/TMA. A homogeneous AlO_x nucleation on graphene using H_2O/TMA at 200 °C can also be achieved by performing ALD either in multipulse mode, whereupon the H_2O/TMA residence time T_{dos} could be extended to reach complete AlOx coverage without necessarily increasing the H_2O/TMA dose pressure P_{dos}. All AlO_x depositions are performed with 550 ALD cycles total. Inset scale bar represents 5 µm and the red lines indicate the ridges of surface features on graphene.

temperatures or a surface modification of the graphene using seed layers, functional groups, and/or a more reactive oxidant to uniformly activate the graphene surface [229, 299]. However, such approaches will degrade the AlO_x film properties and/or the graphene film.

During the ALD of alumina onto graphene under typical conditions (200°C, TMA/H_2O dose of ~0.14 Torr·s, continuous pulse mode), AlO_x is found to preferentially nucleate on high surface energy sites such as ridges and wrinkle edges with continued deposition forming island-like clusters, see

Figure 3.11. For growth of high-quality AlO_x films, extension of the precursor residence time by optimization of pulse sequences encourages a more homogeneous nucleation of AlO_x across the entire film surface, allowing for the deposition of a conformal and pinhole-free ultrathin layer of alumina. This was done through the use of a multipulse mode, which utilizes multiple pulses of the same precursor to extend the dose FWHM (increasing t_{dos}) without increasing P_{dos}, see Figure 3.11. This improvement in film homogeneity was attributed to the increased precursor residence time compensating for the slow adsorption kinetics of low surface energy surfaces and the mass transport of precursors throughout a porous structure. Aluminum oxide (Al_2O_3) coatings were subsequently deposited onto graphitic foams and 3D printed lattices by ALD in a multi-pulse mode at 200°C and 150°C respectively. Al_2O_3 layers of n nm thickness were deposited by applying $n \times 11$ deposition cycles, as calibrated on planar samples via AFM.

3.1.5 ELECTROLESS NICKEL DEPOSITION

Electroless deposition produces uniform and conformal layer of metal onto substrates through the chemical reduction of metal ions from solution, via a supply of electrons from the surface of a metal substrate or catalyst used to initate the reaction. The system requires no external current, with film deposition carried out autocatalytically through the oxidation of a reducing agent in the solution which supplies an internal current. Electroless deposition of nickel is used in this thesis to deposit conformal layers of nickel onto carbonized substrates for subsequent catalytic graphitization in Chapter 6.

Pyrolytically carbonized samples were used as the substrate for the deposition of a 500 nm nickel layer. As samples are non-metallic, Pd-pretreatment was used to provide an initiating catalyst to the surface. Samples were immersed in an aqueous solution of tin chloride (0.1 M $SnCl_2$/0.1 M HCl) for 120 seconds. After a thorough rinse with deionized water, the film was transferred into an aqueous solution of palladium chloride (1.4 mM $PdCl_2$/ 0.25 M HCl). In this step, the surface was activated for nickel deposition by a redox reaction in which the Sn^{2+} ions were oxidized to Sn^{4+} while the Pd^{2+} ions were reduced to metallic Pd. This metallic palladium was used as the catalyst for the autocatalytic reduction of Ni^{2+}. After a thorough rinse with deionized water, Pd-containing films were immersed in an electroless nickel plating bath (Alfa Aesar Nickel plating solution, electroless) for a total of 10 minutes at 85°C, with vigorous stirring. The electroless nickel plating bath was previously ultrasonicated for 30 minutes to degas the solution. Ni deposition proceeded at an average rate of 50 nm/minute, resulting in a conformal 500 nm thick coating of nickel.

3.1.6 CATALYST ETCHING AND MATERIAL TRANSFER

After a CVD process, the catalytic templates must be removed to afford nickel-free graphitic cellular structures in Chapters 4, 5 and 6 or for the transfer of WS_2 monolayers in Chapter 7. All metallic templates in this thesis were removed using wet chemical etching.

MACROSCOPIC GRAPHITIC FOAMS: Due to the high ratio of wall thickness to strut diameter, submersion in H_2O, acetone or isopropyl alcohol was found to collapse the graphitic foam structures fabricated in Chapter 4 due to capillary condensation during drying, see Fig. 3.12. To prevent this, a poly(methyl methacrylate) (PMMA) scaffold was used during the etching process, as was performed by Chen et al. in their original synthesis of free-standing graphene networks. [36]. Samples were dip coated in PMMA (495K, 2% in anisole) for 10 s, then annealed on a hot plate at 180°C for 15 minutes on each side, trimmed along the edges and then etched in 0.5M $FeCl_3$ for 48 hours. Subsequently, the samples were rinsed in de-ionized water, then subjected to a 30 minute etch in 10% HCl solution to remove Fe residue, see Figure 3.15. Finally, samples were repeatedly submerged in DI water as a final wash over a 24 hour period, before being removed and left to dry in ambient air.

At this stage, the graphene foam samples are metal-free but remain supported by the PMMA scaffold. To avoid wet processing steps entirely, the PMMA supporting structure was removed by annealing the sample at 450°C for 60 minutes in a H_2/Ar (40:200 sccm, 50 mBar) atmosphere to produce free-standing graphitic foams (FG). This method has commonly been used in monolayer graphene transfer, and shown to remove even minute residues. [94, 214] Samples were observed under SEM to examine for both damage and residual PMMA, and it was found that 60 minutes was sufficient time to remove all visible PMMA residues. TGA of a FG treated in the same way confirmed the lack of PMMA residues.

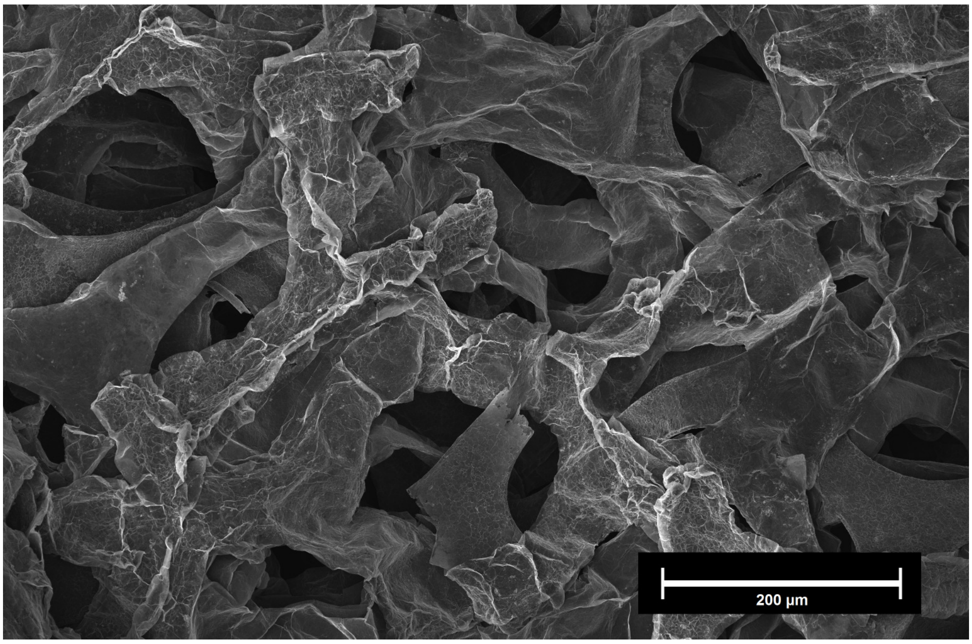

Figure 3.12: A SEM image of a FG collapsed post-etching, due to the capilliary forces present during the evaporation of H_2O or acetone/IPA.

GRAPHENE GYROIDS AND GRAPHITIC MICROFOAMS: Graphene gyroids and pyrolytically converted graphitic microfoams were etched using 0.5M ammonium persulfate [$(NH_4)_2S_2O_8$]. Samples were submerged for 48 hours, before being repeatedly submerged in DI water over a period of 24 hours. Samples were then transferred to a 50:50 DI water/IPA solution, which was replaced with IPA by gradual addition. Samples were then removed and dried in air. A PMMA scaffold was not required, as these structures did not experience any capillary condensation driven collapse.

WS_2 MONOLAYERS: TMDC monolayers similarly require a supporting PMMA scaffold for reproducible transfer [295]. PMMA (A4, 950k) was spun on the as-grown WS_2 on gold at 3000 rpm for 45s as the scaffold layer. The sample is then baked at 120°C for 3min to evaporate the polymer solvent. WS_2 on the backside of the gold foil is removed by reactive ion etching (RIE, 50W, 20s of 150 mTorr CF_4). After RIE, gold is etched by gold etchant (KI/I_2) over a period of 4 hours. The sample is then transferred into DI water several times before being fished out onto the target substrate and gently dried.

3.2 MATERIAL CHARACTERIZATION

3.2.1 SCANNING ELECTRON MICROSCOPY

Scanning electron microscopy (SEM) is used in this thesis for the non-destructive characterization of surface features. A focused beam of electrons is scanned across the surface of a specimen, interacting with the surface through both elastic and inelastic scattering. These interactions generate a variety of signals, such as Auger electrons, secondary electrons (SE), back-scattered electrons (BSE) and X-rays, see Figure 3.13. These signals (usually SE and BSE) are collected by detectors and used to generate images. The SEMs utilized for sample characterization for this thesis were the FEI FEG XL30, LEO 1530VP SEM, FEI Helios NanoLab 600 DualBeam and Zeiss GeminiSEM. Typically, the in-lens detector was selected (when available) for sample imaging due to the efficient collection of incoming secondary electrons (SE), providing high resolution at low voltages.

Secondary electrons are produced through inelastic scattering of the incident electron beam, leading to the excitation of weakly bound valence electrons in the specimen. These excited electrons can move to the sample surface and

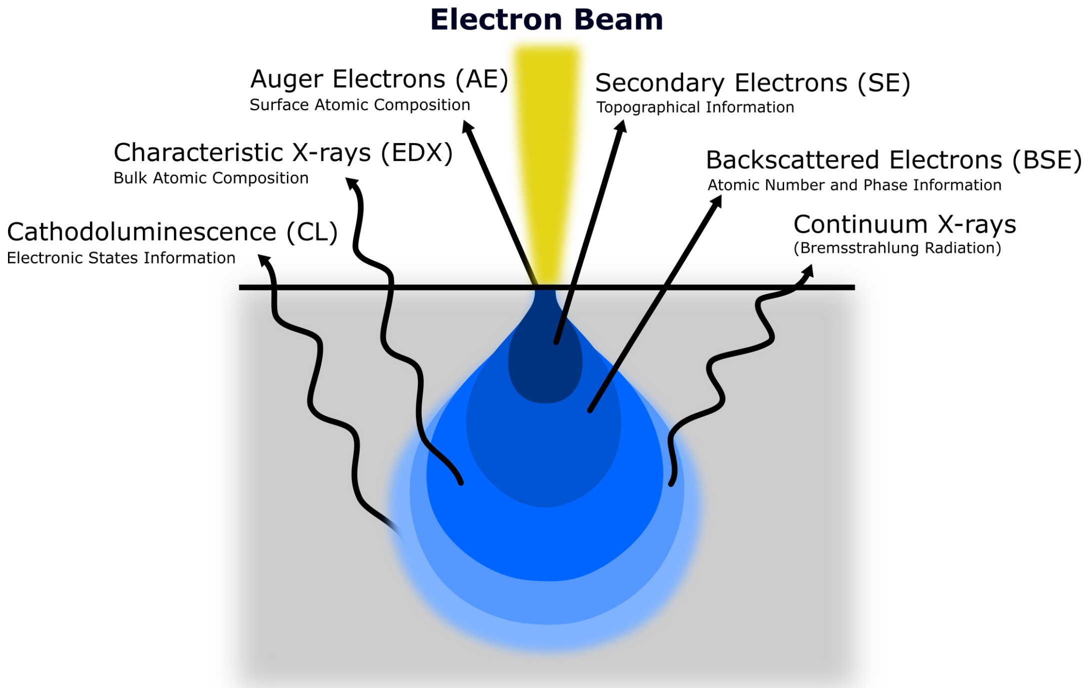

Figure 3.13: Schematic of the interaction volume for an electron beam incident on a surface, showing emission profiles of Auger electrons, secondary electrons, backscattered electrons, characteristic X-rays, continuum X-rays (Bremsstrahlung) and cathodoluminescence. Characteristic information obtainable from each of the respective emissions are also listed.

exit if sufficient energy remains. However, secondary electrons possess low energy (0-50 eV) [205] and hence those which are produced in the bulk of the material are less likely to escape the specimen surface due to loss of energy from interactions occurring during movement through the bulk. Hence, only secondary electrons that are produced in a very small volume under the incident electron beam (~1-10nm deep) will be able to successfully escape. Materials with lower atomic numbers, or use of higher accelerating voltages will generate larger interaction volumes and hence less surface-specific information will be obtained.

Use of SE detection with low accelerating voltages (< 5 kV) enables the acquisition of surface-sensitive topographical information. When imaged with SE, 2D material layer(s) atop a metal catalyst will generally appear successively darker with increasing layer number due to the low SE generation within the

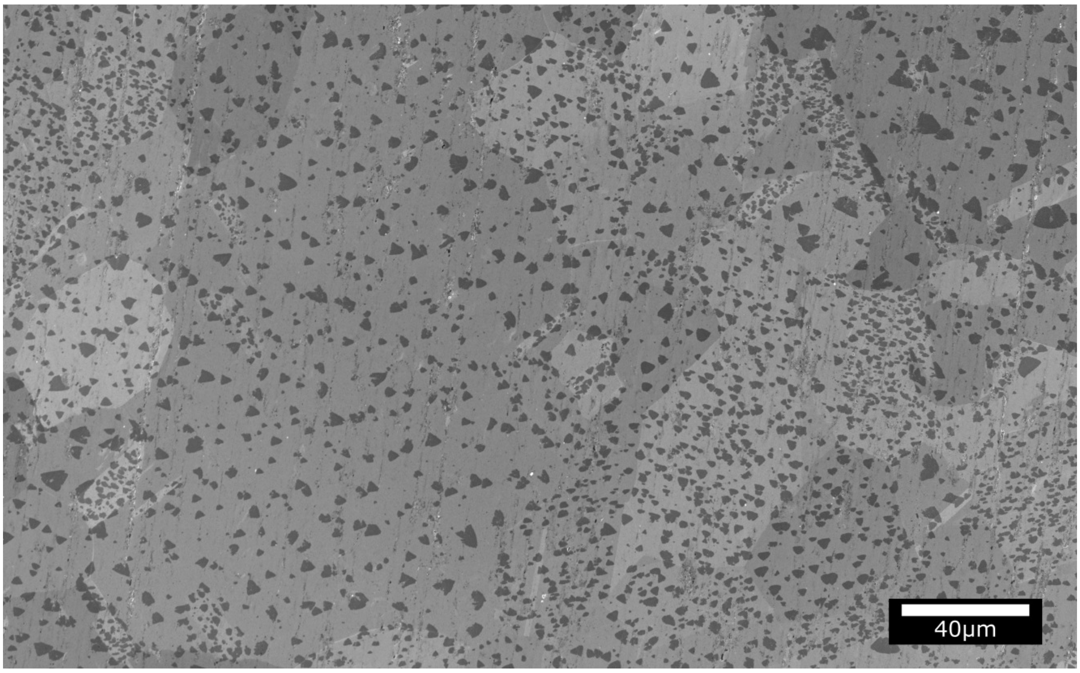

Figure 3.14: SEM image of WS_2 grown on Au showing the variations in contrast from both the WS_2 domains and grain to grain in the polycrystalline substrate.

2D material layer, sensitivity to the work function of the surface and attenuation of the SE emitted from the interaction volume within the catalyst due to the 2D material layer, see Fig. 3.14. Another relevant source of contrast when imaging 2D materials arises from electron channelling in polycrystalline catalysts [205]. When the atomic lattice in a crystalline material is aligned parallel with the incident electron beam, the amount of BSE produced will decrease due to a decrease in the probability of an elastic scattering interaction near the surface of the lattice. Such BSE can contribute to the SE signal by themselves generating SE or simply by possessing low enough energy to be collected by an SE detector. As different grain orientations will possess different degrees of alignment with the incident beam, contrast between grains can be observed, see Fig. 3.14.

3.2.2 ENERGY DISPERSIVE X-RAY SPECTROSCOPY

Complementary to SEM, energy dispersive x-ray spectroscopy (EDX) is a technique that enables the characterization of the elemental composition of the imaged material. In this thesis, EDX is used to qualitatively examine the elemental composition of prepared graphitic foams, to determine whether internal metal templates have been completely removed or not. A FEI FEG XL30 with associated Oxford Instruments Microanalysis X-MAX-80 EDX detector and AZtec software was used in this thesis for EDX analysis of samples.

When the sample is bombarded by the electron beam of the SEM, electrons may be ejected from the atoms comprising the surface ~1 µm of the sample. When resulting electron vacancies are filled by an electron from a higher shell, an X-ray is emitted to balance the energy difference between the two electrons. In this way, the energy of the emitted X-ray is characteristic of a given element. By measuring the energy versus relative counts of X-ray emitted at a specific energy, a spectrum is obtained and can be evaluated for qualitative and quantitative determination of the elements present in a sampled volume. Rastering of the electron beam across the surface of the sample during detection allows for the collection of data across many individual sites (pixels), enabling the creating of EDX maps of relatively large samples, see Figure 3.15.

3.2.3 FOCUSED ION BEAM MILLING

Another complementary technique to SEM, focused ion beam (FIB) milling allows for the site-specific deposition and ablation of material. In this thesis, FIB techniques were used to prepare cross-sections of thin gyroid films. This was necessary in order to characterize the vertical morphology of the structures as they undergo various cleaning and growth procedures. A FEI Helios NanoLab 600 DualBeam was utilized in this work.

In a FIB process, a focused beam of ions is used at low beam currents for imaging, or higher beam currents for site-specific milling. Ions, typically Ga^+,

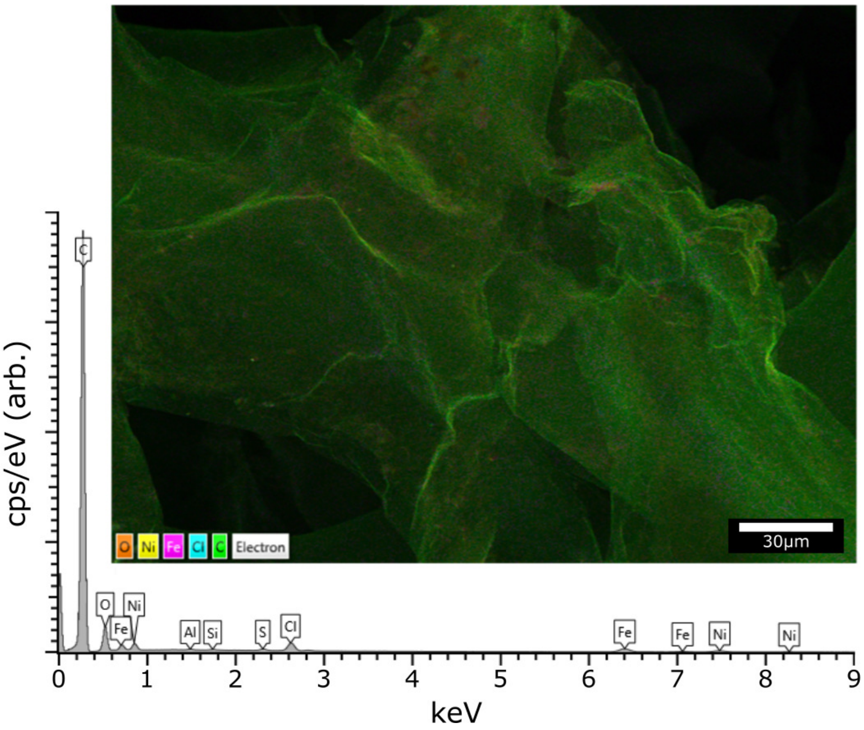

Figure 3.15: Sample EDX image of a macroscopic graphitic foam etched using 1M FeCl over a period of 24h. Significant amounts of Fe, Cl and O could still be detected, motivating further process refinements.

are generated from a liquid metal ion source (LMIS). The ion optics, current (pA to nA) and spot position are adjusted by a stack of electrostatic lenses and apertures. The energy provided by Ga^+ ions colliding into a substrate yields secondary electrons and sputters atoms and ions, whereas interaction with a precursor gas can induce material deposition. This can also lead to Ga implantation and damage (sputtering, amorphization) of the exposed area, see Fig. 3.16a. Imaging, milling and deposition can all happen simultaneously, but adjustment of the ion current and chamber atmosphere change which aspect is more pronounced. All FIB processes herein were carried out at 30kV accelerating voltage.

Ion-beam induced deposition was used to deposit a thin rectangular strip of platinum (1×2.5× 15 µm) atop the gyroid film surface at a current of 0.3 nA. This serves as a protective layer that reduces charging effects and preserves the shape of the interface during the milling process. A platinum precursor

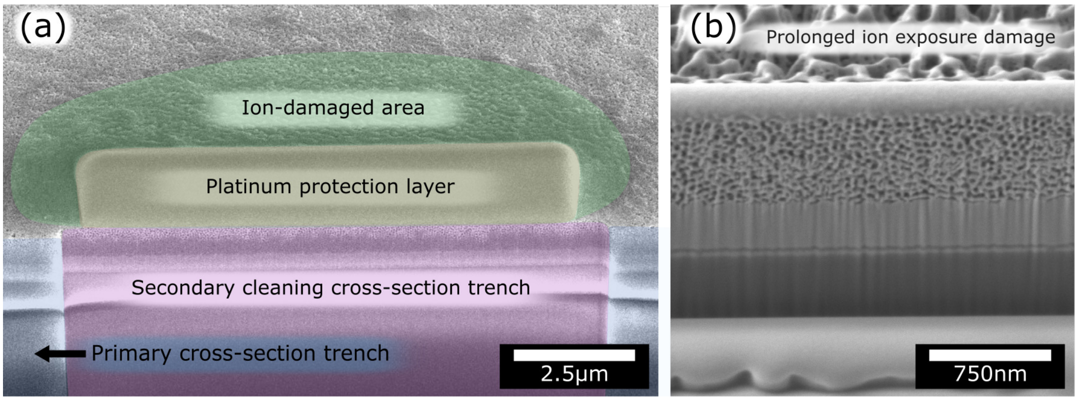

Figure 3.16: Sample FIB images. (a) Completed cross-section of a polymer-contaminated Ni gyroid film, displaying the platinum protection layer, primary cross-section trench, secondary cleaning-cross section trench and the ion-damaged area. (b) FIB cross-section with area of Ni gyroid film showing irregular damage of unprotected areas due to prolonged ion beam exposure.

$[(CH_3)_3Pt(CpCH_3)]$ is introduced into the reaction chamber through a gas injection system nozzle, positioned approximately 150 μm above the sample. Physisorbed precursor is broken down by the ion beam, causing local CVD of Pt, mixed with Ga and C. Subsequent cross sectioning occurs in two steps. A primary trench (7.5×15×20 μm) is milled across the deposited Pt pad using a relatively high ion current (7 nA). Due to sputtering of the milled material, it is necessary to perform a second careful cleaning cross-section that rasters into the cross-sectioned material, see Fig. 3.16a. This is performed at a slower rate, with a lower ion current (0.5 nA), affording a pristine cross-section of nanoscopic features, see Fig. 3.16b.

3.2.4 TRANSMISSION ELECTRON MICROSCOPY

High-resolution transmission electron microscopy (HR-TEM) allows for the visualization of the internal structure of materials at extremely high magnifications (up to ×1,000,000). In HR-TEM, a high energy beam of electrons is transmitted through an ultrathin (< 100 nm) section of material. Interactions of the incident electrons with the material causes the formation of an image. Image contrast can arise from elastic scattering (amplitude contrast, related to mass-thickness or diffraction) and inelastic scattering (phase contrast). Selected area electron diffraction (SAED) is a specialized technique that is used to examine the diffraction pattern generated by the transmitted electrons through a selected area aperture. HR-TEM is used in this thesis to characterize the layer number and graphitization of graphene gyroids in Chapter 5, and WS_2 monolayers in Chapter 7. All HR-TEM images were taken on an Tecnai Osiris TEM. Quanti-foil TEM grids are used as the substrates in the associated HR-TEM studies.

3.2.5 ATOMIC FORCE MICROSCOPY

Atomic force microscopy (AFM) enables the characterization of surface topology with extremely high resolution (~Å). AFM was used in this thesis to determine the thickness of deposited AFM films, waviness of a macroscopic graphitic foam and morphology of solid nickel gyroid and hollow graphene gyroid films. AFM measurements were performed in air at ambient pressure and temperature using a Asylum/Oxford Instruments MFP-3D AFM System. New AFM tips (Bruker MMP-11200-10, n-doped Si) which nominally possessed a 8 nm tip radius, were used for each new set of measurements. Surface topography was acquired in tapping mode at a frequency of 1Hz with a resolution of 1024×1024 pixels, with scan sizes between 5×5 µm and 20×20 µm. Images were processed and analyzed using the software Gwyddion.

3.2.6 RAMAN AND PHOTOLUMINESCENCE SPECTROSCOPY

Raman and photoluminescence (PL) spectroscopy enables the fast, non-destructive spectroscopic characterization of 2D materials, and was used in this thesis to determine the quality of the graphene and WS_2 grown herein. For all measurements and studies carried out herein, a Renishaw Raman InVia microscope was utilized, coupled to a 20 mW, 532 nm wavelength laser and various objectives.

In Raman spectroscopy, a sample is irradiated with a high-intensity monochromatic beam of light and detects the scattered light. A very small fraction of incident light is inelastically scattered, and will possess a shift in energy from the source frequency due to interactions with the vibrational energy levels of the molecules in the sample, see Figure 3.17. The amount of energy change (either lost or gained) by a given photon is characteristic of the nature of each vibration and hence bonding states present in the material. This mechanism hence gives insight into the composition, stress state, quality and amount of the material examined. The intensity of detected light versus frequency shift is plotted to give a Raman spectrum. Photoluminescence, on the other hand, comprises both fluorescence and phosphorescence processes and originates from an absorption/emission process between different electronic energy levels in the material, see Figure 3.17. Hence, PL spectra give insight into the separation of electronic energy levels within a material.

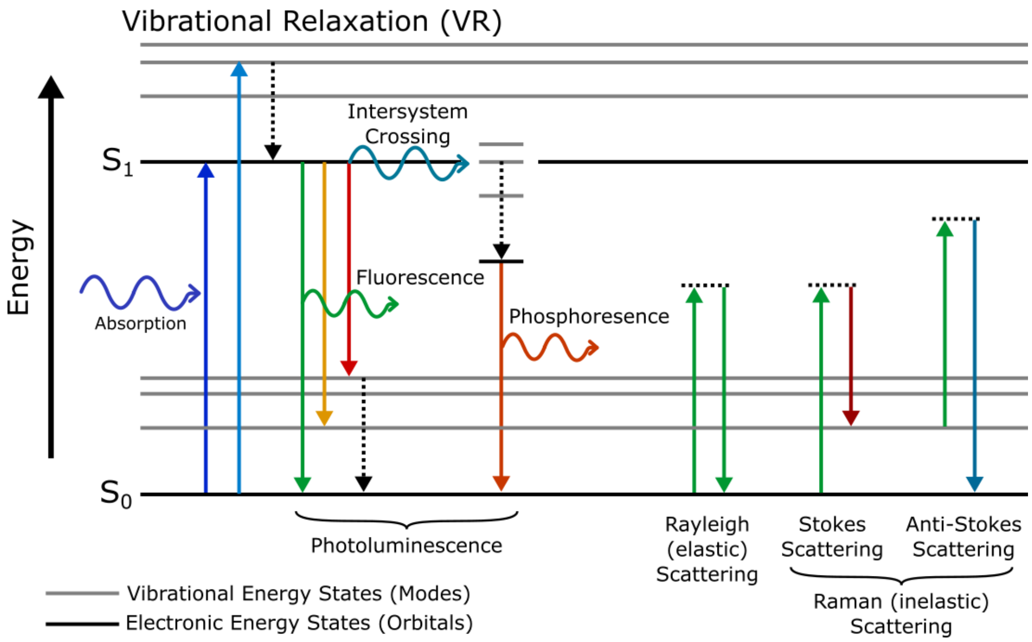

Figure 3.17: Jablonski energy level diagram for optical scattering.

However, the characterization of material quality is localized to the excitation spot. The spatial resolution is typically on the order of 700nm for a 100× objective and the extracted quantities are averaged over the spot size. As many samples tested are both three-dimensional and possess relatively large lateral dimensions, Raman mapping or averaging over a large number (>10) spots across the material surface was used wherever possible to establish a more accurate view of the properties of the graphitic material (quality, layer number, stacking order).

Laser power was adjusted from sample to sample to obtain sufficient signal to noise ratios, while exposure times were limited to below 2s to avoid detrimental laser heating of the specimens. Single spot scans were typically measured with 1% laser power 2s exposure and accumulated 6 times. For Raman mapping, 10% laser power and 0.1s exposure are used for each spot with a step size of 0.5 µm in both x and y directions. A python script was used to apply a simple Lorentzian-Gaussian multipeak fit of known peaks for each point in the map, and subsequently used to generate maps and extract average values of peak intensity, full width half maximum and area. Single spot PL is measured with 0.1% laser power with 1s exposure and accumulated 2 times. For PL mapping, 1% laser power with 0.25s exposure is used for each spot with a step size of 2 µm in both x and y directions. Sample are kept in the same orientation during all mapping measurements to make sure the Raman intensity of the underlying silicon reference peak is unchanged, when relevant.

3.2.7 X-RAY PHOTOELECTRON SPECTROSCOPY

X-ray photoelectron spectroscopy (XPS) is a sensitive technique used for the characterization of elemental composition and associated chemical and electronic states. XPS spectra are obtained by irradiating a material with a beam of X-rays while measuring the kinetic energy and number of electrons that escape from the surface (0 to 10 nm). For all measurements used herein, an ESCALAB 250Xi XPS system was used. XPS was used to perform elemental analysis of fabricated materials such as freestanding graphitic foams or WS_2 films. XPS can not only confirm the presence of elemental impurities in CVD grown films, but also the degree to which those impurities have been chemically bonded into the film.

XPS was carried out at an operating pressure below 10^{-10} mbar. The X-ray source for the XPS was a monochromated Al Kα with a photon energy of

1486.6 eV and a spot size of 200 µm. Where relevant, XPS spectra in Chapter 4 were acquired from the internal walls of laser-cut sample cross-sections to ensure that the collected spectra accurately represent the hollowed sample. XPS spectra in Chapter 7 were taken from the surface of the WS_2 film. As scanned areas are limited in size, measurements were carried out randomly in various regions of the samples and representative scans were selected.

3.2.8 THERMOGRAVIMETRIC ANALYSIS

Thermogravimetric analysis (TGA) is a destructive method for the analysis of thermal behaviour of a material. In TGA, the mass of a sample is continuously monitored as the surrounding temperature is changed in a known atmosphere. This gives insight into physico-chemical phenomena such as desorption and thermal decomposition. In this thesis, TGA was used on graphitic foam samples to determine sample cleanliness and graphitic quality. TGA was carried out in a Perkins-Elmer TGA4000 in synthetic air (20% O_2 in N_2). A 2 µg portion of each sample was ramped at 5°C/min from room temperature to 900°C. During the measurement, the temperature was held for 15 min at 100°C to completely remove adsorbed water. The sample was held at 900°C for 30 minutes before returning to room temperature naturally.

3.2.9 SECONDARY ION MASS SPECTROMETRY

Time of flight secondary ion mass spectrometry (ToF-SIMS) is a surface-sensitive analytical method that is used for elemental and chemical mapping with a sensitivity of up to parts per billion (ppb). In ToF-SIMS, a pulsed ion beam is used to sputter molecules from the surface of the sample, forming secondary ions. These are then accelerated into a flight tube and their masses determined based on the time taken to reach the detector. Depth profiles can be achieved via successive sputtering steps in the same area. All ToF-SIMS measurements herein were performed ex-situ, using a ToF-SIMS IV instrument (ION-TOF Gmbh, Germany) with a base pressure $< 5\times10^{-9}$ mbar.

Surface maps were acquired using 25 keV Bi^{3+} ions from a liquid metal ion gun, with spot size less than 5 µm in spectroscopy mode and a current of 0.1 pA. Large-area maps were built up from multiple concatenated 500×500 μm^2 images (512×512 pixels) and each depth profile was acquired by analysing a 150×150 μm^2 area (128 x 128-pixel density) centred within a 400×400 μm^2 sputtered region in a non-interlaced mode (alternating data acquisition and sputtering cycles). To determine the elemental composition of two different regions within the Au foil (surface and bulk), two different sputtering ions were used. For the gentle sputtering cycles to probe the surface and subsurface composition, an Ar gas cluster ion beam with a cluster size of 2700 ions and an ion current of 0.36 nA was used, while for the coarser sputtering, 10 keV Cs^+ ions with a current of 30 nA were employed. The sputter gun was oriented at 45°to the sample surface. The gas cluster ion beam and liquid metal ion gun were operated during depth profiling at a cycle time of 200 µs, while the Cs^+ liquid metal ion gun was operated at 100 µs. No charge compensation was used during these measurements. Data processing was carried out using Surface Lab software, by selecting relevant peaks in the ToF-SIMS spectra and monitoring their change in intensity over the course of the sputter profiling.

3.2.10 FOUR POINT PROBE RESISTIVITY MEASUREMENTS - VAN DER PAUW

The van der Pauw method utilizes a four-probe system to obtain average resistivity measurements of thin samples. Four electrodes are placed on the perimeter of a sample in a square pattern. Current is caused to flow along one edge of the sample while the voltage across the opposite edge is measured, allowing a resistance to be found according to Ohm's law (obtaining V_1). The source current value is adjusted according to the expected sample resistance, such that the measured voltage falls within the range of accurate measurement. The resistivity can then be derived from a series of repeated measurements made around the periphery of the sample (obtaining V_2, V_3 and V_4), based on following formula:

$$\rho_A = \frac{\pi}{\ln 2} f t_s \frac{V_1 - V_2 + V_3 - V_4}{4I} \tag{3.1}$$

where ρ_A is the volume resistivity in ohm·cm, t_s is the sample thickness in cm, V_1 to V_4 represent the measured voltages around each edge, I is the current in amperes and f is a geometrical factor based on symmetry ($f = 1$ for a symmetric layout).

A Keithley Model 4200-SCS four probe station was used for all the measurements herein. Samples were sectioned into symmetrical square portions and stored in ambient before testing. Probe placements were made at sample corners, and when necessary, samples were electrically contacted by silver paste. The thickness of samples were taken as apparent foam thickness as is standard in the literature [36].

3.3 MECHANICAL CHARACTERIZATION

3.3.1 UNIAXIAL COMPRESSION TESTS

Uniaxial compression tests allow for the extraction of the stress-strain response of a material, and hence the associated mechanical properties such as Young's modulus and yield strength. Visualization of the evolving morphology of the samples during compression also provides insight into the deformation mechanisms taking place within the cellular material. Uniaxial compression tests were used to characterize the mechanical response of free-standing and alumina-coated graphitic foams, as detailed in Chapter 4. Tests were performed on samples of height 1.6 mm and cross-section 5×5 mm. All samples were laser cut to the desired dimensions to ensure that faces were parallel. The density of each sample was deduced by measurement using a high-precision electronic balance.

A custom-built mechanical testing apparatus at the Fraunhofer Institute was used to measure the compressive response of the laser-cut foam samples, see

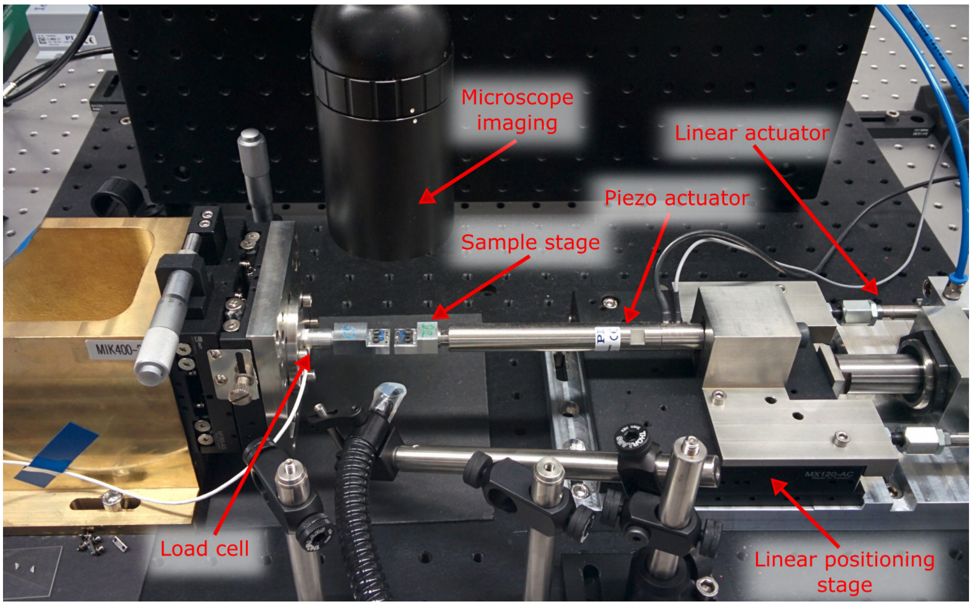

Figure 3.18: Photograph of the uniaxial compression test rig.

Fig. 3.18. This system consists of a stepper-motor driven linear actuator for positioning (50 nm resolution) and a preloaded piezoactuator (1.2 nm resolution) for displacement actuation. A miniature tension/compression load cell was used for force measurement (5 N range and a 2.5 mN resolution). Each specimen was aligned along the loading axis of the test system and fastened electrostatically to a parallel aluminum plate base. All experiments were conducted at a nominal displacement rate of 10 µm/s, implying a strain rate of 1.6×10^{-4} s^{-1}, and the deformation of the microstructure was observed by in-situ microscopic image acquisition.

For all graphitic foams, the compressive modulus (E) was obtained by fitting the linear part of the stress-strain curve by a linear fit. The onset of plasticity, which is represented by the yield strain ϵ_Y, is defined experimentally by the 0.2% offset method. This was determined by offsetting the linear fit in the linear elastic regime by 0.2% strain and finding the point of intercept. The yield stress σ_Y is identified by the stress at the onset of plasticity. The onset of densification, which is represented by the densification strain ε_D, was determined herein by first calculating the compression efficiency η, from which ε_D was then determined from the point of maximum efficiency η_{max} [129].

3.3.2 NANOINDENTATION

Nanoindentation techniques have been widely used for studying the mechanical properties of engineering materials, coatings and films. Nanoindentation was used in this thesis to extract the mechanical response (elastic modulus and hardness) for both nickel solid gyroid and hollow graphene gyroids, and also serves as the basis for the computational modelling performed in this thesis as detailed in Chapter 5.

The primary purpose of quasi-static nanoindentation testing is to establish an elastic modulus and a hardness value for the test material [69]. Hardness is related to the resistance of a material to permanent deformation. It depends on the yield stress of the material and a constraint factor, which is specific to the material, the indenter used and experimental conditions. Modern nanoindentation systems continuously and accurately measure both the load and depth of indenter penetration into the specimen. This measurement is then used to determine an area function and consequently a hardness value based on the tip shape of the indenter used.
Loading–unloading curves (see Figure 3.19b) can be used to extract the mechanical properties of the indented material. The method developed by Oliver and Pharr [176] is extensively used for determining the elastic properties of materials, coatings and films, and is detailed briefly below:

The projected area of the indenter A_c is calculated using the indenters tip area function, shown in Figure 3.19c. For an ideal Berkovich indenter as used herein (see Figure 3.19a), with face angle $\theta \approx 65.27°$, the area function is defined as:

$$A_c = 3\sqrt{3}h_c^2 \tan^2\theta \approx 24.5h_c^2 \tag{3.2}$$

While the nominal contact area A_c is known from δ via the tip area function, the true contact area A_t is typically estimated in the indentation analysis of fully dense metals via an estimation of the true indentation depth h_t via,

$$h_t = h_c - \epsilon \frac{P}{S} \tag{3.3}$$

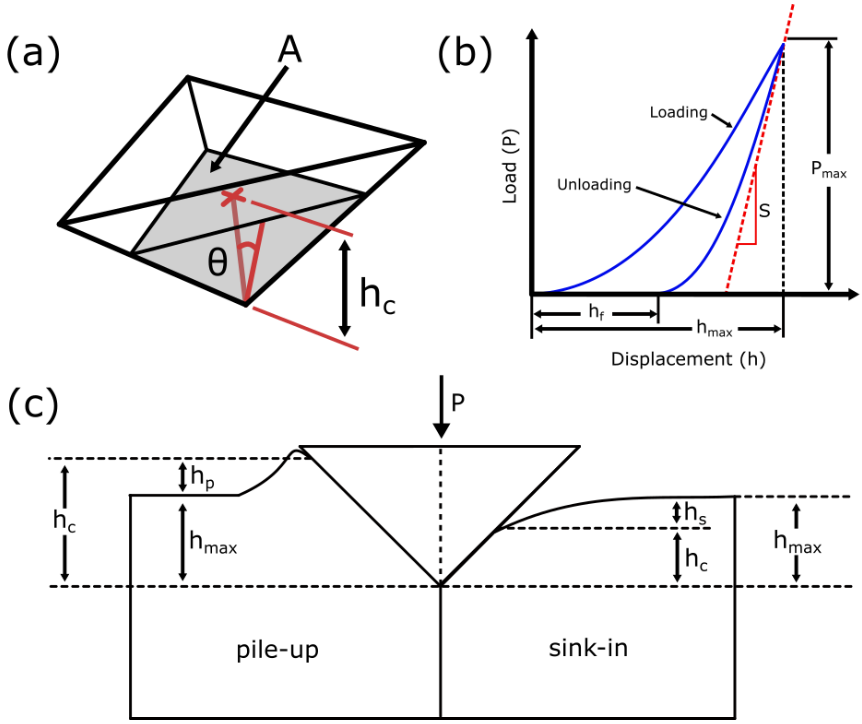

Figure 3.19: (a) Berkovich indenter showing projected area, A, contact depth, h_c, and face angle, θ. (b) Schematic diagram of pile-up and sink-in along the indenter perimeter of contact. (c) Typical load-displacement curve for a nanoindentation test. P_{max}: peak indentation load, h_{max}: indenter displacement at peak load, h_f: final depth of residual indent after unloading, S: initial unloading stiffness.

where S is the unloading stiffness, h_c is the contact depth of penetration and ϵ is a correction factor (typically 0.75 for the Berkovich indenter) to account for the effect of sink-in or pile-up around the indenter. The second term in the equation represents the vertical deflection of the surface at the perimeter of contact. The hardness H at indentation depth δ is then defined as $H(\delta) \equiv P/A_t$, where P and A_t are the applied indentation load and true projected contact area, respectively.

To determine the Young's modulus E of the film, a power law curve $P = c(\delta - \delta_f)^m$ is fitted to the measured unloading response $P(\delta)$ where δ_f, m and c are fitting constants for the measured curve, see Figure 3.19b. The unloading stiffness can then be defined as $S \equiv dP/d\delta$ at the peak load P_{max}, just prior to unloading. The reduced Young's modulus E_R of the film is then given by the Sneddon formula as,

$$E_R = \frac{S}{2}\sqrt{\frac{\pi}{A_t}} \tag{3.4}$$

The film modulus E^F can then be found with the contact relation,

$$\frac{1}{E_R} = \frac{[1-(\nu^I)^2]}{E^I} + \frac{[1-(\nu^F)^2]}{E^F} \tag{3.5}$$

where E^I and ν^I are the Young's modulus and Poisson's ratio of the indenter tip used, and ν^F is the Poisson's ratio of the film tested.

FE simulations can also be used to obtain the various mechanical properties of the materials. Load–displacement curves are generated from a model system with various combinations of mechanical properties. A match to the experimental data of the unknown material with the numerical results from the FE simulations is then found in order to extract the mechanical properties of the analyzed material. Different dimensionless parameters or functions are defined from the loading–unloading curve to solve the problem using iterative algorithms [39, 40, 242] or an incremental manner [53]. A simple inverse FE method is used herein to incrementally minimize the error between a measured and simulated elastic modulus and hardness by adjusting the material parameters within the FE-model used in Chapter 5.

3.3.3 FINITE ELEMENT ANALYSIS

Finite element analysis was used in this thesis to model the gyroid nanostructure three dimensions to determine the effective mechanical properties of both solid and hollow gyroids. FEA was also used to model the continuum properties of the gyroid films using the Deshpande-Fleck constitutive model. The computational simulation using the commercially available software ABAQUS, which is consistently used throughout the literature on cellular mechanics.

3.3.3.1 *The Theory of FEA*

Finite Element Analysis (FEA) is a general discretization procedure for continuum problems posed by mathematically defined statements. In most cases of interest, a field variable such as stress is described throughout a body by a set of partial differential equations (PDEs) that are impossible to solve mathematically for a continuum. FEA is typically used to analyze complex continuum systems where the underlying physics are expressed in either PDE or integral equations, by dividing the problem into smaller areas in the physical system. These areas are known as elements, which are connected by nodes, as shown in Figure 3.20. It is assumed that the field variable acts through or over each element in a predefined manner, which may be, for example, a constant, a linear, a quadratic or a higher order function distribution. Hence, each element is governed by a set of parameters and can be solved numerically for a desired response. The combination of each elemental response over the whole assembly solves the required problem. Typical problem areas of interest include structural analysis, heat transfer, fluid flow, mass transport, and electromagnetic potential.

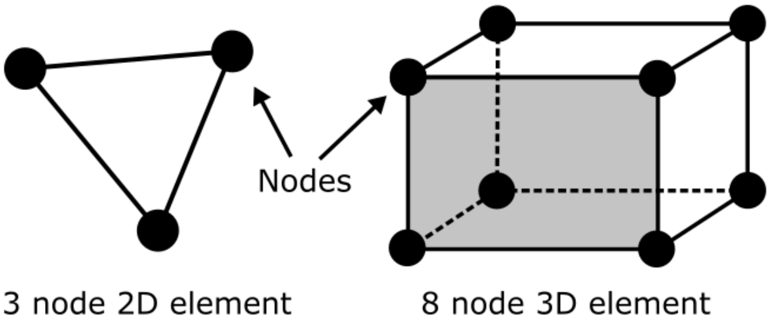

Figure 3.20: Typical first-order finite elements for 2D and 3D analyses.

In the case of stress analysis, as performed herein in Chapter 5, the governing equation to describe the forces induced by displacements at the nodes of a given element e, q_e , is:

$$\begin{Bmatrix} q_1 \\ q_2 \\ \vdots \\ q_m \end{Bmatrix} = \begin{bmatrix} K_{11} & K_{12} & \dots & K_{1m} \\ K_{21} & \ddots & & \vdots \\ \dots & & & \vdots \\ K_{m1} & \dots & \dots & K_{1m} \end{bmatrix} \begin{Bmatrix} u_1 \\ u_2 \\ \vdots \\ u_m \end{Bmatrix} + \begin{Bmatrix} f_1 \\ f_2 \\ \vdots \\ f_m \end{Bmatrix} \tag{3.6}$$

$$\{q_e\} = [K_e]\{u_e\} + \{f_e\} \tag{3.7}$$

Where m are the degrees of freedom at each node of element e, K_e is the stiffness matrix of the element, u_e is the matrix of nodal displacements of the element and f_e gives the nodal forces required to achieve equilibrium of forces acting on the element. These elemental data are combined using the global equation:

$$\{f\} = [K]\{u\} \tag{3.8}$$

Where K is the global stiffness matrix, u summarises all nodal displacements, and f includes all nodal forces required for equilibrium. Boundary conditions are applied to the relevant nodes and the displacements and are then solved using numerical techniques such as Gaussian elimination, Gauss–Seidel iteration or Cholesky square root methods.

3.3.3.2 *FEA in Practice*

The total implementation of a FE method can be broken down into three stages, as seen in Figure 3.21. Each of these stages are briefly outlined in this section, and the discussion of the application of FEA in Chapter 5 will be done in this context.

PRE-PROCESSING STAGE: Pre-processing is a crucial step in the development of a FEA model, beginning with the development of geometry of individual model parts which are discretized into a mesh of elements and combined together into an assembly. The interactions between the parts, material properties, boundary conditions and loads must also be defined before analysis can be carried out.

Key considerations for the pre-processing stage in a FEA experiment can be broken down as follows.

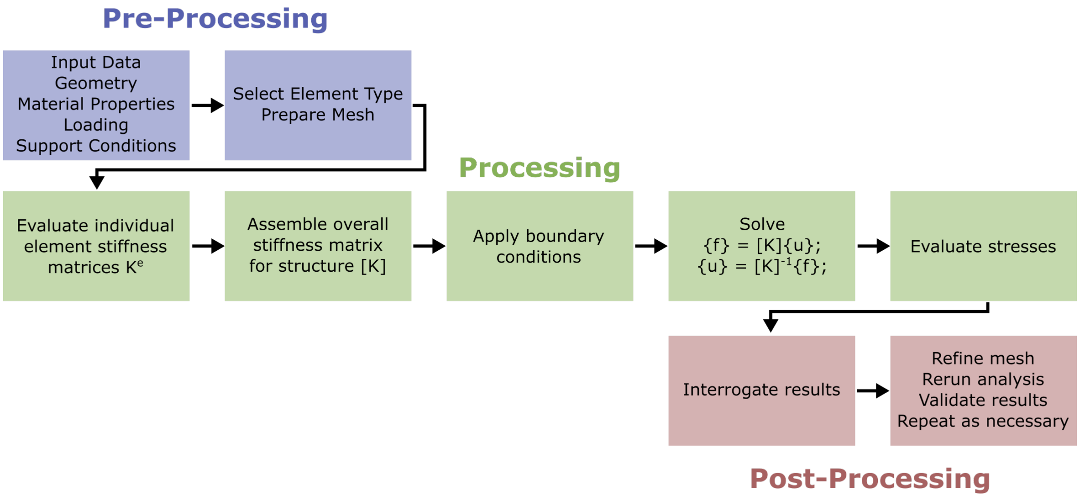

Figure 3.21: Overview of a finite element analysis process for structural simulation.

1. Element boundaries should coincide with structural boundaries.
2. Points of application of forces (and restraints) must coincide with suitable nodes, and any abrupt changes in distributed loading must occur at element boundaries.
3. Nodes should be at the points of interest for which output data are required, e.g. displacements, reaction forces, etc.
4. The selection of element order (e.g. linear, parabolic, cubic) defines the interpolation or shape function of displacements between nodal points, i.e. the order of a polynomial in x , y and z directions, and hence the variation of stress/strain.
5. The element type (e.g. spring, rod, beam, triangular and quadrilateral planar or shell, tetrahedral or hexahedral (brick) element) must to be chosen appropriately.
6. Boundary conditions (e.g. applied loads, fixed nodes and restraints) and material properties must represented accurately.
7. Model geometry must be appropriately meshed.

In the design of a mesh, is important to note that the exact distribution of a load is not important far away from the loaded region, as long as

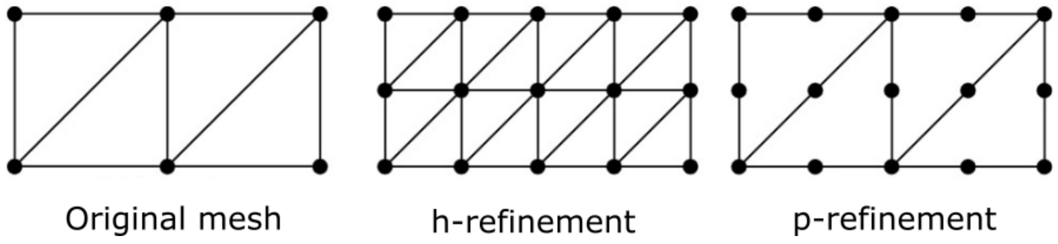

Figure 3.22: The h and p refinement methods are different ways of adding degrees of freedom to the FE model to increase the degree of accuracy.

the resultants of the load are correct. As a consequence, the mesh can be refined only in particular regions of interest and further have a transition zone from fine to coarse mesh. There are two types of refinements (h- and p-refinement) as shown in Figure 3.22. h-refinement relates to the reduction in the element sizes, while p-refinement relates to increasing the order of the element. An important issue for FEA accuracy that is often overlooked is mesh convergence. This is related to how small the elements need to be to ensure that the results of an analysis are not affected by changing the size of the mesh. Should a quantity of interest not change substantially with subsequent mesh refinements, then one can assume the result to have converged.

PROCESSING STAGE: During the solution phase, the finite element software assembles the governing algebraic equations in matrix form and computes the unknown values of the primary field variable(s), as discussed in the FEA theory sub-section 3.3.3

In all analysis performed herein, the displacement method (also known as the stiffness method) is used. In this approach as applied to structural mechanics, the displacements of the nodes are the primary unknowns of the problem. Compatibility conditions requiring that elements connected before loading and remain connected after deformation takes place are initially satisfied. Then the governing equations are expressed in terms of nodal displacements using the equations of equilibrium and an applicable law relating forces to displacements. This allows for the determination of the secondary unknown quantities, including stresses and strains in elements.

POST-PROCESSING STAGE: Post-processing in the context of FEA refers to the evaluation of the solution results followed by sorting, printing and plotting selected outputs from a finite element solution. Once the solution is verified to be free of numerical problems, and sufficiently converged, the quantities of interest may be examined. Key post-processing steps utilized in this thesis are listed below.

1. Visualization of the deformed structure.
2. Displacement magnitudes in three directions.
3. Nodal/element stress magnitude.
4. Time history.

4

UNIAXIAL COMPRESSION OF FREESTANDING AND COMPOSITE 3D GRAPHITIC FOAMS

4.1 AUTHOR CONTRIBUTION

This chapter is based on the publication *"Uniaxial compression of freestanding and composite 3D graphitic foams"* [165]. The bulk of the general approach, sample synthesis and characterization was performed by the author of this thesis. Uniaxial compression tests were performed by co-author A.I. Aria, in collaboration with the Fraunhofer Institute, Germany. Model development was performed with co-author Prof. N Fleck.

4.2 INTRODUCTION

In this chapter, the fabrication of 3D graphitic foams and their uniaxial compressive response is explored. The mechanical response of freestanding graphitic foams was investigated in order to give insight into their dependence of modulus and strength upon relative density and microstructure. This study utilizes commercially available nickel foam templates, which possess large pore sizes (~500 µm) and a stochastically arranged cell structure as the basis for a reproducible model system. An ever increasing body of literature on cellular material mechanics have shown that such disordered cellular architectures will suffer from poor load bearing and stress transfer behaviour. However, when the cell walls of such structures are comprised of layers of an emergent 2D material such as graphene, the operative structure/property relationships become less clear. As discussed in Chapter 2.3.1, graphitic multilayers possess a low out-of-plane shear stiffness and strength compared to their exceptional in-plane modulus. Consequently, it is unclear whether foams made from CVD graphene will possess high stiffness and strength, as dictated by the in-plane properties, or a much lower stiffness and strength due to weak interlayer van der Waals interactions.

A significant portion of the prior literature on the mechanics of graphene foams utilize molecular dynamics simulations of randomly arranged graphene flakes, as in an aerogel (see Chapter 2.2.1.5). Individual works have suggested that external compressive forces are dissipated by flake rippling, impacting and sliding [249]. Under tension, fracturing and tearing of the constituent flakes occur [179]. Furthermore, elasticity has been shown to be sensitive to crosslink density and flake size [250]. Such simulated behaviours are instructive in the prediction of deformation behaviours and hence the design of flake-assembled monoliths. However, CVD graphene-based cellular materials possess a significantly different microstructure that is based on continuous sheets of polycrystalline graphene directly grown in the desired morphology (see Chapter 2.2.1.1). Qin et al. attempted to simulate the behaviour of a CVD graphene assembly, using gyroidal structures that were modelled as a single layer of graphene which was covalently bonded throughout the entire 3D network [201]. These simulated 3D graphene assemblies possessed mechanical scaling relationships of $E \propto \bar{\rho}^{2.73 \pm 0.09}$ and $\sigma \propto \bar{\rho}^{3.01 \pm 0.01}$. Such large power indexes were suggested to have been caused by strong bending-dominated behaviour, and lead to the suggestion that such structures would be 10 times as strong as mild steel at 4.6% of the density, a prediction that has yet to be experimentally realized.

This difficulty in experimentally translating theoretically exemplary 2D material properties exists across every functional property. In the case of CVD graphene-based cellular materials, a major challenge exists in the necessity for the use of a catalytic growth template in the CVD process. Across the literature, the most commonly used is a commercially available nickel foam as was first utilized by Chen et al. [36]. Originally intended for use as a cathode substrate, these foams are produced by CVD of Ni onto open-cell polyurethane substrates, as discussed in Chapter 2.2.1.1. Such foams possess unit cell sizes of ~500 µm and strut sizes of ~75 µm, which stand in stark contrast to the thickness of a graphene layer, which stands at just ~0.335 nm. As a consequence, all reported freestanding CVD-based graphene cellular materials that have utilized similar templates possess cell walls comprised of thick graphitic multilayers (> 60 nm).

One of the few recent mechanical studies by Nieto et al. [169] on a freestanding CVD graphitic foam reported a macroscopic Young's modulus of 60 Pa. This extremely low value was obtained from the extrapolation of cell wall modulus values determined by direct nanoindentation. In tension, a more reasonable macroscopic Young's modulus of 340 kPa was measured. This low value (as compared to pristine graphene) was attributed to defects in the graphene foam structure such as cracked branches and discontinuous sheets, leading to only a small fraction of graphene branches bearing loads. A second study by Yocham et al. [282] compressed foam samples between platens, measuring a modulus of 12.5 kPa. In addition to the study of the quasi-static mechanical properties, Nautiyal et al. studied the damping behaviour using nanoscale dynamic mechanical analysis [166, 167]. They found that graphene foams possessed extraordinary damping capabilities due to energy dissipation through three multiscale dampening mechanisms: ripple formation in sheets, weak interlayer van der Waals interactions and structural branch bending. It must be noted that all of the above studies used samples of FG purchased from the Graphene Supermarket (Calverton, NY, USA), which possessed a density of 4 mg/cm^3 (i.e. $\bar{\rho}$ ~0.002), pore sizes of ~500 µm and wall thicknesses of ~90 nm. This motivated the growth, preparation and subsequent detailed mechanical investigation of such disordered macroscopic CVD graphene foams in this chapter.

In this chapter, open-cell graphitic foams FG are fabricated by CVD using commercially available INCOFOAM nickel templates across a range of relative densities through the optimization of CVD parameters. Such samples possessed graphitic wall thicknesses between 80-150 nm, which was necessary for stability in handling and reproducibility in testing. Process and handling improvements such as material purification via H_2 annealing and precise laser sectioning of samples were also implemented. The compressive responses were measured with a custom built uniaxial compression rig, prepared by collaborators in the Fraunhofer Institute. The mechanical response required an interpretation in terms of a hierarchical micromechanical model, spanning 3 distinct length scales. The power law scaling of elastic modulus and yield strength versus relative density suggests that the cell walls of the FG deform by bending. The length scale of the unit cell of the foam is set by the length of the struts comprising the cell wall, and is termed level I. The cell walls comprise hollow triangular tubes, and bending of these strut-like tubes involves axial stretching of the tube walls. This length scale is termed level II. In turn, the tube walls form a wavy stack of graphitic layers, and this waviness induces interlayer shear of the graphitic layers when the tube walls are subjected to axial stretch. The thickness of the tube wall defines the third length scale, termed level III. It is shown that the addition of a thin, flexible ceramic Al_2O_3 scaffold stiffens and strengthens the foam, yet preserves the power law scaling. The hierarchical model developed herein gives fresh insight into the mechanical properties of foams with cell walls made from emergent 2D layered solids.

4.3 EXPERIMENTAL METHODS

A schematic of the complete fabrication process can be seen in Figure 4.1. Nickel foam templates (MTIXTL, > 99.99%, 95% porosity, 1.6 mm thickness) were purchased and prepared as discussed in Chapter 3.1.1.1. CVD of graphitic multilayers was performed with a CH_4:H_2 ratio of 1:1 to 3:1, as discussed in Chapter 3.1.2.1. A richer hydrocarbon atmosphere was found to result in a higher average number of graphene layers and thus a higher relative density. If required, ALD alumina was then deposited onto the graphitic multilayers. Deposition of a conformal layer of ALD alumina is carried out in multi-pulse mode as detailed in Chapter 3.1.4. All depositions were carried out at 200°C, with 550 cycles total to obtain a 50nm thick layer. Pulse pressure and timing was kept equal between the TMA and H_2O at 0.55 Torr and 3s, respectively. PMMA-supported wet etching is used to remove the internal nickel templates to afford freestanding graphitic foams (FG or Al_2O_3/G), as described in Chapter 3.1.6.

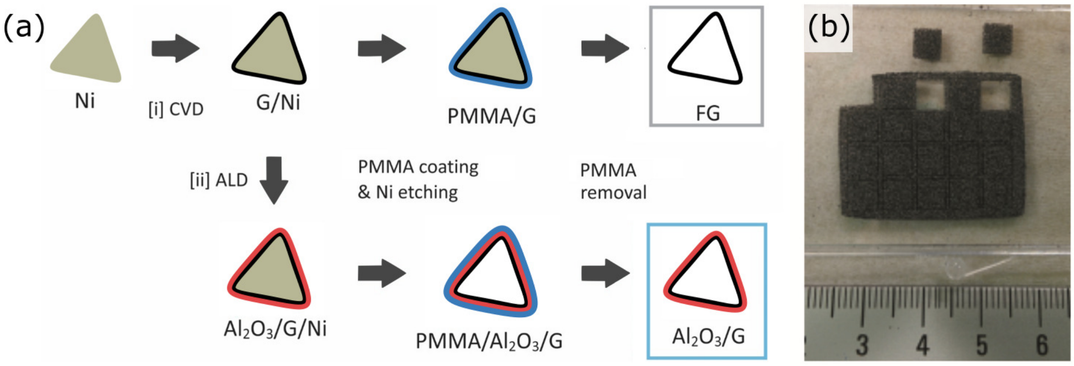

Figure 4.1: (a) Schematic of the sample preparation steps. A nickel network was subjected to a CVD process that encapsulates the templates in multilayer graphene. The network is coated in PMMA which acts as a scaffold as the nickel core is etched. (i) The PMMA scaffold is removed, preserving the structure in a FG. (ii) An intermediate ALD step can provide structures that are encapsulated in a thin AlOx shell. (b) Optical image of a final free-standing graphitic foam, with laser-cut 5×5 mm squares.

For freestanding graphitic foams to be mechanically stable, the walls are grown to multilayer thickness (> 80 nm). While graphitic foams with thinner walls could be fabricated with less carbon-rich recipes, handling of such samples was found to be prohibitively difficult. Electrostatic forces were sufficient to tear apart the foam after removal of the polymeric scaffold. As such, it was judged that transport, sectioning and testing of such samples with any degree of reproducibility would be near impossible, and samples with greater relative density were fabricated. In the literature, FG that possess relative densities below ~0.001 are supported by a polymeric layer [170, 212, 266] due to issues with instability and irreproducibility.

4.4 MATERIAL CHARACTERIZATION

SEM images of the as-fabricated freestanding graphitic (FG), and alumina supported (Al_2O_3/G) foams, are shown in Figure 4.2. The unit cell length (denoted L in Fig. 4.2a) is in the range 200–400 µm for both FG and Al_2O_3/G (Fig. 4.2a). The hollow struts have triangular cross-sections with side lengths of d = 30–70 µm for both FG and Al_2O_3/G (Fig. 4.2b). This large variation in the value of d is inherent to the commercial open-cell Ni templates that are used herein [10, 66]. The cellular geometries of the foams are neither altered by the CVD process nor by the Ni removal, as seen by comparing Figure 4.2 to the SEM of the original Ni foam template (see Figure 4.8). The thickness of the strut walls (denoted by h) is measured from SEM images of the cross-section (Fig. 3c). For FG, h equals 80-150 nm and the relative density $\bar{\rho}$ corresponds to 0.002-0.005 (Fig. 4.2c). This range of relative densities and associated wall thicknesses are comparable to values reported in the literature for device applications [36, 169, 187, 232, 281].

For the ceramic ALD coating, a fixed Al_2O_3 thickness of 50 (±5) nm (Fig. 4.2c) is used, which is sufficiently thin for the alumina to remain flexible [298], but sufficiently thick to give a measureable change in the macroscopic compressive properties. Hence, for Al_2O_3/G samples, h ranges from 130 nm to 200 nm (Fig. 4.2c). HR-TEM of a cross-section of a separate CVD grown graphitic film deposited on the surface of a Ni layer shows graphitic layers running parallel to the metal surface with characteristic (002) graphite spacing, see Fig. 4.3. Other HR-TEM studies have confirmed the formation of covalent bonds at grain boundaries during the CVD process, allowing the in-plane Young's modulus to remain high [175, 182].

The graphitic quality of the as-fabricated foams was characterized by means of Raman spectroscopy, TGA and XPS. Raman maps of the foam unit cells and respective individual Raman spectra are shown in Fig. 4.4. The I_D/I_G ratio map for the FG shows a low defect density ($I_D/I_G < 0.05$) across the entire 300×300 µm area (Fig. 4.4a-c). The I_D/I_G ratio is largely < 0.01, indicating that the graphitic layers are well graphitized (see Fig. 4.4a). The majority

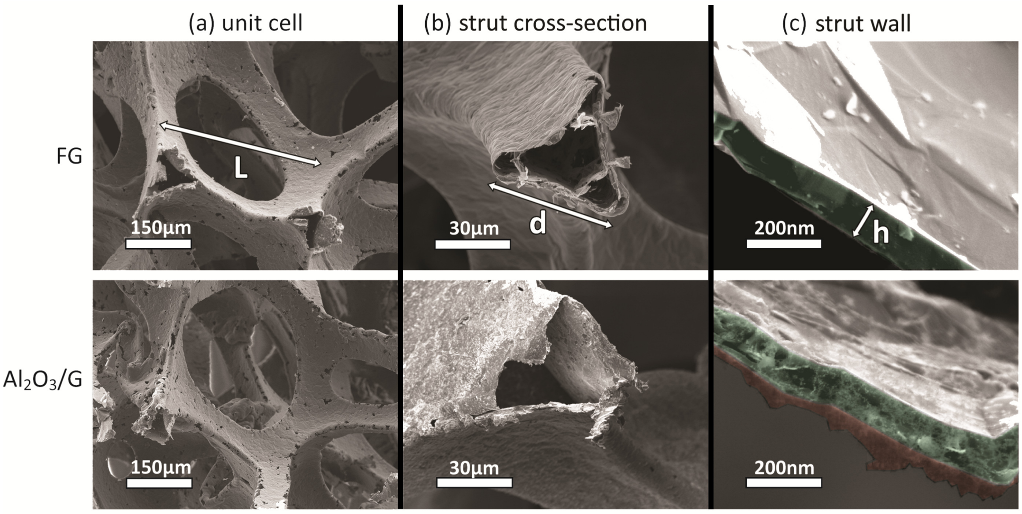

Figure 4.2: SEM images of FG and Al_2O_3/G at different magnifications showing their typical (a) unit cell, (b) strut cross-section, and (c) strut wall. (a) The cellular geometries of FG and Al_2O_3/G closely resemble those of Ni foam templates with approximate unit cell length (L) of 300(±100) μm. (b) A cross-sectional cut shows that the struts of both FG and Al_2O_3/G are hollow with triangular cross-section and equivalent side length (d) of 50(±15) μm. (c) The strut wall of FG consists of hundreds of graphene layers, as highlighted in green, with thickness h that varies between 80 nm and 150 nm. The strut wall of Al_2O_3/G consists of graphene layers and Al_2O_3 film, as highlighted in green and red, respectively, with an overall thickness h that varies between 130 and 200 nm.

of the foam shows an I_{2D}/I_G ratio of 0.3-0.4, which is consistent with $h > 80$ nm, i.e. the multilayered nature of the walls here. The Raman map shows some areas with I_{2D}/I_G ratios > 1, which originate from locally decoupled (due to intercalation or rotation) layers of graphene [124, 189, 193]. Al_2O_3/G samples show a slightly higher I_D/I_G ratio compared to FG, which suggests that a small number of defects in the graphitic layers were introduced during the ALD process. The I_{2D}/I_G ratios of FG and Al_2O_3/G are similarly concentrated around 0.3–0.4, whereas those of PMMA/G are found to be more widely spread between 0.2 and 1 (Fig. 4.6d). Such a difference may be attributed to residual strain introduced by the PMMA scaffold during the fabrication step and thermal strain due to laser irradiation [269]. These strains are then released once the PMMA scaffold is removed from the foam.

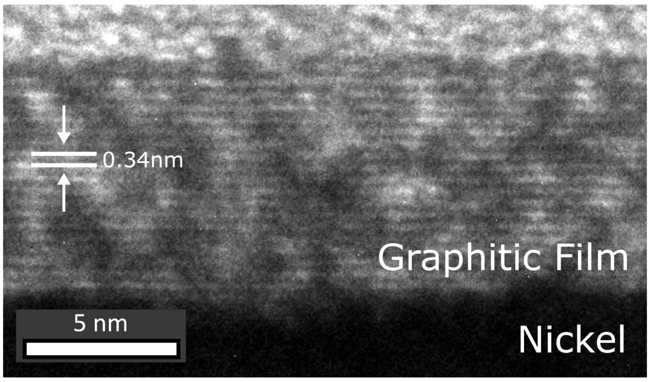

Figure 4.3: HR-TEM of a CVD-deposited few-layer graphene on a Ni template, showing conformal growth of stacked layers. The lattice image taken from a surface cross-section of a CVD-deposited graphitic film on a catalytic film shows graphitic layers running parallel to the metal surface with characteristic (002) graphite spacing. The sample was grown (~1000°C, CH_4(10 sccm)/H_2(600 sccm), 3 min, cooled at ~25°C/min) on a Ni-Au film (550 nm thick, 1.2% Au alloy), with the Au admixture giving improved nucleation control.

TGA in synthetic air (Fig. 4.4d) of FG shows a thermal stability threshold of ~770°C, again highlighting that the walls are well graphitized [244]. PMMA is decomposed in air at a much lower temperature of ~350°C. The absence of a peak in the weight derivative at ~350°C confirms the absence of residual PMMA on the FG. An EDX map image and spectra of a freestanding graphitic foam is shown in Figure 4.5, where only low levels of residual nickel could be detected. XPS analysis confirms the removal of the sacrificial Ni template (Fig. 4.6). The presence of a Ni template on graphene foams can be observed from the survey spectra of G/Ni foams prior to Ni removal, where the peak associated with Ni2p is visible at a binding energy of ~852eV (Fig. 4.6c). On FG, PMMA/G, and Al_2O_3/G foams, this peak is absent. The absence of this peak suggests that the Ni template has been removed to at least a level below the XPS detection limit. The C1s spectrum of FG exhibits a single peak at a binding energy of ~284.5eV that is commonly associated with freestanding sp^2 carbon (Fig. 4.6a). This indicates that the graphene layers in FG are free from both the Ni foam template and sacrificial PMMA layers. On the other hand, the C1s spectrum of PMMA/G foams exhibits additional peaks at binding energies of ~284.8eV and ~288.5eV (Fig.4.6a).

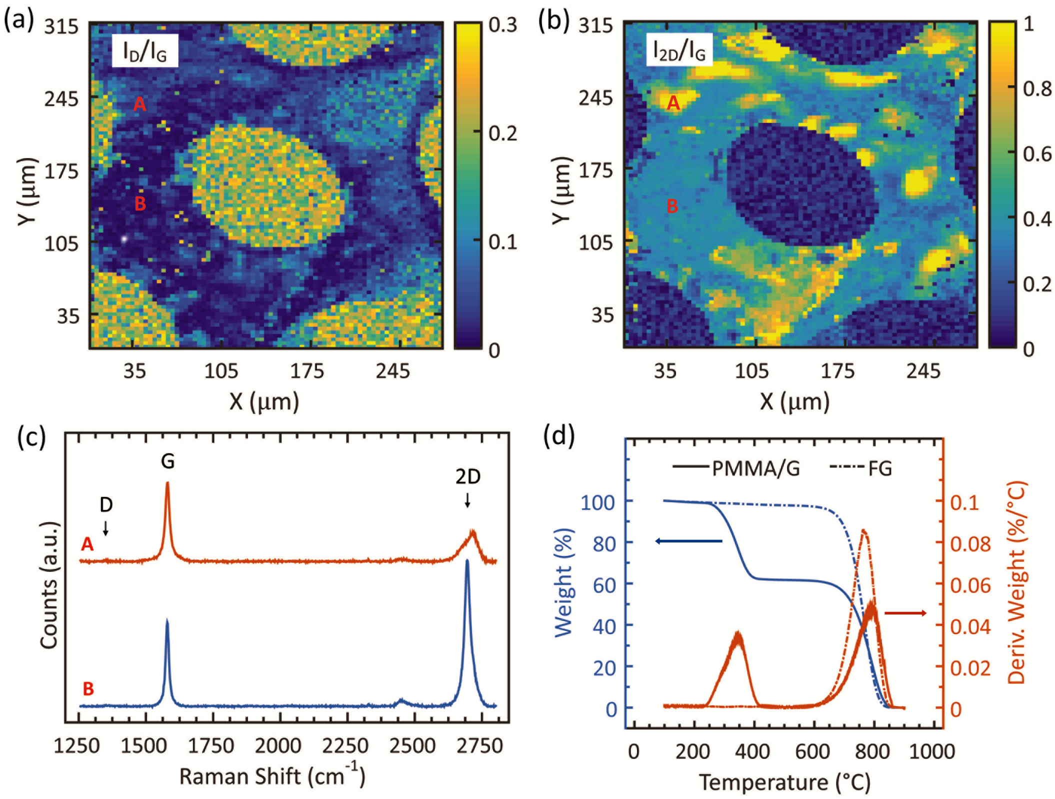

Figure 4.4: Raman spectroscopy map of a FG unit cell represented as (a) I_D/I_G and (b) I_{2D}/I_G intensity ratio. (c) Representative Raman spectra of FG foams taken at areas denoted as A and B in (a) and (b). (d) Thermogravimetric analysis of PMMA/G and FG in air to indicate the complete removal of PMMA scaffold. The PMMA scaffold decomposes in air at ~350°C, while graphitic layers are air stable up to ~770°C.

These peaks indicate the presence of sp^3 and oxygenated carbon species that originate from the PMMA scaffold. Similar to that of FG, the C1s spectrum of Al_2O_3/G exhibits a single peak at a binding energy of ~284.5eV (Fig. 4.6a). This suggests that the graphene layers are not altered by the ALD of Al_2O_3. The presence of the Al_2O_3 scaffold on Al_2O_3/G foams is confirmed by the symmetric peak that is commonly associated with aluminum oxide at a binding energy of ~74.6 eV in the Al2p core level spectra (Fig. 4.6b).

The strut walls exhibit waviness throughout the volume of the foam (see Fig. 4.2b). The length scales of wall waviness are obtained via AFM and SEM

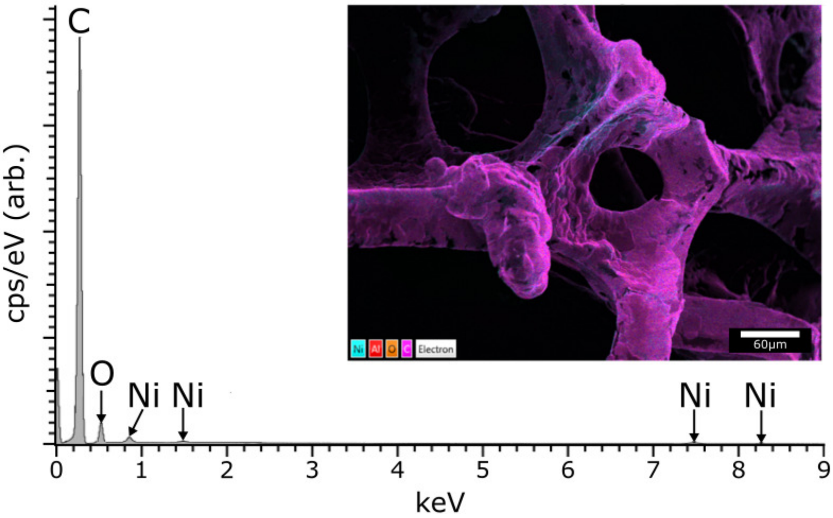

Figure 4.5: EDX map image and spectra of a freestanding graphitic foam. Only low levels of residual nickel could be detected.

imaging of the surface of the strut walls (see Fig.4.7). The line profiles of the wall surfaces indicate a characteristic variation on the scale of a few µm. This roughness was idealized as a sine wave, with a characteristic amplitude w_0 = 0.76 - 2.8 µm and wavelength λ = 3.7 – 18 µm for both FG and Al_2O_3/G (Table 1). It is proposed that the waviness relates to the polycrystalline grain structure of the commercial Ni foams (see Fig. 4.8b), for which grains range in initial size from 4-20 µm, and the presence of multiple different Ni surface orientations as a result of the non-planar shape of the foams, leading to inhomogeneities during CVD of the graphitic layers, see Fig. 4.1a.

LENGTH-SCALE	h(µm)	d(µm)	w_0	λ(µm)
MINIMUM	0.08	35	0.76	3.7
MAXIUMUM	0.20	65	2.8	18

Table 4.1: Summary of key measured waviness length-scales as measured by cross-sectional SEM.

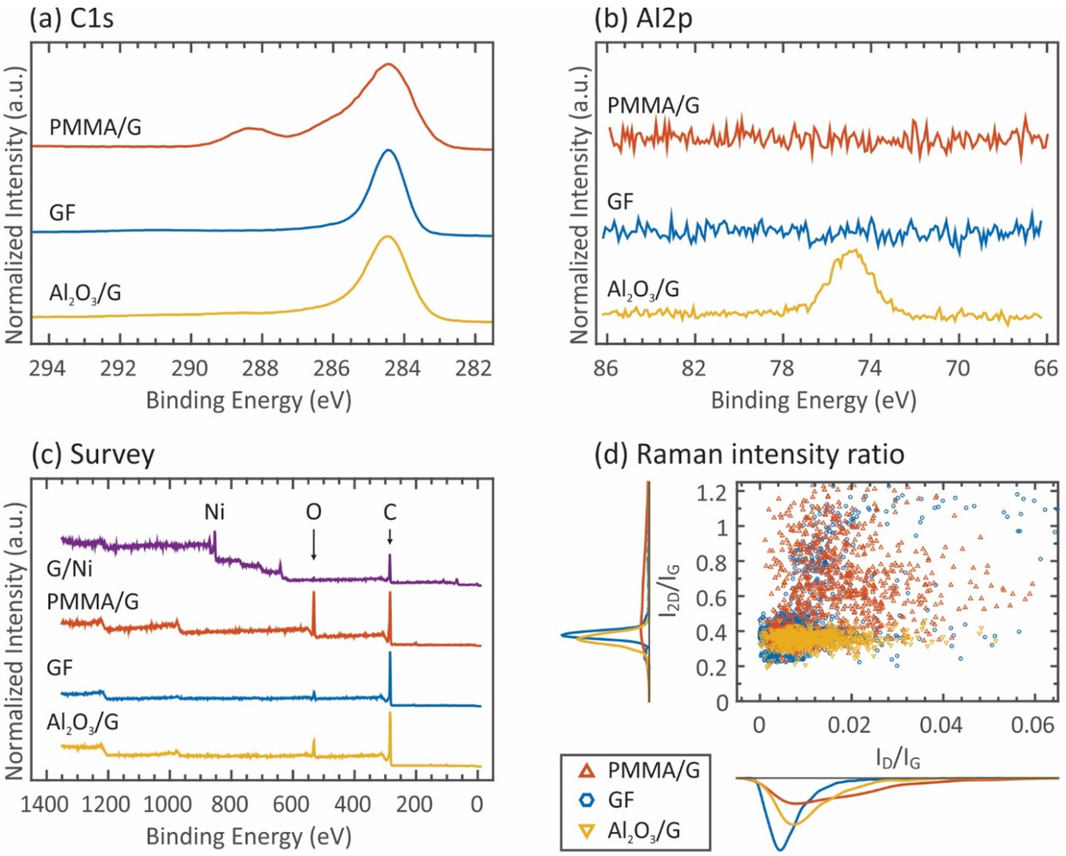

Figure 4.6: C1s (a) and Al2p (b) core-level spectra of FG, PMMA/G, and Al_2O_3/G foams confirming the presence of PMMA and Al_2O_3 scaffolds on PMMA/G and Al_2O_3/G respectively. (c) XPS survey spectra of nickel-free G, PMMA/G, and Al_2O_3/G foams along with that of graphene on Ni foam prior to template removal (G/Ni) as comparison. (d) Distribution of I_D/I_G and I_{2D}/I_G obtained from multiple PMMA/G, FG, and Al_2O_3/G foams. All Raman spectra are obtained using 532nm excitation.

4.4.1 MECHANICAL CHARACTERIZATION

Uniaxial compression tests were carried out as detailed in Chapter 3.3.1. For all graphitic foams, the compressive modulus E was obtained by fitting the linear part of the stress-strain curve to a linear fit. The linear region was defined as the region between 1% strain and 11% strain for FG samples and between 1% strain and 6% strain for Al_2O_3/G samples. The onset of plasticity, which is represented by the yield strain ϵ_Y, is defined by the 0.2% offset

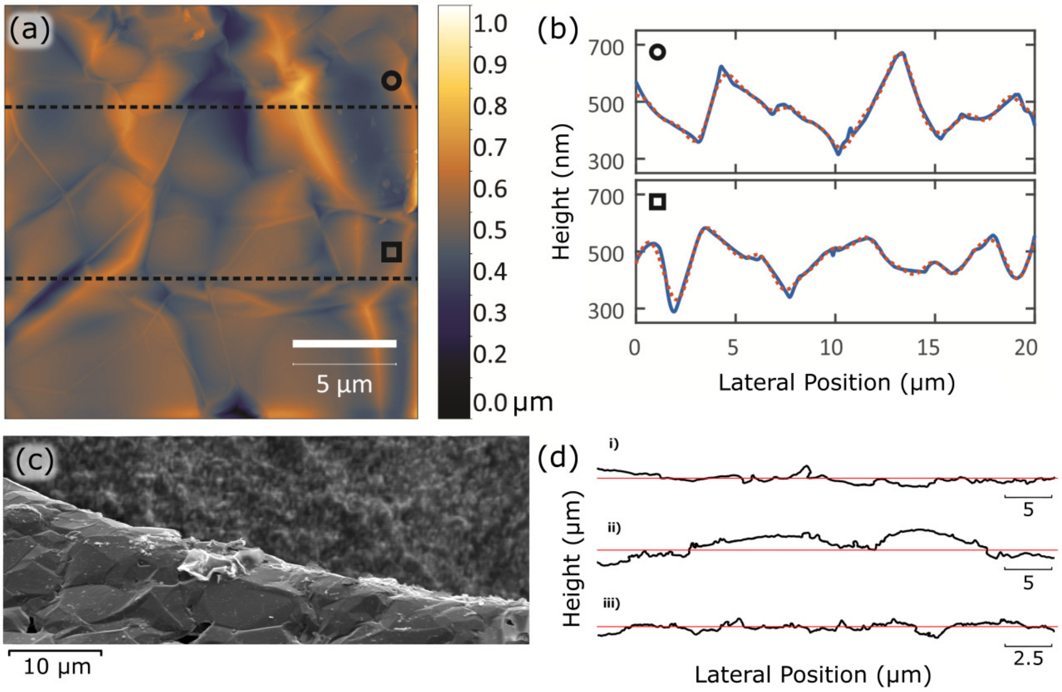

Figure 4.7: Examination of strut waviness from AFM and SEM images. AFM line profiles (a) can be used to extract (b) waviness values. Raw SEM images (c) are processed to find edges, which are extracted (d) and compared to a scale based on the image magnification. Images d-i to iii are edge profiles extracted from separate high-resolution SEM images. Large scale waviness up to an amplitude of 2.8 µm may be present along the length of a number of struts (d-ii).

method. This was determined by offsetting the linear fit in the linear elastic regime by 0.2% strain and finding the point of intercept. The yield stress σ_Y is identified by the stress at the onset of plasticity. The onset of densification, which is represented by the densification strain ϵ_D, was determined by first calculating the compression efficiency η, from which ϵ_D was then determined from the point of maximum efficiency η_{max} [129].

A typical plot of nominal compressive stress σ versus nominal (engineering) strain ϵ for FG is given in Fig. 4.9, for a displacement rate of 10 µms^{-1}. As noted for a wide range of foams [78], three distinct regimes exist: (I) linear elastic for $\epsilon < \epsilon_Y$, (II) plateau $\epsilon_Y < \epsilon < \epsilon_D$, where ϵ_D is a densification strain and (III) densification $\epsilon > \epsilon_D$, (Fig. 4.9a). In regime I, the foam is strained in a

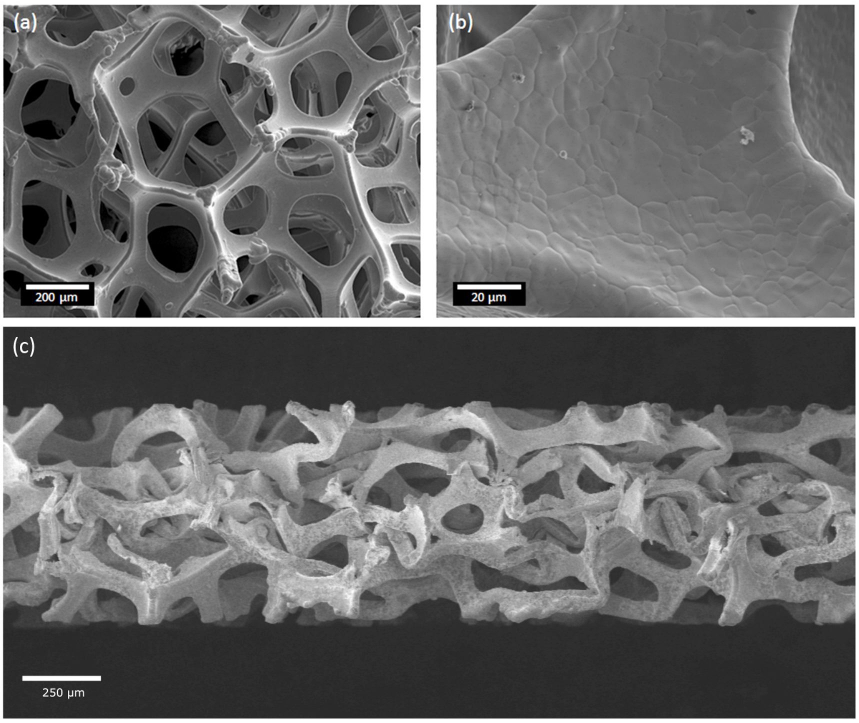

Figure 4.8: (a) Scanning electron microscopy (SEM) images of commercial Ni foam used herein (MTIXTL, purity >99.99%, ~95% porosity, 80-110 pores per inch, 1.6 mm thick, bulk density ~450kg/m^3). The polycrystalline grain structure can be seen in (b), with a grain size ranging from 4-20 µm. A sample post 60% uniaxial compression can be seen in (c).

uniform elastic (i.e. reversible) manner, with no observable damage evolution. The onset of plasticity marks the change from regime I to regime II. There is a clear change in slope in Figure 4.9a at the onset of plastic collapse (at $\epsilon = \epsilon_Y$).

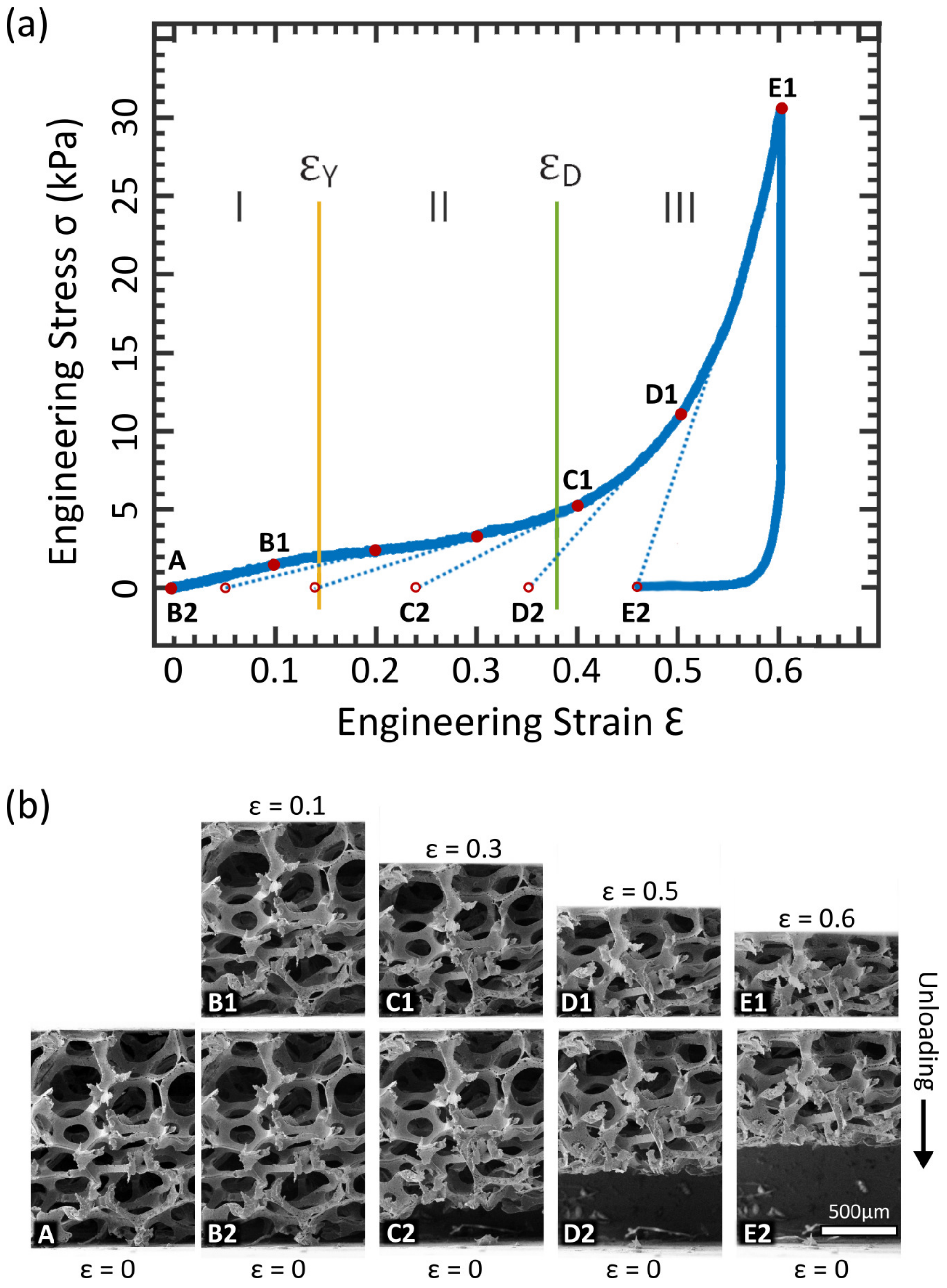

Figure 4.9: (a) Typical nominal stress-strain curve response of FG under compressive load. Three distinct regimes exist: (I) linear elastic $\epsilon < \epsilon_Y$, (II) plateau $\epsilon_Y < \epsilon < \epsilon_D$, and (III) densification $\epsilon > \epsilon_D$. (b) SEM images of a sample subjected to successively larger levels of macroscopic strain ϵ, followed by unloading to zero load. The remnant strain ϵ_r was measured from the associated SEM images. A dotted line is drawn to illustrate this elastic unloading.

In order to obtain insight into the collapse mechanism, a specimen was subjected to successively larger levels of macroscopic strain ϵ, followed by unloading to zero load and measurement of the remnant strain ϵ_r from the associated SEM images, see Fig. 4.9b. A series of dotted lines are shown in Fig. 4.9a to give the end points of this elastic unloading. These images reveal the following:

1. Straining is elastic up to the onset of plastic collapse ($\epsilon = \epsilon_Y = 0.14$) such that $\epsilon_r = 0$. For example, full recovery is observed from an imposed strain level of $\epsilon = 0.1$, (point B_1) as shown in Fig. 4.9a.

2. After straining to a level $\epsilon > \epsilon_Y = 0.14$, the foam exhibits plastic collapse with little observable microcracking or debonding of the struts. For example, elastic unloading from $\epsilon = 0.4$ (point C_1) results in a remnant strain $\epsilon_r = 0.24$ (point C_2).

3. When the specimen is strained to beyond a densification strain $\epsilon_D = 0.38$, the struts impinge upon each other and strong strain hardening occurs. The full unloading curve from $\epsilon = 0.6$ (point E_1), to $\epsilon_r = 0.46$ (point E_2) is also shown in Fig. 4.9a and reveals a non-linear unloading behaviour associated with the elastic relaxation of the distorted microstructure as the strain reduces to ϵ_r.

A higher resolution image of the deformed struts after unloading from $\epsilon = 0.6$ is shown in Fig. 4.10a. Plastic hinges are marked by the arrows in Fig. 4.10a, the formation of which is schematically shown in Fig. 4.10b. The resemblance between the deformed microstructure of the graphitic foam and of the Ni foam template in compression is remarkable; see for example Fig. 4.8. There is little evidence of debonding between graphite layers; the struts maintain their integrity and do not fragment.

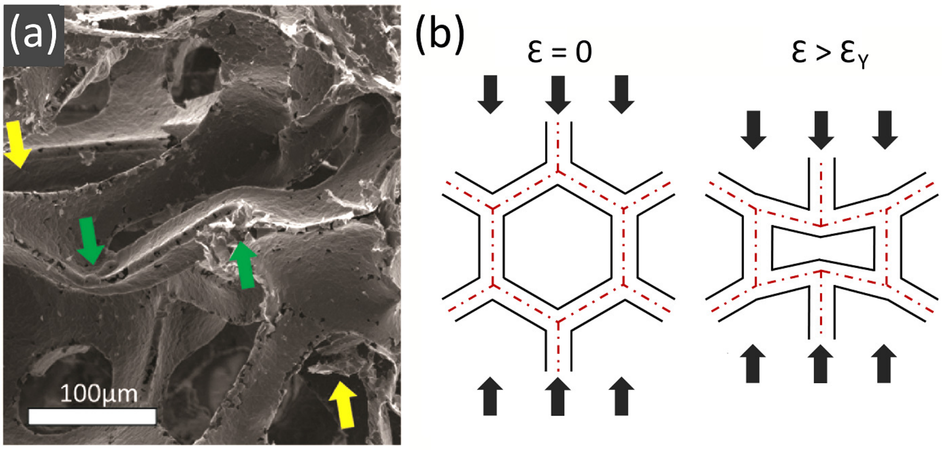

Figure 4.10: (a) Low magnification SEM image of FG foam taken post compression (peak $\epsilon = 0.6$). Green and yellow arrows indicate the plastically deformed and fractured struts, respectively. The green arrows indicate a pair of plastic hinges formed on the deformed strut. The yellow arrows indicate the direction of the compressive force. (b) Schematic of the plastically deformed strut at $\epsilon > \epsilon_Y$, with the cell structure skeleton outlined in red. The struts undergo bending when the foam is subjected to compressive force. Since the strut ends are rigid and act as rotation-fixed but translation-free constraints, a pair of plastic hinges is formed on the strut.

Nominal stress-strain responses of FG and Al_2O_3/G foams are compared in Fig. 4.11a and 4.11b. Both the FG and Al_2O_3/G foams display similar strain hardening behaviours, each exhibiting a plateau in stress between the yield point and densification point $\epsilon_Y < \epsilon < \epsilon_D$ (Fig. 4.11a). Note that the Al_2O_3/G foam does not exhibit catastrophic brittle failure, consistent with the fact that 50 nm thick Al_2O_3 films are able to sustain small bending radii [298]. Recall from Gibson-Ashby [77] that a brittle foam exhibits a characteristic jagged stress versus strain curve compared to the smooth curves of Fig. 4.11a. For FG foams, the transition from the elastic regime I to the plastic regime II occurs at a yield strain ϵ_Y in the range 0.17 to 0.40, depending on the magnitude of the relative density $\bar{\rho}$ (in the range 0.002 to 0.005). In contrast, for the Al_2O_3/G foams, yields occurs at ϵ_Y in the range 0.08 to 0.21, again depending on the density of the sample measured.

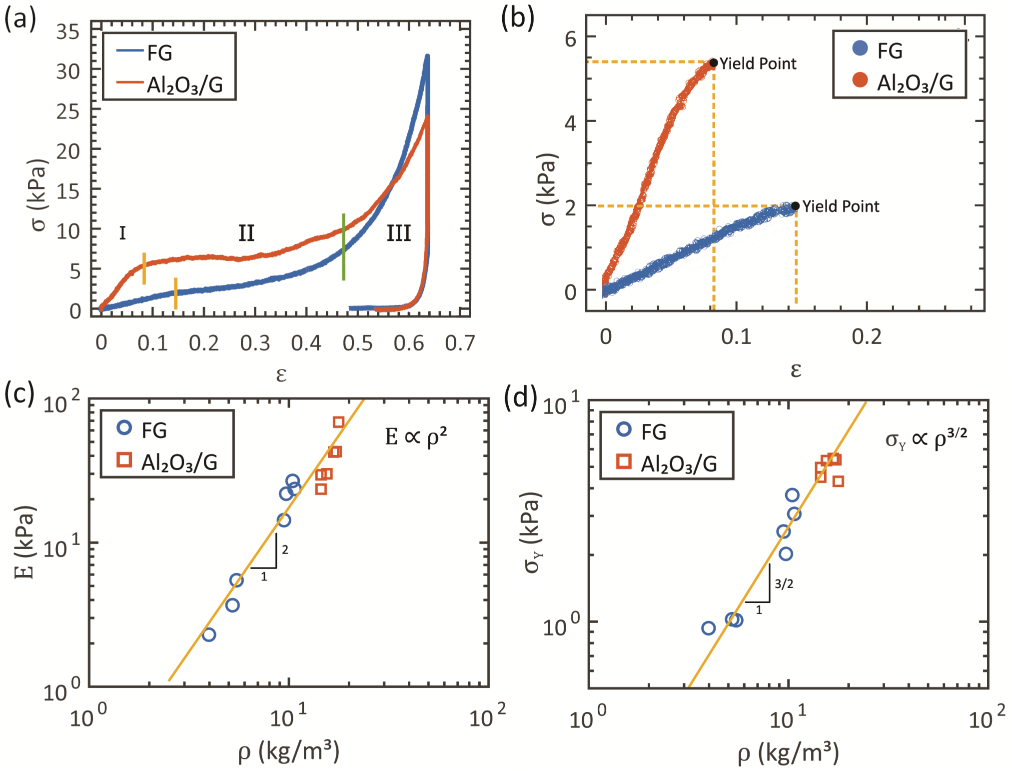

Figure 4.11: (a) Typical nominal stress-strain ($\sigma - \epsilon$) response of FG and Al_2O_3/G under compressive load with a displacement rate of ~10 µm/s. The onset of plasticity $\epsilon = \epsilon_Y$, is indicated by the yellow line, while the onset of densification $\epsilon = \epsilon_D$, is indicated by the green line. (b) Sample $\sigma - \epsilon$ curves of FG and Al_2O_3/G in the linear elastic regime. The yield stress (σ_Y) is given by the stress at σ_Y, while the compressive modulus (E) is obtained by a linear fit. Plot of E (c) and σ_Y (d) of FG and Al_2O_3/G as a function of their apparent density (ρ). The yellow fit in (c) and (d) indicate scaling of $E \propto \rho^2$ and $\sigma_Y \propto \rho^{3/2}$, respectively.

A linear fit to the log-log plots of Figures 4.11c and 4.11d was performed. The slope of the E versus ρ plot has a best fit value of 1.99 (with a 95% confidence interval of 1.66 and 2.32). Similarly, for the σ_Y versus ρ plot the best fit slope is 1.32 (with a 95% confidence interval of 1.12 and 1.53). Recall that Gibson-Ashby [77] show that the scaling law reads $E \propto \rho^2$ for cell-wall bending and $E \propto \rho$ for cell-wall stretching. Similarly, the correlation between σ_Y and ρ reads $\sigma_Y \propto \rho^{3/2}$ for cell wall bending and $\sigma_Y \propto \rho$ for cell-wall stretching. Taken together, the data of Figs. 4.11c and 4.11d support the conclusion that these materials behave as bending-dominated open-cell foams.

It is important to distinguish between the macroscopic density ρ of a foam, when treating it as a homogeneous solid, and the density ρ_s of the cell wall material. For the monolithic free standing graphitic foam, the relative density is $\bar{\rho}=\rho/\rho_s$. Note that $\bar{\rho}$ is identical to the volume fraction of cell wall material in the foam. In contrast, for the composite case of an Al_2O_3/G foam, it is straightforward to measure ρ, but more involved to determine ρ_s as due account must be made for the proportion of Al_2O_3 versus graphite. The scaling laws of Gibson-Ashby were established in terms of $\bar{\rho}$ for a monolithic foam and the power-law index is unchanged when strength or modulus is plotted in terms of $\bar{\rho}$ rather than ρ.

4.4.2 COMPARISON TO OTHER STATE-OF-THE-ART FOAMS

Figure 4.12 summarizes the sensitivity of the normalized compressive Young's modulus and yield strength of graphene-based aerogels to their relative densities. The constituent bulk material is again graphite. Note that our hierarchical model predicts that the yield strength scales as $\bar{\rho}^{3/2}$. In contrast, the observed yield strength for these alternative foams scale as $\bar{\rho}^{2.4}$. This discrepancy can be traced to the fact that these aerogel foams comprise interlocked platelets of exfoliated graphene, bonded with relatively weak van der Waals forces or binding agents, rather than the continuous sheets of graphene that make up the foams in our study.

To highlight the advantages of CVD grown lattice structure, the enhanced conductivity of the CVD grown graphitic foams is compared to other state of the art graphene-based foams. Figure 4.13 shows the correlation between electrical conductivity (1/R) of FG, PMMA/G, and Al_2O_3/G foams to their apparent density ρ. Electrical conductivity was measured by the four point probe van de Pauw method (see Chapter 3.2.10), with thickness taken as apparent foam thickness as is standard in the literature. All graphitic foams used here exhibit exceptional electrical conductivity of > 7 S/cm. For FG, the electrical conductivity increases from ~7 S/cm to ~20 S/m when ρ is doubled to ~11.1 kg/m^3. While the presence of PMMA and Al_2O_3 scaffolds

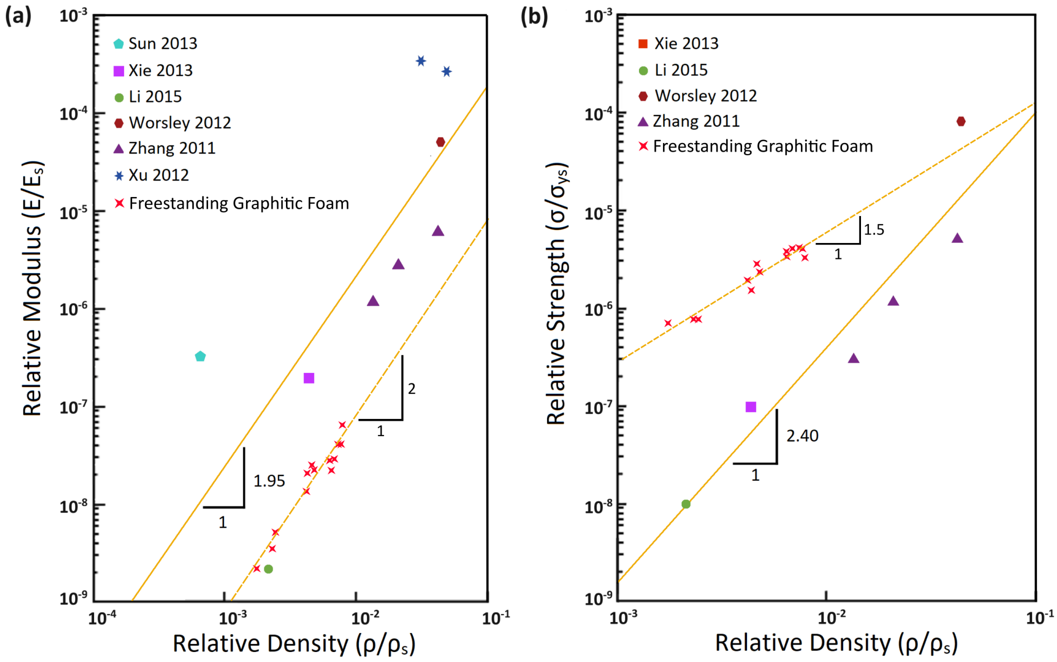

Figure 4.12: Normalized compressive Young's modulus (a) and yield strength (b) of graphene oxide foams as a function of relative density. The power law fit is plotted according to classical scaling laws, finding slopes of 1.95 and 2.40 and scaling constants of 0.017 and 0.025 for (a) and (b) respectively. ρ_s=2270 mg/cm^3, E_s = 1.06 TPa, and σ_{ys} = 130 GPa are used for the density, Young's modulus, and yield strength of graphene for its in-plane mechanics, which are used to normalize the properties of graphene aerogels.

decreases the electrical conductivity, the effect is not significant as it only decreases to ~14 S/cm and ~16 S/cm, respectively. More importantly, all CVD grown graphitic foams measured here are more conductive, by more than one order of magnitude, than other state-of-the-art graphitic aerogels and carbon nanotube foams at the same density range [14, 200, 202, 264, 297, 308]. Our measured conductivity values are comparable to previously reported values for CVD graphene composite foams [36]. The conductivity measured herein refers to the given environmental conditions. Graphene/graphite wall conductivity can be increased by charge transfer doping and intercalation.

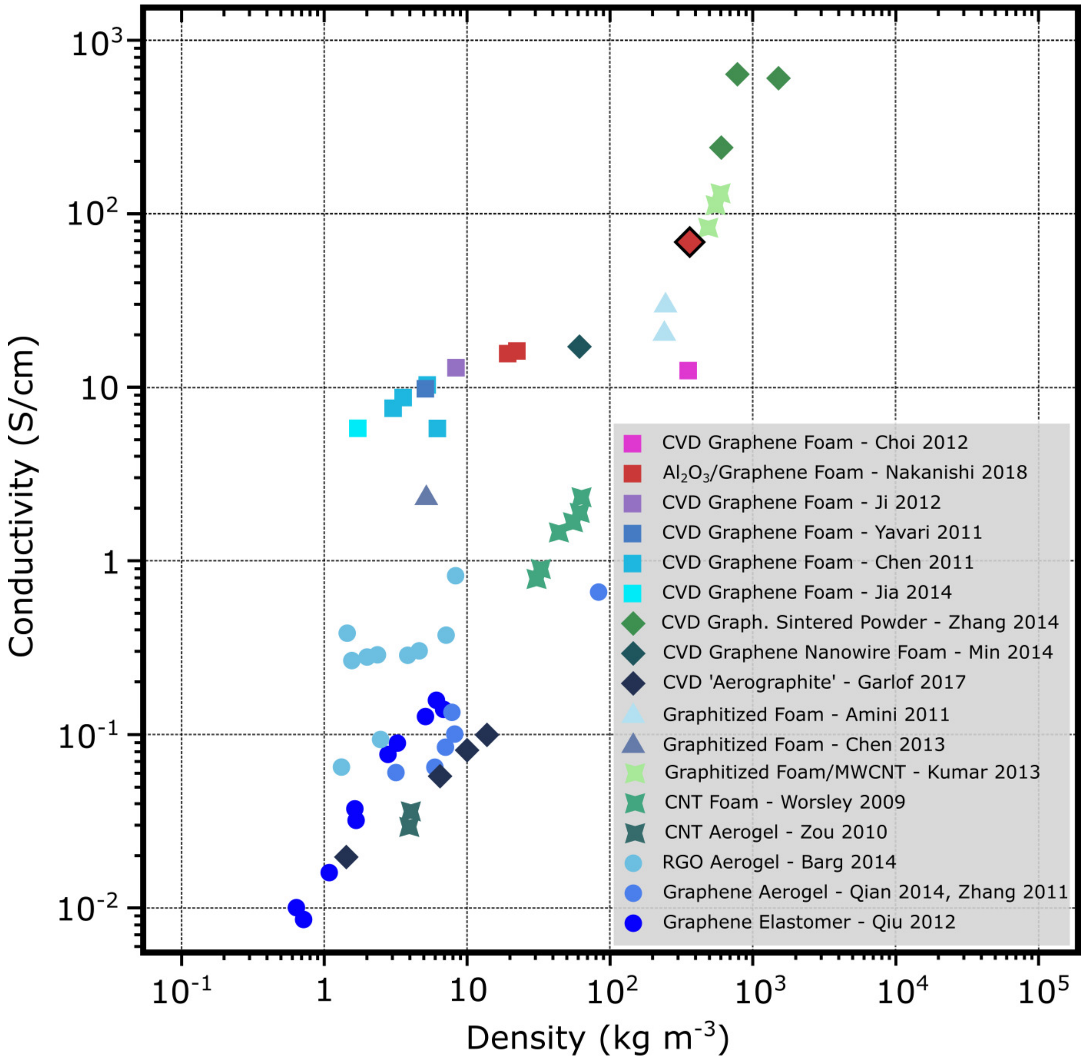

Figure 4.13: An Ashby chart showing the correlation between electrical conductivity (1/R) and apparent density (ρ) for FG, Al_2O_3/G, and PMMA/G foams. Other state-of-the-art low density materials reported in previous literatures are also presented as reference, see [3, 14, 34, 36, 42, 74, 98, 100, 117, 160, 200, 202, 264, 281, 293, 297, 308].

4.5 RESULTS AND DISCUSSION

4.5.1 GRAPHITIC FOAM WALL THICKNESS AND STRUCTURE

The micromechanical Gibson-Ashby approach [77] for bending-dominated open-cell foams is adopted in order to interpret the response of the FG and

Al_2O_3/G foams. The foams in this study are idealized by unit cells with hollow struts of triangular cross-section. The struts have a length L, an equivalent side length d, and a wall thickness h, see Fig. 4.14a,b. The observed dependence of modulus and yield strength of the FG and Al_2O_3/G foam in Fig. 4.11c,d reveals that $E \propto \rho^2$ and $\sigma_{ys} \propto \bar{\rho}^{3/2}$, consistent with strut bending, as anticipated for 3D open-cell foams and lattices of low nodal connectivity [78]. The previous literature on graphene/graphite foams [169, 201] has assumed that the pre-factors of the Gibson-Ashby power-law scaling relations [77] are the same as those for metallic and polymeric open-cell foams. However, the deformation mechanisms for the struts of a graphitic foam are much more complex than those of solid struts. The cell walls are hollow, and are made from a layered graphitic structure of low shear modulus and strength.

A hierarchical micromechanical model spanning three distinct length scales is developed to interpret the mechanical response of the foams in this study. The length scale of the unit cell of the foam is determined by the length of the struts comprising the cell wall, and is termed level I. The cell walls comprise hollow triangular tubes, and the bending curvature of these strut-like tubes involves axial stretching of the tube walls, and this length scale is termed level II. In turn, the tube walls form a wavy stack of graphitic layers, and this waviness induces interlayer shear of the graphitic layers when the tube walls are subjected to axial stretch. The thickness of the tube wall defines the third length scale, termed level III. It is emphasized that the hierarchical model of the present study is an idealization to highlight the significance of the microstructure on three length scales. The properties of the bulk solid, the connectivity and shape of cell edges and faces, and the relative density $\bar{\rho}$ of a cellular solid are the main features that influence cellular properties [10]. Simple scaling laws have been previously derived for idealized cell geometries:

$$\frac{E}{E_s} = \alpha\bar{\rho}^n \tag{4.1}$$

$$\frac{\sigma}{\sigma_{ys}} = \beta\bar{\rho}^m \tag{4.2}$$

where the relative density $\bar{\rho}$ is the macroscopic apparent density of the foam divided by the density of the constituent solid material. The exponents n and

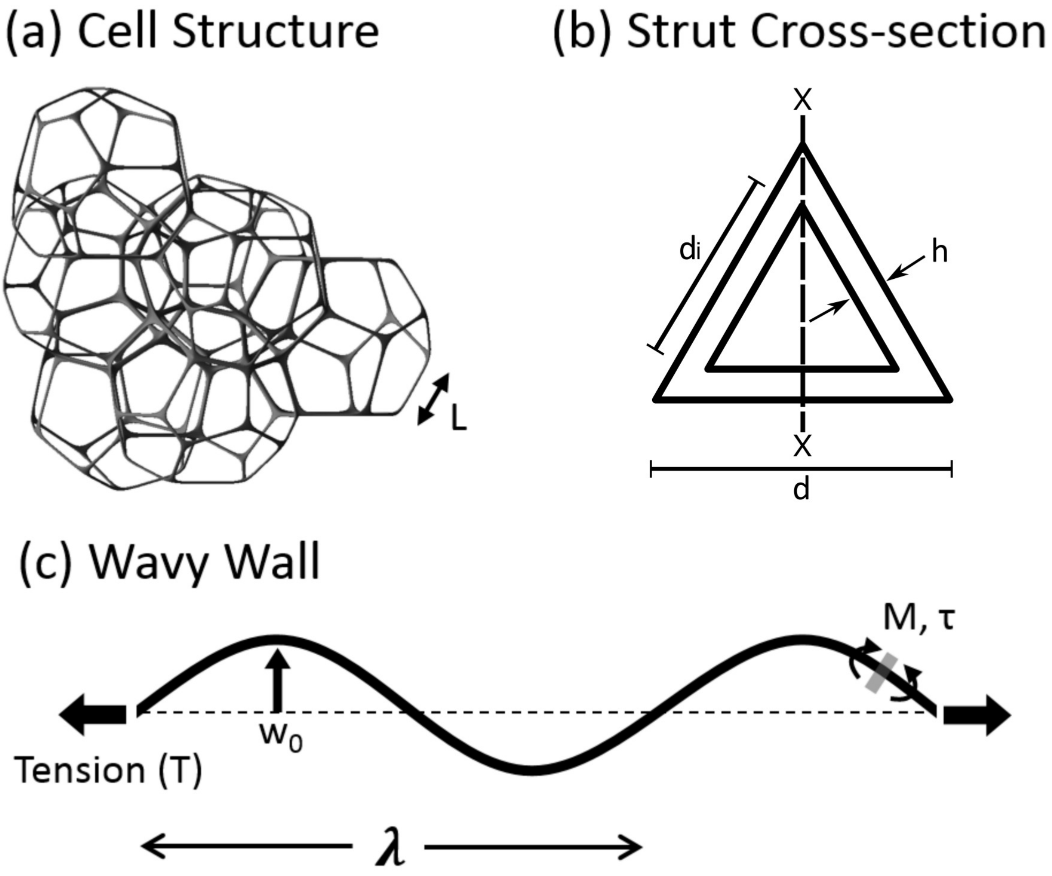

Figure 4.14: FG and Al_2O_3/G structure idealization. (a) The Weaire-Phelan open-cell foam structure, a bending-dominated, idealized foam of cells with equal volume. For the foams studied herein, the struts are hollow with an approximate length of L. (b) Strut schematic illustrating the hollow triangular cross-section with a side length of d, internal side length d_i, bending axis X–X and a wall thickness of h. (c) Wall level schematic of a cell wall loading in the micromechanical models used herein. The wall waviness is represented as a sine wave of amplitude w_0 and wavelength λ. In a wavy wall subjected to an axial tension or compression, misalignment induces bending loads and transverse shear forces on the cross-section of the cell wall, leading to the suggested wall bending or wall shear deformation modes.

m reflect the deformation mode of the struts within the foam [10, 12], and the observed values of $n = 2$, $m = 3/2$ are indicative of strut bending behaviour. The pre-factors α and β depend upon the details of the microstructure [12, 23, 207]. These scaling laws adequately describe the macroscopic foam behaviour for many types of macrocellular foams [306], including ceramics, metals and polymers [4, 5, 84, 304]. These power laws are used in order to interpret the response of the graphitic foams of the present study. It is found that the measured values for the pre-factors α and β of Eq. 4.1 and 4.2 respectively are 7.8x10^{-4} and 6.5x10^{-5}, see Fig. 4.11c and 4.11d. These differ greatly from the previously assumed magnitude of pre-factors $\alpha = 1$ and $\beta = 0.3$, as taken from the literature for metallic or polymeric open-cell foams [10, 78]. This motivates an investigation into the influence of hollow struts and wavy anisotropic cell walls on the values for the pre-factors (α,β).

It is recognized that (non-layered) ceramic nano-lattices deform elastically and recover upon unloading [96]. This contrasts with the observed behaviour of the multilayered graphite. Furthermore, the graphitic foams of the present study deform in a different manner to that of elastic-brittle ceramic foams, see for example Gibson-Ashby [78]. Such foams display a highly jagged stress versus strain response associated with the sequential fracture of individual struts at the loading plateau. No such fragmentation of the struts is observed in the present study. Thus, there is no need to account for fracture energy (such as surface energy) in the hierarchical model.

4.5.2 THE ROLE OF HOLLOW STRUTS

First, the implications of hollow struts on the stiffness and yield strength is investigated, by using the concept of shape factors [11]. The shape factor is a multiplicative scaling factor which expresses the amplification of a mechanical property (such as mechanical modulus), due to a choice of geometry. This factor is normalized by that of a solid circular beam of equal cross-sectional area to that of the geometry under consideration. Shape factors must be taken into consideration to account for this discrepancy between the measured values of the pre-factors α and β of the current study and the standard values of α=1 and β=0.3, as derived for open-cell foams [78].

Consider the case of an open-cell foam, with cell walls in the form of hollow triangular tubes of wall thickness h, strut side length d and internal strut side length d_i, as shown in Fig. 4.14b. Assume that the cell walls are made from a solid of Young's modulus E_s and yield strength σ_{ys}. It is further assumed that the strut is bending under an applied moment caused by the macroscopic compression of the foam. A reference cell wall of solid circular cross-section of diameter D is used, of cross-sectional area equal to that of the hollow tube, implying $D^2 = 12dh/\pi$. The shape factor for elastic bending ϕ_{Be}, and the shape factor for yield in bending ϕ_{By} are thus considered.

4.5.2.1 *Shape factor for elastic bending* ϕ_{Be}

The bending stiffness of the hollow triangular tube equals ϕ_{Be} times that of the solid circular bar. To begin, consider a beam of length l, under a uniform moment M such that the ends have a relative rotation θ. Then, the bending stiffness S_B is

$$S_B \equiv \frac{M}{\theta} = \frac{E_s I}{l} \tag{4.3}$$

where I is the second moment of area.

Write I_h and I_s as the second moment of area of a hollow triangular beam and solid circular bar, respectively. For bending about the axis X–X of Fig. 4.14, I_h reads as

$$I_h = \frac{1}{32\sqrt{3}}\left[\left(d_i + \frac{4}{\sqrt{3}}h\right)^4 - d_i^4\right] \approx \frac{hd^3}{6} \tag{4.4}$$

for $h/d \ll 1$, and the shape factor ϕ_{Be} follows as

$$\phi_{Be} = \frac{S_{Bh}}{S_{Bs}} = \frac{I_h}{I_s} \approx \frac{2\pi}{27}\frac{d}{h} \tag{4.5}$$

thereby defining the relevant shape factor for elastic bending of the cell wall struts in the form of hollow tubes.

4.5.2.2 *Shape factor for yield in bending* ϕ_{By}

Next, consider the plastic collapse of a hollow triangular bar and of the solid circular bar of equal cross-sectional area. Upon noting that the plastic collapse moment of the hollow triangular bar M_{Ph} and solid circular bar M_{Ps} are given by $M_{Ph} = \sqrt{3}hd^2\,\sigma_{ys}$ and $M_{Ps} = D^3\sigma_{ys}/6$ respectively, the relevant shape factor reads

$$\phi_{By} = \frac{\pi\sqrt{\pi}}{4}\frac{d}{h}^{1/2} \tag{4.6}$$

4.5.3 EFFECT OF SHAPE FACTORS

A direct comparison with Eq. 4.1 and 4.2 implies that $\alpha = \phi_{Be}$ and $\beta = 0.3\phi_{By}$. Using values of wall thickness h and strut width d, as measured by cross-sectional SEM, the value of the shape factor for elastic bending is determined to be $\phi_{Be} \approx 80$, and the shape factor for failure in bending $\phi_{By} \approx 30$. Shape factors exceeding unity are typical of hollow sections [64]. However, these values are several orders of magnitude too large when compared to the experimentally determined values for the constants of proportionality, indicating that the high-aspect ratio cross-sectional shape alone cannot account for the significant reduction in stiffness and strength. As such, an explanation at a lower length scale is sought, that of the walls of the hollow triangular struts.

4.5.4 THE ROLE OF WALL WAVINESS

It is emphasized that the above calculation of shape factors for a hollow triangular beam is based on the assumption that the walls of the hollow cross-section are perfectly straight. In reality the walls are wavy, as demonstrated by the high-resolution SEM images in Fig. 4.15. The walls of the hollow tubes are subjected to a gradient of axial stress from tension in the top fiber to compression in the bottom fiber when the tube is subjected to a bending moment M. Recall that these walls comprise a multilayered stack of graphitic sheets, see Fig. 4.2. When this wavy stack of sheets is subjected to an axial tension or compression, this misalignment induces bending loads and transverse shear forces on the cross-section of the cell wall. The wavy sheet responds by bending and by shear deflections, which lead to a change in the axial length of the wavy stack of sheets.

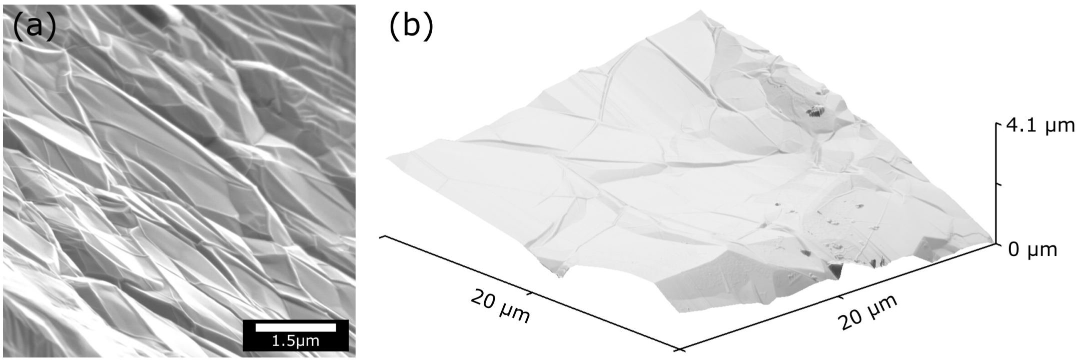

Figure 4.15: Images of the surface of as-grown graphitic layers, demonstrating the waviness present due to the polycrystalline substrate and wrinkling arising from a mismatch in the thermal expansion coefficient after cooling. (a) SEM images of a tilted strut surface. (b) Large 20×20 μm AFM image of the graphitic surface.

4.5.4.1 *Wall bending*

The cell wall waviness is idealized by a sine wave of amplitude w_0 and wavelength of λ, such that the transverse deflection in the initial, unloaded state is

$$w(x) = w_0 \sin\left(\frac{2\pi x}{\lambda}\right) \tag{4.7}$$

The axial compliance of each face of the triangular strut is increased due to waviness. Consequently, bending due to this waviness will introduce a knock-down factor k_{Be} in the effective modulus of the cell walls and also in the macroscopic modulus of the foam. Likewise, the axial strength of the cell walls are reduced by a factor k_{By} due to waviness.

The macroscopic modulus of an elastic foam, upon neglecting correction factors, is given by

$$E = \bar{\rho}^2 E_s \tag{4.8}$$

when cell wall bending dominates the response, that is $\alpha = 1$ and $n = 2$, as discussed by Gibson-Ashby [77]. In the presence of the shape factor ϕ_{Be} and the knockdown factor k_{Be} at two structural hierarchies, Eq. 4.8 becomes,

$$E = \phi_{Be} k_{Be} \bar{\rho}^2 E_s \tag{4.9}$$

This is of the form of Eq. 4.1 but with a correction pre-factor α now given by

$$\alpha = \phi_{Be} k_{Be} \tag{4.10}$$

Likewise, the macroscopic yield strength for bending-dominated open-cell foams, absent any correction factor, is

$$\sigma_y = 0.3\bar{\rho}^{3/2}\sigma_{ys} \tag{4.11}$$

implying $\beta = 0.3$ and $m = 3/2$. Now modify Eq. 4.11 with the presence of the shape factor ϕ_{By} and the knockdown factor k_{By} at two structural hierarchies, such that

$$\sigma_y = 0.3\phi_{By} k_{By} \bar{\rho}^{3/2}\sigma_{ys} \tag{4.12}$$

This is of the form of Eq. 4.2 but with a correction pre-factor β given by

$$\beta = 0.3\phi_{By} k_{By} \tag{4.13}$$

The derivations for the formulae for k_{Be} and k_{By} are now respectively given.

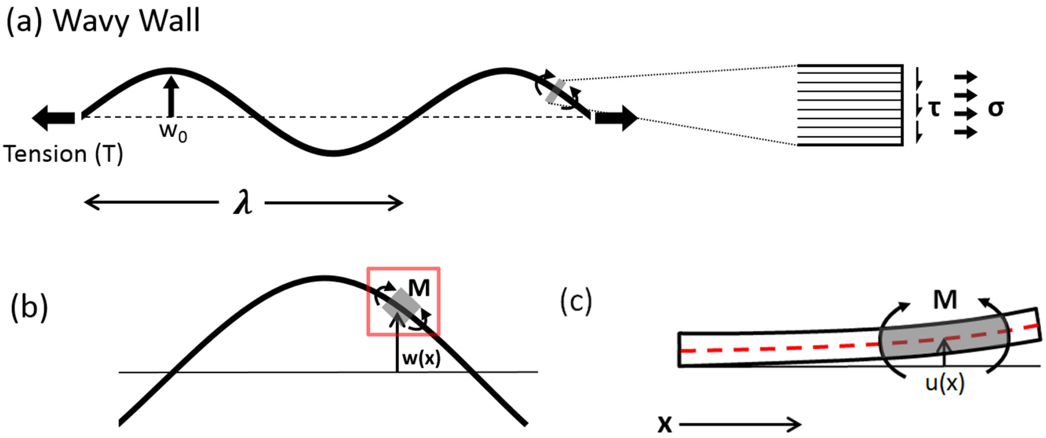

Figure 4.16: Schematics for microscale wall bending. (a) In the wavy strut wall, an axial tension acts along the waviness (amplitude w_0, wavelength λ). Shear and bending moments are induced by the axial force T. (b) The transverse deflection at a given point described by $w(x)$. When the wall is at an angle to the acting T, a localized bending moment will arise. At section x, $M = Tw(x)$. (c) This bending moment tends to straighten the walls by giving them a transverse deflection $u(x)$ in the opposite direction to $w(x)$.

WALL BENDING CASE – AXIAL COMPLIANCE OF A WAVY BEAM: Treat the cell wall as a beam of height h and assume that the axial straining of a wavy beam is driven by an end tension T, as depicted in Fig. 4.16. Under an end tension T, the beam bends locally due to a bending moment $M = Tw$, and consequently the beam straightens and lengthens.

Consider a wavy beam of bending modulus E subjected to an axial tension T. The wavy beam has an initial transverse deflection at a given point $w(x)$ of the form,

$$w(x) = w_0 \sin\left(\frac{2\pi x}{\lambda}\right) \tag{4.14}$$

where w_0 is the amplitude of the waviness and λ is the wavelength (see Figure 4.16a).

The axial tension T induces a bending moment M at a given cross-section x such that,

$$M = -Tw(x) \tag{4.15}$$

This bending moment distribution results in an additional transverse deflection $u(x)$ in the opposing direction to $w(x)$ such that,

$$M = EI\frac{d^2u}{dx^2} \tag{4.16}$$

where I is the second moment of area for the beam.

Solution of the above Eqs. 4.15 and 4.16, allows us to determine the amount of transverse deflection experienced by the beam at section x,

$$u(x) = u_0 \sin\frac{2\pi x}{\lambda} \tag{4.17}$$

$$u(x) = -\frac{T}{EI}\left(\frac{\lambda}{2\pi}\right)^2 w_0 \sin\left(\frac{2\pi x}{\lambda}\right) \tag{4.18}$$

where w_0 is the amplitude of the waviness.

The additional deflection $u(x)$ reduces the waviness of the beam, and the associated axial strain due to this bending action is given by,

$$\epsilon_b = \frac{w_0^2 T}{2EI} \tag{4.19}$$

Now, recall that the axial strain ϵ_s in a straight wall under a tension T is given by,

$$\epsilon_s = \frac{T}{EA} \tag{4.20}$$

where A is the cross-sectional area of the wall.

Consequently, the knock-down factor k_{Be} due to waviness-induced bending is

$$k_{Be} = \frac{\epsilon_s}{\epsilon_b} = \frac{2I}{Aw_0^2} \tag{4.21}$$

For a wall of thickness h, this expression reduces to

$$k_{Be} = \frac{1}{6}\left(\frac{h}{w_0}\right)^2 \tag{4.22}$$

WALL BENDING CASE – AXIAL STRENGTH OF A WAVY BEAM BENDING UNDER AN APPLIED TENSION: A similar analysis can be applied to determine the knockdown in yield strength of the foam due to cell wall waviness. Again, treat each face of the hollow triangular strut as a wavy strip of rectangular cross-section $b \times h$, such that the initial transverse deflection at a given point is described by $w(x)$, as defined by Eq. 4.14. The challenge is to determine the axial plastic collapse load by hinge formation at the location of maximum waviness of the wavy beam and to normalize it by the axial strength $P_a = \sigma_{ys} bh$ for a straight beam under axial tension. This gives us the knockdown factor k_{By}.

Equate the maximum bending moment in the wavy beam due to an applied axial force P to the plastic collapse moment of the section M_P, to give

$$M_p = P \cdot w_0 \tag{4.23}$$

where,

$$M_p = \frac{\sigma_{ys} bh^2}{4} \tag{4.24}$$

Hence the axial collapse load of the wavy beam reads,

$$P = \frac{\sigma_{ys} bh^2}{4w_0} \tag{4.25}$$

and the knockdown factor follows immediately as

$$k_{By} = \frac{h}{4w_0} \tag{4.26}$$

4.5.4.2 *Wall shear*

Cell wall waviness can induce an alternative deformation mechanism, that of cell-wall shear. Consider a wavy face of the triangular tube with a shear modulus G_s and shear strength τ_{ys}. Shear deformation may provide a significant contribution to the axial compliance of the wavy cell wall, as it is generally recognized that a stack of graphite sheets has a much lower shear modulus than in-plane tensile modulus. The wavy multilayer walls of the hollow triangular struts undergo shear loading when the faces of the struts are loaded by axial stress. Recall that these axial stresses arise from bending of the cell walls of the open-cell foam, as shown in Figure 4.17. Then, the axial stiffness of the wavy beam of thickness h is knocked-down from that of the equivalent straight beam by a factor k_{Se}, and likewise the axial strength is knocked down by a factor k_{Sy}.

The relation between macroscopic foam modulus E and yield stress σ_y due to cell wall shear follows from insertion of these knock-down factors into Eq. 4.8 to give

$$E = \phi_{Be} k_{Se} \bar{\rho}^2 E_s \tag{4.27}$$

implying that

$$\alpha = \phi_{Be} k_{Se} \tag{4.28}$$

Likewise, the yield strength of the foam now reads

$$\sigma_y = 0.3 \phi_{By} k_{Sy} \bar{\rho}^{3/2} \sigma_{ys} \tag{4.29}$$

$$\beta = 0.3 \phi_{By} k_{Sy} \tag{4.30}$$

The derivations for the formulae for k_{Se} and k_{Sy} are now respectively given.

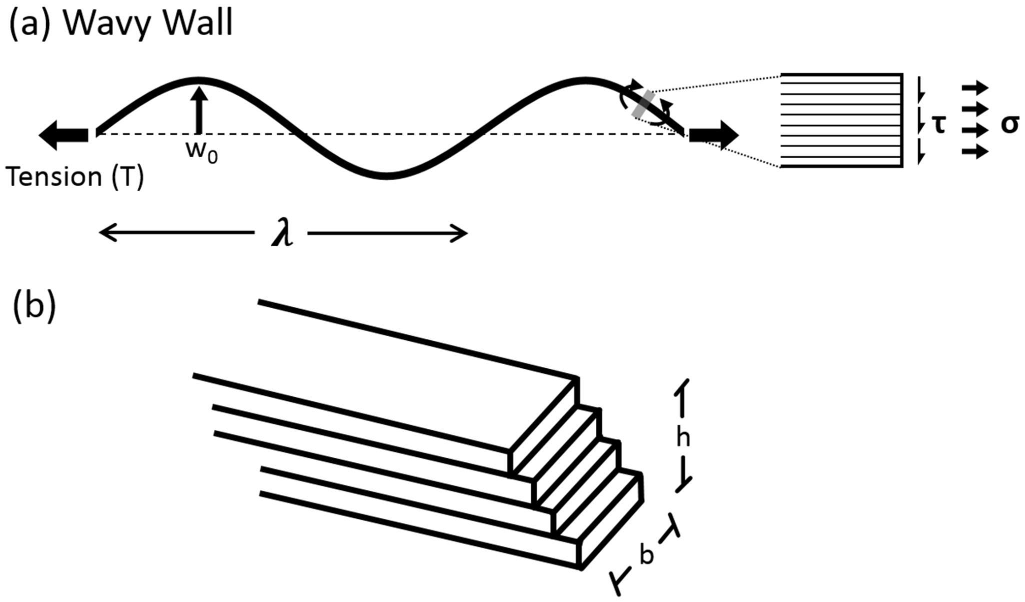

Figure 4.17: Schematics for microscale interlayer wall shearing. (a) The waviness of the strut wall is described by the transverse deflection $w(x) = w_0 \sin\left(\frac{2\pi x}{\lambda}\right)$ where w_0 is the amplitude of the waviness and λ is the wavelength. (b) In a small section of a wavy wall, since the wall is largely at an angle to the acting T, an interlayer shear stress τ is created between the layers of the multilayer graphitic wall.

WALL SHEAR CASE - AXIAL COMPLIANCE OF A WAVY BEAM DUE TO INTERLAYER WALL SHEAR: The wavy walls of the hollow triangular struts will deform by longitudinal shear under an axial load due to the finite misalignment angle dw/dx of the wavy walls with respect to the loading direction, see Figure 4.17. To extract the knock-down in axial stiffness due to the shear of the anisotropic wavy walls k_S, we compare the extensibility of the wavy beam to that of the straight wall case, by making use of a virtual work argument.

The shear stress τ on a rectangular cross-section $b \times h$ of the wavy beam is related to the axial force P according to

$$\tau = \frac{P}{bh}\frac{dw}{dx} \tag{4.31}$$

where $w(x)$ is defined in Eq. 4.14. The resulting shear strain γ reads,

$$\gamma = \frac{\tau}{G_s} \tag{4.32}$$

in terms of the longitudinal shear modulus G_s of the layered solid. This shear strain distribution over one wavelength λ of the beam leads to an axial extension Δ such that,

$$\Delta \cdot \delta P = \int_0^{\lambda} \delta\tau \cdot \gamma b h dx \tag{4.33}$$

for any virtual $\delta\tau$ and associated end load δP. Suitable substitution of Eqs. 4.31, 4.32 and 4.14 into Eq. 4.33 gives,

$$\frac{\Delta}{\lambda} = 2\pi^2 \left(\frac{w_0}{\lambda}\right)^2 \frac{P}{G_s b h} \tag{4.34}$$

Now recall that the axial strain Δ/λ due to the imposition of an axial load P on a perfectly straight face is given by,

$$\frac{\Delta}{\lambda} = \frac{P}{b h E_s} \tag{4.35}$$

Upon dividing Eq. 4.35 by Eq. 4.34 we obtain the required knockdown factor for the foam modulus due to waviness-induced shear as

$$k_{Se} = \frac{1}{2\pi^2} \frac{G_s}{E_s} \left(\frac{\lambda}{w_0}\right)^2 \tag{4.36}$$

WALL SHEAR CASE - AXIAL STRENGTH OF A WAVY BEAM DUE TO SHEAR YIELD UNDER AN APPLIED TENSION: The final step is to determine the axial strength of a wavy beam due to longitudinal shear yield. Assume that each face of the hollow triangular strut has the waviness profile $w(x)$ as stated in Eq. 4.14, and yields when the shear stress τ on a section, as given by

$$\tau = \frac{P}{bh} \frac{dw}{dx} \tag{4.37}$$

attains a yield value τ_y.

Then, upon making use of Eq. 4.14, we obtain

$$P = \frac{bh}{2\pi} \frac{\lambda}{w_0} \tau_y \tag{4.38}$$

Now normalize this by the axial yield strength of a non-wavy face sheet to obtain the required knock-down factor

$$k_{S_y} = \frac{1}{2\pi}\frac{\lambda}{w_0}\frac{\tau_{ys}}{\sigma_{ys}} \tag{4.39}$$

4.5.5 FAILURE MODES

It is emphasized that the multi-scale model assumes that the knock-down factors at each length scale act independently of each other. This is reasonable when there is a wide separation of length scales, as in the present study. Accordingly, the overall knock-down factor is determined by the product of knock-down factors at each length scale. It is clear from Chapter 4.5.4 that there exists a strong dependence of macroscopic modulus and strength on the amplitude of the wall waviness w_0.

In order to assess which failure mode is active, waviness amplitude values were determined that are in agreement with measured values of macroscopic modulus and strength, assuming that the hollow cell walls of the foam undergo either bending or shear. Predictions of the amplitude of waviness w_0 are obtained from Eq. 4.10, 4.13, 4.28 and 4.30. It is found that wall shear implies waviness amplitudes in the range of 0.45 µm to 22 µm, whereas hollow wall bending calls for waviness amplitudes of 11 µm to 5800 µm. (Table 4.2). SEM images of edge profiles of the graphitic struts reveal waviness amplitudes on the order of 2.8 µm, indicating that the deformation of multilayer graphitic foams is dominated by interlayer shear rather than intralayer bending. This is consistent with the large contrast between the high in-plane Young's modulus and low out-of-plane shear modulus of multilayer graphene [224].

The above hierarchical model uses the language of plasticity theory, with the notion that bending of the struts is by plastic slip between planes of the graphitic walls. This is consistent with observations on the nanoscale of the deformation of CVD grown graphitic layers in cantilever beams [138]. Carbon nanotubes also display similar behaviour with longitudinal plastic

SCENARIO	PREDICTED w_0 VALUE (μm)
WALL BENDING	11 - 26 (elastic) w_0 = 2700 - 5800 (plastic)
WALL SHEAR	2.1 - 22 (elastic) w_0 = 0.45 - 4.8 (plastic)

Table 4.2: Summary of key length-scales. Theoretically required w_0 were calculated using measured variables for wall thickness (h) and strut side wall length (d).

shear between the layers of a nanotube [87, 199]. Compared to other 3D graphene-based assemblies [126, 236, 263, 274, 297], uniaxial compression studies on graphene-based aerogels have observed yield strength scaling as $\bar{\rho}^{2.4}$ (see Fig. 4.12). Recall that $\sigma_y \propto \bar{\rho}^{3/2}$ in the present study. The discrepancy between values for the exponent can be traced to the fact that aerogel foams comprise a percolating network of stacked graphitic platelets, rather than the continuously grown sheets that form the foams in our study that afford a more electrically conductive networked structure (see Fig. 4.13).

4.6 CONCLUSIONS

The compressive response of freestanding CVD graphitic foams has been measured for a range of relative densities, and a three level hierarchical model has been developed to explain the dependence of modulus and strength upon relative density and microstructure. As the basis for a reproducible model system, commercial Ni templates and a graphitic wall thickness larger than 80 nm in combination with process and handling improvements such as H_2 annealing and laser sectioning are used. The power law dependence of compressive modulus and yield strength of the open-cell foam suggests that the cell walls undergo beam bending (level I). However, the measured pre-factors in the power laws are several orders of magnitude lower than those observed for conventional polymeric and metallic open-cell foams. This knock-down is traced to the following microstructural features. The cell struts are hollow tubes (level II), with wavy walls, and consequently the axial stiffness and strength of the faces of the tube are degraded by the waviness (level III). By comparing predicted levels of waviness with measured values, it is demonstrated that the dominant failure mechanism is inter-layer shear rather than in-plane bending of the wavy walls. These factors lead to a multiplicative knock-down in macroscopic properties.

The addition of a thin, flexible ceramic ALD Al_2O_3 scaffold to the freestanding graphitic foams was also explored. There is an increasing body of literature to suggest that ultrathin ceramic metamaterials exhibit ductile behaviour when wall thicknesses fall below 100 nm [96, 156, 298, 303]. The results of the present study are consistent with these findings; the graphitic foams tested herein possess a cell wall thickness on the order of 80-150 nm, with a 50 nm thick alumina scaffold. It was found that this thin ceramic scaffold increases the strength and stiffness of the foams while still conforming to the same scaling laws as those exhibited by the freestanding graphitic foams. The micromechanical, hierarchical model presented here represents a first step towards an understanding of foams with cell walls made from emergent 2D layered solids across multiple length scales.

5

NANOINDENTATION OF FREESTANDING 3D GRAPHENE GYROIDS

5.1 AUTHOR CONTRIBUTION

This chapter is based on the manuscript *The indentation response of the hollow graphene gyroid nanolattice*, which is currently in preparation. The bulk of the general approach, sample synthesis, FEA, and characterization was performed by the author of this thesis. The nickel gyroid thin film lattices of various thicknesses were manufactured by block co-polymer self-assembly, with co-author Tomasz Cebo. Nanoindentation experiments were carried out with co-author Prof. David Labonte. Tof-SIMS experiments were carried out by co-author Vlad-Petru Veigang-Radulescu.

5.2 INTRODUCTION AND MOTIVATION

In Chapter 4, a three-level hierarchical model was used to explain the observed mechanical behaviour of a graphitic foam. Based on observation and the power law dependence of the compressive modulus and yield strength of the open-cell graphitic foams across a range of relative densities, it was determined that the struts of the foam undergo bending-dominated deformation (level I). Little to no breakage and fracturing of the struts was observed in compressed samples. Such struts were hollow (level II), and possessed wavy walls (level III) due to the shape inheritance of the polycrystalline substrate and relaxation after internal template removal. This waviness increases axial compliance of the tube faces, and by comparing the predicted levels of waviness with measured values it was determined that the dominant failure mechanism occurs via inter-layer shear rather than in-plane bending of the wavy walls. These factors lead to a multiplicative knock-down in the macroscopic properties.

As discussed in Chapter 2.1.1, the relationship between macroscopic properties and relative density $\bar{\rho}$ is dictated by the topology of a lattice material. A large portion of the literature [30, 60, 170, 240, 253] have utilized similar commercial nickel foams as catalytic templates due to the ease of acquisition, resulting in graphitic foams that possess disordered structures and a low connectivity of three struts per node. These foams will inevitably behave as bending-dominated lattices and possess lower strengths and stiffnesses when compared to a stretching-dominated lattice at the same $\bar{\rho}$. Stochastic systems consistently demonstrate inferior structural performance, motivating the development of graphene-based cellular structures with long-range periodic order and more efficient stress transfer and load bearing behaviour. One such possibility is to use a continuously curved shell geometry, which is unable to bend without stretching and will consequently possess a power law exponent n that is closer to unity [91, 108]. CVD graphene foams with bicontinuous shell architectures based on spinodal topologies have been prepared from dealloyed Ni films with ~3μm pore sizes. While the cellular structure is still disordered, these materials were found to possess mixed deformation modes of stretching and bending [107], resulting in scaling relationships of $E \propto \bar{\rho}^{1.6}$ and $\sigma \propto \bar{\rho}^{1.1}$.

The manufacture of structured nanoscale cellular solids has only recently been enabled by developments in precision manufacturing techniques. Such nanolattices possess efficient load bearing and stress transfer behaviour, and have demonstrated exceptional mechanical behaviour such as high yield strain for metallic lattices [78, 209] and, a high fracture strain for ceramic lattices [156], a nearly constant specific stiffness at ultra-low density [303], and ultra-high effective strengths of the constituent cell walls [57, 111]. Structured nanolattices have thereby expanded material property space, as seen in the plot of strength versus density of Figure 1.1. These novel mechanical characteristics arise from rationally designed cellular architecture (see Chapter 2.1.1) combined with nanoscale size effects on material strength. Strength can increase dramatically with decreasing structural size largely due to the elimination of defects [9, 61, 116]. The bulk strength of metals and ceramics are orders of magnitudes smaller than their theoretical limits due to the presence of imperfections such as dislocations, grain boundaries and voids. Consider the tensile strength of a strut of cross-sectional thickness t. If the strut exists, then it can only contain defects of dimension less than t. Consequently, the maximum size of a defects that a strut can contain must decrease as the strut gets smaller, if it is to exist. This 'smaller is stronger' phenomenon is active in these nanolattices, whereby the length scale of architecture is reduced to a scale small enough to exploit size-dependent strengthening. Pyrolytically derived ceramic nanolattices [16], atomic layer deposited hollow-beam ceramic nanolattices [96] and the nickel double gyroid nanolattice [111] have reported mechanical behaviours that benefit from such size effects.

The nickel single gyroid nanolattice is used here in Chapter 5, as both a catalytic template for the production of hollow CVD graphene gyroid nanolattices and as a comparative model nanolattice during the study of mechanical behaviour. The gyroid is a triply periodic minimal surface (TPMS) discovered by Schoen in 1970, and has garnered significant interest as a framework for periodic nanolattices which possess a high surface area to volume ratio, and a uniform cell and pore size which are beneficial for systems requiring functional nanostructures [49]. Recent research has demonstrated the preparation of nanoscale solid single gyroids [93] and inter-connected solid double gyroids [111] from the in-filling of phase-separated block co-polymers, as discussed in Chapter 2.2.2.3. Hollow gyroid topologies have subsequently been prepared using a specialized CVD technique [29], or through ALD of metal oxide layers [148].

As a natural structure formed from an energy-minimization process [218], the mechanical properties of the gyroid lattice have also garnered significant interest. Khaderi et al. [110] utilized FEA of the multi-axial collapse simulations of an idealized slender beam model with uniform circular cross-section to predict the elastic-plastic response of the gyroid lattice, which was found to be reasonably isotropic. The gyroid lattice is seen to deform with a bending-dominated elasto-plastic response occurring for all deviatoric loading states. Likewise, the effective elastic and plastic properties of the solid double gyroid unit [110] have been computed using unit cell FEA. The predicted variations of elastic modulus E and yield strength σ_y with relative density $\bar{\rho}$ for both the beam model and solid double gyroid were found to scale as $E \sim \bar{\rho}^2 E_s$ and $\sigma_y \sim \bar{\rho}^{3/2} \sigma_{ys}$, consistent with bending-dominated behaviour. Nanoindentation measurements of a fabricated nickel double gyroid lattice were used to calibrate an inverse FEA, extracting the associated properties of the parent nickel. It was found that the predicted yield strength of the struts (5.7 GPa) approached the theoretical strength of nickel, due to the lack of dislocations in the nanoscale struts [110].

Other prior studies have examined the theoretical mechanical properties of hollow graphene gyroid lattices through the use of molecular dynamics simulations. However, such models assume that the walls of the gyroid lattice are made from a single layer of entirely covalently bonded graphene, leading to predictions of remarkable electrical [178] and mechanical [104, 159, 201] properties. In reality, the cell walls of fabricated graphene gyroid lattices are comprised of multiple layers of graphene [29]. As such, it is of interest if interlayer shearing within the wavy multilayered graphene walls will cause a multiplicative knock down in the macroscopic properties of multilayered graphene gyroid lattices, as was found for macroscopic foams in Chapter 4.

In this chapter, the manufacture and mechanical characterization of a solid nickel gyroid and the associated CVD graphene gyroid lattice is discussed. These ordered nanolattices contain a unit cell of 60 nm, with nickel solid strut thickness on the order of 15 nm and graphene wall thicknesses of 3 nm. A combination of nanoindentation and multi-scale FEA is used to deduce, for the first time, the macroscopic effective properties of these gyroid-based materials and the constituent cell wall properties.

5.3 EXPERIMENTAL METHODS

5.3.1 MANUFACTURE OF GYROID NANOLATTICES

Nickel solid gyroid thin films of selected film thicknesses were manufactured by block co-polymer self-assembly as described in Chapter 3.1.1.2. Gyroid lattices were manufactured as a thin film on top of a 350 nm layer of fluorine-doped tin oxide (FTO) coating, which, in turn, sat on a borosilicate glass slide of thickness 2.2 mm. The resulting nickel solid gyroid possessed a unit cell size of 60 nm and a fill fraction of 40% (that is, relative density $\bar{\rho} = 0.4$), see Fig. 3.3. Multilayer graphene was deposited with a carbon-predosing methodology as described in Chapter 3.1.2.2. Etching of the internal nickel template as described in Chapter 2.3 affords a clean and freestanding lattice, henceforth referred to as the hollow graphene gyroid. The final structure of the hollow graphene gyroid strongly resembles the original TPMS gyroid surface. A schematic of the production process and morphology of final gyroid nanolattices are shown in Figure 5.1.

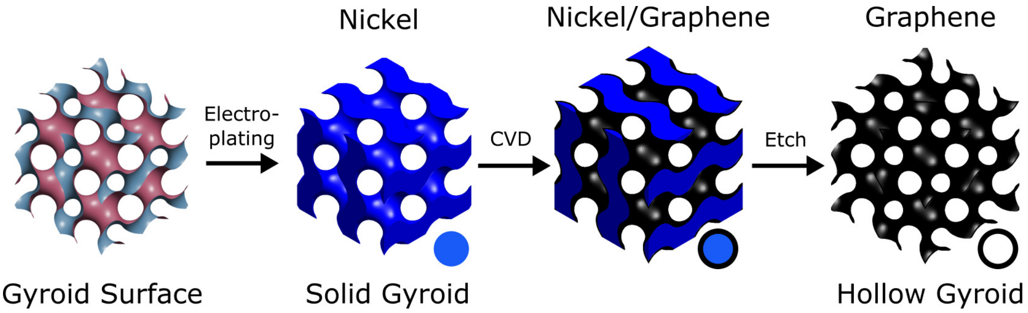

Figure 5.1: Schematic of the templated growth of the hollow gyroid from a solid gyroid. Section shown is a 3x3x3 segment of the gyroid lattice.

As previously discussed in Chapter 2.4.3, the acetylene pre-dosing process is designed to increase the uptake of carbon into the nickel template prior to reaching the growth temperature. This lead to saturation of the finely porous

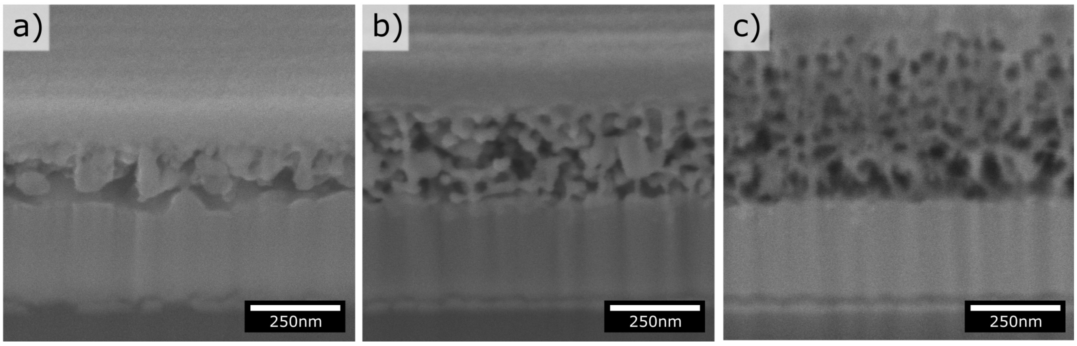

Figure 5.2: SEM cross-sectional images of thermally coarsened gyroid films, following CVD processing at 650°C.

catalyst and the formation of stabilizing surface graphitic deposits and nickel surface carbides, prior to reaching the growth temperature [29]. However, the gyroid films remained extremely sensitive to the process temperature due to the fine struts with a 15nm diameter. Growth at 650°C was found to cause severe coarsening below the film surface for the thinner gyroid films, as can be seen in Figure 5.2. Lowering of the growth temperature to 625°C allowed for the internal structure of the Ni gyroid films to remain well preserved, see Fig. 5.3.

5.3.2 CHARACTERIZATION OF GYROID NANOLATTICES

Scanning electron microscopy (SEM) and atomic force microscopy (AFM) micrographs of the top surface of the nickel solid gyroid film are shown in Figure 5.3 and 5.4, showing the clearly resolved nanostructure. A cleaved cross-section in Figure 5.3d clearly displays the layered structure of the gyroid/FTO/glass. Careful cross sections of the gyroid films were prepared using focused ion-beam (FIB) milling (Figs 5.5, 5.6) in order to determine the film thickness. Long-range order is evident through a vertical slice of the gyroid films, and it is clear that the hollow graphene gyroid inherits its topology from that of the nickel gyroid template. Similar images were used to measure the film thickness at multiple locations for each sample; the film thickness of each sample is 300, 500 and 700 nm ± 25 nm. The gyroid films tested in this study have an average roughness of R_a = 25 nm.

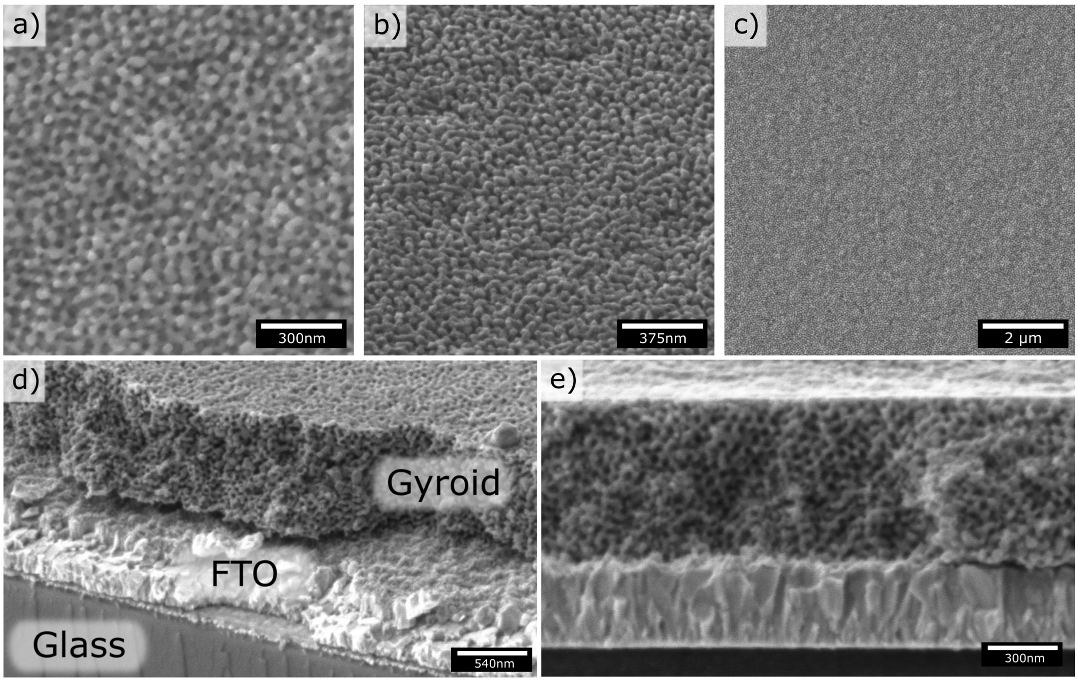

Figure 5.3: SEM images of the nickel gyroid (a,b,c) surface. (d) Cleaved edge showing the nickel gyroid film on top of the FTO/glass substrate. (e) High magnification image of the cross section, showing the long-range order present in the nickel gyroid film.

In order to determine the nature of the graphitization, Raman spectra were taken with a Renishaw inVia spectrometer under 532 nm excitation, see Fig. 5.7a. Characteristic D, G and 2D peaks are observed, consistent with the growth of multilayer graphene gyroids [29]. A prominent D-band and red shifted G-band are present, which can be attributed to the presence of many small, disordered [189] and strained [171] graphene domains. These characteristics arise from the nanoscale growth surface and high local curvature of the nickel gyroid template [29] used to prepare graphene gyroids. To confirm the complete removal of the internal nickel template from the freestanding graphene gyroid, ToF-SIMS depth profiling was performed on a graphene gyroid film, see Fig. 5.7b. Argon cluster sputtering (5 keV, 2700 ions, 0.36 nA) was used to probe the entire thickness of as-grown samples. The C^+ carbon signal was stable throughout the thickness of the gyroid layer, but then reduces as an SnO^+ signal appears, indicating the end of the graphene gyroid film, and the beginning of the FTO layer. The nickel Ni^+ signal is

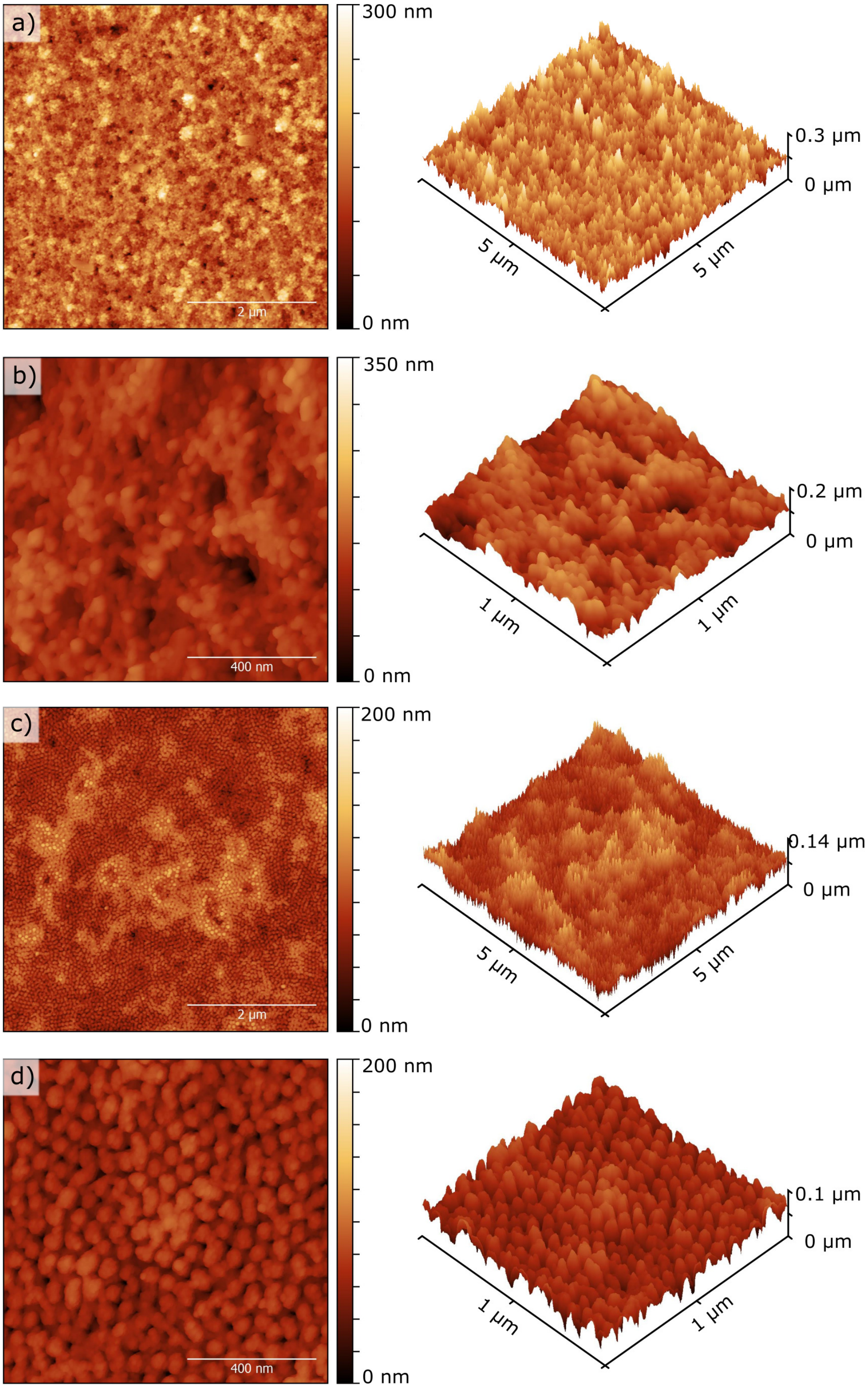

Figure 5.4: AFM images of the (a,b) graphene and (c,d) nickel gyroid surfaces.

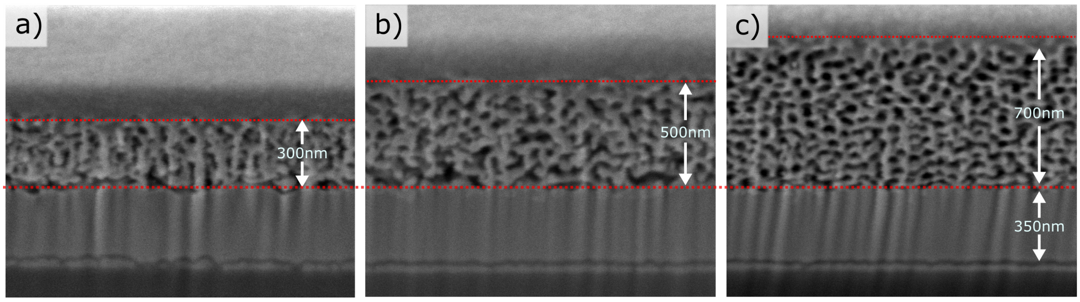

Figure 5.5: Cross-sectional SEM images of nickel solid gyroid films. FTO and glass layers are clearly visible. Thickness was measured across multiple points as (a) 300 nm (b) 500 nm and (c) 700 nm ± 25 nm. Capping layer is platinum, deposited as a part of the FIB milling process.

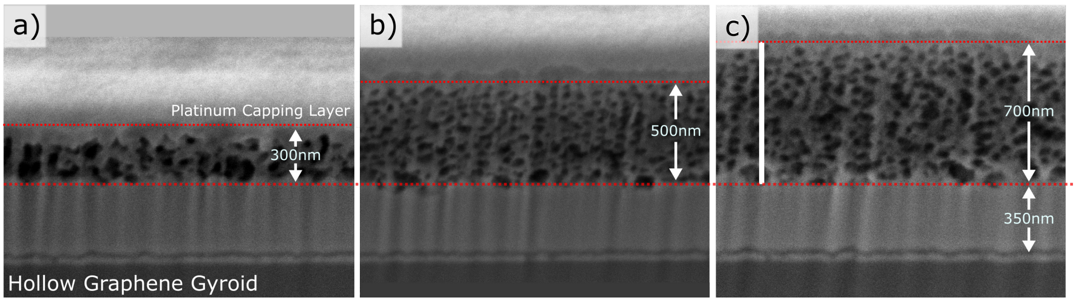

Figure 5.6: Cross-sectional SEM images of freestanding hollow graphene gyroids. Film thickness and structure is retained across each sample. Capping layer is platinum, deposited as a part of the FIB milling process.

negligible throughout the scan, suggesting that the etching and rinsing steps have successfully removed the internal template.

HR-TEM samples were prepared from as-grown graphene gyroids by first removing the graphene gyroid film from their substrate with a razor blade and then using wet transfer via water lift-off onto Au-supported holey carbon grids. Bright-field transmission electron microscopy images were taken as described in Chapter 3.2.4, at 80 kV accelerating voltage in order to prevent beam damage to the material. HR-TEM images confirm a lattice spacing of approximately 0.33 nm, corresponding to the interlayer spacing of multi-layer graphene. The cell walls of the hollow gyroid comprises 8-10 layers of graphene, see Fig. 5.7c. This corresponds to a total wall thickness of 3 nm, which is consistent with a final relative density of $\bar{\rho} \approx 0.14$, based on the solid

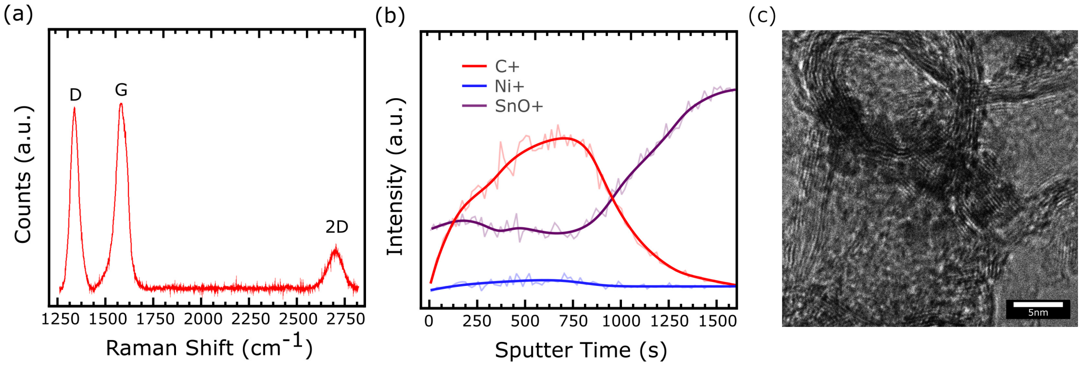

Figure 5.7: (a) Representative Raman spectra of the hollow graphene gyroid surface. Prominent D, G and 2D peaks are present, characteristic of multilayer graphene. (b) ToF-SIMS depth profile of the hollow gyroid lattice. A negligible Ni^+ signal is present throughout the bulk of the lattice, confirming complete removal of the internal template after etching. (c) HR-TEM image of a hollow graphene gyroid channel with diameter of ~15nm.

gyroid template $\bar{\rho} \approx 0.4$ and a unit cell size of 60 nm. The sheet resistance was measured using the van der Pauw method as discussed in Chapter 3.2.10. Graphene gyroids were floated on the surface of a hydrochloric acid/deionized water bath (0.1M) and transferred via lift-off onto non-conductive glass, before being electrically contacted at the corners by silver paste.

5.3.3 INDENTATION MEASUREMENT PROTOCOL

Nanoindentation tests were performed on sets of three thicknesses of nickel gyroid and graphene gyroid films, using a Hysitron Ub1 Nanoindenter system of depth resolution 0.04 nm. The Berkovitch tip had a tip radius of 50 nm and a half angle of 65.35°, as measured from the central axis to a pyramidal flat. The tip was considered to be sufficiently sharp to be pyramidal at an indentation depth $\delta \geqslant 50$ nm. Sixteen separate indentation tests were carried out on each of the gyroid films. Samples were indented in a 4 by 4 array with a $50\,\mu\text{m}$ spacing in both lateral directions to ensure that the strain field due to each indent did not interact with each other. For each test, the peak load in each cycle was progressively increased up to the maximum load of 11 mN for nickel and 1 mN for the hollow graphene gyroids. Twelve partial load/unload cycles with equal peak load spacing were performed per test. Each loading and unloading segment was of duration 2s, with a 2s hold time between each segment. During each unloading cycle, the load was reduced to 50% of the prior load. The modulus and hardness were extracted from these measurements using the standard Oliver and Pharr [176] procedure. The detailed assumptions of this analysis are outlined in Chapter 3.3.2.

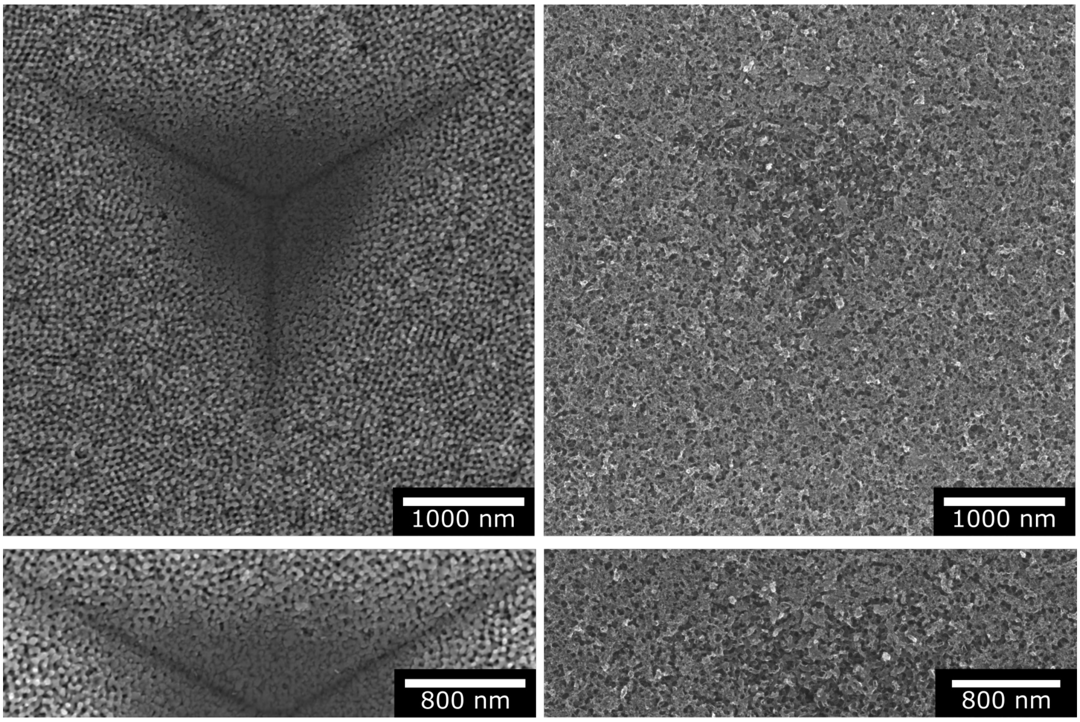

Figure 5.8: SEM of the nickel solid gyroid and hollow graphene gyroid taken post-indentation. A clear impression of the Berkovitch tip is present in the nickel solid gyroid lattice after indentation, with minimal elastic recovery. Surface SEM image of the hollow graphene gyroid displaying minimal damage after indentation to $\delta_{max}/h \approx 0.79$.

5.3.4 MEASURED PROPERTIES

SEM micrographs, and surface profiles of the films post-indentation are given in Figures 5.8 and 5.9. For the case of the solid nickel gyroid films, indentation leads to plastic deformation of the gyroid lattice with limited elastic recovery of the indent (see Figs 5.8 and 5.9). In contrast, for the graphene gyroid lattice, an indent of $\delta_f/h \approx 0.13$ remains after indentation to $\delta_{max}/h \approx 0.79$, indicating that a significant amount of elastic recovery has occurred. SEM images of the hollow graphene gyroid after indentation show minimal plastic deformation (Fig. 5.8). The level of elastic recovery remained high ($\delta_f/h \approx 0.39$) even after indentation to $\delta_{max}/h \approx 0.99$. Note that deep indents lead to plastic deformation of the underlying FTO layer, thereby reducing the relative degree of elastic recovery.

The measured values of unloading modulus E_R and of hardness H are plotted in Fig. 5.18 as a function of the normalized indentation depth δ/h. The hardness H is relatively independent of indent depth δ, for $0.2 < \delta/h < 0.5$. At high values of indent depth ($\delta/h > 0.5$) H increases with increasing δ/h due to indentation of the substrate. The largest scatter in the measured values of E_R and of H occur for the thinnest gyroid films, due to the high roughness of the FTO layer relative to the layer thickness h for the thinnest films.

5.4 NUMERICAL SIMULATIONS

The Young's modulus and uniaxial compressive yield strength of the solid and hollow gyroid lattice cannot be measured directly from the nanoindentation measurements reported above. In this chapter a multi-scale numerical analysis is utilized to extract the effective mechanical properties of the gyroid lattice and parent materials, for both the solid nickel and hollow graphene cases. Khaderi et al. [111] have previously derived power law scaling equations for the elastic constants of the solid gyroid lattice through numerical simulation of an idealized slender-beam model of the gyroid lattice. However, the slender beam approximation slightly underestimates the modulus and strength of solid gyroid lattices with $\bar{\rho} > 0.15$. Analysis of the double gyroid lattice, which comprise two interpenetrating single gyroids of opposite chirality, has also been performed up to a limit of each single gyroid possessing a relative density of $\bar{\rho} = 0.19$. The solid gyroid tested herein possesses a relative density $\bar{\rho} = 0.4$, motivating the numerical simulation of solid gy-

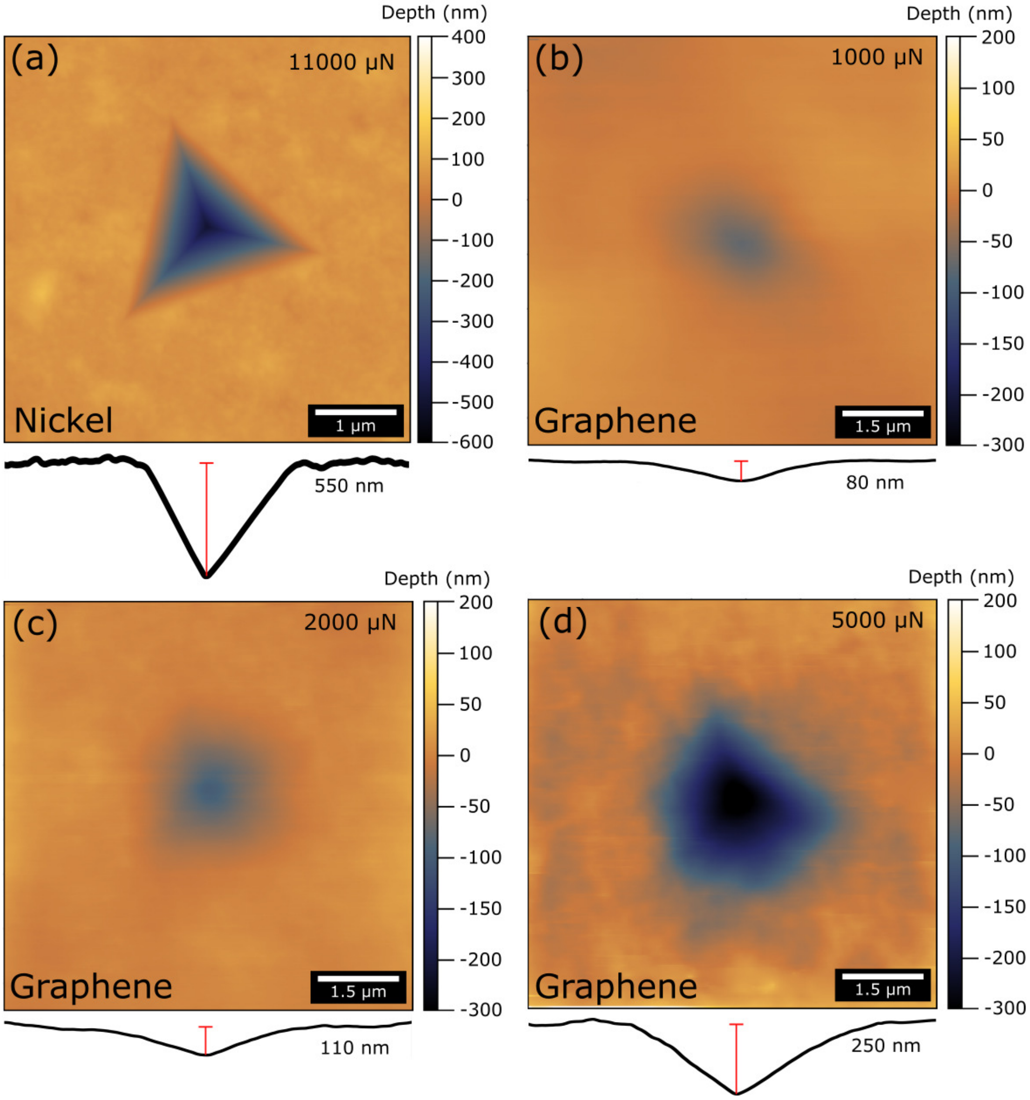

Figure 5.9: Surface profiles of the (a) nickel solid gyroid and (b, c, d) hollow graphene gyroid taken post-indentation. Remnant indentation profiles after progressive indentation loading (b) 1000 µN, (c) 2000 µN, (d) 5000 µN was applied to the hollow graphene gyroid lattice.

roid unit cells with $\bar{\rho}$ up to 0.5 herein. A comparative plot of the effective properties of the solid single gyroid calculated herein against the slender beam model [111] and double gyroid model [110] can be found in Figure 5.12.

5.4.1 EFFECTIVE PROPERTIES OF THE GYROID LATTICES

The unit cells for the solid gyroid and hollow gyroid are shown in Figure 5.10. The gyroid unit cells are constructed using the approximation to the single gyroid morphology as proposed by Lambert et al. [120]. This approximation suggests the surface of a single gyroid can be represented by a function $F(x,y,z) - t_0 = 0$,

$$F \equiv \sin(2\pi x)\cos(2\pi y) + \sin(2\pi y)\cos(2\pi z) + \sin(2\pi z)\cos(2\pi z) \tag{5.1}$$

where (x,y,z) are the Cartesian coordinates aligned with the cubic directions of the gyroid lattice, as shown in Fig. 5.10. The scaling parameter t_0 controls the distance of the surface from the $t_0 = 0$ surface, and hence determines the relative density of the gyroid lattice. The solid gyroid is constructed by infilling the space $F - t_0 \geqslant 0$ to obtain the volume shown in Figure 5.10a. The constructed hollow gyroid volumes were based on the templated surface growth of graphene, and hence had a fixed t_0 such that the internal surface was equal to the relative density $\bar{\rho} = 0.4$ of the solid gyroid. The hollow gyroid was constructed by varying a second scaling parameter t_1 and infilling the space between two gyroid surfaces $F - t_0 = 0$ and $F - t_1 = 0$, to obtain the unit cell as shown in Figure 5.10b.

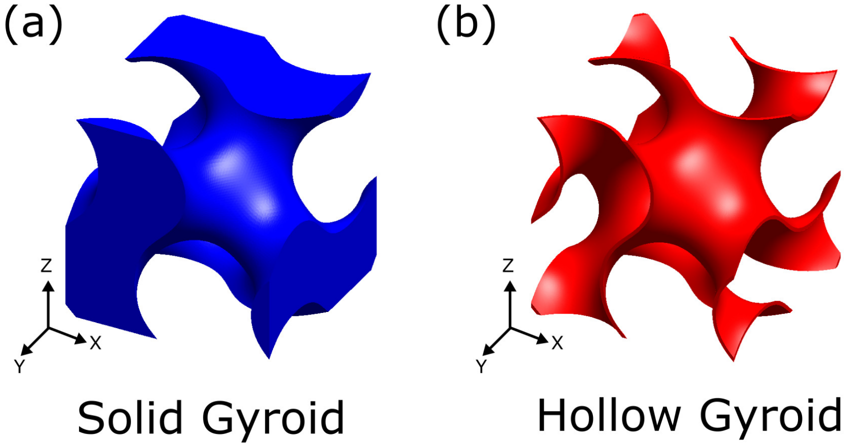

Figure 5.10: Representative volume elements of the solid gyroid and hollow gyroid lattices. In this sketch, a solid gyroid with $\bar{\rho} = 0.4$ and hollow gyroid with $\bar{\rho} = 0.05$ are shown.

Periodic cell finite element calculations were then performed on each of the constructed volumes to determine the effective elastic and plastic properties using the commercial finite element package ABAQUS. The gyroid geometry was meshed using uniform four-noded linear tetrahedral elements (C3D4 in ABAQUS notation). The mesh density was chosen such that a halving of the mesh size results in less than 1% change in macroscopic modulus or strength of the lattice. To achieve this, each FEA model comprised approximately 3×10^5 elements. As the wall thickness to diameter ratio of each of the hollow gyroids simulated herein exceeded 0.03, shell elements were not used [191] and the volumes were meshed as before, with an average of 1×10^6 elements generated per model. Macroscopically, each gyroid deforms by stretching and/or bending and hence an elastic-ideally plastic solid material response was used for the FEA herein. The strut material was modelled with isotropic elasticity and J2 plasticity, behaving as an elastic-ideally plastic solid of Young's modulus E_S, Poisson ratio ν_S and yield strength σ_S. It is assumed that ν_S = 0.3 and the yield strain $\epsilon = \sigma_S/E_S$ equals 0.03.

The imposition of displacement boundary conditions such that plane boundary surfaces remain plane will over-constrain the representative volume element, leading to an overestimation of the homogenized elastic properties [270]. Thus, node-to-node periodic conditions are applied, which allow deformed boundary surfaces to distort in a non-planar fashion. In general, every pair of nodes (denoted as +x and -x) on two opposite faces of the cubic unit cell are linked through linear constraint equations for each degree of freedom [177]. Dummy reference points are defined in the FEA in order to impose boundary displacements and accommodate rigid body motion. Applied displacements on the representative volume element surface are applied by imposing fixed displacements on the associated reference point, which are linked to the nodes of an entire face. The value of the reaction force at a reference point is the sum of principle boundary nodal forces generated at the relevant boundary nodes. The reaction forces on the reference point is used to determine the macroscopic stress that corresponds to the applied strain. Thus, simulations were then conducted to determine the three independent elastic constants of the unit cell, as well as the shear moduli

G and yield strengths σ_S. The stress at 0.2% offset was taken as the yield strength. The average result of the extracted elastic and plastic properties are presented herein.

In order to evaluate the elastic and plastic Poisson's ratio values for the lattices, an incremental Poisson's Ratio was obtained throughout the loading program. At each time step, the x-displacements of all nodes that originally constituted the -x and +x faces of the material are averaged, and then a difference is taken between the two. The same thing is done for y-displacements on the -y and +y faces, and these are taken as the x strains and y strains, which are then averaged to obtain a transverse strain. The difference between this transverse strain from the last time step is then divided by the applied z-strain from the latest time step to obtain an incremental Poisson's Ratio. Elastic and plastic Poisson's ratio scalars are then extracted from the two plateau regions of this curve. The elastic Poisson's ratio ν, was calculated from the first simulated strain increment. The plastic Poisson's ratio ν_P, was determined from the incremental Poisson's ratio during the plastic flow regime.

The relative densities of the unit cells were varied across a range of FEA simulations by varying the scaling parameters t_0 and t_1. The predicted variations of the effective mechanical properties with the relative density $\bar{\rho}$ are plotted in Fig. 5.11. At low relative densities the values of E and G decrease drastically with a decrease in the relative density. This is because at low relative densities, material is concentrated at the Plateau borders. Above this region, curve fitting of the relationships for the solid gyroid lattice (denoted by •) yields the following scaling relationships,

$$\frac{E^{\bullet}}{E_s} = 0.90\bar{\rho}^{2.11} \tag{5.2}$$

$$\frac{G^{\bullet}}{E_s} = 0.38\bar{\rho}^{1.81} \tag{5.3}$$

$$\frac{\sigma^{\bullet}_{YS}}{E_s} = 0.48\bar{\rho}^{1.55} \tag{5.4}$$

In comparison, the scaling obtained by Khaderi et al. [111] based on an idealized slender beam model of the gyroid lattice was $E = 0.426\bar{\rho}^2 E_S$, $G = 0.329\bar{\rho}^2 E_S$ and $\sigma_{YS} = 0.415\bar{\rho}^{1.5}\sigma_S$. The geometrical factors C and scaling factors n are largely in agreement between both models. However, the scaling of the effective modulus in the solid model contains a C value (C = 0.90) that is over twice that of the slender beam model (C = 0.426). This can be attributed to a lack of plateau borders in the slender beam model, which reduces the amount of solid material aligned to each of the uniaxial loading directions. The scaling of $E^\bullet$, $G^\bullet$ and $\sigma^\bullet_{YS}$ with $\bar{\rho}$ indicate that the lattice will deform mainly by bending, twisting or buckling of the struts under uniaxial strain and shear. This has been observed in both FEA simulation [111] and macroscopic compression of 3D printed gyroids [151] and is caused by the low nodal connectivity of the gyroid lattice. The variation of effective mechanical properties for the hollow gyroid lattice (as denoted by $\circ$) is plotted in Fig. 5.11c,d. The following scaling relationships are found,

$$\frac{E^\circ}{E_s} = 0.41\bar{\rho}^{1.09} \tag{5.5}$$

$$\frac{G^\circ}{E_s} = 0.19\bar{\rho}^{1.13} \tag{5.6}$$

$$\frac{\sigma^\circ_{YS}}{\sigma_S} = 0.46\bar{\rho}^{1.08} \tag{5.7}$$

The scaling exponents for the hollow gyroid lattice imply stretching-dominated behaviour. This result is consistent with TPMS sheet-based lattices [108, 109] and shell spinodal topologies [91] at comparable relative densities. The stretching-dominated deformation was attributed to the hollow gyroid being comprised of doubly curved surfaces, which cannot be readily bent without the introduction of significant membrane stresses.

The cell wall response of the two gyroid architectures under macroscopic uniaxial compression are shown in Figure 5.13. The von-Mises stress distribution, equivalent (effective) plastic strain and σ_{11} stress distribution are shown for

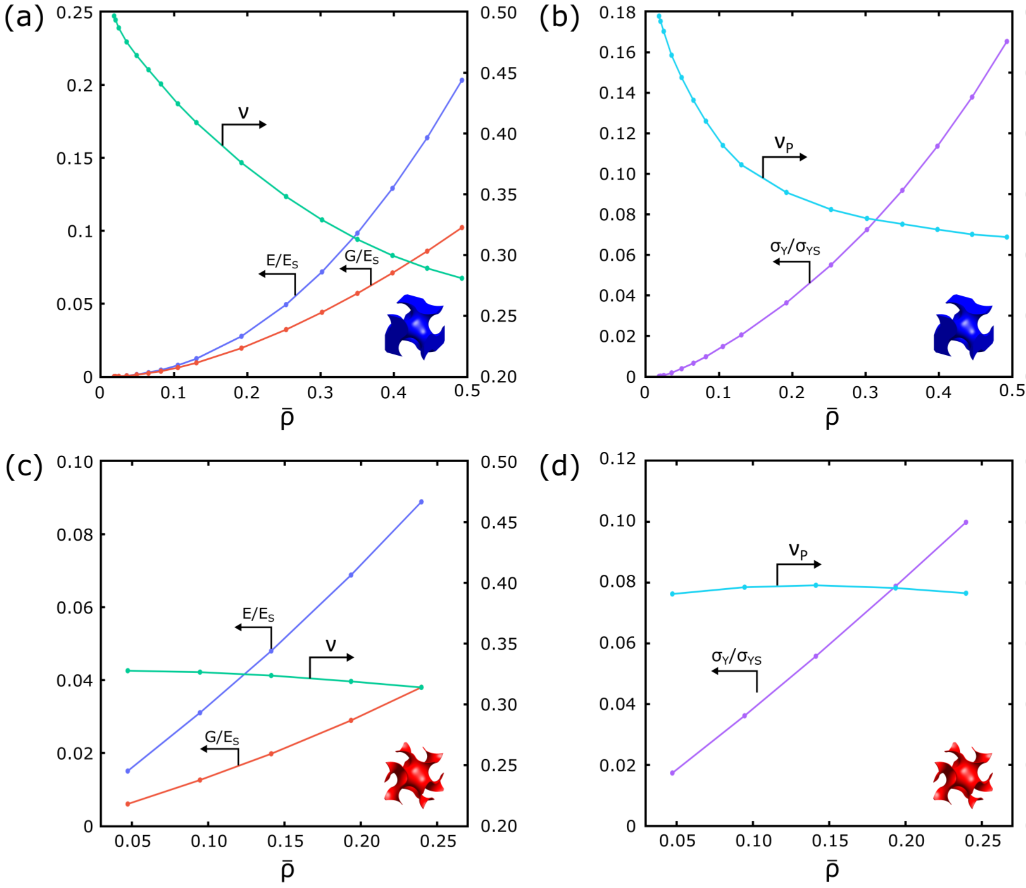

Figure 5.11: Representative volume elements of the solid gyroid and hollow gyroid lattices. In this sketch, a solid gyroid with $\bar{\rho}$=0.4 and hollow gyroid with $\bar{\rho}$=0.05 are shown.

the two different architectures at different strain levels. For comparison purposes, the same parent material properties (E = 200 GPa, σ_{YS} = 6 GPa, ν = 0.3) and same choice of color contours are used for the two lattices. The relative densities of the lattices shown are $\bar{\rho}$=0.4 and $\bar{\rho}$=0.14 for the solid and hollow gyroids respectively, corresponding to those of the fabricated gyroid lattices as determined in Chapter 5.3.2. The solid gyroid is shown to deform with strut bending as macroscopic uniaxial compression progresses, displaying a significant concentration of stress and plastic deformation within the solid gyroid struts, see Fig. 5.13c. In contrast, the walls of the hollow gyroid lattice are unable to bend without stretching. This stretching-dominated behaviour leads to the σ_{11} stress and plastic strain occurring in a more distributed

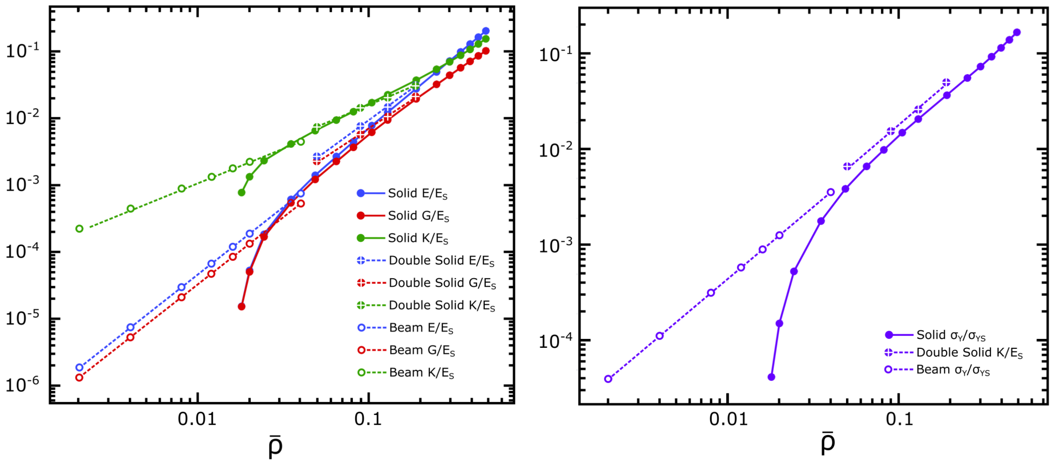

Figure 5.12: Comparative plot of the FEA predictions of the effective mechanical properties of the solid gyroid model used herein, the beam gyroid lattices and the normalized solid double gyroid model as used by Khaderi et al. [110, 111].

arrangement over the hollow gyroid surface when compared to the solid gyroid unit cell. Molecular dynamics simulations of a hollow gyroid lattice under macroscopic uniaxial compression have shown the development of high stress bands isolated by lower stress regions, leading to complicated crumpling geometries evolving under high strains [104].

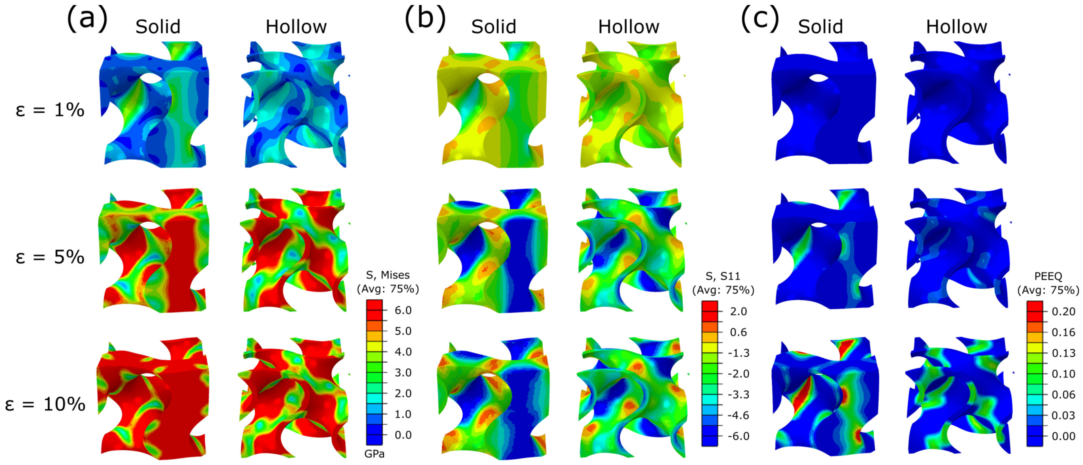

Figure 5.13: Representative volume elements of the solid gyroid and hollow gyroid lattices. In this sketch, a solid gyroid with $\bar{\rho}$=0.4 and hollow gyroid with $\bar{\rho}$=0.05 are shown.

5.5 INDENTATION RESPONSE OF SINGLE GYROID FILMS

In the nanoindentation experiments presented in Chapter 5.3.3, the contact width of the indenter is significantly greater than the unit cell size of the gyroids (60 nm) for the majority of recorded indentation depths. Hence, the discreteness of the gyroid microstructure is expected to play a negligible role in the indentation response. Furthermore, previous analysis of the single gyroid lattice by Khaderi et al. [111] has shown that both the elastic and plastic properties of the gyroid lattice are sufficiently isotropic for use in the Deshpande-Fleck isotropic crushable foam model. The Deshpande-Fleck isotropic crushable foam model has been used to successfully model nanoporous metals [110, 142, 188], and is employed herein as a homogenized continuum model for the macroscopic response of the gyroid lattice during the indentation process.

The main difficulty with the characterization of thin coatings using depth-sensing indentation tests is related to the determination of the contributions of the substrate and the film to the measured properties. In order to measure the Young's modulus of the film, a commonly used rule is to limit the maximum indentation depth to less than 10% of the film's thickness [176]. However, this procedure cannot be applied to very thin films, for which very low indention depths are needed. Hence, to determine the mechanical properties of the thin gyroid films, numerical simulations of the Berkovitch indentation tests were performed. In the inverse FEA method used herein, the parent material modulus E_S and strength σ_{YS} can be treated as unknown parameters and varied to bring the simulated and measured indentation responses into good agreement for each film thickness [6].

5.6 FINITE ELEMENT MODELLING OF INDENTATION EXPERIMENTS

Quasi-static finite strain indentation calculations were simulated using the commercial finite element package ABAQUS. Using three-dimensional FEA models in the simulation of a nanoindentation experiment is a computationally demanding process. Thus, a simplified axisymmetric model is applied (Fig. 5.14) to model the indentation of each gyroid film.

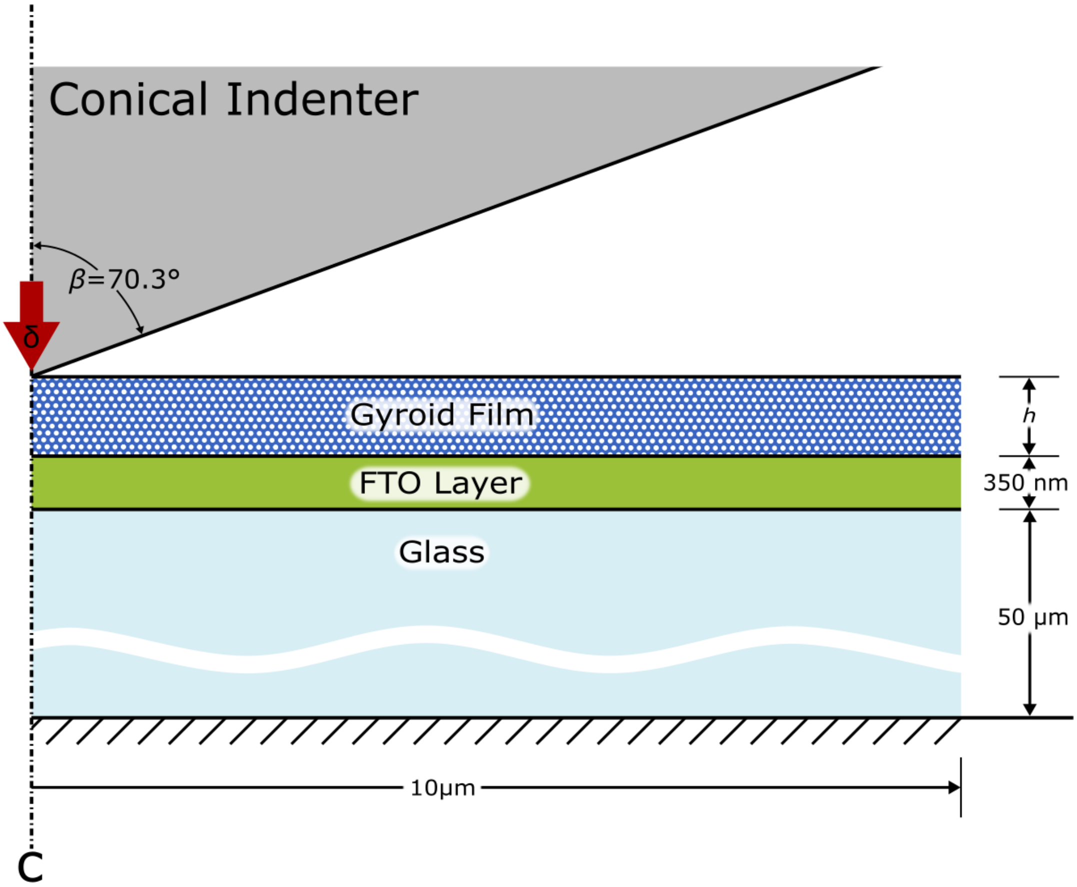

Figure 5.14: Schematic of the axisymmetric conical indentation model used to simulate the Berkovich nanoindentation response of gyroid films on a FTO/glass substrate.

5.6.1 MODEL GEOMETRY AND MATERIAL PROPERTIES

A standard Berkovitch indenter was used in all experimental work and subsequently in the model. The Berkovitch tip is a three-sided pyramid with sides that converge to a radius of curvature of 50 nm at the tip, with a half-angle of 65.35°, as per the manufacturer's specifications (Hysitron Inc. MN, USA). One face of the Berkovitch indenter was represented in the axisymmetric model as a rigid body analytical surface with semi-angle β=70.3°and tip radius of 50 nm such that the nominal contact area A_C is the same as the Berkovitch tip [161]. The Berkovich tip is made of diamond, an extremely stiff and hard material, and hence deformation of the tip would not be expected to occur during nanoindentation. These assumptions are a widely accepted approach in FEA analysis of material nanoindentation [81].

The gyroid block is modelled herein as a layered deformable solid, with film thicknesses accurately reflecting the thicknesses of each sample as measured via FIB (see Fig. 5.5 and 5.6). The single gyroid lattice was modelled using the isotropic crushable foam model of Deshpande and Fleck [56], the details of which are discussed in Chapter 5.6.1.3. The glass substrate is modelled as a linear elastic solid, with thickness 50 µm and radius 10 µm, possessing a modulus of 69.6 GPa and Poisson's ratio 0.3. A 350 nm thick FTO layer is present between the gyroid film and glass substrate, modelled as linear elastic solid with modulus 150 GPa and Poisson's ratio of 0.3 as determined via a separate indentation test on an annealed FTO/glass substrate, see 5.15. This is consistent with previous indentation studies on thermally annealed FTO layers [72] of similar thicknesses. The lower surface of each of these interactions were defined as the slave surface and the adjacent surface of each film was defined as the master surface. The normal behaviour between the two surfaces was defined by hard contact. As such, each of these layers was assumed to be ideally bonded to each other.

Surface roughness measurements provided in Chapter 5.3.2 demonstrate that the actual gyroid surface was not perfectly flat, which can have a significant influence over the mechanical properties extracted from nanoindentation

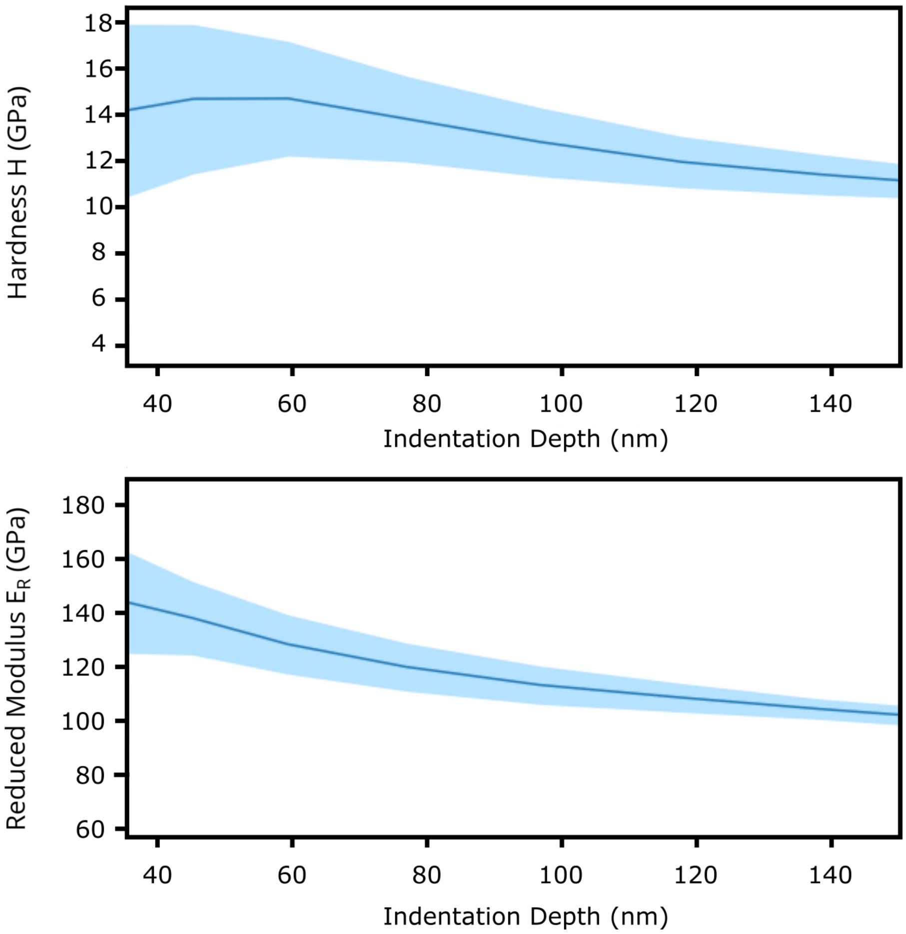

Figure 5.15: Measured hardness H and reduced modulus E_R for the FTO/glass used as the substrate for the gyroid films. FTO/glass was annealed in a blank CVD process equivalent to that used for the growth of the hollow graphene gyroids.

tests [102]. All gyroid film surfaces tested in this study had an average roughness $R_a \approx 20$ nm, as measured across 5×5 μm areas. Under high load nanoindentation testing conditions, indent depths were typically at least ten times the mean surface roughness measurement. For the purposes of modelling, a flat indentation surface is assumed herein.

5.6.1.1 *Boundary Conditions and Loading*

Loading was applied in the FEA model by inducing a negative global y-direction displacement of the indenter into the gyroid film. To assist in obtaining convergence in the FEA model, simulations were controlled by the displacement of the indenter, rather than force. The model scope excludes time-dependent behaviour. Therefore, no holding period was used, nor rest periods between indents of incremental loading. Simulation of incremental load experiments involved pairs of load-unload cycling with the indent depth increasing in 50 nm increments, up to 80% of the total film thickness, and retracting half the distance indented in the previous step.

The bottom of the model was fixed in the z direction, while a symmetric boundary condition was imposed on the centre line. The boundary conditions and loading used in the FEA model are shown in Figure 5.14. Contact between the indenter surface and gyroid film was modelled using the Master-Slave surface contact algorithm within ABAQUS. Friction is ignored in this study, as the effect of friction is only pronounced in the calibration of elasto-plastic constitutive material models and with respect to the study of pile-up, which are not relevant in this study.

5.6.1.2 *Mesh Generation*

Mesh generation involves the selection of an appropriate element type and level of mesh refinement for areas with concentrated high magnitude loads. The mesh density of a part will reflect the loading and boundary conditions, with the aim of avoiding sharp gradients where stress and strain fields change rapidly. Mesh refinement also improves the performance of FEA as it is possible to reduce the number of elements in regions where many elements are unnecessary, such as in areas that are far away from the point of load application. In the nanoindentation problem, refinement of the mesh was performed at the region of tip contact with the gyroid film due to high local stresses and sharp contact conditions.

Analytical rigid surfaces, as used to model the indenter, require no mesh generation. Thus mesh generation was only performed for the gyroid block sample. To reduce the complexity of the mesh, a single element type was maintained throughout the entire part. The 2D axisymmetric model consisted of linear (first-order) 4-node reduced integration axisymmetric elements (ABAQUS CAX4R). First-order elements are more appropriate for conditions involving contact and severe element distortion, as occurs during a nanoindentation process, and reduced integration elements are very cost-effective, taking less time to solve. However, reduced integration elements are susceptible to a phenomena called 'hourglassing', where uncontrollable mesh distortion occurs when elements distort such that the calculation of strains at the element's integration points results in zero values. While ABAQUS features an hourglass control option to reduce such effects, a sufficiently fine mesh density in areas of high stress concentration was used to control the effects of this problem.

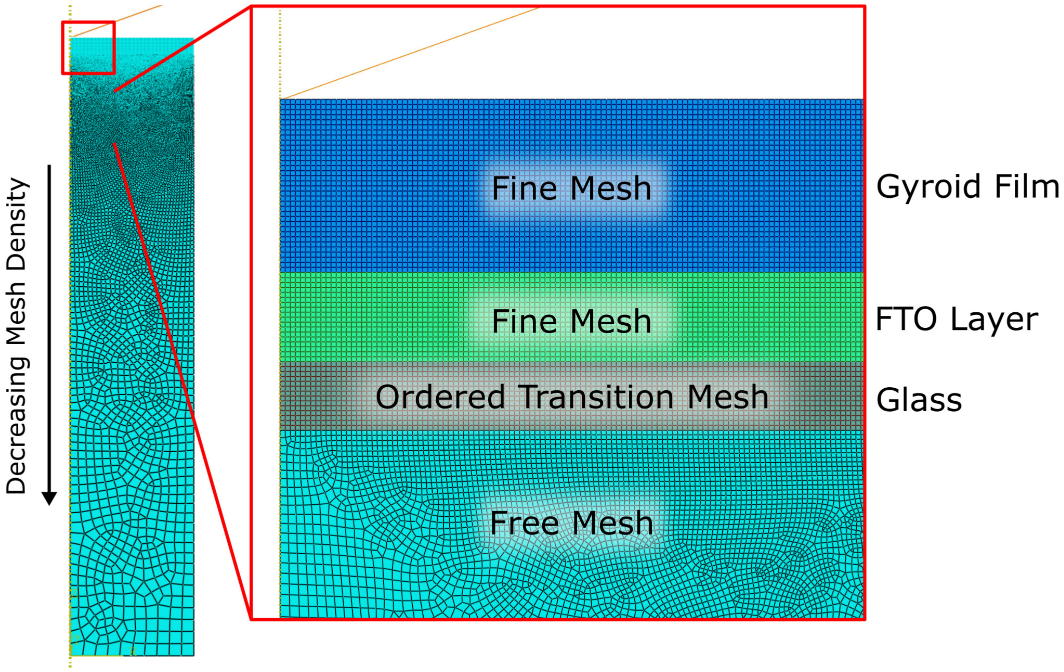

Figure 5.16: Geometry and meshing conditions of the idealised axisymmetric model.

The mesh refinement was achieved by partitioning the gyroid block into the constituent layers, as depicted in Figure 5.16. To do this, the gyroid film and FTO layer were meshed homogeneously with a fine (20 nm) mesh. The glass layer was partitioned to create a small sublayer at the interface between the FTO and glass, which was similarly finely meshed (20 nm), in order to avoid any issues with interlayer interactions. This mesh was gradually relaxed as the distance from the point of loading grew larger to improve the FEA performance. The mesh density was increased until the point where a

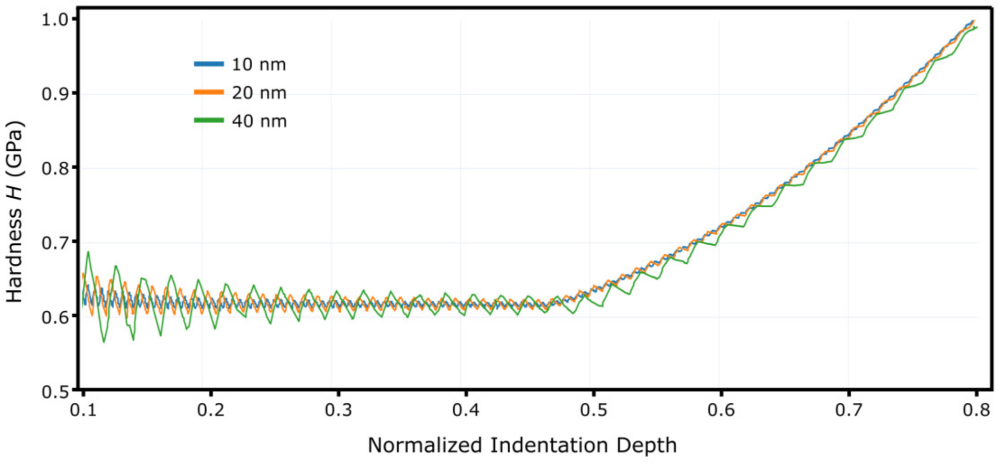

Figure 5.17: Simulated hardness for the 700 nm thick nickel solid gyroid film across a range of mesh densities. Indentation depth is normalized against the thickness of the nickel solid gyroid film. Increasing the mesh resolution improves the accuracy of the final solution. Listed value is equal to the finest mesh size used in that calculation.

doubling of the mesh density led to less than 1% difference in the predicted indentation response (see Fig. 5.17)

5.6.1.3 *Crushable Foam Model*

The isotropic crushable foam model of Deshpande and Fleck is a constitutive model that assumes symmetric behaviour in tension and compression, and that the evolution of the yield surface is governed by an equivalent plastic strain which has contributions from both the volumetric plastic strain and the deviatoric plastic strain. Use of the crushable foam model also implies that the indentation response is modelled over multiple grains and the result represents a ensemble average of the gyroid properties over multiple orientations. A brief description of this model and its calibration to the gyroid films now follows.

Let s_{ij} be the deviatoric stress and the von-Mises effective stress $sigma_e$ can be expressed as

$$\sigma_e \equiv \sqrt{(3/2)s_{ij}s_{ij}} \tag{5.8}$$

The isotropic yield surface of the gyroid lattice can then be expressed by

$$\hat{\sigma} - Y(\hat{\epsilon}^p) = 0 \tag{5.9}$$

where the equivalent stress $\hat{\sigma}$ is a homogeneous function of σ_e and the mean stress $\sigma_m \equiv \sigma_{kk}/3$ according to

$$\hat{\sigma}^2 \equiv \frac{1}{1 + \left(\frac{\alpha}{3}\right)^2} \left[\sigma_e^2 + \alpha^2 \sigma_m^2\right] \tag{5.10}$$

and $\hat{\epsilon}^p$ is the plastic strain work-conjugate to $\hat{\sigma}$. Additionally, $Y(\hat{\epsilon}^p)$ is the uniaxial yield strength that is a function of $\hat{\epsilon^p}$ and the parameter α expresses the ratio of deviatoric to hydrostatic strength. The normalization factor on the right-hand side of Eq. 5.10 is chosen such that $\hat{\sigma}$ denotes the stress in a uniaxial tension or compression test. Normality of plastic flow is assumed, implying that the plastic Poisson's ratio ν_p is related to α via

$$\nu_p = \frac{1/2 - (\alpha/3)^2}{1 + (\alpha/3)^2} \tag{5.11}$$

A typical compressive response for a cellular material is characterized by a plateau strength σ_Y followed by densification due to contact between cell walls at large deformation. For periodic lattices, it has been demonstrated that this densification strain ϵ_D is reasonably independent of the relative density. Following Khaderi et al. [110] the yield surface $Y(\hat{\epsilon}^p)$ will have the form

$$Y(\hat{\epsilon}^p) = \begin{cases} \sigma_Y & Y(\hat{\epsilon}^p) \leqslant \epsilon_D \\ \sigma_Y + h_p(\hat{\epsilon}^p - \epsilon_D) & \text{otherwise} \end{cases} \tag{5.12}$$

Where the hardening rate is h_p is assumed to be equal to the Young's modulus E of the gyroid lattice. In line with previous studies on the densification strain of gyroidal structures, for the solid gyroid it is assumed that ϵ_D = 0.6 [110], whereas for the hollow gyroid it is assumed that ϵ_D = 0.7 [1]. The total strain increment ϵ is given by the sum of elastic and plastic strain increments.

5.6.1.4 *Post-Processing*

The predicted load-displacement behaviour was extracted from the FEA model by the reaction force of the rigid body reference node of the indenter.

The reduced modulus E_R and hardness H were extracted using the Oliver and Pharr method [176] as described in Chapter 3.3.2. The contact area versus depth relation was taken as $A_c = \pi\delta^2 \tan^2\beta \approx 24.5\delta^2$ and hardness $H = P(\delta)/A_c(\delta)$ at depth δ. The reduced modulus is obtained by fitting a power law to the unloading curve and subsequent use of the Sneddon equation as described in Chapter 3.3.2. Negligible pile-up or sink-in is observed around the edges of the indented area, consistent with the assumptions required to extract E_R and H from the indentation measurements.

Predictions of the reduced modulus E_R and hardness H as a function of the normalized indentation depth δ/h are included in Figure 5.18. From the numerical simulations of the effective material properties in Chapter 5.4.1 it follows that, for the solid gyroid, $E^\bullet = 0.129E_S^\bullet$, $\sigma_Y^\bullet = 0.114\sigma_{YS}^\bullet$ and $\nu_p^\bullet \approx 0.321$. Similarly, for the hollow gyroid, $E^\circ = 0.048E_S^\circ$, $\sigma_Y^\circ = 0.056\sigma_{YS}^\circ$ and $\nu_p^\circ \approx 0.398$. These can be used to draw conclusions regarding the constituent material properties of the gyroid lattices. The measured and predicted indentation responses were brought into agreement across each film thickness when the Young's modulus and uniaxial compressive strength of the solid gyroid film were given the values of E = 25 GPa and σ_{YS} = 0.51 GPa. This implies that the apparent modulus of the parent nickel is E_S = 194 GPa with yield strength σ_{YS}= 4.49 GPa. Hence, the inferred Young's modulus of the parent solid is consistent with that of electroplated nickel thin films, which possess an E_S of 205 GPa [143]. However, the parent material strength σ_{YS} is twice that of electrodeposited or pure nickel [225]. This result is consistent with previous observation of lattice materials with nanoscale strut diameters [110, 188].

For the hollow gyroid lattice, the film properties were found to be to E = 1.2 GPa and δ_{YS} = 0.055, implying parent material properties of E_S = 25.0 GPa and σ_{YS} = 0.99 GPa. These values are significantly lower than the commonly quoted E = 1060 GPa and σ_{YS} = 130 GPa for monolayer graphene [121]. In addition, for $\delta/h > 0.6$, the measured increase in H and E_R is seen to exceed the best-fit predicted response for the crushable foam model due to interaction with the hard FTO underlayer. Note that the influence of wrinkles and the weakness of graphene multilayers under shear will

(a) Nickel Solid Gyroid

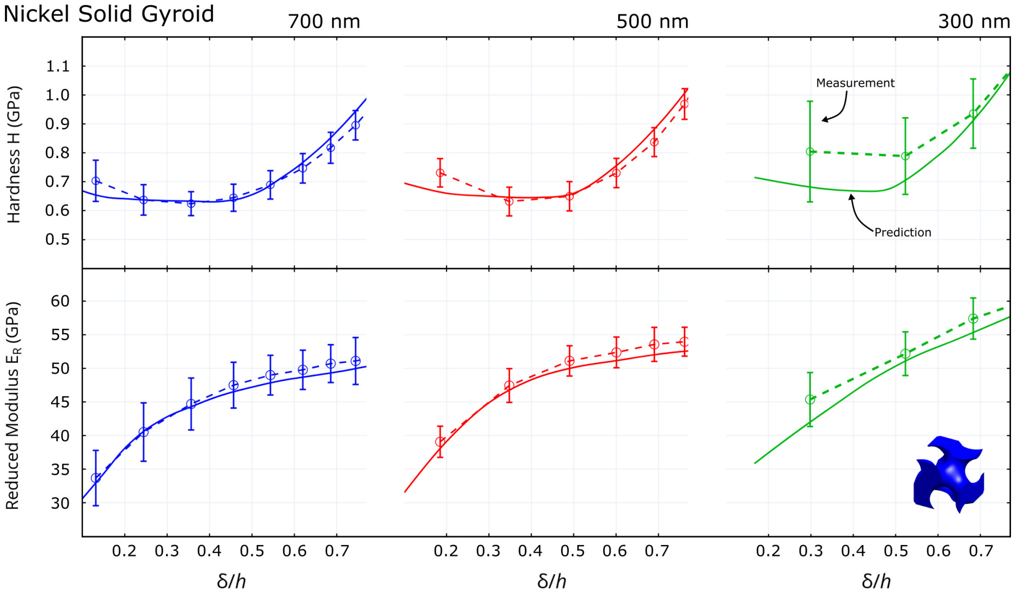

(b) Graphene Shell Gyroid

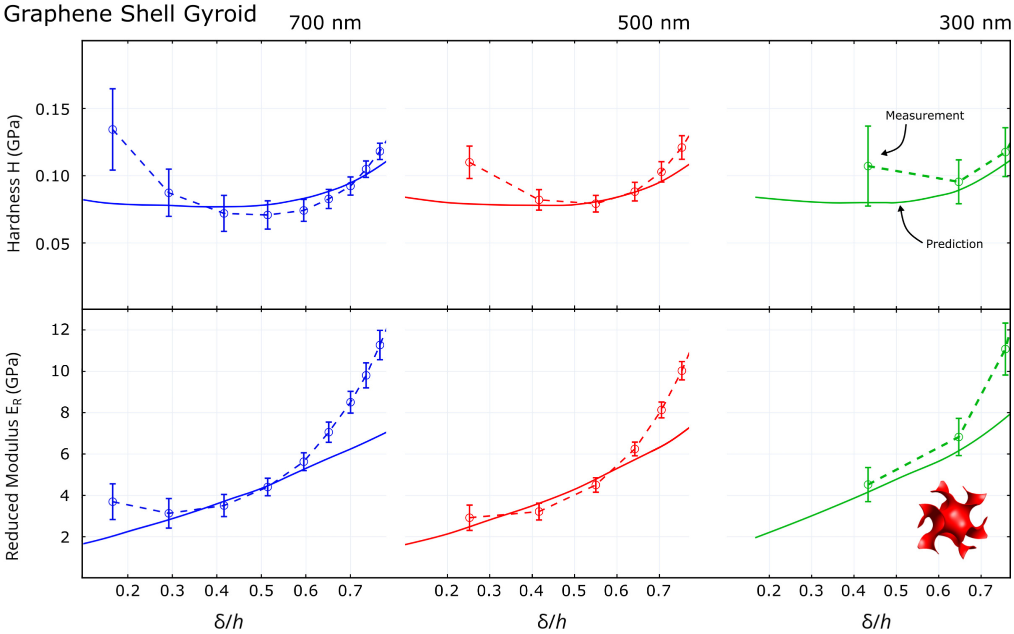

Figure 5.18: Hardness H and reduced modulus E_R of the (a) solid and (b) hollow gyroid films as a function of the normalized indentation depth δ/h. The error bars indicate the standard deviation over the 16 tests conducted on each film. The FEA predictions with nickel solid gyroid film properties $E^{\bullet} = 25$ GPa, $\nu^{\bullet} = 0.3$ and $\sigma_Y^{\bullet} = 510$ MPa and hollow graphene gyroid film properties $E^{\circ} = 1.2$ GPa, $\nu^{\circ} = 0.32$ and $\sigma_Y^{\circ} = 55$ MPa are included.

significantly increase the compliance of the bending-dominated behaviour [165], as discussed in Chapter 5.4.

5.7 HOLLOW GRAPHENE GYROID DEFORMATION

The mechanical response of the hollow graphene gyroids can be interpreted in terms of the hierarchical micromechanical model described in Chapter 4. The highest level is set by the strut length scale of the gyroid unit cell (level I). The cell structure is comprised of hollow stocky tubes, and deformation of these strut-like tubes involves axial stretching of the tube walls (level II). This is supported by the power law scaling of elastic modulus and yield strength, and the numerical simulation of the stress distribution in the unit cell, see Figure 5.13. At the lowest level, the tube walls are composed of a wavy stack of graphitic layers, motivating the examination of whether this waviness will induce interlayer shear of the graphitic layers when the tube walls are subjected to axial stretch (level III).

Examination of HR-TEM images such as Figure 5.19a demonstrate that a small degree of cell wall waviness is present (wavelength $\lambda \approx$ 5-15 nm), due to the relaxation of the 3 nm thick cell walls as the solid nickel template was removed. Upon loading, the walls of the gyroid lattice undergo stretching and bending, however the axial compliance of each cell wall is degraded by waviness. When the wavy stack of sheets is subjected to an axial strain, the misalignment induces transverse shear forces on the cross-section of the cell wall. The wall responds by nanoscale shear deflections, which lead to a change in the axial length. Thereby, the axial stiffness and axial strength of each cell wall is dictated by the out-of-plane shear properties of the multilayer graphene. This nanoscale wall shear deformation mode has been shown to provide a significant contribution to the axial compliance of a wavy cell wall in macroscopic graphitic foams [165], as multilayer graphene possesses a much lower interlayer shear modulus and strength in comparison to their in-plane properties.

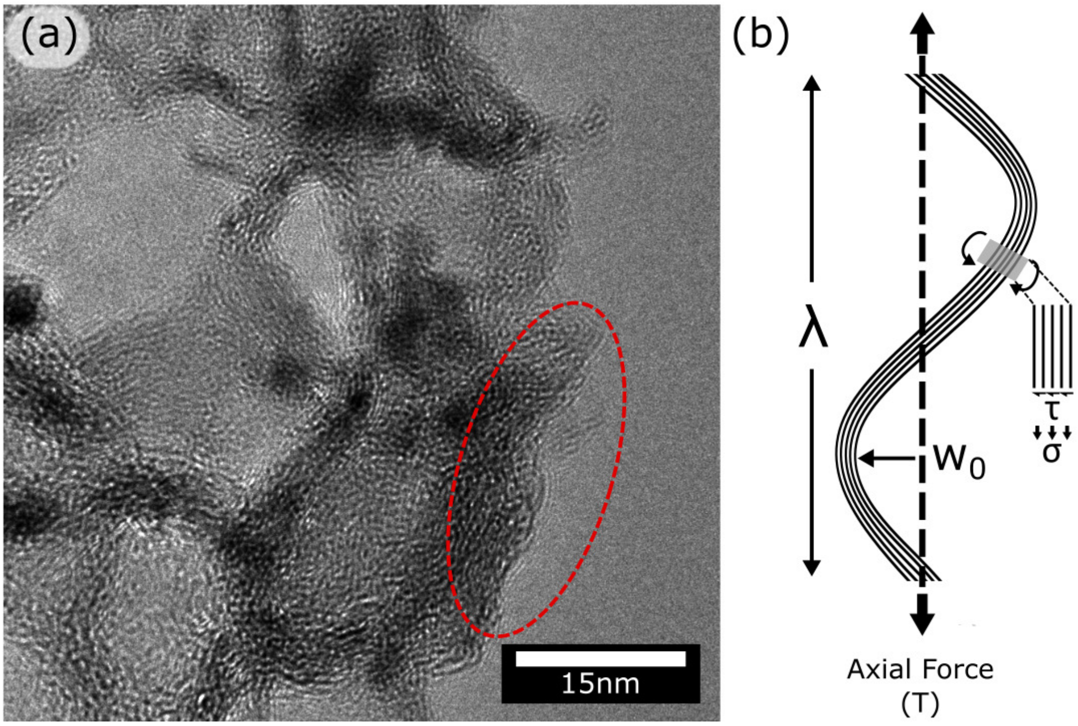

Figure 5.19: (a) HR-TEM image of a graphene gyroid showing wall waviness of the multilayer graphene structure. (b) Wall level schematic idealizing the waviness as a sine wave of amplitude w_0 and wavelength λ. In a wavy wall subjected to an axial tension, misalignment induces transverse shear forces on the cross-section of the cell wall, leading to interlayer shearing.

To determine if this deformation mode is active in the multilayered hollow graphene gyroid lattice, the relevant knockdown factors are obtained by treating the cell wall as a beam of height h and assuming that the axial straining of a wavy beam is driven by an end tension T as depicted in Fig. 5.19b. Then, the axial stiffness of the wavy beam of thickness h is knocked-down from that of the equivalent straight beam by a factor k_{Se}, and likewise the axial strength is knocked down by a factor k_{Sy}, where

$$k_{Se} = \frac{1}{2\pi^2}\frac{G_s}{E_s}\left(\frac{\lambda}{w_0}\right)^2 \tag{5.13}$$

$$k_{Sy} = \frac{1}{2\pi}\frac{\lambda}{w_0}\frac{\tau_{ys}}{\sigma_{ys}} \tag{5.14}$$

see Chapter 4.5.4.2 for a detailed derivation. Based on these expressions, the required waviness amplitudes ω_0 were determined for the measured

SCALING	MEASURED VALUES	REQUIRED VALUES
	$E = 1.2$ GPa	
	$\sigma_y = 0.055$ GPa	
$E \sim \frac{0.41}{2\pi}\left(\frac{\lambda}{w_0}\right)^2 \bar{\rho}^{1.09} G_S$	$\bar{\rho} = 0.14$	$\omega_0 = 0.1 - 1.2$ nm (elastic)
$\sigma_y \sim \frac{0.46}{2\pi}\frac{\lambda}{w_0}\bar{\rho}^{1.08}\tau_{ys}$	$\lambda \approx 5\text{-}15$ nm	$\omega_0 = 0.001 - 0.33$ nm (plastic)
	$G_S \approx 0.2\text{-}5$ GPa	
	$\tau_{ys} \approx 0.001\text{-}0.1$ GPa	

Table 5.1: Examination of hollow gyroid lattice deformation behaviour. Theoretically required waviness amplitudes ω_0 for the multilayer graphene that constitute the walls of the lattice were calculated using the calculated effective mechanical properties and measured variables for E, σ_y, $\bar{\rho}$ and λ. Values based on direct measurement of interlayer shear strength and modulus using tip-based methods were used for the assumed values of G_s and τ_{ys}.

values of macroscopic modulus and strength to be in agreement. This was calculated using the numerically simulated effective mechanical properties of the hollow gyroid unit cell with key measured physical properties, see Table 5.1. Due to a significant weakness in interlayer shear only very modest waviness amplitudes (ω_0 ~1 nm) are required, and it is concluded that these values demonstrate that nanoscale interlayer wall shearing is the dominant mechanism of elastic and plastic deformation of the cell walls of the hollow graphene gyroid lattice.

5.8 GYROIDS IN MATERIAL PROPERTY SPACE

A plot of compressive strength versus density is shown in Figure 1.1, comparing the properties of the gyroid lattices tested herein to other state-of-the-art lattice materials across different strut length-scales. The measured strength of nickel solid gyroid rivals that of fully dense high strength Ni alloys, such as Inconel (highlighted in Fig. 1.1.). This is consistent with other reports of nanoscale lattices such as nickel inverse opals [188] and for nickel double-gyroids [110]. Furthermore, the strength to density ratio of the bending-dominated solid gyroid lattice exceeds that of the stretching-dominated micron-scale octet truss lattice, due to the size-strengthening effect present in the nanoscale gyroidal struts. Size-independent structural effects are demonstrated by the order of magnitude increase in compressive strength over nanoporous Cu and Au films at similar relative densities and strut widths [88].

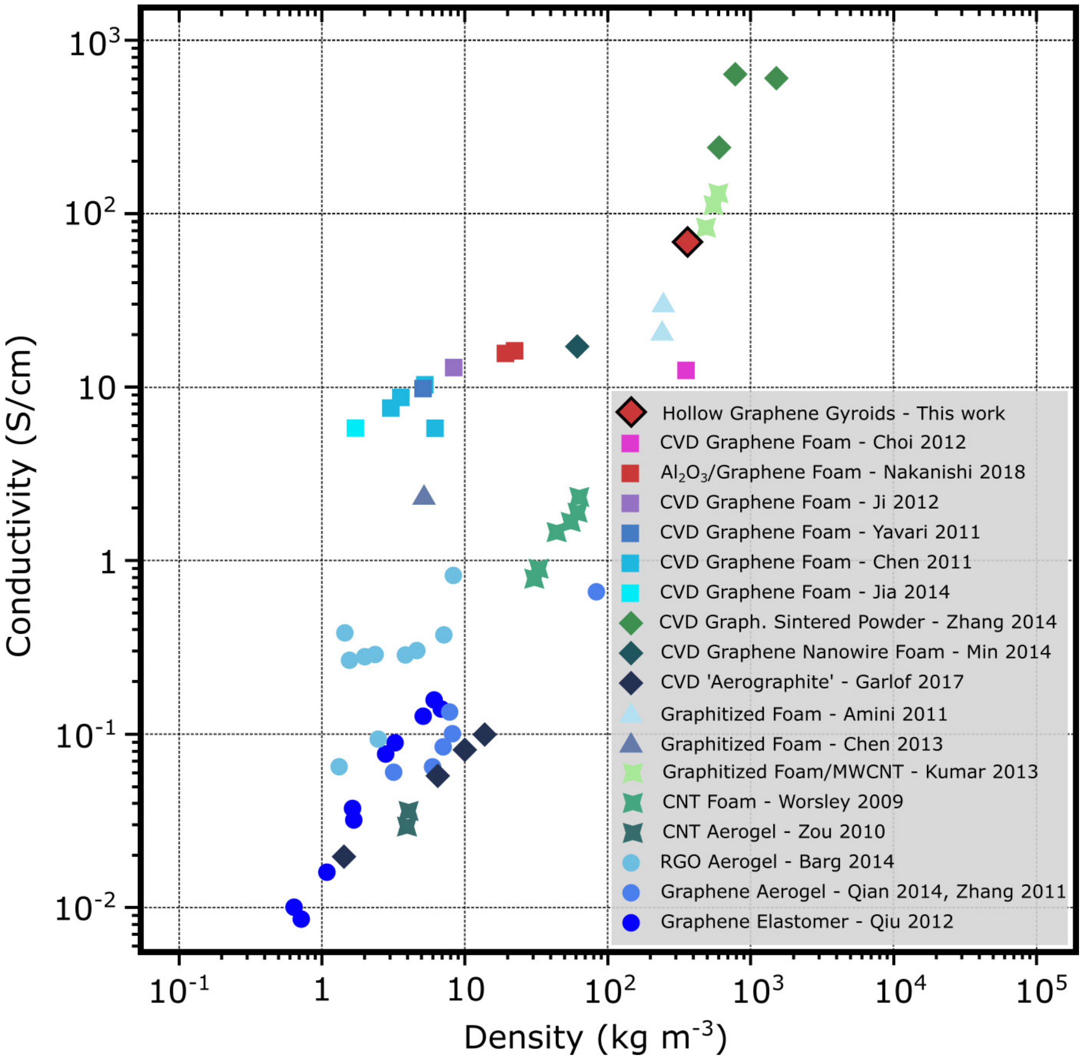

Figure 5.20: Electrical conductivity (S/cm) versus density (kg m^{-3}) of the hollow graphene gyroid film. Other state-of-the-art low density carbon cellular materials [3, 14, 34, 36, 42, 74, 98, 100, 117, 160, 200, 202, 264, 281, 293, 297, 308] reported in the literature are also included for comparison.

Similarly, fitted modulus and strength of the hollow graphene gyroid suggest that these nanoscale structures have a high compressive strength to density ratio, exceeding that of microscale metallic octahedral and octet lattices of similar relative densities (see Figure 1.1). This suggests that some of the size-dependent properties of graphene are maintained, though a large knockdown in the modelled parent properties is seen as compared to the values of the in-plane mechanical properties of graphene. This is attributed to interlayer shearing within the wavy walls of the multilayered graphene providing a significant contribution to the axial compliance. It is noted that the recovery of the hollow graphene gyroid from high levels of compressive strain is remarkably high, in contrast to macroscale templated graphene foams [165]. Lattice recoverability after compression is found in other low-density hollow lattices, owing to elastic shell buckling coupled to a size-strengthening effect [156, 213]. Recoverability of the hollow graphene gyroids are also improved by a more efficient stress distribution in the loaded lattice, as discussed in Chapter 5.4.1.

Size-dependent effects can influence material properties outside of mechanical properties, such as electrical conductivity. A plot of electrical conductivity versus density is shown in Fig. 5.20, comparing the hollow graphene gyroid against a range of graphene-based cellular materials. The measured conductivity of the hollow graphene gyroid (87 S/cm) [29] is shown to greatly exceed materials based on flake assembly methods such as graphene aerogels (0.01-2.5 S/cm) and many other CVD-based foams (typically 10-17 S/cm). As shown in Fig. 5.20, electrical conductivity is linked to the density of the graphene structure which will determine inter-flake resistance and the average cross section available for conduction, and hence the overall rate of electron transfer throughout. Hence, CVD-grown graphene foams prepared from dense 3D templates such as compressed nickel powders have demonstrated greater conductivity (233-680 S/cm) and possess a correspondingly high density (610-1070 kg/m^3).

5.9 CONCLUSIONS

Indentation measurements and numerical simulations are reported to estimate the mechanical properties of a nickel solid gyroid lattice and hollow graphene gyroid lattice. Nickel gyroid films of thicknesses 300, 500 and 700 nm with unit cell sizes on the order of 60 nm and a relative density of 40% were manufactured by block co-polymer self-assembly and electro-deposition of Ni. Hollow graphene gyroid lattices were prepared through a CVD method using nickel lattices as a template for the growth of multilayer graphene, resulting in a cell wall thickness of 3 nm corresponding to a relative density of approximately 14%. Berkovich nano-indentation tests were then performed to determine both the hardness and modulus of the films.

A multi-scale finite element analysis was performed to extract both the effective mechanical properties of the gyroid films and the associated properties of the parent material. The solid gyroid lattice was shown to possess a bending-dominated deformation mode, in contrast with the stretching-dominated hollow gyroid lattice. Both gyroid films were shown to have high yield strength to density ratios, exceeding many other state-of-the-art lattice materials at equal relative densities. This is attributed to the size-strengthening effect present in nanoscale nickel struts and graphitic walls. Despite this, the modelled parent material properties of the graphene gyroids is significantly less than the value for pristine monolayer graphene, due to knockdown factors arising from interlayer shearing within the wavy walls of the multilayered graphene. The size-dependent behaviour of materials also influences the conductivity of the hollow gyroid lattice, which exceeds that of other state-of-the-art graphene-based cellular materials. Graphene gyroids combine size-dependent mechanical and electrical properties with a topology of high structural efficiency. As such, these structures offer enhanced multi-functionality for a wide range of emerging applications where high levels of conductivity, surface area, mechanical strength and elastic recovery are required.

6

STRUCTURAL GRAPHITIC MICROFOAMS VIA SHRINKAGE AND CATALYTIC CONVERSION

6.1 AUTHOR CONTRIBUTION

This chapter is based on the manuscript *Structural graphitic microfoams via shrinkage and catalytic conversion of polymer scaffolds*, which is currently in preparation. The general approach, sample synthesis and characterization was performed by the author of this thesis.

6.2 INTRODUCTION AND MOTIVATION

In Chapters 4 and 5, the fabrication and characterization of CVD-grown graphitic foams was performed for both a disordered macroscopic foam and ordered nanoscale gyroid lattice. It was found that both materials possess significantly reduced elastic moduli and yield strength due to the increased axial compliance of a wavy cell wall. It was determined, based on comparison of calculated knockdown factors to the measured mechanical properties of graphene multiplayers, that the axial straining within the cell wall occurs via shearing of the multilayered wavy cell-walls. This deformation mechanism introduced large knockdown in the continuum mechanical properties of the graphitic foams, which possessed negligible amounts of elastic recovery. In contrast, the graphene gyroid lattice was found to benefit from its hollow

TPMS based structure, which afforded the structure a stretching-dominated deformation mode. This allowed the hollow graphene gyroid lattices to possess high strength and significant elastic recovery after indentation, despite also experiencing knockdown due to nanoscale interlayer wall shearing. It was also found that both foams possessed high conductivity to relative density ratios, exceeding those of foams made from flake assembly methods.

These insights have clearly demonstrated how the structural and electrical properties of functional carbon foams are strongly linked to the 3D structure and level of graphitisation. Directly converted 3D graphenic networks such as the FG and graphene gyroid lattices prepared in Chapters 4 and 5 possess high conductivity arising from the lack of inter-sheet junctions present in flake-assembly methods. However, preparation of high quality graphitic materials without the use of a supporting catalyst typically requires pyrolysis and further heat treatment to temperatures in excess of 2500°C [17, 27]. This has motivated catalytic approaches which have been demonstrated using many different carbon precursors including gaseous hydrocarbons as part of a CVD process or using solid carbon precursors such as polymers [25, 290], biomass [234] and recycled carbon [237].

However, the preparation of structured graphitic foams with sub-mm unit cell sizes remains a significant challenge. While the manufacture of stochastic foams is scalable, such foams consistently demonstrate inferior structural performance, leading to interest in the development of cellular structures with long-range periodic order and controllable unit cell morphology. Interference lithography [272], inverse opals [284] and polymer phase separation [29] have all been used to prepare patterned catalytic templates that have been successfully converted to freestanding 3D graphene lattices with long-range order. However, each templating method is only able impart specific patterns, and hence possess partial shape control.

Additive manufacturing techniques have been utilized as an open platform for the preparation of lattice materials with full shape control. This has allowed for the design of lattice materials that take full advantage of geometry-based scaling effects, possessing higher stiffness, strengths and energy absorption capacities than their foamed counterparts with random geometry. These include methods involving the sintering of metallic powders with lasers [241] or electron beams [27] or the curing of sequential layers of light sensitive resin have prepared lattices with mesoscale unit cell sizes. Recent development of microdimensional fabrication techniques such as two photon lithography [156, 251] have allowed for the fabrication of structured nano- and micro-lattices with unprecedented mechanical properties [16], see Figure 1.1. However, the scalability of such structures is limited by the low throughput and limited build size of high-resolution additive manufacturing techniques. In general, as the average strut size of the material is reduced cellular materials become more challenging to produce at volume. Comparisons between cellular materials with a variety of material strut length scales and demonstrated fabrication scales are plotted in Figure 6.1.

An appealing approach for overcoming this challenge is to 3D pattern materials at an easily implementable larger size scale, and to subsequently shrink the template while preserving its geometry. Pyrolytic shrinkage has been previously demonstrated with both bulk foamed polymers [34] and photopolymers [16] used in 2-photon direct laser writing. Such pyrolysis process results in the removal of the bulk side-chain species, leaving behind a disordered carbon allotrope primarily composed of sp^2-bonded carbon [105]. A typical reduction in volume of 75% can thereby be achieved [296] down to unit cell sizes of 1 µm. However, the lateral dimensions of lithographically fabricated lattices are limited to hundreds of microns, and the resulting pyrolytic carbon materials remain non-conductive.

In this chapter, a multifaceted approach is presented for the production of structurally ordered graphitic microfoams. The direct shrinkage and catalytic conversion of commercial polymer foams and 3D printed templates as facile, low-cost method to scalably reach and control sub-200 µm unit cell sizes and a high level of graphitisation at temperatures below 1100 °C. 3D printed cubic polymer lattices are converted to an identically-shaped carbonaceous network with shrinkage controlled via an atomic layer deposited oxide coating up

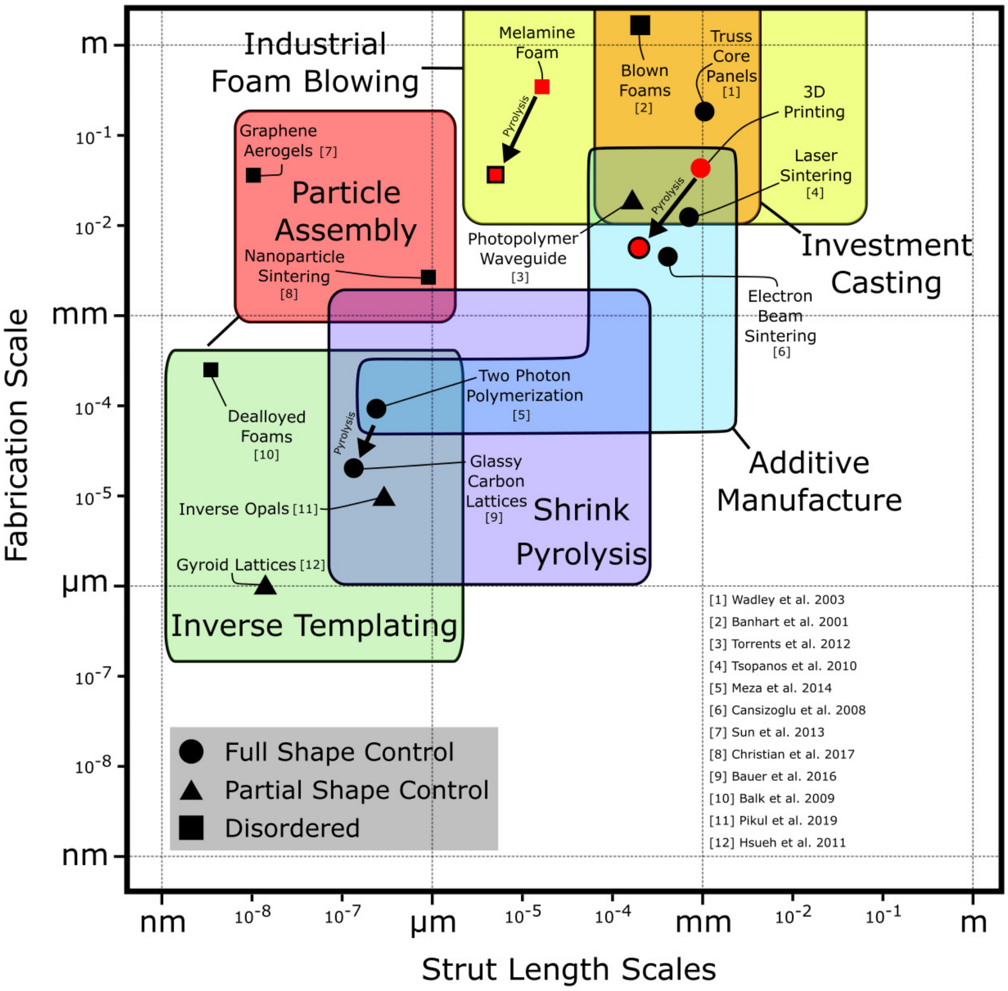

Figure 6.1: Comparison of cellular materials across a range of material strut width and fabrication scales. A range of state-of-the-art and industrial methods are highlighted, comparing industrial methods such as foam blowing and investment casting to recently developed high-resolution fabrication methods such as two photon lithography and gyroid film self-assembly.

to a maximum 125× decrease in volume and over 95% mass loss through slow carbonization. This is accompanied by a reduction in the unit cell size from 1000 µm to 170 µm, and strut widths from 550 µm to 65 µm. The structures are subsequently coated with a sacrifical metal catalyst by electroless deposition to achieve efficient graphitisation while maintaining structural integrity. The underlying mechanisms and opportunities to tailor the processes and structure to manifold application needs are then discussed.

6.3 EXPERIMENTAL

A commercial melamine foam and cubic lattice produced from resin stereolithography (SLA) were purchased and cleaned in acetone then isopropyl alcohol. If required, aluminum oxide (Al_2O_3) coatings were subsequently deposited onto the polymeric templates by ALD in a multi-pulse mode at 150°C, as described in detail in Chapter 3.1.4. Use of a multi-pulse mode allowed for extended exposure periods in order to achieve the conformal coating of the surface of the cellular materials. Polymeric templates were then subjected to a slow pyrolytic carbonization process as described in Chapter 3.1.2.1.

Electroless nickel deposition was then used to deposit a conformal 500 nm thick layer of nickel, as described in Chapter 3.1.5. The nickel-coated samples were then placed in a hot-wall CVD reactor for the pyrolytic graphitization of graphene multilayers, see Chapter 3.1.2.1. Metal-free samples were then fabricated by removing the sacrificial Ni template completely from the surface of the converted samples using wet chemical etching as described in Chapter 3.1.5. A polymeric scaffold was not needed to prevent the collapse of the graphitic structure due to the strength of the underlying amorphous carbon network.

All as-grown and composite samples are then characterized by scanning electron microscopy (SEM, Carl Zeiss SIGMA VP) at acceleration voltage of 2 kV. SEM was performed in a Philips XL 30 SEM. Raman spectra were measured at room temperature using a Renishaw In-Via spectrometer with a 532 nm wavelength laser and equipped with a 20x and 50x objectives. Low exposure times and special attention was used to avoid laser heating of the specimen. Bulk resistivity was measured using a four-probe station (Keithley Model 4200-SCS) via the Van der Pauw method as described in Chapter 3.2.10. Samples were measured after drying for one week and were electrically contacted by silver paste. Values presented represent the average across each sample group (melamine or resin lattice).

6.4 RESULTS AND DISCUSSION

Carbon foams with sub-mm unit cells were synthesized by means of thermal conversion and shrinking of commercially available cellular materials. Melamine foams have previously been coated in reduced GO flakes for use as elastic oil-water separators [127, 265], and prior carbonization [34] (N_2, 1 atm, 1000°C) of melamine foams have afforded non-conductive carbon foams with 4x shrinkage that remained elastic under compression up to 80%. Melamine foams are cheaply available, and possess a low density (~8 $\mathrm{mg/cm^{-3}}$) and high porosity (> 99%), motivating their use as a polymeric template. The synthesis scheme for the pyrolytic shrinkage of commercial melamine foam to form a carbonized network (CN) is shown in Fig. 6.2a, along with SEM images at each step of the process. Foam samples were thermally converted to an identically-shaped carbonaceous network with a 8x decrease in volume and approximately 50% mass loss, see Fig. 6.2c. The cellular geometries of the commercial melamine foam are typical of open-cell foams, with an approximate unit cell length scale of 100 µm. The increased level of shrinkage and brittle characteristic is attributed to the reduced pressure used during the carbonization process, which encouraged the release of N-containing gases and a more thorough carbonization. The characteristic Raman spectra of the untreated melamine resin [221] can be seen in Fig. 6.2b. An explicit strong peak at $\nu \approx$ 980-990 $\mathrm{cm^{-1}}$ is a signature of all melamine-containing compounds, arising from a triazine ring breathing mode. A set of peaks around ν = 1250-1600 $\mathrm{cm^{-1}}$ is mainly ascribed to vibrations of $N\text{-}CH_2\text{-}O$ groups, and are assigned to ring stretching and side-chain asymmetric C-N stretching vibrations, while the peak at ν = 2960 $\mathrm{cm^{-1}}$ is associated with C-H stretching vibrations in the formaldehyde part of the resin.

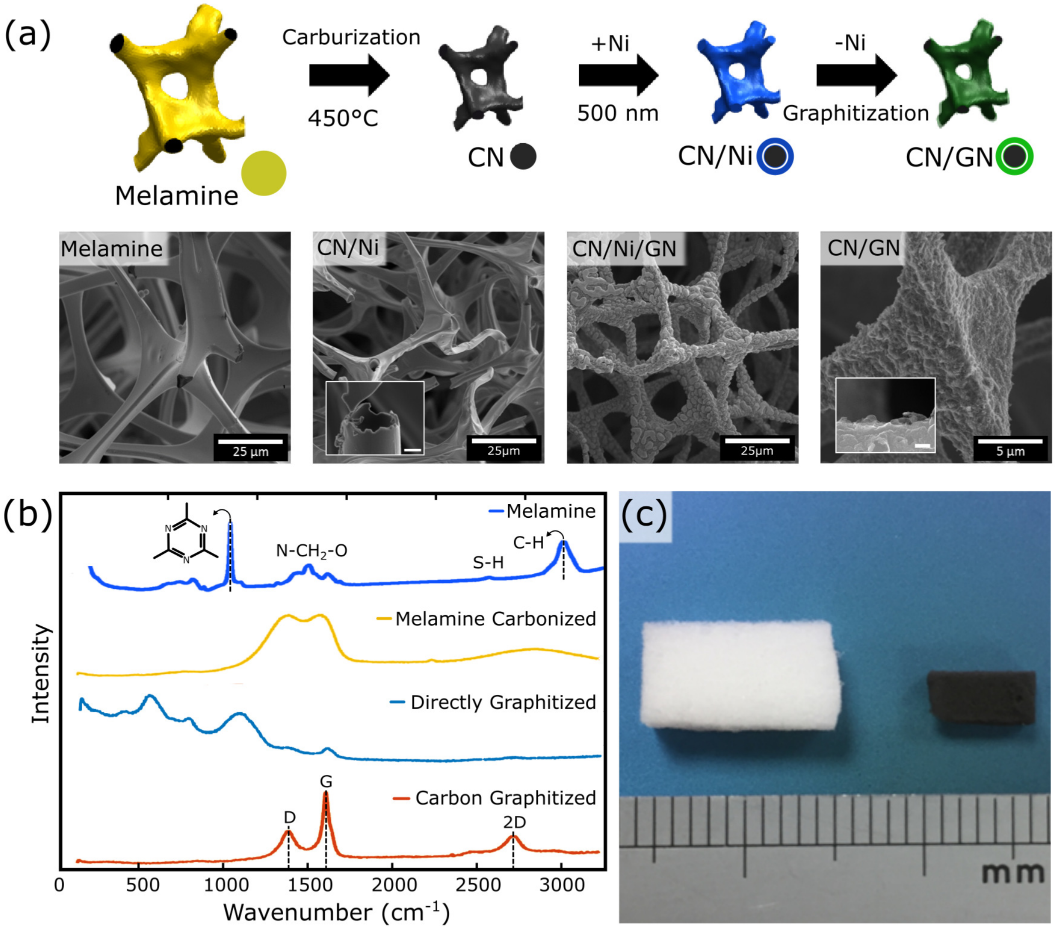

Figure 6.2: (a) Schematic and associated SEM images for the shrinkage and subsequent conversion of melamine foams to a graphenic network (inset scalebars 1 µm). (b) Raman spectra of pristine melamine foam displays characteristic vibrational signatures containing ring bending (500-800 cm^{-1}), triazine ring breathing (975 cm^{-1}), N-CH$_2$-O group vibrations (1250–1600 cm^{-1}), trace S-H vibrations (2500 cm^{-1}) and strong C-H stretching (3000 cm^{-1}). (c) Optical images of the melamine foam before and after processing, illustrating the dramatic reduction in volume and change in color after carbonization.

After carbonization, the Raman spectrum is consistent with that of low-temperature glassy carbon (Fig. 6.2b). This is characterized by a broad double peaked feature at approximately 1350 cm^{-1} and 1560 cm^{-1}, which is distinctive of graphitic carbons. The feature at 1350 cm^{-1} can be attributed to the D band, originating from double-resonant Raman scattering [204]. The peak at 1560 cm^{-1} can be assigned to the G band, arising from an optical phonon mode with E_{2g} symmetry associated with in-plane stretching of sp^2

hybridized carbon [35, 67]. Both peaks are broad, owing to the low temperature (450 °C) of carbonization limiting the amount of graphitization in the carbonization process [105].

Previous carbon foams derived from melamine possessed a bulk conductivity of just 6.8×10^{-2} S/cm^{-1} after carbonization at 1000°C, only rising to 2.1 S/cm^{-1} at a temperature of 1800°C [34]. Hence, herein we investigate the use of this carbon network as a carbon source for the growth of a continuous graphitic film. For more efficient catalytic graphitization of the carbon network, a conformal Ni layer was deposited as can be seen in the inset Fig. 6.4a, which displays the hollow coating around a broken strut. After graphitization, islands of Ni are seen to form due to the self-diffusion of the thin coating. Removal of the Ni catalyst reveals a textured graphitic layer which is supported by the glassy carbon network beneath, Fig. 6.3d. Self-diffusion of the nickel layer is more prominent in the melamine foams, which can be attributed to the smoother surface post-shrinkage. Images taken at higher accelerating voltages reveal the continuous graphitic coating that surround the shrunken amorphous carbon skeleton, suggesting that graphene growth and nucleation occurs prior to significant catalyst diffusion, see inset Fig. 6.3. Only small areas of the carbonized foam remain uncovered, see Fig. 6.3c,d.

As a control experiment, the direct catalytic graphitization of the untreated melamine foam was carried out with the same process and was found to be unsuccessful, see Fig. 6.2b. This is likely due to the disruption of the Ni coating by the decomposing polymer, as well as the strong presence of non-carbon elemental species in the melamine resin, which leach out during the carbonization process and is taken up by the Ni layer, poisoning the catalytic effect on graphene nucleation and growth. Additionally, typical graphene foams with macroscopic templates require the use of a PMMA scaffold or critical point drying due to the effect of capillary forces that collapse the foam [36]. The presence of the amorphous carbon backbone allows for the 3D cellular geometry of the graphitic layers to be well preserved during the Ni removal.

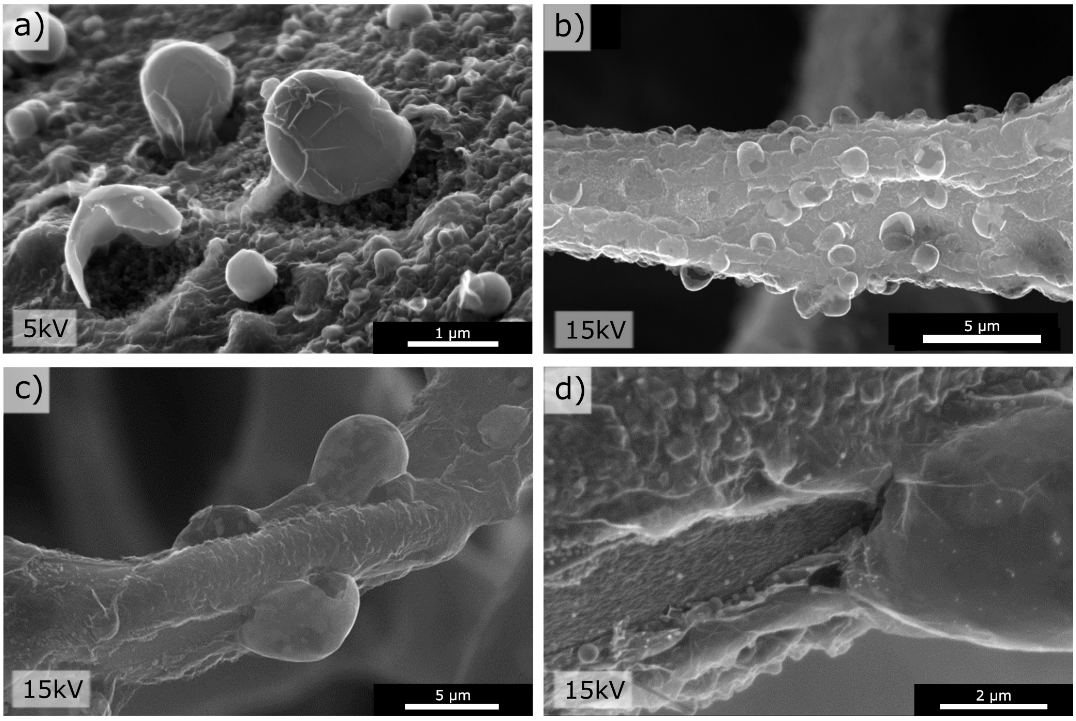

Figure 6.3: SEM images of a polymer shrunk and graphitized melamine foam at different accelerating voltages. (a) Graphitic carbon shells present on the surface of the amorphous carbon network due to the self-diffusion of the thin catalytic nickel layer. (b) Higher (15 kV) accelerating voltages reveals the the thin graphitic film present on the amorphous carbon struts post nickel-etching. (c,d) Image of crack in graphitic film, showing the surface of the carbonaceous network underneath.

In comparison to stochastic foams, structured lattice materials can be significantly more weight-efficient due to improved load distribution and stress transfer behaviour throughout the lattice. Furthermore, control over pore size and cell structure can enhance the surface area and influence the tortuosity of fluid flow through the porous media. To demonstrate the application of the shrinkage and conversion method to structured materials, a commercially printed 3D cubic lattice, see Fig. 6.4, is processed in a similar way. SLA printed resin formulations, as used herein, commonly utilize radical photoinitators combined with acrylate-based monomers, each of which differ depending on the proprietary design of the resin [133]. Cubic lattice samples were converted to an identically-shaped carbonaceous network with 125x decrease in volume through the slow carbonization process, reducing the unit cell size from 1000 µm to 170 µm, and strut widths from 550 µm to 65 µm, see Fig. 6.5. The more dramatic reduction in volume is accompanied by an increase in mass loss to over 95%. This is attributed to differences in the breakdown and decomposition behaviour of the polymer resin.

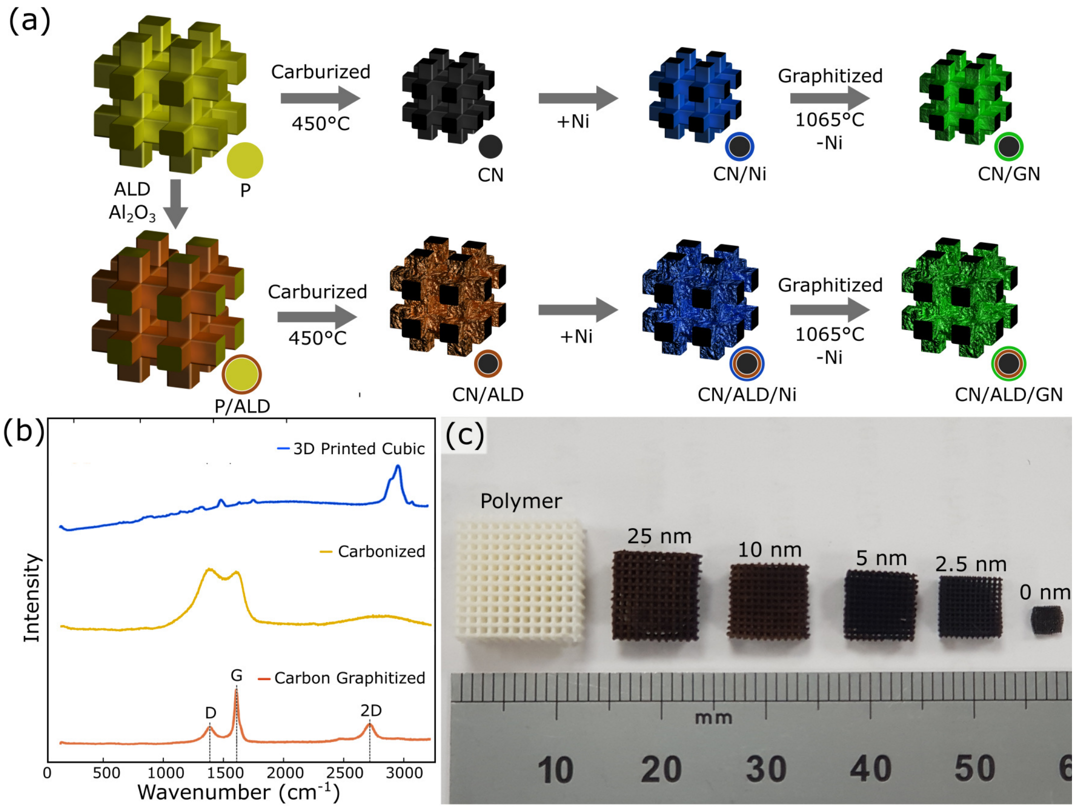

Figure 6.4: (a) Schematic for the shrinkage and conversion of a cubic resin lattice to graphitic network, with up to 125× decrease in volume. (b) Representative Raman spectra taken on samples as labelled. Pre-carbonized samples developed a characteristic multilayer graphitic Raman signature. (c) Optical images demonstrating an 80% shrinkage in each direction occurs after process completion resulting in an over 125× reduction in volume. Addition of a 25, 10, 5 or 2.5 nm thick alumina layer allows for the attenuation of the shrinkage and development of surface wrinkling (alumina thicknesses shown left to right).

The changes in chemical character during the conversion process are assessed by Raman spectroscopy. The characteristic Raman spectra of the untreated resin can be seen in Figure 6.5. The strong peak at approximately 2940 cm^{-1} can be attributed to C-H stretching, arising from CH, CH_2 and CH_3 groups in a diverse range of side chains and microenvironments. After carbonization at

450°C, the spectroscopic signatures have been converted to a pyrolytic carbon spectrum as before, indicating that the chemical characters have become homogenized despite having very different initial elemental compositions. After addition of Ni and further annealing, clear multilayer graphene signatures can be observed across the surface of the 3D lattice. The control experiment of processing a resin lattice without carbonization does not result in a multilayer graphene coating and additionally leads to a total loss of structure. This is again likely due to the disruption of the Ni coating by the decomposing resin structure, which changes size significantly during carbonization.

To control the shrinkage of the polymer template during carbonization, a thin conformal ceramic coating was added to the surface of the 3D printed resin, through the use of pulsed long-exposure ALD. The surface of the resin lattice (Figure 6.5) was smooth before heating. When heated, a biaxial compressive stress is applied to the surface of the polymer due to the shrinking polymer. A stress mismatch between the shrink material and coating causes a pronounced wrinkling of the shrunken surface. The alumina layer also markedly influences the final shrink ratio of the carbonized template, see Fig. 6.5c. A 2.5 nm alumina layer is found to reduce the shrink ratio of the cubic lattice to 9x, further decreasing down to 4x for a 25 nm thick layer. In this way, the final surface roughness and surface area can be controlled. This shrunken template can then be used to grow a thin graphitic film coating, with carbon diffusion to the nickel catalyst occurring through cracks and holes in the ALD alumina layer. The characteristic wrinkles of the as-grown graphene film can be seen in Fig. 6.5. The conductivity of the catalytically converted lattices was found to be 3.3 S/cm for the melamine foam, and 0.8 S/cm for the cubic lattice. These conductivity values are in line with graphene aerogels, while possessing reduced graphene loading, which was estimated via the available surface area to be 1 wt% for the melamine foam and between 0.1 and 0.3 wt% for the cubic lattices. Conductivity values were highly dependent on the unit cell size and hence surface area available within the volume for graphene growth.

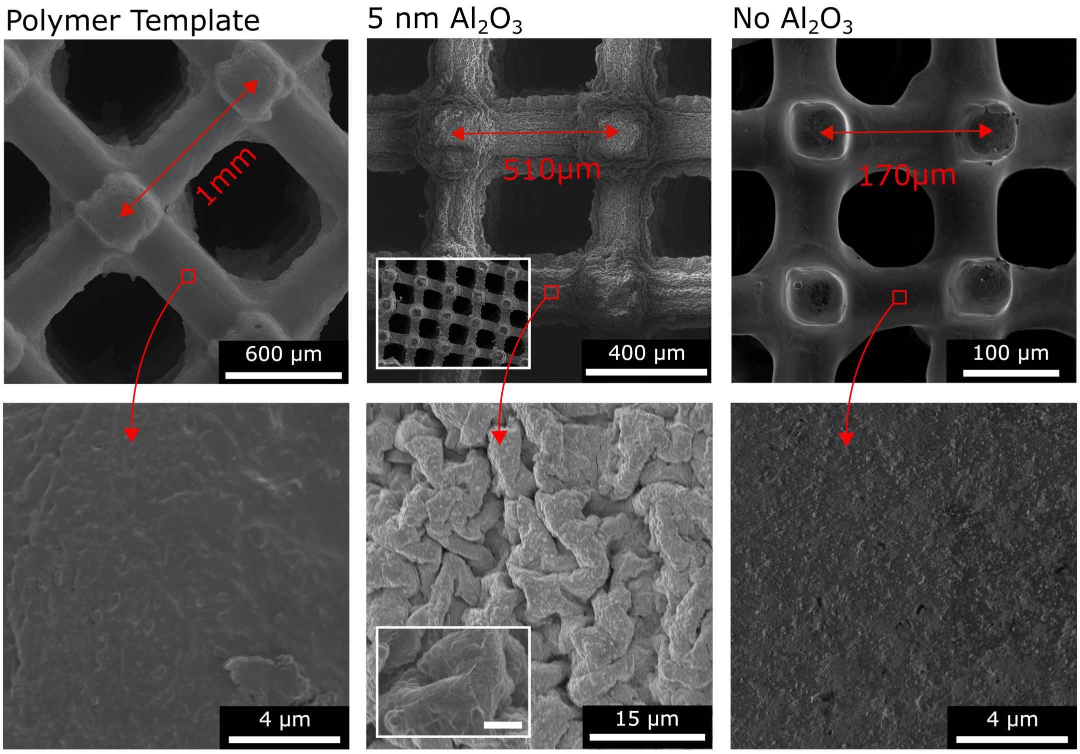

Figure 6.5: SEM images of an ALD alumina-arrested shrinkage process applied to 3D printed cubic lattices. 3D printed lattices begin at 1mm unit cell size, which shrinks down to 170 μm after carbonization without an additional alumina layer, representing a >5× shrinkage in each lateral direction and an overall >125× reduction in volume. Addition of 5 nm of alumina by ALD results in reduced shrinkage and a pronounced wrinkling of the lattice surface. Low magnification inset shows large-area isotropic shrinkage. High magnification inset shows the characteristic wrinkling of the graphene surface atop the pyrolytic carbon strut (inset scale bar 500 nm).

The carbon foams presented herein combine the properties of structurally ordered porous materials, i.e. low density, high geometric surface area, permeability and mechanical stability with the intrinsic properties of graphitic films such as electrical and thermal conductivity as well as resistance to chemical corrosion. These physical properties are promising for manifold electrochemical or catalytic applications. However, the shrinkage and conversion approach detailed herein may easily be extended to other polymers and to coatings beyond multilayer graphene or and ALD alumina. Shrinkage of thermoplastic films such as extruded polyolefins have resulted up to a 95% reduction in lateral dimensions [168], highlighting the possibility for 3D printing polymers that may be optimized to allow for greater isotropic 3D shrink ratios. Furthermore, partially or fully inorganic polymers may degrade to form cellular materials formed of constituent materials such as doped carbon [180] or ceramics [48], which will possess substantially different physical properties [286]. Application of other surface coatings to the polymer pre- or post-shrinkage presents a further range of possible functional materials. Wrinkling of transparent indium tin oxide (ITO) layers have enabled increases in the energy conversion efficiency of flat photovoltaic devices [291], owing to surface area enhancement and improved light trapping behaviour. Similar enhancements are possible in catalytic applications through the addition of catalytically active nanomaterials prior to shrinkage, allowing for the preparation of high surface area catalysts post shrinkage.

6.5 CONCLUSIONS

The direct shrinkage and catalytic conversion of commercial polymer foams and 3D printed templates offers a very simple and low-cost method for reaching identically-shaped structures with sub-200 µm unit cell sizes. Furthermore, the shrink polymer method is capable of converting structures on the scales that can be realized by the conventional additive manufacturing techniques, or existing commercial polymeric foams. The addition of an ALD alumina layer prior to shrinkage between induces a surface stress mismatch during pyrolysis, introducing surface wrinkling to the strut surface. The alumina layer was also shown to control the overall shrink ratio, depending on the thickness added, reducing the shrinkage ratio from 125x to 4x after addition of 25 nm of alumina. Furthermore, efficient conversion of the pyrolytic carbon was demonstrated through the use of electroless deposition and further catalytic graphitization, resulting in the formation of a conductive multilayer graphenic coating at temperatures below 1100 °C. The methods herein present the facile production of multifunctional cellular materials with sub-mm unit cells, tuneable size, roughness and conductivity.

7

CATALYTICALLY ENHANCED MOCVD OF MONOLAYER WS_2

7.1 AUTHOR CONTRIBUTION

This chapter is based on the manuscript *Catalytically enhanced metal organic chemical vapour deposition of monolayer* WS_2, which is currently in preparation. The general approach, sample synthesis and characterization was performed by the author of this thesis. ToF-SIMS measurements was carried out by co-author Vlad-Petru Veigang-Radulescu. Device fabrication and testing, and HR-TEM/SAED characterization was performed by co-author Dr. Ye Fan.

7.2 INTRODUCTION AND MOTIVATION

Chapters 4, 5 and 6 has focused on the growth and characterization of graphitic foams across a range of unit cell length scales and regularity. As the first experimentally discovered 2D material, both the growth and physical properties of graphene have been extensively investigated, research which has enabled the development of processes for the combined preparation and investigation of CVD graphene-based cellular materials as discussed in this thesis. However, the family of emergent 2D materials has rapidly grown to include members which intrinsically possess wide range of optical and electronic properties. In the case of graphene, the calculated band dispersion has shown that the conduction and valence bands touch at six Dirac points in the Brillouin zone where energy dispersions are linear with respect to momentum. This is a unique property that leads to a high observed charge carrier mobility. However, as a gapless semi-metal, pristine graphene cannot be used in electronic devices without the presence of band gap opening mechanisms. This has lead to interest in the development of TMDC monolayers, a family of 2D materials which possess a characteristic layered structure of hexagonally packed transition metal atoms sandwiched between two layers close-packed chalcogenide elements (S, Se or Te).

Tungsten disulfide (WS_2) is a prominent material from the TMDC family, exhibiting a wide direct band gap ($E_g \approx 2$eV), strong spin-orbit coupling and bright room-temperature PL [149, 254] in its monolayer form. As a prototypical 2D semiconductor, WS_2 has promise in a range of applications including (opto-) [76] electronics [203] to spintronics and sensors [190]. The edges of WS_2 films also have promise as a catalyst, possessing a free energy of hydrogen adsorption that is close to neutral. As WS_2 is also resistant to corrosion in concentrated electrolyte solutions, WS_2 is an ideal candidate as the catalyst for hydrogen photoproduction via photocatalytic decomposition of water [155, 233, 278]. Furthermore, the catalytic activity has been shown to be dependent on the number of active centres and material phase [247], which may be influenced by the MOCVD processing conditions. This motivates the investigation of monolayer WS_2 growth on planar substrates in this chapter for future incorporation into high surface area 3D cellular materials.

Research on TMDC crystal growth has historically focused on bulk materials [132], while the emergent application-driven need is for the scalable growth of electronic-grade 2D layers/films [24]. The latter, however, remains a significant challenge due to the lack of understanding of the underlying reaction mechanisms for any of the various growth techniques. Powder vaporisation methods are currently the most widespread production method, based on the sublimation of solid precursors in a hot-walled reactor. These methods offer a flexible platform to demonstrate TMDC layer growth, and have reported of monolayer WS_2 crystal domains >100 μm on inert substrates including SiO_2/Si [210], and sapphire [277], as well as on metals such as Au [73, 288], and Ni-Ga alloys [71]. However, the thermal evaporation and decomposition of solid-state precursors that determine the growth atmosphere are difficult to accurately control and modulate. This restricts uniformity and scalability, and makes such powder based techniques too complex to behave as a reproducible model system for the advancement of the required fundamental understanding of crystal growth. For instance, nucleation can occur in the gas phase or on the substrate, and this is often not clear. [125] Moreover, defects and trapped states [97] as well as unintentional metallic dopants [136] remain common issues. On the other hand, molecular beam epitaxy (MBE) offers a high level of growth parameter control, and has been widely employed for TMDC studies to explore van der Waals epitaxy [99, 114, 239]. However, MBE demands ultra-high vacuum environments, while domain sizes of as-grown TMDC layers remain often smaller compared to other methods [24]. Driven by the need for low-cost, high through-put and industry compatibility, MOCVD and related ALD type techniques have emerged as prime candidates for integrated manufacturing of electronic-grade TMDC layers.

MOCVD of WS_2 thin films with µm domain sizes have been demonstrated on insulating amorphous and crystalline substrates including SiO_2/Si and c-plane sapphire [47, 50], yet the understanding of the underlying growth mechanisms and thus control over layer microstructure is still in its infancy. These inert substrates were chosen for their low surface roughess and ability to limit potential side reactions with the precursor gases, though they tend to lead to slow growth rates in the MOCVD process. Reported MOCVD growth times for monolayer WS_2 are often on the order of hours for complete coverage [43, 45, 106]. Carbon contamination introduced by organic precursors is a major challenge for MOCVD, and a range of metal and chalcogen precursors have been explored to address this challenge for TMDCs [43, 45], which are often toxic or difficult to handle. While standard MOCVD is based on co-exposure of the constituent precursors, sequential exposure patterns similar to ALD processes have also been explored [86]. However, unlike 3D materials, for TMDCs such choice of sequential exposure is less obvious, in particular since layer-by-layer growth for 2D materials is largely dictated by their anisotropic layered crystal structure. ALD-type approaches to date have shown limited TMDC layer control and rather low crystallinity [86, 197]. The same typically holds for 'direct conversion' approaches, where the metal is e.g. deposited by physical vapour deposition and then exposed to chalcogenide precursors [152, 183, 289]. Most literature on these MOCVD and sequential exposure approaches has focussed on inert/dielectric substrates and possible catalytic enhancement has not been explored in detail.

In this chapter, the growth of tungsten disulfide (WS_2) on catalytic gold substrates in a two-step MOCVD process is systematically explored. The catalytic behaviour of gold enables low pressure MOCVD of WS_2 with high yield rate at low partial pressure of precursor gas. Here the ultrafast growth of 100% monolayer WS_2 film within several minutes is demonstrated. Significant catalytic effects of Au are demonstrated for the metal organic chemical vapour deposition (MOCVD) of WS_2 monolayer films, using a simple sequential exposure pattern of low cost, less-toxic precursors, namely tungsten hexacarbonyl [THC; $W(CO)_6$] and dimethylsulfide [DMS; $S(CH_3)_2$]. This sequential exposure pattern, combined with the use of a cold-walled reactor, minimises precursor pre-reactions and encourages a reaction path bound to the substrate surface. This model system is employed to explore the effects of using a metal substrate for such MOCVD processes, specifically Au, motivated by its prior use in surface science [82], and powder vaporisation methods for WS_2 and other 2D materials [73, 113, 288].

It is found that the use of Au allows a reduction of the DMS pressure, required to nucleate and grow WS_2, of more than one order of magnitude. This reduction in turn allows a minimisation of the carbon contamination of as-grown WS_2, which has been a major challenge with this precursor chemistry to date. The reaction scheme exhibits a self-limiting behaviour to monolayer WS_2 and full coverage can be achieved by one exposure cycle of 10 minutes in total at a growth temperature of 700°C, which compares favourably to prior MOCVD growth times which are often in excess of 1 hour. The deconstructed MOCVD process allows for a process-resolved understanding of the role of each process step, which is discussed in the context of previous 2D crystal growth literature.

7.3 EXPERIMENTAL

All as-received gold substrates were annealed for 6 hours at 1025°C under total pressure of 800mbar with H_2:Ar=1:9 to encourage grain growth and ensure that surfaces were as free as possible of organic contamination. Prior to growth, samples were treated by oxygen RIE (150 mTorr, 50 W, 5 minutes) to remove surface carbon contamination. 2-step MOCVD growth of WS_2 on Au was then performed as described in Chapter 3.1.3. The transfer of monolayer WS_2 films was performed using catalyst etching as described in Chapter 3.1.6. CVD and transfer of hBN was used for the examination of the catalytic effect of the gold substrate during sulfurization, see Figure 7.3. hBN was grown on 25 µm thick platinum (Pt) foils (99.99%, Alfa Aesar) and transferred using a bubbling method, as described in detail in reference [255].

Both Raman and PL spectra of samples are taken as described in detail in Chapter 3.2.6. To calculate integrated peak intensities, the Au baseline is taken and subtracted from all measured spectra. Peak intensities and full widths at half maximums were extracted from the spectra using a python script applying a simple Lorentzian-Gaussian multipeak fit, see Fig. 7.1, and averaged across each of the 1600 points. TEM grids (Quanti-foil) are used as the substrate for WS_2 in the associated HR-TEM studies as described in Chapter 3.2.4. After transfer of the PMMA/WS_2 onto the HR-TEM grid, the sample is dried overnight then baked at 150°C for 30 minutes to soften the polymer and increase the adhesion of the WS_2 to the grid. The PMMA scaffold layer is then removed by dissolving in acetone. All measurements are taken under 80keV acceleration voltage. Selected-area electron diffraction (SAED) are taken over a large area of gridded spots. Crystal orientations of the sample are then calculated from the relative rotation between each SAEDs.

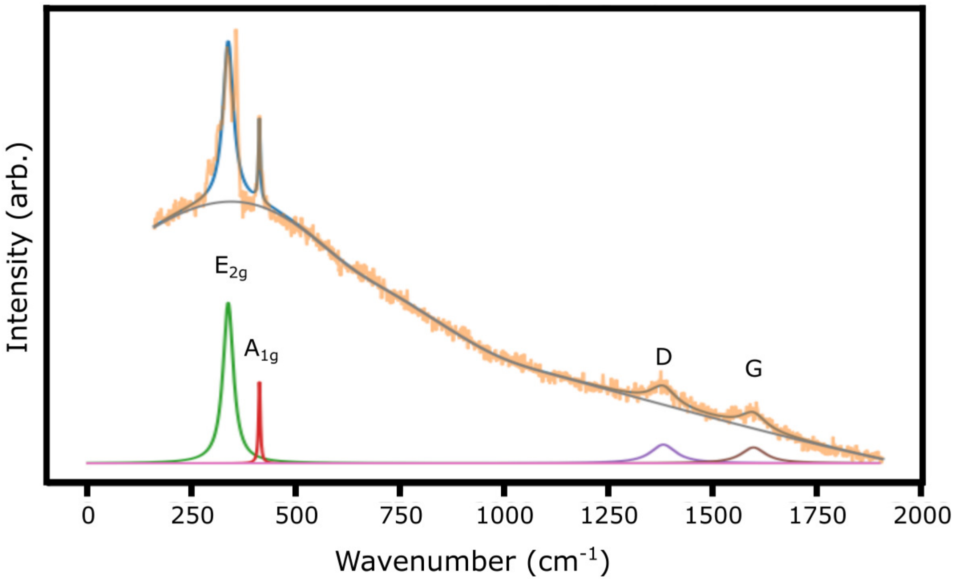

Figure 7.1: Sample Lorentzian-Gaussian multipeak fit of the WS_2 spectra for a point Raman scan in a 20×20 µm map. Peak intensities and full width half maximum values are averaged across each of the 1600 points per map scan.

Ex-situ ToF-SIMS measurement were performed using a ToF-SIMS IV instrument as described in Chapter 3.2.9. Data processing was carried out by selecting relevant peaks in the ToF-SIMS spectra and monitoring their change in intensity over the course of the sputtering. Spectra were acquired in both positive and negative polarity, monitoring the evolution of WS_2, hBN, WO_3, carbon, oxygen, sulphur, and gold by selecting the WS^{3-}, BN^- (or B^+), WO^{3-}, C^{2-}, O^-, S^- and Au^{3-} peaks, respectively. C^{2-} was chosen as the representative for carbon over monoatomic C^-, which is more prone to fragment from other residual oxides or other adventitious species. Good indicators for bulk Au were polyatomic species such as Au^{2-} or Au^{3-}, from which the latter was chosen due to a higher intensity level.

The spectra were calibrated using both low and high mass elements and the peaks were assigned in good agreement with theoretical vs experimental isotope identification. WS^{3-} was selected as most representative peak for WS_2 assignment as it had the highest intensity among all W_xS_y species during analysing a reference sample with exfoliated WS_2 on SiO_2. Comparison of carbon contamination levels between samples was performed by normalising the spectra against the WS^{3-} peak, knowing that there is a surface monolayer of WS_2. When quantifying the level of carbon in the samples, the surface ~1 nm was removed from the analysis to mitigate the contribution of adventitious carbon from ambient exposure prior to measurement. This was determined by the point at which the H^- and CH^- signals drop to a local minimum at the surface. All depth profiles were normalized to the total ion intensity, using a point-to-point normalization, allowing for consistent comparison between the samples.

The field effect mobility of WS_2 was measured by fabrication of a 2-terminal FET on 300nm SiO_2 on p-doped silicon. Evaporated In(20nm)/Au(80nm) act as the source and drain contact for all devices. After device fabrication, the chip is encapsulated by 10nm ALD Al_2O_3 to prevent degradation. The device is current-annealed by performing a gate sweep under high source-drain bias (10V) until the transfer curve is stable. All measurements are performed at room temperature under ambient conditions. A halogen lamp (λ_{peak} ~906nm, I ~30mW·cm^{-2}) is used to test the light response of the sample.

7.4 RESULTS AND DISCUSSION

A schematic overview of the employed MOCVD process with a sequential exposure pattern is shown in Figure 7.2. Commercial poly-crystalline Au foils are annealed and oxygen plasma cleaned prior to loading into the MOCVD reactor (Figure 7.2b-i). This is followed by a low pressure (5×10^{-6} mbar) THC exposure step, which is referred to as "metallization" (Figure 7.2b-iii). THC is an established precursor for W film deposition that readily decomposes at 700°C, particularly on metallic surfaces [215]. At the given conditions, it was found that a metallization time of 5 minutes leads to sufficient W deposition for complete WS_2 coverage on Au in the sulfurization (Figure 7.2b-iv) step. This deconstructed process thereby converts the W on the Au surface to WS_2, as indicated in Figure 7.2b-iv. DMS partial pressures are varied between 0.01 mbar to 1 mbar during sulfurization to closely examine its influence on the quality of the WS_2 film. For the given process, a continuous WS_2 coverage is found for DMS partial pressures larger than 0.05mbar (Figure 7.2b,v).

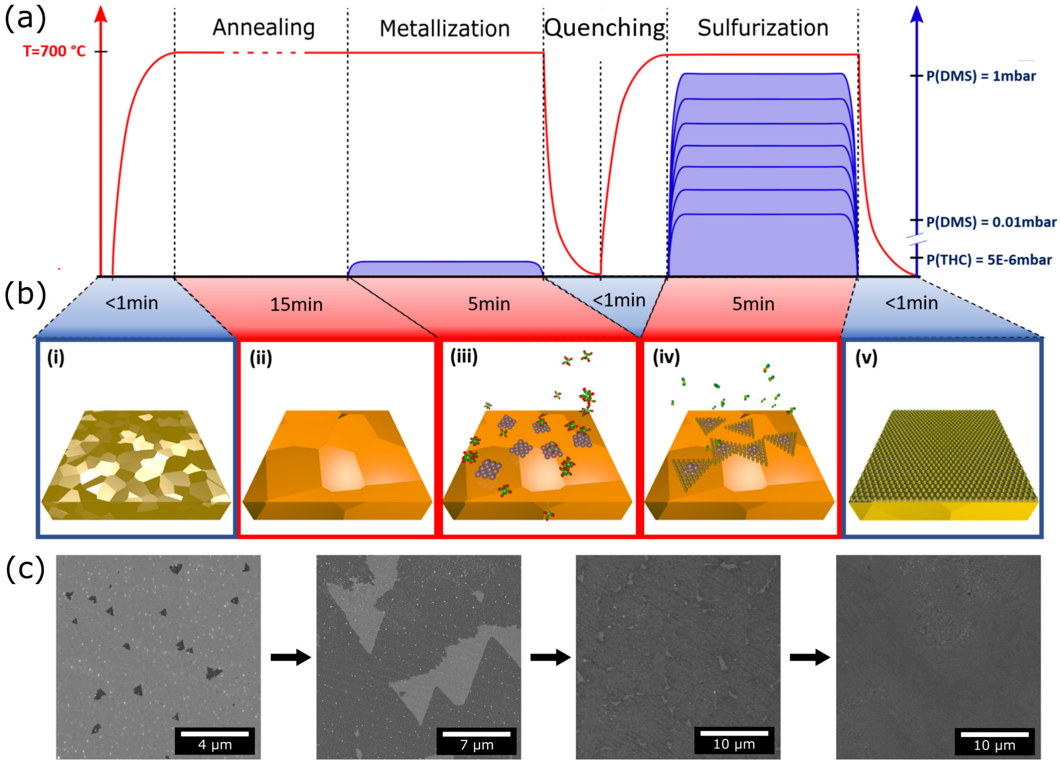

Figure 7.2: Schematic of 2-step MOCVD procedure for WS_2 on Au foil. (a) Key growth parameters: the sample is heated to and kept at 700°C and first exposed to THC. The sample is then quenched to prevent potential uncontrolled pre-reactions between the two precursors. This is followed by heating to 700°C again, and exposure to DMS. The pressure of DMS is varied to study its influence on carbon contamination. (b) Key growth processes: (i) Poly-crystalline Au foil exhibits grain growth upon annealing (ii). (iii) Deposition of W during metallization. (iv) Sulfurization of W seeds. (v) WS_2 covered Au after MOCVD. The as-grown WS_2 is monolayer and poly-crystalline. (c) Evolution of WS_2 film growth from nucleation to domain growth and merging.

Before discussion of the detailed growth mechanism of MOCVD WS_2 on Au, a comparison of the deconstructed process used herein is made to previous literature. First, an attempt to grow WS_2 on Au with a similar sequential exposure pattern but with different precursors (i.e. WO_3 and S) was reported to be unsuccessful, even though large domains could be produced by co-exposure of these two precursors [73]. This can be attributed to the volatility of any deposited WO_3. Secondly, the direct conversion of TMDC materials from metallic layers [184, 289] report that only thin layers of deposited W can be efficiently converted to WS_2. Similarly, it is found that once the W film is too thick, e.g. when sputtered W films (~100nm) or W foils (~25 µm) are used, no 2D WS_2 can be reliably grown after sulfurization with the process parameters used herein.

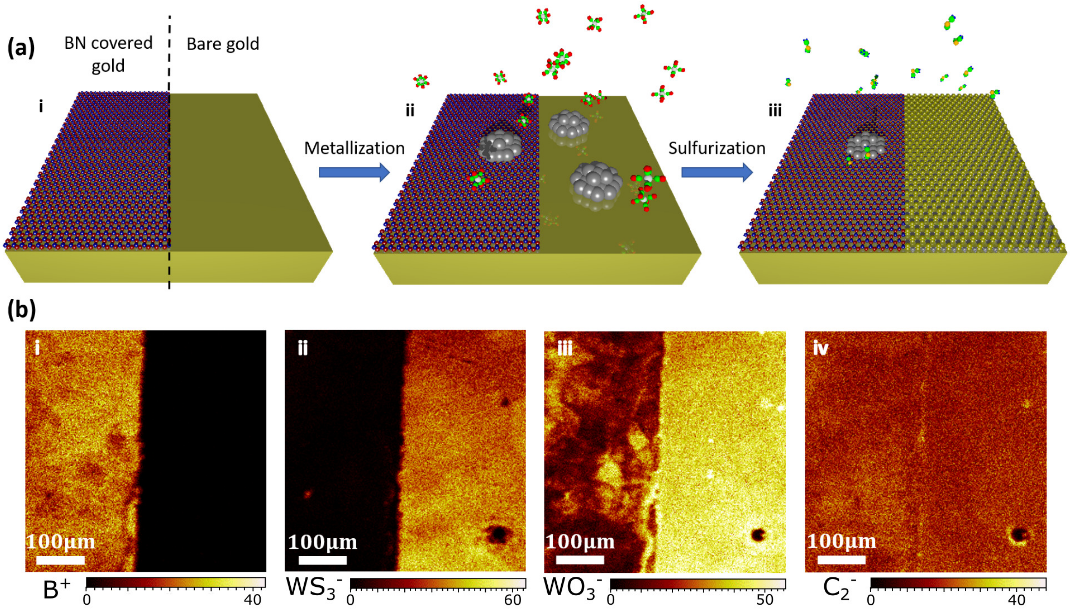

Figure 7.3: WS_2 growth on Au partially covered by monolayer hBN. (a) Schematic of sample and MOCVD procedure with metallization and sulfurization: (i) Half of the Au catalyst is covered by monolayer hBN before MOCVD. (ii) During metallization process, tungsten (grey clusters) deposits on both hBN covered and not covered area. (iii) During sulfurization, only tungsten on Au is converted to WS_2. (b) Select ToF-SIMS surface images of sample after complete MOCVD process: (i) B+ image corresponding to hBN coverage; (ii) WS^{-3} image corresponding to WS_2 coverage; (iii) WO^{-3} image to characterize W coverage; (iv) C_2^- image to characterize residual carbon.

The effects of Au on the MOCVD reaction are explored by comparing the WS_2 growth behaviour on the Au foil with and without hexagonal boron nitride (hBN) coverage, as illustrated in Figure 7.3 a. The coverage with inert hBN prevents any direct precursor contact with the Au surface, and thus suppresses any direct catalytic effects of Au. Further, it is expected that adatom mobilities will differ between the two areas. Post-growth ToF-SIMS imaging is used to map the growth results as shown in Figure 7.3b. Figure 7.3(b, i) shows a 500 µm × 500 µm map of the detected B^+ ion species, that act as a fingerprint for the presence of the hBN film. The map demonstrates continuous hBN coverage on Au after WS_2 growth and confirms that the hBN film remains intact throughout the MOCVD process. Figure 7.3b-ii shows a map of the detected WS^{-3} ion species to fingerprint the presence of WS_2. It was found that WS_2 film forms only on the Au surface where there is no hBN coverage. This highlights that even a monolayer of hBN can fully inhibit the TMDC growth reaction, suggesting a strong catalytic role of the Au substrate, which is further supported by the SEM images and Raman map presented in Figure 7.4. The unreacted W will be oxidized in air post-growth, which enables the specific identification of unreacted W through the imaging of WO^{-3} ion species as shown in Figure 7.3b-iii. W is thus found on both the hBN covered and uncovered Au surface. This is consistent with the ready thermal decomposition of the THC precursor at the metallisation temperature in the absence of any catalytic substrate effect [215]. The more sporadic W coverage on hBN may be due to increased desorption or increased W adatom mobility. The sequential exposure pattern used herein demonstrates that the selective growth of WS_2 on Au is determined by the sulfurization step, i.e. that DMS dissociation here is catalytically enhanced by Au. To rule out the influence of residual polymer atop the hBN film has on the decomposition of DMS, Figure 7.3 (b, iv) presents a map of the detected C_2^- ion species present on the surface as a fingerprint for such carbon contamination. No difference in the average carbon level between the hBN covered and uncovered Au surface is observed. A DMS pressure of 0.1 mbar is used, which does not result in significant carbon contamination as explored in detail below.

Unintentional doping with carbon is a common issue for MOCVD processes [152]. TMDC MOCVD is no exception, and there are numerous reports of deleterious carbon incorporation into TMDC films [43, 45]. To minimize contamination more difficult-to-handle precursors are often employed, such as replacing organic chalcogenide precursors with H_2S [45, 47]. A number

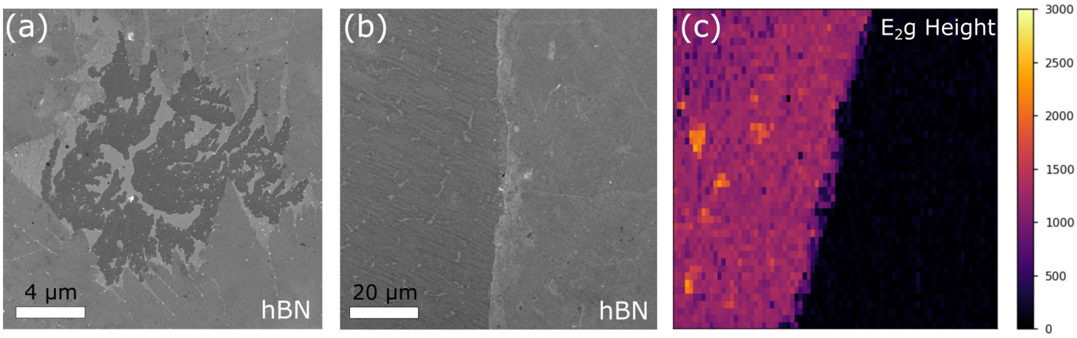

Figure 7.4: WS_2 growth on Au partially covered by monolayer hBN. (a) SEM image of partial growth of WS_2 within a crack in the hBN film. (b) SEM image of the interface between WS_2 covered gold and hBN covered gold, post-growth. (c) Raman map of characteristic E_{2g} height of as-grown WS_2 film. Dark area is area covered by hBN film, which prevented growth.

of more complex or toxic precursors have been reported, particularly for ALD-type reactions, driven by the motivation to have the metal oxidation state of the precursor closer to the +IV oxidation state in the WS_2 or MoS_2 film [86]. In this study, the least hazardous, easiest to implement precursors are used for both the metal and sulfur, and contamination is managed through use of a catalytic substrate. Figure 7.3 has already shown that DMS dissociation is the key step in WS_2 film formation. This is consistent with a less reactive chalcogenide containing precursor, and thus TMDC MOCVD typically require very high overpressures of the chalcogenide precursor [45, 295].

Raman spectroscopy and ToF-SIMS scans are shown in Figure 7.5b and c, highlighting the influence of DMS partial pressure during sulfurization on the carbon contamination of as-grown WS_2 on Au. Figures 7.5a,b plot the intensity of characteristic Raman peaks for WS_2 and amorphous carbon (a-C) (Au baseline subtracted) for DMS pressures from 0.03mbar to 1 mbar during sulfurization (Figure 7.2). For comparison, Figure 7.5a also shows the spectra for plain, annealed Au foil (red curve, bottom) and Au foil that has only undergone sulfurization (without prior metallization) at 1 mbar (light blue curve, top). The data shows that the a-C Raman peak intensities increase

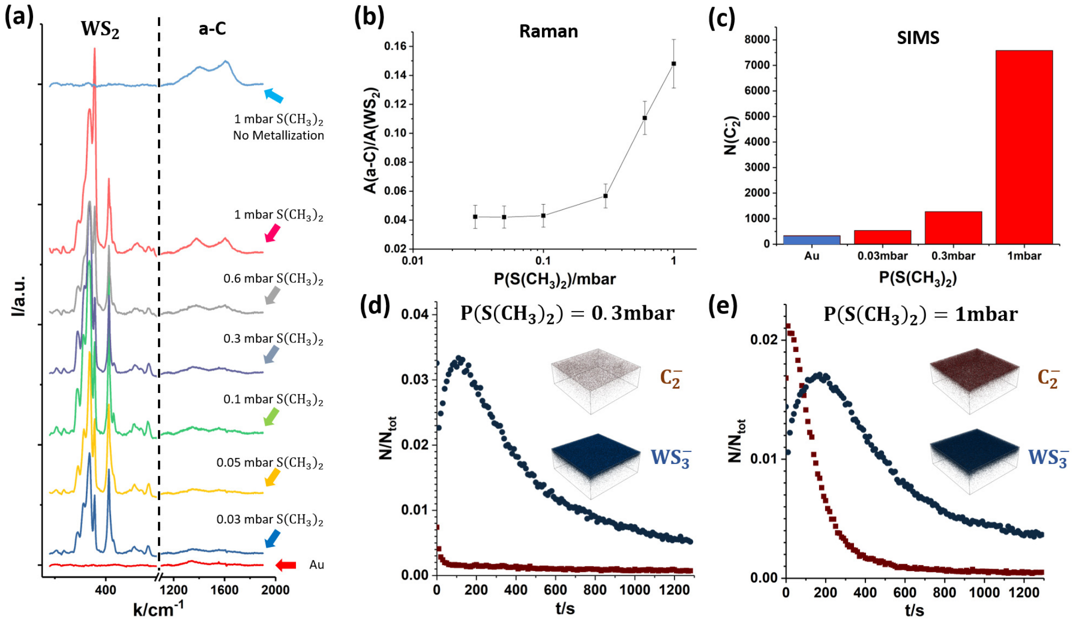

Figure 7.5: Carbon contamination introduced during sulfurization step: (a) Raman spectra of samples treated with different sulfurization conditions. (b) Integrated Raman peak intensity ratio (A) between amorphous carbon (a-C) and WS_2 vs. DMS pressure during sulfurization. The error bar is 5 times of the variation in each measurement. (c) ToF-SIMS C_2^- ion intensity vs. DMS pressure during sulfurization. (d,e) ToF-SIMS depth profile for C_2^- and WS^{-3} count for WS_2 monolayer on Au foil comparing low (0.3 mbar, (d)) and high (1 mbar, (e)) DMS pressures during sulfurization. Both carbon and WS_2 are distributed uniformly over the 150 µm × 150 µm detection region.

with increasing partial pressures of DMS. For clarity, Figure 7.5b plots the integrated Raman peak intensity of a-C normalized against the integrated peak intensity of WS_2. This highlights that the carbon contamination increases significantly past a sulfurization DMS partial pressure of 0.3 mbar. This finding is consistent with a report by Choudhury et al., which found strong contamination from the use of carbon-containing sulfur precursors (diethyl sulfide) for MOCVD TMDC growth in the mbar pressure range [45]. This contamination suppressed the PL response of the grown films and was consistent for all samples grown across a range of temperatures, from 650 to 850°C. In comparison, Choudhury et al. found that samples grown using H_2S remained free of carbon contamination, as determined by Raman spectroscopy and the strength of the PL response. Herein, only a small amount of carbon signal can be observed in the Raman spectra of samples grown with a sulfurization DMS partial pressure up to 0.3 mbar, such that a strong PL response is maintained.

Hence, the catalytic effect of Au on DMS dissociation is demonstrated to enable the lowering of the required DMS partial pressure for monolayer WS_2 formation by approximately 2 orders of magnitude compared to previous MOCVD studies [45]. To show the continuity and uniformity of the as-grown MOCVD WS_2 on gold, large scale ToF-SIMS surface scans of MOCVD grown WS_2 films at different sulfurization partial pressures are provided in Figure 7.6. A normalized ToF-SIMS signal of C_2^- is shown on the right, comparing carbon contamination levels between the two process conditions. In samples grown with high DMS exposures, a significant amount of carbon can be detected by ToF-SIMS in the same place as WS_2.

In order to further confirm the correlation between DMS partial pressure and carbon contamination, ToF-SIMS depth profiling is employed with a very gentle sputter rate to measure the chemical environment of monolayer WS_2 on Au surface. The depth profiles of carbon and WS_2 are summarized in Figures 7.5c-e. Among the many carbon species that are detectable due to the complex decomposition profile of DMS, the most intense C_2^- ion signal is used herein to indicate carbon contamination. In Figure 7.5c the C_2^- ion intensity of the as-annealed Au foil is additionally added as a reference for the level of adsorbed carbon contamination due to sample transfer in air. The ToF-SIMS data (Figure 7.5c) confirms the trend seen in the Raman spectroscopy data (Figure 7.5b) with the carbon concentration increasing with increasing DMS partial pressure.

Representative ToF-SIMS 3D depth profile images of fully grown WS_2 monolayers on Au foil comparing low (0.3 mbar, Figure 7.5d) and high (1 mbar, Figure 7.5e) DMS pressures during sulfurization. The inset 3D ion images show that in both samples the C_2^- and WS_3^- ion intensities are laterally uniform across the measured 150 µm × 150 µm area. However, the C_2^- ion intensity on the Au surface is significantly higher for the sample sulfurized in

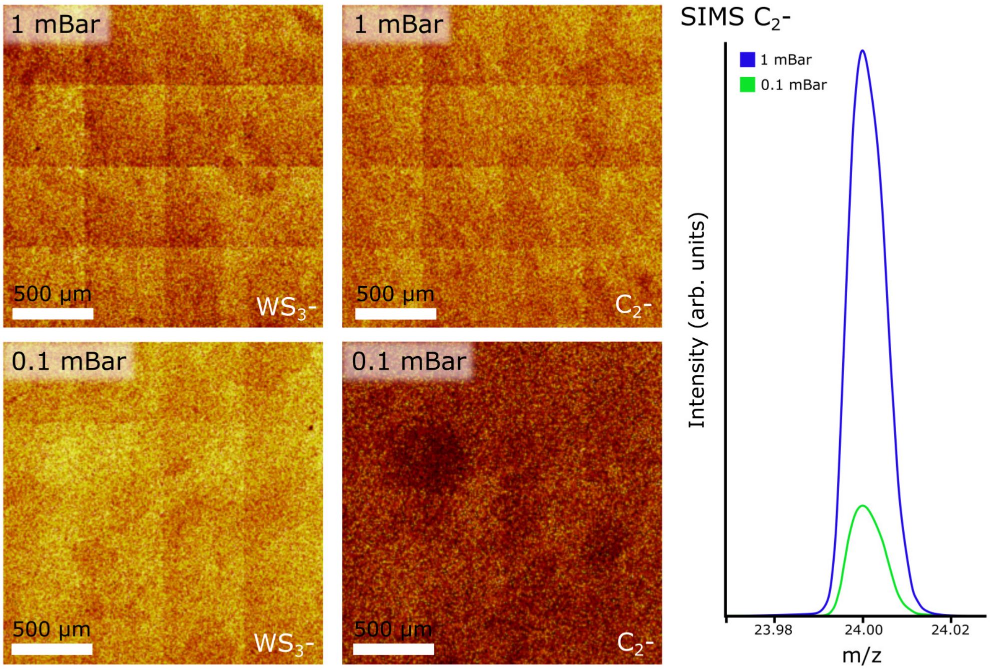

Figure 7.6: Large scale ToF-SIMS imaging of WS_2. (a) ToF-SIMS surface maps of WS_2 grown with 1mbar DMS during sulfurization. (b) ToF-SIMS surface maps of WS_2 grown with 0.1 mbar DMS during sulfurization. (c) Normalized ToF-SIMS signal of C_2^-. In samples grown with high Ps^-, a significant amount of carbon can be detected by ToF-SIMS in the same place as WS_2. All ion intensities are normalized against total spot intensity.

1mbar DMS. Furthermore, the ToF-SIMS depth profile shows that for samples grown with a low DMS partial pressure, the carbon contamination appears only on the very surface and quickly diminishes upon further probing further through the WS_2 layer and into Au (Figure. 7.5d). In contrast, for high DMS partial pressures, a much higher C_2^- ion intensity is detected on and away from the surface, indicating a heavier carbon contamination on the as-grown WS_2.

ToF-SIMS is also used to investigate the elemental species that are present in the Au bulk, after growth. Au does not form any stable compound with either W or S under these experimental conditions and thus it is expected the W and S solubility in Au to be negligible [195, 196]. Sputtering is carried out at a higher rate using Cs^+ ions, allowing for the detection of W, S, O,

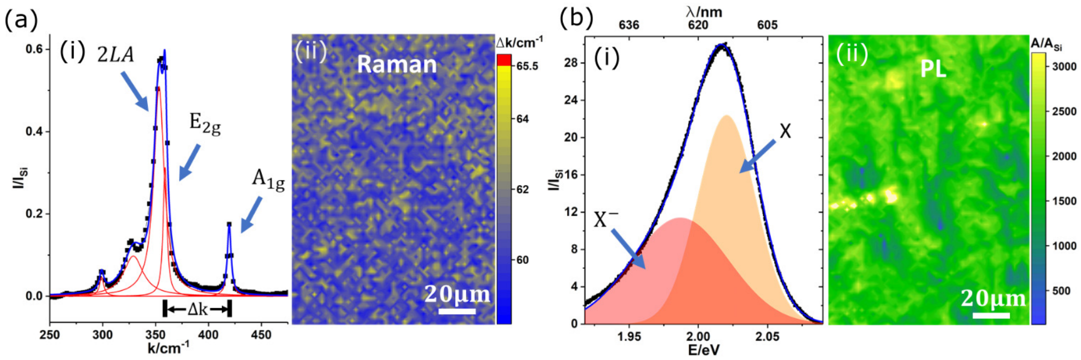

Figure 7.7: Characterization of continuous WS_2 film via 2-step MOCVD process (0.1 mbar DMS). (a) Raman spectroscopy characterization of WS_2 film transferred on SiO_2/Si. (i) Typical Raman Spectrum normalized by the Raman peak of Si. (ii) Raman mapping of frequency difference between E_{2g} and A_{1g}. No multilayer WS_2 (i.e. frequency difference larger than $65.5 cm^{-1}$, marked by red colour) is observed. (b) PL characterization of WS_2 film transferred on SiO_2/Si substrate. (i)Typical PL spectrum normalized by the Raman peak of Si. The exciton (X) and trion (X^-) peaks are labelled. (ii) Integrated PL intensity mapping normalized by the integrated Raman intensity of Si. The strong PL confirms the single-layer nature of the WS_2 film.

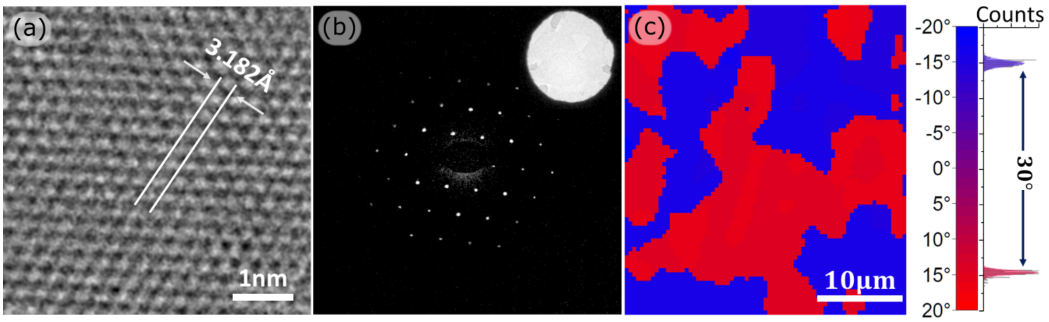

Figure 7.8: (a) HR-TEM of the WS_2 film transferred on Quanti-foil TEM grid. Lattice distance is measured as ~3.2 Å. (b) SAED of WS_2 film. The sharp 6-fold diffraction pattern indicates good crystallinity. The inset shows bright field HR-TEM image of the SA. (c) HR-TEM diffraction mapping of WS_2 film. The WS_2 film has average domain size of around 10 μm with a bimodal crystal orientation with 30°rotation (FWHM < 1°).

and C to a depth of ~400nm. As shown in Figure 7.9a and b, the elemental distribution in bulk Au is not strongly influenced by the growth condition, supporting the theory that the catalytic reaction is surface limited. Moreover, the concentration of S and W both diminish rapidly after the surface layer, due to the low solubility of both elements in Au at thermal equilibrium. The insets in Figure 7.9 also provide the results measured by Ar^+ sputtering, in which the measurement is confined to only the top ~10 nm from very surface, where only the carbon signal differs significantly.

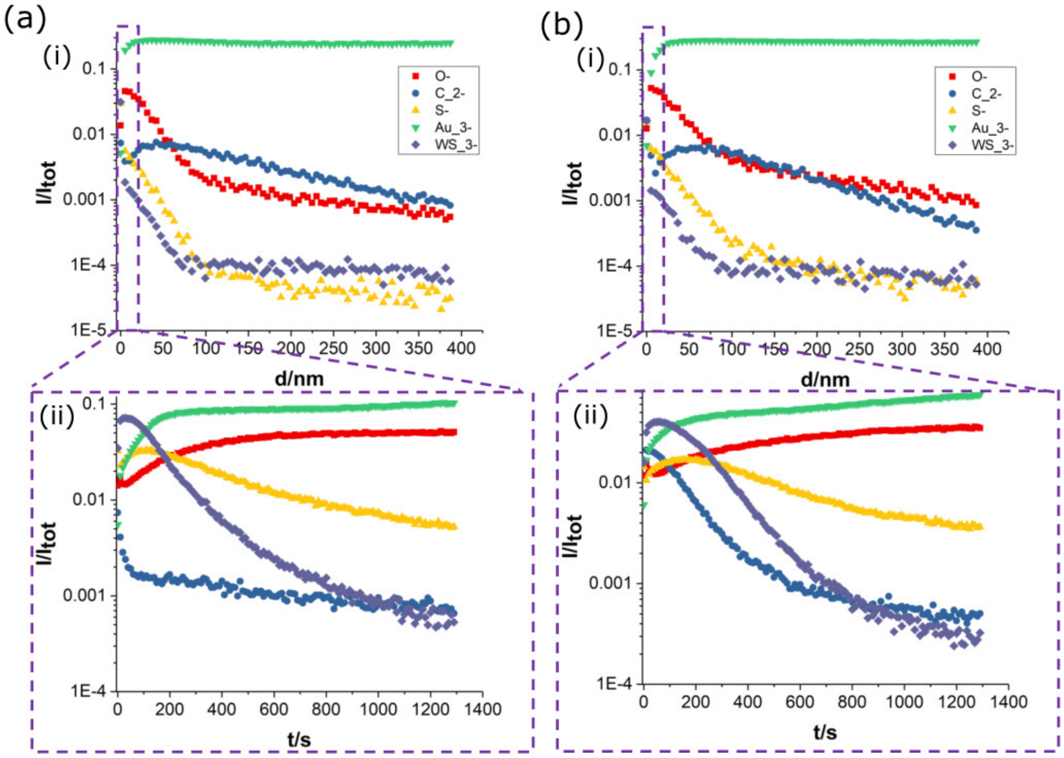

Figure 7.9: ToF-SIMS depth profile of different ion species. (a) Depth profile taken on WS_2 grown by 0.3 mbar DMS sulfurization. (i) is the rough depth profile, sputtered by Cs^+. (ii) is the fine depth profile, sputtered by Ar^+. (b) Depth profile taken on WS_2 grown by 1 mbar DMS sulfurization. (i) is the rough depth profile, sputtered by Cs^+. (ii) is the fine depth profile, sputtered by Ar^+.

The demonstrated catalytic MOCVD process not only enables the minimization of carbon contamination via ultra-low DMS pressure, but simultaneously allows for full WS_2 monolayer coverage to be achieved within a 10 minute exposure time (Figure 7.2), which is significantly faster in comparison to most previously reported TMDC MOCVD processes with monolayer growth times that are typically reported to required well over a few hours [43, 45, 106]. Figure 7.7 shows the further characterization of WS_2 films as grown by the optimised 2-step MOCVD process with 0.1 mbar DMS, after transfer of the WS_2 layer onto SiO_2/Si wafer support for Raman and photo-luminescence (PL) measurements, or Quantifoil support for TEM. A representative Raman spectrum of the WS_2 is shown in Figure 7.7a-i with E_{2g} and A_{1g} vibration modes measured at 356.9 cm^{-1} and 417.6 cm^{-1} respectively, possessing full-width-half-maximums (FWHM) of 4.3 cm^{-1} and 4.2 cm^{-1} respectively. This is in line with previously reported Raman measurements using a 532 nm laser excitation for WS_2 transferred onto SiO_2 [19, 153]. A map of the frequency difference between the A_{1g} and E_{2g} peak is shown in Figure 7.7a-ii, which is known to sensitively depend on the number of WS_2 layers. Based on previous literature, 65.5 cm^{-1} was chosen the threshold to distinguish between monolayer and bi-layer WS_2 [46]. Using this method, no WS_2 multilayer region is detected across the representative sample area of 108 µm × 154 µm, see Figure 7.7a-ii. The monolayer nature of as-grown WS_2 is further confirmed by the strong PL peak with exciton energy of ~2.02 eV (Figure. 7.7b-i). A significant trion peak around 1.98 eV is detectable similar to previous reports on CVD WS_2 [186]. A map of normalized integrated PL intensity is shown in Figure 7.7b-ii, as taken in the same area sampled by Raman mapping. The measured PL intensity is significantly stronger across the whole sample than the Si and WS_2 Raman signals, consistent with monolayer WS_2 [149].

HR-TEM images are shown in Figure 7.8a and b, along with diffraction mapping results for a transferred WS_2 film. The representative HR-TEM image in Figure 7.8a confirming the hexagonal lattice structure, highlights the crystallinity of the WS_2. The lattice constant is approximately 3.18 Å, which is consistent with theory [164, 220], and previously measured results [65]. The selected-area electron diffraction (SAED) analysis present in Figure 7.8b shows a clear hexagonal diffraction pattern with sharp spots. In order to determine the crystal orientation over a reasonably large area, over 200 diffraction patterns across a 40 µm × 40 µm WS_2 film area were taken to construct the map shown in Figure 7.8c. Two dominating crystal orientations rotated by 30°±1.5°are found as highlighted by the bi-polar distribution (Figure 7.8c). Based on this data, the average WS_2 grain size is of the order of 10 μm, which compares favourably to previous literature on MOCVD TMDC materials on non-catalytic substrates with typical domain sizes on the order of a few μm [45]. The measured transfer curve of the two-terminal field effect transistor (FET) structure is shown in Figure 7.10, where 2D conductivity is plotted as a function of back gate voltage. Field effect mobility of the WS_2 was measured as 0.51 Vs/cm^2 in light and 0.40 Vs/cm^2 in dark which are comparable with previously reported values [73, 300]. The threshold voltage does not vary much with and without light, i.e. 29.2 V in light and 30.4 V in dark. However, the field effect mobility of these devices were significantly lower than those prepared from WS_2 films grown using powder-based methods, which have achieved field-effect mobilities of up to 50.5 Vs/cm^2 [287].

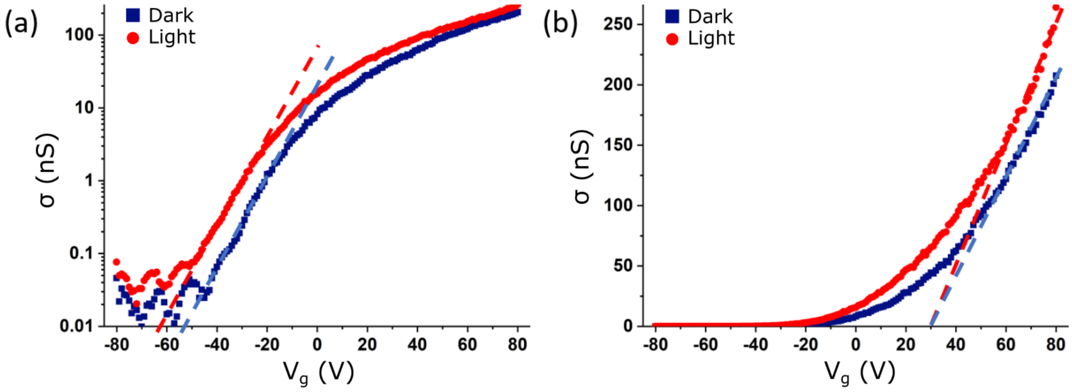

Figure 7.10: Transfer measurement of WS_2. (a) Semi-log plot. (b) Linear plot. Both plots are measured with and without light.

The results herein unveils several unique features of the catalytically enhanced growth of MOCVD 2D TMDC materials. Self-limiting growth of monolayer WS_2 films is demonstrated for the range of deconstructed MOCVD process parameters used herein. Monolayer control of TMDC growth has proven to be non-trivial, with unwanted multilayer regions commonly found in previous reports. Within the reported range of DMS partial pressures used herein, WS_2 was produced directly on gold, but not on WS_2, hBN-covered gold, or pure W foil (~25 μm thickness). The self-limiting growth is attributed to the critical role of Au in activating DMS dissociation and hence the sulfur supply during the sulfurization step. It should be noted that the uncatalysed thermal decomposition of DMS is expected to be slow and incomplete at the reaction temperature in this report (i.e. 700°C) [115, 243]. The observed catalytic dependence is consistent with previous reports that multilayer TMDC will grow if the deposited metal on Au is sulfurized by more active sulfur precursors that will decompose without the need for catalytic support [82]. In addition to the catalytic effect of Au, the self-limiting growth pattern of MOCVD on Au is also a result of the strong interaction between as-grown WS_2 and gold. Similar to WS_2 on gold after vacuum annealing, the as-grown WS_2 on Au cannot be transferred by electrochemical delamination [73], which indicates that a strong interaction exists between WS_2 and Au. The as-grown WS_2 film seals Au tightly and suppresses intercalation of precursors, thus preventing additional growth underneath the existing WS_2 layer.

Moreover, the catalytic effect of Au on the sulfurization of tungsten enables WS_2 to grow under a significantly reduced DMS pressure, efficiently minimizing the carbon contamination. Sapphire or SiO_2/Si wafers were also tested as growth substrates, but neither substrate allowed for WS_2 deposition under the growth conditions reported herein. Although prior work on Au catalysed DMS dissociation is limited, thermal deposition of DMS on oxides are well-documented. Many side reactions typically resulting in carbon deposition occurs and this is likely the source of carbon contamination found in previous reports [45, 115]. Due to its high melting point, W deposited during the metallization step is likely to be present as nanoparticles. As such, the Au surface is decorated by W during the sulfurization step and thus either bare gold or the W nanoparticles on Au could act as the catalyst during sulfurization. However, direct sulfurization of ~10 µm films of W was unsuccessful, and it is hence more likely that precursor breakdown is induced by a strong Au-S interaction prior to S adatom diffusion to surface W particulates. Furthermore, tungsten is known to react with carbon to form tungsten carbide [145], which could be one of the major side reactions when the sulfur supply is insufficient or carbon supply is in excess, as in the case of MOCVD WS_2 on SiO_2 or sapphire. The precursor pressures of both metallization (5×10^{-6} mbar) and sulfurization (0.01 mbar to 1 mbar) are much lower when compared with conventional MOCVD or powder-vaporization CVD, presenting the efficient production of monolayer WS_2 films.

Finally, the HR-TEM data presented in Figure 7.8 shows a strong bimodal distribution of WS_2 orientations. The average grain size of the Au foil used herein is ~100 µm. Hence the analysed film area is likely to originate from one Au facet, and this data again indicates that the substrate strongly influences growth, be it via Au step edges or S-Au interactions. A similar epitaxial relation between TMDC and c-plane sapphire has been previously demonstrated [285] with only one orientation but larger FWHM in the distribution of orientations. In this way, a move to single crystalline Au surfaces will provide an avenue for further improvement in film control and homogeneity. During sulfurization, W atoms can either diffuse through the gold surface or by chemical gas transport (e.g. by forming unstable compound vapour like WS_3 and re-deposit). Reports on W adatom mobility on Au were not found, but given the high self-diffusivity of Au, higher surface mobilities are expected in comparison to covalently bonded oxide surfaces like sapphire or SiO_2. However, it is shown here that for a short 10 minute exposure cycle on a poly-crystalline Au surface full WS_2 monolayer coverage can be achieved which is of interest to future error tolerant process development.

7.5 CONCLUSIONS

In this chapter, a deconstructed MOCVD model process is used to demonstrate the significant catalytic effect of Au on the MOCVD of monolayer WS_2. In particular, the effective catalytic dissociation of sulfur precursors, such as DMS, enables the possibility of using low toxicity precursors while retaining low carbon contamination and fast growth times. The much lower chalcogen precursor pressures not only leads to self-limiting monolayer coverage but makes the overall process much more efficient and gives wider compatibility with standard growth reactors. Furthermore, lower pressures also enables future direct in-situ observation of the growth of similar MOCVD processes to further progress the understanding of the underlying mechanisms. While Au is used herein, which requires subsequent WS_2 transfer for typical device applications, these findings also motivate further studies on catalytic enhancement of dielectric support films, which would allow transfer-free device integration. These insights also link to ALD-type and direct conversion processes, and it is hoped this can open further comparative studies of co- and sequential exposure patterns, fostering the understanding of key underlying mechanisms for future integrated manufacturing of TMDCs and other 2D materials.

8

SUMMARY AND SUGGESTIONS FOR FUTURE WORK

This thesis has investigated the CVD processing of a range of catalytic templates to open new routes towards the controlled fabrication of foams and lattices, whose cell walls are comprised of layered 2D materials. Both a disordered macroscopic foam and ordered nanoscale gyroid lattice were used as catalytic templates for the growth of freestanding multilayer graphitic cellular materials. Mechanical testing of such new fabricated materials was then undertaken in order to examine the deformation and failure mechanisms of these unique cellular materials. This lead to the development of a new hierarchical model framework with particular attention to the deformation response of the wavy multilayered cell wall material. Further, the facile preparation of structured graphitic microfoams and the monolayer growth of an emergent TMDC material, WS_2, are reported.

Firstly, a reproducible synthesis pathway based on the CVD of high quality, conformal layers of graphene in combination with template removal and handling optimizations was developed in order to ensure the fabrication of freestanding monolithic stochastic foams across varying relative densities. Subsequent mechanical characterization found that these stochastic foams behaved as bending-dominated cellular materials with large knockdowns in both elastic modulus and yield strength arising from waviness in the strut walls. This waviness, which emerges from inheritance of the polycrystalline template texture and relaxation after template removal, was found to increase the axial compliance of each cell wall through nanoscale wall shearing. Thus, the mechanical properties of the graphitic foams become dependent on the interlayer shear modulus and strength of graphitic layers, which are significantly less than their in-plane properties.

In the second part of this thesis, a nanoindentation study across multiple film thicknesses was used to compare solid nickel gyroid lattices to the CVD-fabricated hollow graphene gyroid lattices. Nanoscale gyroidal templates were used to examine the effects of using a stretching-dominated cell morphology, which possess enhanced load bearing and stress transfer behaviour, and to investigate if the nanoscale wall shearing mechanisms observed in the Chapter 4 were active in these nanoscale lattices. Further, a hierarchical FEA approach was utilized to numerically analyse the effective mechanical properties of both the solid and hollow gyroid unit cell, as well as a homogenized lattice in a nanoindentation simulation. These structured gyroids were found to experience size-dependent strengthening, with both the solid and hollow gyroid lattice possessing high strength to density ratios. Furthermore, the hollow graphene gyroid lattice was found to have a high degree of elastic recovery after indentation and high levels of electrical conductivity. However, the effect of waviness and nanoscale interlayer shearing was still found to cause a reduction in the modelled material properties of the multilayer graphene cell wells, which were far below their theoretical in-plane values.

A third study investigated the preparation of alternative microscale templates in the form of carbonized microfoams. These cellular materials were produced through the slow pyrolysis of commerically available melamine foams and 3D printed resin lattices produced through additive manufacturing. It was found that the 3D structure of such foams could be retained through carbonization, which induced isotropic shrinkage of up to 125x and mass loss of up to 95%. Addition of thin conformal films of alumina induced lower degrees of shrinkage and introduced surface roughness due to a stress mismatch between the shrinking polymer and the ALD coating. Furthermore, efficient graphitization of the carbonized materials was achieved through catalytic graphitization, after the electroless deposition of a nickel layer. Such shrunken graphitic microfoams possessed unit cell and strut sizes that were below the lower limit available to commercial 3D printing techniques. The multifaceted approach hence allows for the facile production of conductive carbon cellular materials with full shape control, while still possessing sub-mm unit cells and tuneable size and roughness.

A final study examined a deconstructed MOCVD process with a sequential exposure pattern in order to develop a step resolved understanding of the growth of WS_2 on Au foil. The Au substrate was found to have a strong influence on both DMS breakdown and WS_2 film formation due to the strong interaction between Au and sulfur. Use of Au was found to catalyse the breakdown of DMS, allowing for a large reduction in the pressure required to form WS_2. In turn, this significantly reduced carbon contamination from precursor breakdown, allowing for the production of high quality WS_2 films. As-grown WS_2 films were also found to interact strongly with the underlying Au substrate, resisting electrochemical delamination and displaying grain dependent orientation, leading to self-limiting film formation through the suppression of further precursor intercalation. Furthermore, the entire process can be achieved with a single exposure cycle lasting just 10 minutes. Hence, the error-tolerant and economical production of high-quality monolayers of WS_2 was demonstrated.

Fundamentally, the preparation of cellular materials from emergent 2D materials aims to combine the unique functional properties of both systems. Future preparation of porous WS_2 foams may enable the preparation of high yield hydrogen evolution systems with greater accessible surface area and a stress-tolerant cellular geometry. However, a large knockdown in continuum elastic moduli and yield strengths due to nanoscale interlayer wall shearing is shown to persist in both bending-dominated macroscopic foams and stretching-dominated nanoscale lattices. This deformation mechanism is dependent on the strength of interlayer interactions as well as the existence and degree of waviness present in the cell walls. In cases where density is inconsequential, ALD scaffolds (such as used in Chapter 4) or internal supporting structures (such as is present in Chapter 6) can serve to stiffen and strengthen such functional carbon foams. Else, the optimization of interlayer shear moduli and strength through interface engineering or use of heterostructures with stronger interlayer interactions may give rise to more resilient cellular materials with cell walls composed of emergent 2D materials.

Alternatively, the successful growth and isolation of a monolayered cellular material may entirely eliminate the knockdown due to interlayer shear and realize the exemplary mechanical properties that have been predicted by simulation. For few-layer samples, use of a structured nanoscale template is necessary to avoid collapse due to capillary or electrostatic forces, and to take advantage of the efficiencies of structural scaling present in regular stretching-dominated structures. However, with the CVD growth recipes used herein, it is shown that nanoscopic, highly curved templates possess high nucleation and hence defect density. The type of template used is intimately linked to the nature of both catalyst pre-treatment and process optimization, which here possess additional complexity due to the likelihood of thermal coarsening at high processing temperatures. Further avenues of study may therefore examine the template-specific optimization of CVD graphene growth in order to prepare 3D monoliths constructed from a single high-quality layer of 2D material.

Finally, alternative mechanical tests or avenues of analysis are likely to afford further insight into the mechanical behaviour these 3D cellular materials with cell walls comprised of 2D materials. A continuum damage mechanics or fracture mechanics based view may examine the initiation, propagation and fracture of these materials under uniaxial tension or cyclic loading schemes. Again, an approach examining multiple length scales would be ideal, linking the continuum material properties with strut and wall-level behaviour as they relate to fracture and tearing. This would also lend itself to an examination of the effect of initial defect density and quality of the graphitic layers.

BIBLIOGRAPHY

1. Abueidda, D. W., Elhebeary, M., Shiang, C.-S. (, Pang, S., Abu Al-Rub, R. K. & Jasiuk, I. M. Mechanical properties of 3D printed polymeric Gyroid cellular structures: Experimental and finite element study. *Materials & Design* **165,** 107597 (Mar. 2019).
2. Amani, H., Mostafavi, E., Arzaghi, H., Davaran, S., Akbarzadeh, A., Akhavan, O., Pazoki-Toroudi, H. & Webster, T. J. Three-Dimensional Graphene Foams: Synthesis, Properties, Biocompatibility, Biodegradability, and Applications in Tissue Engineering. *ACS Biomaterials Science and Engineering* **5,** 193–214 (2018).
3. Amini, N., Aguey-Zinsou, K. F. & Guo, Z. X. Processing of strong and highly conductive carbon foams as electrode. *Carbon* **49,** 3857–3864 (2011).
4. Andrews, E. W., Gibson, L. J. & Ashby, M. F. The creep of cellular solids. *Acta Materialia* **47,** 2853–2863 (1999).
5. Andrews, E., Sanders, W. & Gibson, L. J. Compressive and Tensile Behaviour of Aluminium Foams. *Materials Science and Engineering* **270,** 113–124 (1999).
6. Antunes, J. M., Fernandes, J. V. & Sakharova, N. A. On the determination of the Young ' s modulus of thin films using indentation tests. **44,** 8313–8334 (2007).
7. Aria, A. I., Kidambi, P. R., Weatherup, R. S., Xiao, L., Williams, J. A. & Hofmann, S. Time Evolution of the Wettability of Supported Graphene under Ambient Air Exposure. *The Journal of Physical Chemistry C* **120,** 2215–2224 (Feb. 2016).

8. Aria, A. I., **Nakanishi, K.**, Xiao, L., Braeuninger-Weimer, P., Sagade, A. A., Alexander-Webber, J. A. & Hofmann, S. Parameter Space of Atomic Layer Deposition of Ultrathin Oxides on Graphene. *ACS Applied Materials & Interfaces* **8,** 30564–30575 (Nov. 2016).
9. Arzt, E. Size effects in materials due to microstructural and dimensional constraints: a comparative review. *Acta Materialia* **46,** 5611–5626 (Oct. 1998).
10. Ashby, M. F. The properties of foams and lattices. *Philosophical transactions. Series A, Mathematical, physical, and engineering sciences* **364,** 15–30 (2006).
11. Ashby, M. F. *Materials Selection in Mechanical Design* 5th, 660. ISBN: 9780081005996 (Butterworth-Heinemann, 2016).
12. Ashby, M. F., Evans, A., Fleck, N. A., Gibson, L. J., Hutchinson, J. W. & Wadley, H. N. Metal foams: a design guide. *Materials & Design* **23,** 119 (2002).
13. Bailey, T. S., Pham, H. D. & Bates, F. S. Morphological behavior bridging the symmetric AB and ABC states in the poly(styrene-b-isoprene-b-ethylene oxide) triblock copolymer system. *Macromolecules* **34,** 6994–7008 (2001).
14. Barg, S., Perez, F. M., Ni, N., do Vale Pereira, P., Maher, R. C., Garcia-Tuñon, E., Eslava, S., Agnoli, S., Mattevi, C. & Saiz, E. Mesoscale assembly of chemically modified graphene into complex cellular networks. *Nature Communications* **5,** 4328 (July 2014).
15. Bates, F. S. & Fredrickson, G. H. Block copolymers-designer soft materials. *Physics Today* **52,** 32–38 (1999).
16. Bauer, J., Schroer, A., Schwaiger, R. & Kraft, O. Approaching theoretical strength in glassy carbon nanolattices. *Nature Materials* **15,** 438–443 (Feb. 2016).
17. Bauer, J., Meza, L. R., Schaedler, T. A., Schwaiger, R., Zheng, X. & Valdevit, L. Nanolattices: An Emerging Class of Mechanical Metamaterials. *Advanced Materials* **29,** 1–26 (2017).

18. Bažant, Z. P. Size effect on structural strength: a review. *Archive of Applied Mechanics (Ingenieur Archiv)* **69,** 703–725 (Nov. 1999).
19. Berkdemir, A., Gutiérrez, H. R., Botello-Méndez, A. R., Perea-López, N., Elías, A. L., Chia, C.-I. I., Wang, B., Crespi, V. H., López-Urías, F., Charlier, J.-C. C., Terrones, H. & Terrones, M. Identification of individual and few layers of WS2 using Raman Spectroscopy. *Scientific Reports* **3,** 1–8 (Dec. 2013).
20. Bhaviripudi, S., Jia, X., Dresselhaus, M. S. & Kong, J. Role of kinetic factors in chemical vapor deposition synthesis of uniform large area graphene using copper catalyst. *Nano Letters* **10,** 4128–4133 (2010).
21. Blakslee, O. L., Proctor, D. G., Seldin, E. J., Spence, G. B. & Weng, T. Elastic constants of compression-annealed pyrolytic graphite. *Journal of Applied Physics* **41,** 3373–3382 (1970).
22. Braeuninger-Weimer, P., Brennan, B., Pollard, A. J. & Hofmann, S. Understanding and Controlling Cu-Catalyzed Graphene Nucleation: The Role of Impurities, Roughness, and Oxygen Scavenging. *Chemistry of Materials* **28,** 8905–8915 (2016).
23. Brezny, R. & Green, D. J. Characterization of edge effects in cellular materials. *Journal of Materials Science* **25,** 4571–4578 (Nov. 1990).
24. Briggs, N., Subramanian, S., Lin, Y.-C., Eichfeld, S., Jariwala, B., Bhimanapati, G., Zhang, K. & Robinson, J. A. (Invited) Realizing 2D Materials Via MOCVD. *ECS Transactions* **75,** 725–731 (Sept. 2016).
25. Byun, S.-j., Lim, H., Shin, G.-y., Han, T.-h., Oh, S. H., Ahn, J.-h., Choi, H. C. & Lee, T.-W. Graphenes Converted from Polymers. *The Journal of Physical Chemistry Letters* **2,** 493–497 (Mar. 2011).
26. Cabrero-Vilatela, A., Weatherup, R. S., Braeuninger-Weimer, P., Caneva, S. & Hofmann, S. Towards a general growth model for graphene CVD on transition metal catalysts. en. *Nanoscale* **8,** 2149–2158 (Jan. 2016).
27. Cansizoglu, O., Harrysson, O., Cormier, D., West, H. & Mahale, T. Properties of Ti-6Al-4V non-stochastic lattice structures fabricated via electron beam melting. *Materials Science and Engineering A* **492,** 468–474 (Sept. 2008).

28. Cao, X., Shi, Y., Shi, W., Lu, G., Huang, X., Yan, Q., Zhang, Q. & Zhang, H. Preparation of Novel 3D Graphene Networks for Supercapacitor Applications. *Small* **7,** 3163–3168 (Nov. 2011).

29. Cebo, T., Aria, A. I., Dolan, J. A., Weatherup, R. S., **Nakanishi, K.**, Kidambi, P. R., Divitini, G., Ducati, C., Steiner, U. & Hofmann, S. Chemical vapour deposition of freestanding sub-60 nm graphene gyroids. *Applied Physics Letters* **111** (2017).

30. Chabi, S., Peng, C., Yang, Z., Xia, Y. & Zhu, Y. Three dimensional (3D) flexible graphene foam/polypyrrole composite: towards highly efficient supercapacitors. *RSC Adv.* **5,** 3999–4008 (2015).

31. Chen, C., Lu, T. J. & Fleck, N. A. Effect of imperfections on the yielding of two-dimensional foams. *Journal of the Mechanics and Physics of Solids* **47,** 2235–2272 (Sept. 1999).

32. Chen, J., Li, S. L., Gao, F. & Tao, Z. L. Synthesis and characterization of WS2 nanotubes. *Chemistry of Materials* **15,** 1012–1019 (2003).

33. Chen, M., Tao, T., Zhang, L., Gao, W. & Li, C. Highly conductive and stretchable polymer composites based on graphene/MWCNT network. *Chemical communications (Cambridge, England)* **49,** 1612–4 (2013).

34. Chen, S., He, G., Hu, H., Jin, S., Zhou, Y., He, Y., He, S., Zhao, F. & Hou, H. Elastic carbon foam via direct carbonization of polymer foam for flexible electrodes and organic chemical absorption. *Energy & Environmental Science* **6,** 2435 (2013).

35. Chen, Z. Y., Zhao, J. P., Yano, T., Ooie, T., Yoneda, M. & Sakakibara, J. Observation of sp3 bonding in tetrahedral amorphous carbon using visible Raman spectroscopy. *Journal of Applied Physics* **88,** 2305 (Sept. 2000).

36. Chen, Z., Ren, W., Gao, L., Liu, B., Pei, S. & Cheng, H.-M. Three-dimensional flexible and conductive interconnected graphene networks grown by chemical vapour deposition. *Nature Materials* **10,** 424–428 (June 2011).

37. Chen, Z., Xu, C., Ma, C., Ren, W. & Cheng, H. M. Lightweight and flexible graphene foam composites for high-performance electromagnetic interference shielding. *Advanced Materials* **25,** 1296–1300 (2013).

38. Cheng, C. F., Hsueh, H. Y., Lai, C. H., Pan, C. J., Hwang, B. J., Hu, C. C. & Ho, R. M. Nanoporous gyroid platinum with high catalytic activity from block copolymer templates via electroless plating. *NPG Asia Materials* **7,** e170–8 (2015).

39. Cheng, Y. T. & Cheng, C. M. Scaling relationships in conical indentation in elastic-plastic solids with work-hardening. *Materials Research Society Symposium - Proceedings* **522,** 139–144 (1998).

40. Cheng, Y.-T. & Cheng, C.-M. Relationships between hardness, elastic modulus, and the work of indentation. *Applied Physics Letters* **73,** 614–616 (Aug. 1998).

41. Chhowalla, M., Shin, H. S., Eda, G., Li, L.-J., Loh, K. P. & Zhang, H. The chemistry of two-dimensional layered transition metal dichalcogenide nanosheets. *Nature Chemistry* **5,** 263–275 (Apr. 2013).

42. Choi, B. G., Yang, M., Hong, W. H., Choi, J. W. & Huh, Y. S. 3D macroporous graphene frameworks for supercapacitors with high energy and power densities. *ACS Nano* **6,** 4020–4028 (2012).

43. Choi, S. H., Stephen, B., Park, J.-H., Lee, J. S., Kim, S. M., Yang, W. & Kim, K. K. Water-Assisted Synthesis of Molybdenum Disulfide Film with Single Organic Liquid Precursor. *Scientific Reports* **7,** 1983 (Dec. 2017).

44. Chou, S.-L., Wang, J.-Z., Chew, S.-Y., Liu, H.-K. & Dou, S.-X. Electrodeposition of MnO2 nanowires on carbon nanotube paper as freestanding, flexible electrode for supercapacitors. *Electrochemistry Communications* **10,** 1724–1727 (Nov. 2008).

45. Choudhury, T. H., Simchi, H., Boichot, R., Chubarov, M., Mohney, S. E. & Redwing, J. M. Chalcogen Precursor Effect on Cold-Wall Gas-Source Chemical Vapor Deposition Growth of WS2. *Crystal Growth and Design* **18,** 4357–4364 (2018).

46. Chow, P. K., Singh, E., Viana, B. C., Gao, J., Luo, J., Li, J., Lin, Z., Elías, A. L., Shi, Y., Wang, Z., Terrones, M. & Koratkar, N. Wetting of Mono and Few-Layered WS2 and MoS2 Films Supported on Si/SiO2 Substrates. *ACS Nano* **9,** 3023–3031 (Mar. 2015).

47. Chung, J. W., Dai, Z. R. & Ohuchi, F. S. WS2 thin films by metal organic chemical vapor deposition. *Journal of Crystal Growth* **186,** 137–150 (1998).

48. Colombo, P. Mechanical properties of silicon oxycarbide ceramic foams. *Journal of the American Ceramic Society* **51,** 2245–2251 (2001).

49. Crossland, E. J., Kamperman, M., Nedelcu, M., Ducati, C., Wiesner, U., Smilgies, D. M., Toombes, G. E., Hillmyer, M. A., Ludwigs, S., Steiner, U. & Snaith, H. J. A bicontinuous double gyroid hybrid solar cell. *Nano Letters* **9,** 2807–2812 (2009).

50. Cwik, S., Mitoraj, D., Mendoza Reyes, O., Rogalla, D., Peeters, D., Kim, J., Schütz, H. M., Bock, C., Beranek, R. & Devi, A. Direct Growth of MoS2 and WS2 Layers by Metal Organic Chemical Vapor Deposition. *Advanced Materials Interfaces* **5,** 1800140 (Aug. 2018).

51. D'Abaco, G. M., Mattei, C., Nasr, B., Hudson, E. J., Alshawaf, A. J., Chana, G., Everall, I. P., Nayagam, B., Dottori, M. & Skafidas, E. Graphene foam as a biocompatible scaffold for culturing human neurons. *Royal Society Open Science* **5** (2018).

52. Dalton, A. B., Collins, S., Muñoz, E., Razal, J. M., Ebron, V. H., Ferraris, J. P., Coleman, J. N., Kim, B. G. & Baughman, R. H. Super-tough carbon-nanotube fibres. *Nature* **423,** 703 (2003).

53. Dao, M., Chollacoop, N., Van Vliet, K. J., Venkatesh, T. A. & Suresh, S. Computational modeling of the forward and reverse problems in instrumented sharp indentation. *Acta Materialia* **49,** 3899–3918 (2001).

54. Dathbun, A. & Chaisitsak, S. *Effects of three parameters on graphene synthesis by chemical vapor deposition* in *The 8th Annual IEEE International Conference on Nano/Micro Engineered and Molecular Systems* (IEEE, Apr. 2013), 1018–1021. ISBN: 978-1-4673-6352-5.

55. Deshpande, V., Ashby, M. & Fleck, N. Foam topology: bending versus stretching dominated architectures. *Acta Materialia* **49,** 1035–1040 (Apr. 2001).

56. Deshpande, V. & Fleck, N. Isotropic constitutive models for metallic foams. *Journal of the Mechanics and Physics of Solids* **48,** 1253–1283 (June 2000).

57. Do Rosário, J. J., Lilleodden, E. T., Waleczek, M., Kubrin, R., Petrov, A. Y., Dyachenko, P. N., Sabisch, J. E., Nielsch, K., Huber, N., Eich, M. & Schneider, G. A. Self-Assembled Ultra High Strength, Ultra Stiff Mechanical Metamaterials Based on Inverse Opals. *Advanced Engineering Materials* **17,** 1420–1424 (2015).

58. Dolan, J. A., Saba, M., Dehmel, R., Gunkel, I., Gu, Y., Wiesner, U., Hess, O., Wilkinson, T. D., Baumberg, J. J., Steiner, U. & Wilts, B. D. Gyroid Optical Metamaterials: Calculating the Effective Permittivity of Multidomain Samples. *ACS Photonics* **3,** 1888–1896 (2016).

59. Dong, X., Wang, J., Wang, J., Chan-Park, M. B., Li, X., Wang, L., Huang, W. & Chen, P. Supercapacitor electrode based on three-dimensional graphene-polyaniline hybrid. *Materials Chemistry and Physics* **134,** 576–580 (2012).

60. Dong, X., Wang, X., Wang, L., Song, H., Zhang, H., Huang, W. & Chen, P. 3D graphene foam as a monolithic and macroporous carbon electrode for electrochemical sensing. *ACS Applied Materials and Interfaces* **4,** 3129–3133 (2012).

61. Dresselhaus, M. S., Chen, G., Tang, M. Y., Yang, R., Lee, H., Wang, D., Ren, Z., Fleurial, J. P. & Gogna, P. New directions for low-dimensional thermoelectric materials. *Advanced Materials* **19,** 1043–1053 (2007).

62. Du, X., Skachko, I., Barker, A. & Andrei, E. Y. Approaching ballistic transport in suspended graphene. *Nature Nanotechnology* **3,** 491–495 (Aug. 2008).

63. Falin, A., Cai, Q., Santos, E. J., Scullion, D., Qian, D., Zhang, R., Yang, Z., Huang, S., Watanabe, K., Taniguchi, T., Barnett, M. R., Chen, Y., Ruoff, R. S. & Li, L. H. Mechanical properties of atomically thin boron

nitride and the role of interlayer interactions. *Nature Communications* **8,** 1–9 (2017).

64. Fan, H. L. & Fang, D. N. Enhancement of mechanical properties of hollow-strut foams: Analysis. *Materials and Design* **30,** 1659–1666 (2009).

65. Fan, Y., Robertson, A. W., Zhou, Y., Chen, Q., Zhang, X., Browning, N. D., Zheng, H., Rümmeli, M. H. & Warner, J. H. Electrical Breakdown of Suspended Mono- and Few-Layer Tungsten Disulfide via Sulfur Depletion Identified by in Situ Atomic Imaging. *ACS Nano* **11,** 9435–9444 (Sept. 2017).

66. Feng, X.-Q., Xia, R., Li, X. & Li, B. Surface effects on the elastic modulus of nanoporous materials. *Applied Physics Letters* **94,** 011916 (Jan. 2009).

67. Ferrari, A. & Robertson, J. Interpretation of Raman spectra of disordered and amorphous carbon. *Physical Review B* **61,** 14095–14107 (2000).

68. Filippov, A. E., Dienwiebel, M., Frenken, J. W., Klafter, J. & Urbakh, M. Torque and twist against superlubricity. *Physical Review Letters* **100** (2008).

69. Fischer-Cripps, A. C. *Nanoindentation* ISBN: 978-1-4899-0515-4 (Springer New York, New York, NY, 2002).

70. Frank, I. W., Tanenbaum, D. M., van der Zande, A. M. & McEuen, P. L. Mechanical properties of suspended graphene sheets. *Journal of Vacuum Science & Technology B: Microelectronics and Nanometer Structures* **25,** 2558 (2007).

71. Fu, L., Fu, L., Sun, Y., Wu, N., Mendes, R. G., Chen, L., Xu, Z., Zhang, T., Rümmeli, M. H., Rellinghaus, B., Pohl, D. & Zhuang, L. Direct Growth of MoS2/h-BN Heterostructures via a Sulfide-Resistant Alloy. *ACS Nano* **10,** 2063–2070 (Feb. 2016).

72. Gao, Q., Jiang, H., Li, M., Lu, P., Lai, X., Li, X., Liu, Y., Song, C. & Han, G. Improved mechanical properties of SnO2:F thin film by structural modification. *Ceramics International* **40,** 2557–2564 (Mar. 2014).

73. Gao, Y., Liu, Z., Sun, D. M., Huang, L., Ma, L. P., Yin, L. C., Ma, T., Zhang, Z., Ma, X. L., Peng, L. M., Cheng, H. M. & Ren, W. Large-area synthesis of high-quality and uniform monolayer WS2on reusable Au foils. *Nature Communications* **6,** 1–10 (2015).

74. Garlof, S., Mecklenburg, M., Smazna, D., Mishra, Y. K., Adelung, R., Schulte, K. & Fiedler, B. 3D carbon networks and their polymer composites: Fabrication and electromechanical investigations of neat Aerographite and Aerographite-based PNCs under compressive load. *Carbon* **111,** 103–112 (Jan. 2017).

75. Geim, a. K., Novoselov, K. S., Geim A. K. & Novoselov K. S. The rise of graphene. *Nat. Mater.,* 183–191 (2007).

76. Georgiou, T., Jalil, R., Belle, B. D., Britnell, L., Gorbachev, R. V., Morozov, S. V., Kim, Y.-j. J., Gholinia, A., Haigh, S. J., Makarovsky, O., Eaves, L., Ponomarenko, L. A., Geim, A. K., Novoselov, K. S. & Mishchenko, A. Vertical field-effect transistor based on graphene-WS2 heterostructures for flexible and transparent electronics. *Nature Nanotechnology* **8,** 100–103 (2013).

77. Gibson, L. J. & Ashby, M. F. The Mechanics of Three-Dimensional Cellular Materials. *Proceedings of the Royal Society A: Mathematical, Physical and Engineering Sciences* **382,** 43–59 (July 1982).

78. Gibson, L. J. & Ashby, M. F. *Cellular Solids: Structure and Properties* ISBN: 131602542X (Cambridge University Press, 1997).

79. Gómez-Navarro, C., Burghard, M. & Kern, K. Elastic Properties of Chemically Derived Single Graphene Sheets. *Nano Letters* **8,** 2045–2049 (July 2008).

80. Gordon, R., Hausmann, D., Kim, E. & Shepard, J. A Kinetic Model for Step Coverage by Atomic Layer Deposition in Narrow Holes or Trenches. *Chemical Vapor Deposition* **9,** 73–78 (Mar. 2003).

81. Gouldstone, A., Chollacoop, N., Dao, M., Li, J., Minor, A. & Shen, Y. Indentation across size scales and disciplines: Recent developments in experimentation and modeling. *Acta Materialia* **55,** 4015–4039 (July 2007).

82. Grønborg, S. S., Ulstrup, S., Bianchi, M., Dendzik, M., Sanders, C. E., Lauritsen, J. V., Hofmann, P. & Miwa, J. A. Synthesis of Epitaxial Single-Layer MoS 2 on Au(111). *Langmuir* **31,** 9700–9706 (Sept. 2015).

83. Gutiérrez, H. R., Perea-López, N., Elías, A. L., Berkdemir, A., Wang, B., Lv, R., López-Urías, F., Crespi, V. H., Terrones, H. & Terrones, M. Extraordinary room-temperature photoluminescence in triangular WS2 monolayers. *Nano Letters* **13,** 3447–3454 (2013).

84. Hagiwara, H. & Green, D. J. Elastic Behavior of Open-Cell Alumina. *Journal of the American Ceramic Society* **70,** 811–815 (1987).

85. Hakamada, M. & Mabuchi, M. Mechanical strength of nanoporous gold fabricated by dealloying. *Scripta Materialia* **56,** 1003–1006 (June 2007).

86. Hao, W., Marichy, C. & Journet, C. Atomic layer deposition of stable 2D materials. *2D Materials* **6** (2019).

87. He, X. Q., Kitipornchai, S. & Liew, K. M. Buckling analysis of multi-walled carbon nanotubes: A continuum model accounting for van der Waals interaction. *Journal of the Mechanics and Physics of Solids* **53,** 303–326 (2005).

88. Hodge, A. M., Biener, J., Hayes, J. R., Bythrow, P. M., Volkert, C. A. & Hamza, A. V. Scaling equation for yield strength of nanoporous open-cell foams. *Acta Materialia* **55,** 1343–1349 (2007).

89. Hofmann, S. *et al.* In situ Observations of Catalyst Dynamics during Surface-Bound Carbon Nanotube Nucleation. *Nano Letters* **7,** 602–608 (Mar. 2007).

90. Holt, C. M., Murphy, S., Gray, M. R. & Mitlin, D. Electrocatalytic hydrogenation of 2-cyclohexen-1-one in a high sulfur environment using a carbon-supported nanostructured tungsten sulfide catalyst. *Catalysis Communications* **12,** 314–317 (2010).

91. Hsieh, M.-T., Endo, B., Zhang, Y., Bauer, J. & Valdevit, L. The mechanical response of cellular materials with spinodal topologies. *Journal of the Mechanics and Physics of Solids* **125,** 401–419 (Apr. 2019).

92. Hsueh, H. Y., Huang, Y. C., Ho, R. M., Lai, C. H., Makida, T. & Hasegawa, H. Nanoporous gyroid nickel from block copolymer templates via electroless plating. *Advanced Materials* **23,** 3041–3046 (2011).
93. Hsueh, H.-Y. & Ho, R.-M. Bicontinuous ceramics with high surface area from block copolymer templates. *Langmuir : the ACS journal of surfaces and colloids* **28,** 8518–29 (2012).
94. Ishigami, M., Chen, J. H., Cullen, W. G., Fuhrer, M. S. & Williams, E. D. Atomic Structure of Graphene on SiO 2. *Nano Letters* **7,** 1643–1648 (June 2007).
95. Ito, Y., Tanabe, Y., Qiu, H. J., Sugawara, K., Heguri, S., Tu, N. H., Huynh, K. K., Fujita, T., Takahashi, T., Tanigaki, K. & Chen, M. High-quality three-dimensional nanoporous graphene. *Angewandte Chemie - International Edition* **53,** 4822–4826 (2014).
96. Jang, D., Meza, L. R., Greer, F. & Greer, J. R. Fabrication and deformation of three-dimensional hollow ceramic nanostructures. *Nature Materials* **12,** 893–898 (Oct. 2013).
97. Jeong, H. Y., Jin, Y., Yun, S. J., Zhao, J., Baik, J., Keum, D. H., Lee, H. S. & Lee, Y. H. Heterogeneous Defect Domains in Single-Crystalline Hexagonal WS2. *Advanced Materials* **29,** 1–6 (2017).
98. Ji, H., Zhang, L., Pettes, M. T., Li, H., Chen, S., Shi, L., Piner, R. & Ruoff, R. S. Ultrathin Graphite Foam: A Three-Dimensional Conductive Network for Battery Electrodes. *Nano Letters* **12,** 2446–2451 (May 2012).
99. Ji, Q., Zhang, Y., Gao, T., Zhang, Y., Ma, D., Liu, M., Chen, Y., Qiao, X., Tan, P. H., Kan, M., Feng, J., Sun, Q. & Liu, Z. Epitaxial monolayer MoS2 on mica with novel photoluminescence. *Nano Letters* **13,** 3870–3877 (Aug. 2013).
100. Jia, J., Sun, X., Lin, X., Shen, X., Mai, Y.-w. & Kim, J.-k. Exceptional Electrical Conductivity and Fracture Resistance of 3D Interconnected Graphene Foam/Epoxy Composites. *ACS Nano* **8,** 5774–5783 (June 2014).

101. Jiang, W., Xin, H. & Li, W. Microcellular 3D graphene foam via chemical vapor deposition of electroless plated nickel foam templates. *Materials Letters* **162,** 105–109 (2016).

102. Jiang, W. G., Su, J. J. & Feng, X. Q. Effect of surface roughness on nanoindentation test of thin films. *Engineering Fracture Mechanics* **75,** 4965–4972 (2008).

103. Johansson, A. S., Lu, J. & Carlsson, J. O. TEM investigation of CVD graphite on nickel. *Thin Solid Films* **252,** 19–25 (1994).

104. Jung, G. S. & Buehler, M. J. Multiscale Mechanics of Triply Periodic Minimal Surfaces of Three-Dimensional Graphene Foams. *Nano Letters* **18,** 4845–4853 (2018).

105. Jurkiewicz, K., Pawlyta, M., Zygadło, D., Chrobak, D., Duber, S., Wrzalik, R., Ratuszna, A. & Burian, A. Evolution of glassy carbon under heat treatment: Correlation structureâmechanical properties. *Journal of Materials Science* **53,** 3509–3523 (2018).

106. Kang, K., Xie, S., Huang, L., Han, Y., Huang, P. Y., Mak, K. F., Kim, C.-J. J., Muller, D. & Park, J. High-mobility three-atom-thick semiconducting films with wafer-scale homogeneity. *Nature* **520,** 656–660 (Apr. 2015).

107. Kashani, H., Ito, Y., Han, J., Liu, P. & Chen, M. Extraordinary tensile strength and ductility of scalable nanoporous graphene. *Science Advances* **5** (Feb. 2019).

108. Al-Ketan, O., Rezgui, R., Rowshan, R., Du, H., Fang, N. X. & Abu Al-Rub, R. K. Microarchitected Stretching-Dominated Mechanical Metamaterials with Minimal Surface Topologies. *Advanced Engineering Materials* **20** (Sept. 2018).

109. Al-Ketan, O., Rowshan, R. & Abu Al-Rub, R. K. Topology-mechanical property relationship of 3D printed strut, skeletal, and sheet based periodic metallic cellular materials. *Additive Manufacturing* **19,** 167–183 (2018).

110. Khaderi, S. N., Scherer, M. R. J., Hall, C. E., Steiner, U., Ramamurty, U., Fleck, N. A. & Deshpande, V. S. The indentation response of Nickel nano double gyroid lattices. *Extreme Mechanics Letters* **10,** 15–23 (2017).

111. Khaderi, S., Deshpande, V. & Fleck, N. The stiffness and strength of the gyroid lattice. *International Journal of Solids and Structures* **51,** 3866–3877 (Nov. 2014).

112. Kidambi, P. R., Ducati, C., Dlubak, B., Gardiner, D., Weatherup, R. S., Martin, M.-B., Seneor, P., Coles, H. & Hofmann, S. The Parameter Space of Graphene Chemical Vapor Deposition on Polycrystalline Cu. *The Journal of Physical Chemistry C* **116,** 22492–22501 (Oct. 2012).

113. Kiraly, B., Liu, X., Wang, L., Zhang, Z., Mannix, A. J., Fisher, B. L., Yakobson, B. I., Hersam, M. C. & Guisinger, N. P. Borophene Synthesis on Au(111). *ACS Nano* **13,** 3816–3822 (2019).

114. Koma, A., Sunouchi, K. & Miyajima, T. Fabrication and characterization of heterostructures with subnanometer thickness. *Microelectronic Engineering* **2,** 129–136 (Oct. 1984).

115. Koshelev, C. N., Mashkina, A. V. & Kalinina, N. G. Decomposition of dimethyl sulfide in the presence of Al2O3, and catalyst deactivation. *Reaction Kinetics and Catalysis Letters* **39,** 367–372 (Sept. 1989).

116. Kraft, O., Gruber, P. A., Mönig, R. & Weygand, D. Plasticity in Confined Dimensions. *Annual Review of Materials Research* **40,** 293–317 (2010).

117. Kumar, R., Dhakate, S. R., Gupta, T., Saini, P., Singh, B. P. & Mathur, R. B. Effective improvement of the properties of light weight carbon foam by decoration with multi-wall carbon nanotubes. *Journal of Materials Chemistry A* **1,** 5727–5735 (2013).

118. Kvetková, L., Duszová, A., Hvizdoš, P., Dusza, J., Kun, P., Balázsi, C. & Kvetkova, L. Fracture toughness and toughening mechanisms in graphene platelet reinforced Si3N4 composites. *Scripta Materialia* **66,** 793–796 (May 2012).

119. Kwak, M. J., Ramadoss, A., Yoon, K. Y., Park, J., Thiyagarajan, P. & Jang, J. H. Single-Step Synthesis of N-Doped Three-Dimensional Graphitic Foams for High-Performance Supercapacitors. *ACS Sustainable Chemistry and Engineering* **5,** 6950–6957 (2017).

120. Lambert, C. A., Radzilowski, L. H., Thomas, E. L., Surfaces, C., Sep, S., Lambert, B. C. A. & Radzilowski, L. H. Triply periodic level surfaces as models for cubic tricontinuous block copolymer morphologies. *Philosophical Transactions of the Royal Society of London. Series A: Mathematical, Physical and Engineering Sciences* **354,** 2009–2023 (Sept. 1996).

121. Lee, C., Wei, X., Kysar, J. W. & Hone, J. Measurement of the Elastic Properties and Intrinsic Strength of Monolayer Graphene. *Science* **321,** 385–388 (July 2008).

122. Lee, G.-H., Cooper, R. C., An, S. J., Lee, S., van der Zande, A., Petrone, N., Hammerberg, A. G., Lee, C., Crawford, B., Oliver, W., Kysar, J. W. & Hone, J. High-strength chemical-vapor-deposited graphene and grain boundaries. *Science* **340,** 1073–6 (May 2013).

123. Lee, J.-S., Ahn, H.-J., Yoon, J.-C. & Jang, J.-H. Three-dimensional nanofoam of few-layer graphene grown by CVD for DSSC. *Physical Chemistry Chemical Physics* **14,** 7938 (2012).

124. Lenski, D. R. & Fuhrer, M. S. Raman and optical characterization of multilayer turbostratic graphene grown via chemical vapor deposition. *Journal of Applied Physics* **110,** 013720 (July 2011).

125. Li, H., Li, Y., Aljarb, A., Shi, Y. & Li, L. J. Epitaxial Growth of Two-Dimensional Layered Transition-Metal Dichalcogenides: Growth Mechanism, Controllability, and Scalability. *Chemical Reviews* **118,** 6134–6150 (2018).

126. Li, J., Zhao, S., Zhang, G., Gao, Y., Deng, L., Sun, R. & Wong, C.-P. A facile method to prepare highly compressible three-dimensional graphene-only sponge. *Journal of Materials Chemistry A* **3,** 15482–15488 (2015).

127. Li, L., Wang, K., Huang, Z., Zhang, C. & Liu, T. Highly ordered graphene architectures by duplicating melamine sponges as a three-dimensional deformation-tolerant electrode. *Nano Research* **9,** 2938–2949 (Oct. 2016).

128. Li, N., Chen, Z., Ren, W., Li, F. & Cheng, H. M. Flexible graphene-based lithium ion batteries with ultrafast charge and discharge rates. *Proceedings of the National Academy of Sciences of the United States of America* **109,** 17360–17365 (2012).

129. Li, Q. M., Magkiriadis, I. & Harrigan, J. J. Compressive Strain at the Onset of Densification of Cellular Solids. *Journal of Cellular Plastics* **42,** 371–392 (2006).

130. Li, X. L., Ge, J. P. & Li, Y. D. Atmospheric pressure chemical vapor deposition: An alternative route to large-scale MoS2 and WS2 inorganic fullerene-like nanostructures and nanoflowers. *Chemistry - A European Journal* **10,** 6163–6171 (2004).

131. Liao, S., Zhai, T. & Xia, H. Highly adsorptive graphene aerogel microspheres with center-diverging microchannel structures. *Journal of Materials Chemistry A* **4,** 1068–1077 (2016).

132. Lieth, R. *Preparation and Crystal Growth of Materials with Layered Structures* (ed Lieth, R. M. A.) ISBN: 978-90-481-8344-9 (Springer Netherlands, Dordrecht, 1977).

133. Ligon, S. C., Liska, R., Stampfl, J., Gurr, M. & Mülhaupt, R. Polymers for 3D Printing and Customized Additive Manufacturing. *Chemical Reviews* **117,** 10212–10290 (2017).

134. Lim, Y., Heo, J.-I., Madou, M. & Shin, H. Monolithic carbon structures including suspended single nanowires and nanomeshes as a sensor platform. *Nanoscale research letters* **8,** 492 (2013).

135. Liu, K., Chen, Y.-M. M., Policastro, G. M., Becker, M. L. & Zhu, Y. Three-Dimensional Bicontinuous Graphene Monolith from Polymer Templates. *ACS Nano* **9,** 6041–6049 (June 2015).

136. Liu, P., Luo, T., Xing, J., Xu, H., Hao, H., Liu, H. & Dong, J. Large-Area WS2 Film with Big Single Domains Grown by Chemical Vapor Deposition. *Nanoscale Research Letters* **12,** 558 (Dec. 2017).

137. Liu, X., Qi, X., Zhang, Z., Ren, L., Hao, G., Liu, Y., Wang, Y., Huang, K., Wei, X., Li, J., Huang, Z. & Zhong, J. Electrochemically reduced graphene oxide with porous structure as a binder-free electrode for high-rate supercapacitors. *RSC Advances* **4,** 13673 (2014).

138. Liu, Y., Xu, Z. & Zheng, Q. The interlayer shear effect on graphene multilayer resonators. *Journal of the Mechanics and Physics of Solids* **59,** 1613–1622 (2011).

139. Liu, Z., Yang, J., Grey, F., Liu, J. Z., Liu, Y., Wang, Y., Yang, Y., Cheng, Y. & Zheng, Q. Observation of microscale superlubricity in graphite. *Physical Review Letters* **108** (2012).

140. Liu, Z., Zhang, S.-M., Yang, J.-R., Liu, J. Z., Yang, Y.-L. & Zheng, Q.-S. Interlayer shear strength of single crystalline graphite. *Acta Mechanica Sinica* **28,** 978–982 (Aug. 2012).

141. Luan, V. H., Tien, H. N., Hoa, L. T., Hien, N. T. M., Oh, E.-S., Chung, J., Kim, E. J., Choi, W. M., Kong, B.-S. & Hur, S. H. Synthesis of a highly conductive and large surface area graphene oxide hydrogel and its use in a supercapacitor. *J. Mater. Chem. A* **1,** 208–211 (2013).

142. Lührs, L., Soyarslan, C., Markmann, J., Bargmann, S. & Weissmüller, J. Elastic and plastic Poisson's ratios of nanoporous gold. *Scripta Materialia* **110,** 65–69 (Jan. 2016).

143. Luo, J. K., Flewitt, A. J., Spearing, S. M., Fleck, N. A. & Milne, W. I. Young's modulus of electroplated Ni thin film for MEMS applications. *Materials Letters* **58,** 2306–2309 (2004).

144. Luo, Y.-R. *Comprehensive Handbook of Chemical Bond Energies* ISBN: 9780429128684 (CRC Press, Mar. 2007).

145. Luthin, J. & Linsmeier, C. Carbon films and carbide formation on tungsten. *Surface Science* **454,** 78–82 (2000).

146. Ma, Q., Yang, L., Jiang, Z., Song, Q., Xiao, M., Zhang, D., Ma, X., Wen, T. & Cheng, G. Three-Dimensional Stiff Graphene Scaffold on Neural Stem Cells Behavior. *ACS Applied Materials and Interfaces* **8,** 34227–34233 (2016).

147. Ma, Q., Yang, L., Jiang, Z., Song, Q., Xiao, M., Zhang, D., Ma, X., Wen, T. & Cheng, G. Three-Dimensional Stiff Graphene Scaffold on Neural Stem Cells Behavior. *ACS Applied Materials and Interfaces* **8,** 34227–34233 (2016).

148. Ma, W. C., Huang, W. S., Ku, C. S. & Ho, R. M. Nanoporous gyroid metal oxides with controlled thickness and composition by atomic layer deposition from block copolymer templates. *Journal of Materials Chemistry C* **4,** 840–849 (2015).

149. Mak, K. F. & Shan, J. Photonics and optoelectronics of 2D semiconductor transition metal dichalcogenides. *Nature Photonics* **10,** 216–226 (Apr. 2016).

150. Margolin, A., Deepak, F. L., Popovitz-Biro, R., Bar-Sadan, M., Feldman, Y. & Tenne, R. Fullerene-like WS2 nanoparticles and nanotubes by the vapor-phase synthesis of WCln and H2S. *Nanotechnology* **19** (2008).

151. Maskery, I., Sturm, L., Aremu, A., Panesar, A., Williams, C., Tuck, C., Wildman, R., Ashcroft, I. & Hague, R. Insights into the mechanical properties of several triply periodic minimal surface lattice structures made by polymer additive manufacturing. *Polymer* **152,** 62–71 (Sept. 2018).

152. Maury, F. Recent Trends in the Selection of Metal-Organic Precursors for MOCVD Process. *Le Journal de Physique IV* **05,** C5–449–C5–463 (June 1995).

153. McCreary, K. M., Hanbicki, A. T., Jernigan, G. G., Culbertson, J. C. & Jonker, B. T. Synthesis of Large-Area WS2 monolayers with Exceptional Photoluminescence. *Scientific Reports* **6,** 1–7 (2016).

154. Mecklenburg, M., Schuchardt, A., Mishra, Y. K., Kaps, S., Adelung, R., Lotnyk, A., Kienle, L. & Schulte, K. Aerographite: Ultra Lightweight,

Flexible Nanowall, Carbon Microtube Material with Outstanding Mechanical Performance. *Advanced Materials* **24,** 3486–3490 (July 2012).

155. Merki, D. & Hu, X. Recent developments of molybdenum and tungsten sulfides as hydrogen evolution catalysts. *Energy and Environmental Science* **4,** 3878–3888 (2011).
156. Meza, L. R., Das, S. & Greer, J. R. Strong, lightweight, and recoverable three-dimensional ceramic nanolattices. *Science* **345,** 1322–1326 (Sept. 2014).
157. Michailidis, N., Stergioudi, F., Omar, H., Papadopoulos, D. & Tsipas, D. N. Experimental and FEM analysis of the material response of porous metals imposed to mechanical loading. *Colloids and Surfaces A: Physicochemical and Engineering Aspects* **382,** 124–131 (2011).
158. Mieszala, M., Hasegawa, M., Guillonneau, G., Bauer, J., Raghavan, R., Frantz, C., Kraft, O., Mischler, S., Michler, J. & Philippe, L. Micromechanics of Amorphous Metal/Polymer Hybrid Structures with 3D Cellular Architectures: Size Effects, Buckling Behavior, and Energy Absorption Capability. *Small* **13,** 1–13 (2017).
159. Miller, D. C., Terrones, M. & Terrones, H. Mechanical properties of hypothetical graphene foams: Giant Schwarzites. *Carbon* **96,** 1191–1199 (2016).
160. Min, B. H., Kim, D. W., Kim, K. H., Choi, H. O., Jang, S. W. & Jung, H.-T. Bulk scale growth of CVD graphene on Ni nanowire foams for a highly dense and elastic 3D conducting electrode. *Carbon* **80,** 446–452 (Dec. 2014).
161. Min, L., Wei-min, C., Nai-gang, L. & Ling-Dong, W. A numerical study of indentation using indenters of different geometry. *Journal of Materials Research* **19,** 73–78 (Jan. 2004).
162. Mittal, G., Dhand, V., Rhee, K. Y., Park, S.-j., Lee, W. R., Yop, K., Park, S.-j. & Ro, W. A review on carbon nanotubes and graphene as fillers in reinforced polymer nanocomposites. *Journal of Industrial and Engineering Chemistry* **21,** 11–25 (Jan. 2015).

163. Molas, M. R., Nogajewski, K., Slobodeniuk, A. O., Binder, J., Bartos, M. & Potemski, M. The optical response of monolayer, few-layer and bulk tungsten disulfide. *Nanoscale* **9,** 13128–13141 (2017).

164. Molina-Sánchez, A. & Wirtz, L. Phonons in single-layer and few-layer MoS2 and WS2. *Physical Review B - Condensed Matter and Materials Physics* **84** (2011).

165. **Nakanishi, K.**, Aria, A. I., Berwind, M. F., Weatherup, R. S., Eberl, C., Hofmann, S. & Fleck, N. A. Compressive behavior and failure mechanisms of freestanding and composite 3D graphitic foams. *Acta Materialia* **159,** 187–196 (Oct. 2018).

166. Nautiyal, P., Boesl, B. & Agarwal, A. The mechanics of energy dissipation in a three-dimensional graphene foam with macroporous architecture. *Carbon* **132,** 59–64 (2018).

167. Nautiyal, P., Mujawar, M., Boesl, B. & Agarwal, A. In-situ mechanics of 3D graphene foam based ultra-stiff and flexible metallic metamaterial. *Carbon* **137,** 502–510 (Oct. 2018).

168. Nguyen, D., Taylor, D., Qian, K., Norouzi, N., Rasmussen, J., Botzet, S., Lehmann, M., Khine, M., Halverson, K. & Khine, M. Better shrinkage than Shrinky-Dinks. *Lab on a Chip* **10,** 1623–1626 (2010).

169. Nieto, A., Boesl, B. & Agarwal, A. Multi-scale intrinsic deformation mechanisms of 3D graphene foam. *Carbon* **85,** 299–308 (Apr. 2015).

170. Nieto, A., Dua, R., Zhang, C., Boesl, B., Ramaswamy, S. & Agarwal, A. Three Dimensional Graphene Foam/Polymer Hybrid as a High Strength Biocompatible Scaffold. *Advanced Functional Materials* **25,** 3916–3924 (July 2015).

171. Ning, G., Fan, Z., Wang, G., Gao, J., Qian, W. & Wei, F. Gram-scale synthesis of nanomesh graphene with high surface area and its application in supercapacitor electrodes. *Chemical Communications* **47,** 5976 (2011).

172. Niu, Z., Chen, J., Hng, H. H., Ma, J. & Chen, X. A leavening strategy to prepare reduced graphene oxide foams. *Advanced Materials* **24,** 4144–4150 (2012).

173. Nørskov, J. K., Bligaard, T., Logadottir, A., Bahn, S., Hansen, L. B., Bollinger, M., Bengaard, H., Hammer, B., Sljivancanin, Z., Mavrikakis, M., Xu, Y., Dahl, S. & Jacobsen, C. J. Universality in heterogeneous catalysis. *Journal of Catalysis* **209,** 275–278 (2002).

174. Novoselov, K. S. Electric Field Effect in Atomically Thin Carbon Films. *Science* **306,** 666–669 (Oct. 2004).

175. Obraztsov, A. N., Obraztsova, E. A., Tyurnina, A. V. & Zolotukhin, A. A. Chemical vapor deposition of thin graphite films of nanometer thickness. *Carbon* **45,** 2017–2021 (2007).

176. Oliver, W. & Pharr, G. An improved technique for determining hardness and elastic modulus using load and displacement sensing indentation experiments. *Journal of Materials Research* **7,** 1564–1583 (1992).

177. Omairey, S. L., Dunning, P. D. & Sriramula, S. Development of an ABAQUS plugin tool for periodic RVE homogenisation. *Engineering with Computers* **35,** 567–577 (Apr. 2019).

178. Owens, J. R., Daniels, C., Nicolaï, A., Terrones, H. & Meunier, V. Structural, energetic, and electronic properties of gyroidal graphene nanostructures. *Carbon* **96,** 998–1007 (2016).

179. Pan, D., Wang, C., Wang, T.-C. & Yao, Y. Graphene Foam: Uniaxial Tension Behavior and Fracture Mode Based on a Mesoscopic Model. *ACS Nano* **11,** 8988–8997 (Sept. 2017).

180. Paraknowitsch, J. P., Thomas, A. & Antonietti, M. A detailed view on the polycondensation of ionic liquid monomers towards nitrogen doped carbon materials. *Journal of Materials Chemistry* **20,** 6746–6758 (2010).

181. Park, C. & Nutt, S. R. Strain rate sensitivity and defects ina steel foam. *Materials Science and Engineering: A* **323,** 358–366 (Jan. 2002).

182. Park, H. J., Meyer, J., Roth, S. & Skákalová, V. Growth and properties of few-layer graphene prepared by chemical vapor deposition. *Carbon* **48,** 1088–1094 (Apr. 2010).

183. Park, J., Choudhary, N., Smith, J., Lee, G., Kim, M. & Choi, W. Thickness modulated MoS2 grown by chemical vapor deposition for transparent and flexible electronic devices. *Applied Physics Letters* **106,** 012104 (Jan. 2015).
184. Park, J., Lee, W., Choi, T., Hwang, S. H., Myoung, J. M., Jung, J. H., Kim, S. H. & Kim, H. Layer-modulated synthesis of uniform tungsten disulfide nanosheet using gas-phase precursors. *Nanoscale* **7,** 1308–1313 (2015).
185. Patera, L. L., Africh, C., Weatherup, R. S., Blume, R., Bhardwaj, S., Castellarin-Cudia, C., Knop-Gericke, A., Schloegl, R., Comelli, G., Hofmann, S. & Cepek, C. In situ observations of the atomistic mechanisms of Ni catalyzed low temperature graphene growth. *ACS Nano* **7,** 7901–7912 (2013).
186. Peimyoo, N., Shang, J., Cong, C., Shen, X., Wu, X., Yeow, E. K. & Yu, T. Nonblinking, intense two-dimensional light emitter: Monolayer WS2 Triangles. *ACS Nano* **7,** 10985–10994 (2013).
187. Pettes, M. T., Ji, H., Ruoff, R. S. & Shi, L. Thermal Transport in Three-Dimensional Foam Architectures of Few-Layer Graphene and Ultrathin Graphite. *Nano Letters* **12,** 2959–2964 (June 2012).
188. Pikul, J. H., Özerinç, S., Liu, B., Zhang, R., Braun, P. V., Deshpande, V. S. & King, W. P. High strength metallic wood from nanostructured nickel inverse opal materials. *Scientific Reports* **9,** 719 (Dec. 2019).
189. Pimenta, M. A., Dresselhaus, G., Dresselhaus, M. S., Cançado, L. G., Jorio, A. & Saito, R. Studying disorder in graphite-based systems by Raman spectroscopy. *Phys. Chem. Chem. Phys.* **9,** 1276–1290 (2007).
190. Ping, J., Fan, Z., Sindoro, M., Ying, Y. & Zhang, H. Recent Advances in Sensing Applications of Two-Dimensional Transition Metal Dichalcogenide Nanosheets and Their Composites. *Advanced Functional Materials* **27,** 1605817 (May 2017).
191. Pingle, S. M., Fleck, N. A., Deshpande, V. S. & Wadley, H. N. G. Collapse mechanism maps for a hollow pyramidal lattice. *Proceedings of the Royal*

Society A: Mathematical, Physical and Engineering Sciences **467,** 985–1011 (Apr. 2011).

192. Polsen, E. S., McNerny, D. Q., Viswanath, B., Pattinson, S. W. & John Hart, A. High-speed roll-to-roll manufacturing of graphene using a concentric tube CVD reactor. *Scientific Reports* **5,** 10257 (Sept. 2015).
193. Poncharal, P., Ayari, A., Michel, T. & Sauvajol, J.-L. Raman spectra of misoriented bilayer graphene. *Physical Review B* **78,** 113407 (Sept. 2008).
194. Poserin, V., Marcuson, S., Shu, J. & Wilkinson, D. S. CVD technique for Inco nickel foam production. *Advanced Engineering Materials* **6,** 454–459 (2004).
195. Predel, B. In *Ac-Au - Au-Zr* (ed Madelung, O.) 1–1 (Springer-Verlag, Berlin/Heidelberg, 2005). ISBN: 3-540-15516-3.
196. Predel, B. In *Ac-Au - Au-Zr* 1–1 (Springer-Verlag, Berlin/Heidelberg).
197. Pyeon, J. J., Kim, S. K. S. H., Jeong, D. S., Baek, S.-H., Kang, C.-Y., Kim, J.-S. & Kim, S. K. S. H. Wafer-scale growth of MoS2 thin films by atomic layer deposition. *Nanoscale* **8,** 10792–10798 (2016).
198. Qi, M., Ren, Z., Jiao, Y., Zhou, Y., Xu, X., Li, W., Li, J., Zheng, X. & Bai, J. Hydrogen kinetics on scalable graphene growth by atmospheric pressure chemical vapor deposition with acetylene. *Journal of Physical Chemistry C* **117,** 14348–14353 (2013).
199. Qian, D., Wagner, G. J., Liu, W. K., Yu, M.-F. & Ruoff, R. S. Mechanics of carbon nanotubes. *Applied Mechanics Reviews* **55,** 495 (2002).
200. Qian, Y., Ismail, I. M. & Stein, A. Ultralight, high-surface-area, multifunctional graphene-based aerogels from self-assembly of graphene oxide and resol. *Carbon* **68,** 221–231 (Mar. 2014).
201. Qin, Z., Jung, G. S., Kang, M. J. & Buehler, M. J. The mechanics and design of a lightweight three-dimensional graphene assembly. *Science Advances* **3,** e1601536 (Jan. 2017).
202. Qiu, L., Liu, J. Z., Chang, S. L., Wu, Y. & Li, D. Biomimetic superelastic graphene-based cellular monoliths. *Nature Communications* **3,** 1241 (Dec. 2012).

203. Radisavljevic, B., Whitwick, M. B. & Kis, A. Integrated circuits and logic operations based on single-layer MoS2. *ACS Nano* **5,** 9934–9938 (2011).

204. Reich, S. & Thomsen, C. Raman spectroscopy of graphite. *Philosophical transactions. Series A, Mathematical, physical, and engineering sciences* **362,** 2271–2288 (2004).

205. Reimer, L. *Scanning Electron Microscopy* ISBN: 978-3-642-08372-3 (Springer Berlin Heidelberg, Berlin, Heidelberg, 1998).

206. Rho, H., Lee, S., Bae, S., Kim, T.-W. W., Su Lee, D., Jung Lee, H., Yeon Hwang, J., Jeong, T., Kim, S., Ha, J.-S. S. & Hyun Lee, S. Three-Dimensional Porous Copper-Graphene Heterostructures with Durability and High Heat Dissipation Performance. *Scientific Reports* **5,** 12710 (Oct. 2015).

207. Roberts, A. P. & Garboczi, E. J. Elastic properties of model random three-dimensional open- cell solid. **50,** 33–55 (2002).

208. Robertson, J. Heterogeneous catalysis model of growth mechanisms of carbon nanotubes, graphene and silicon nanowires. *Journal of Materials Chemistry* **22,** 19858–19862 (2012).

209. Ronan, W., Deshpande, V. S. & Fleck, N. A. The tensile ductility of cellular Solids: The role of imperfections. *International Journal of Solids and Structures* **102-103,** 200–213 (Dec. 2016).

210. Rong, Y., Fan, Y., Leen Koh, A., Robertson, A. W., He, K., Wang, S., Tan, H., Sinclair, R. & Warner, J. H. Controlling sulphur precursor addition for large single crystal domains of WS2. *Nanoscale* **6,** 12096–12103 (Sept. 2014).

211. Roselin, L. S., Juang, R. S., Hsieh, C. T., Sagadevan, S., Umar, A., Selvin, R. & Hegazy, H. H. Recent advances and perspectives of carbon-based nanostructures as anode materials for Li-ion batteries. *Materials* **12** (2019).

212. Sagar, R. U. R., Galluzzi, M., Wan, C., Shehzad, K., Navale, S. T., Anwar, T., Mane, R. S., Piao, H.-G., Ali, A. & Stadler, F. J. Large, Linear, and Tunable Positive Magnetoresistance of Mechanically Stable Graphene Foam-Toward High-Performance Magnetic Field Sensors. *ACS Applied Materials & Interfaces* **9,** 1891–1898 (Jan. 2017).
213. Salari-Sharif, L., Valdevit, L. & Schaedler, T. A. Energy dissipation mechanisms in hollow metallic microlattices. *Journal of Materials Research* **29,** 1755–1770 (2014).
214. Salehi-Khojin, A., Estrada, D., Lin, K. Y., Bae, M. H., Xiong, F., Pop, E. & Masel, R. I. Polycrystalline graphene ribbons as chemiresistors. *Advanced Materials* **24,** 53–57 (2012).
215. Samuel Boyd Knapp. *Kinetics of the Thermal Decompostion of Tungsten Hexacarbonyl* PhD thesis (1966).
216. Sanders, W. & Gibson, L. J. Reduction in Young's Modulus of Aluminum Foams Due to Cell Wall Curvature and Corrugation. *Porous and Cellular Material for Structural Applications* **521,** 53–57 (1998).
217. Savini, G., Dappe, Y. J., Öberg, S., Charlier, J. C., Katsnelson, M. I. & Fasolino, A. Bending modes, elastic constants and mechanical stability of graphitic systems. *Carbon* **49,** 62–69 (2011).
218. Scherer, M. R., Li, L., Cunha, P. M., Scherman, O. A. & Steiner, U. Enhanced electrochromism in gyroid-structured vanadium pentoxide. *Advanced Materials* **24,** 1217–1221 (2012).
219. Schueller, O. & Brittain, S. Fabrication and characterization of glassy carbon MEMS. *Chemistry of Materials* **4756,** 1399–1406 (1997).
220. Schutte, W., De Boer, J. & Jellinek, F. Crystal structures of tungsten disulfide and diselenide. *Journal of Solid State Chemistry* **70,** 207–209 (Oct. 1987).
221. Semenov, A. V., Pergament, A. L. & Pikalev, A. A. Raman spectroscopy of melamine-formaldehyde resin microparticles exposed to processing in complex plasma. *Journal of Raman Spectroscopy* **47,** 1293–1297 (2016).

222. Sha, J., Gao, C., Lee, S.-K., Li, Y., Zhao, N. & Tour, J. M. Preparation of Three-Dimensional Graphene Foams Using Powder Metallurgy Templates. *ACS Nano* **10,** 1411–1416 (Jan. 2016).

223. Shao, Y., Wang, J., Wu, H., Liu, J., Aksay, I. a. & Lin, Y. Graphene based electrochemical sensors and biosensors: A review. *Electroanalysis* **22,** 1027–1036 (2010).

224. Shen, Y. & Wu, H. Interlayer shear effect on multilayer graphene subjected to bending. *Applied Physics Letters* **100,** 1–4 (2012).

225. El-Sherik, A., Erb, U., Palumbo, G. & Aust, K. Deviations from hall-petch behaviour in as-prepared nanocrystalline nickel. *Scripta Metallurgica et Materialia* **27,** 1185–1188 (Nov. 1992).

226. Sherrell, P. C. & Mattevi, C. Mesoscale design of multifunctional 3D graphene networks. *Materials Today* **19,** 428–436 (2016).

227. Shi, J.-l. L., Tang, C., Peng, H.-J. J., Zhu, L., Cheng, X.-B. B., Huang, J.-Q. Q., Zhu, W. & Zhang, Q. 3D Mesoporous Graphene: CVD Self-Assembly on Porous Oxide Templates and Applications in High-Stable Li-S Batteries. *Small* **11,** n/a–n/a (2015).

228. Shi, W., Zhu, J., Sim, D. H., Tay, Y. Y., Lu, Z., Zhang, X., Sharma, Y., Srinivasan, M., Zhang, H., Hng, H. H. & Yan, Q. Achieving high specific charge capacitances in Fe 3 O 4 /reduced graphene oxide nanocomposites. *Journal of Materials Chemistry* **21,** 3422–3427 (2011).

229. Shin, W. C., Bong, J. H., Choi, S.-Y. Y. & Cho, B. J. Functionalized graphene as an ultrathin seed layer for the atomic layer deposition of conformal high- k dielectrics on graphene. *ACS Applied Materials and Interfaces* **5,** 11515–11519 (Nov. 2013).

230. Shulmeister, V. *Modelling of the Mechanical Properties of Low-Density Foams Proefschrift* PhD thesis (Delft University of Technology, 1998). ISBN: 9042300256.

231. Simone, A. E. & Gibson, L. J. Effects of solid distribution on the stiffness and strength of metallic foams. *Acta Materialia* **46,** 2139–2150 (1998).

232. Singh, E., Chen, Z., Houshmand, F., Ren, W., Peles, Y., Cheng, H. M. & Koratkar, N. Superhydrophobic graphene foams. *Small* **9,** 75–80 (2013).

233. Sobczynski, A., Yildiz, A., Bard, A. J., Campion, A., Fox, M. A., Mallouk, T., Webber, S. E. & White, J. M. Tungsten disulfide: a novel hydrogen evolution catalyst for water decomposition. *The Journal of Physical Chemistry* **92,** 2311–2315 (Apr. 1988).

234. Song, H., Xu, S., Li, Y., Dai, J., Gong, A., Zhu, M., Zhu, C., Chen, C., Chen, Y., Yao, Y., Liu, B., Song, J., Pastel, G. & Hu, L. Hierarchically Porous, Ultrathick, âBreathableâ Wood-Derived Cathode for Lithium-Oxygen Batteries. *Advanced Energy Materials* **8,** 1701203 (Feb. 2018).

235. Stoller, M. D., Park, S., Zhu, Y., An, J. & Ruoff, R. S. Graphene-Based Ultracapacitors. *Nano Letters* **8,** 3498–3502 (Oct. 2008).

236. Sun, H., Xu, Z. & Gao, C. Multifunctional, Ultra-Flyweight, Synergistically Assembled Carbon Aerogels. *Advanced Materials* **25,** 2554–2560 (May 2013).

237. Sun, L., Tian, C., Li, M., Meng, X., Wang, L., Wang, R., Yin, J. & Fu, H. From coconut shell to porous graphene-like nanosheets for high-power supercapacitors. *Journal of Materials Chemistry A* **1,** 6462 (2013).

238. Tasnim, N., Thakur, V., Chattopadhyay, M. & Joddar, B. The Efficacy of Graphene Foams for Culturing Mesenchymal Stem Cells and Their Differentiation into Dopaminergic Neurons. *Stem Cells International* **2018,** 1–12 (June 2018).

239. Tiefenbacher, S., Sehnert, H., Pettenkofer, C. & Jaegermann, W. Epitaxial films of WS2 by metal organic van der Waals epitaxy (MO-VDWE). *Surface Science* **318,** 8–11 (Oct. 1994).

240. Tsang, C.-H. a., Hui, K. S. N., Hui, K. S. N. & Ren, L. Deposition of Pd/graphene aerogel on nickel foam as a binder-free electrode for direct electro-oxidation of methanol and ethanol. *J. Mater. Chem. A* **2,** 17986–17993 (2014).

241. Tsopanos, S., Mines, R. A. W., McKown, S., Shen, Y., Cantwell, W. J., Brooks, W. & Sutcliffe, C. J. The Influence of Processing Parameters on the Mechanical Properties of Selectively Laser Melted Stainless Steel Microlattice Structures. *Journal of Manufacturing Science and Engineering* **132,** 041011 (2010).

242. Tunvisut, K., O'Dowd, N. P. & Busso, E. P. Use of scaling functions to determine mechanical properties of thin coatings from microindentation tests. *International Journal of Solids and Structures* **38,** 335–351 (Jan. 2001).

243. Vandeputte, A. G., Reyniers, M. F. & Marin, G. B. Theoretical study of the thermal decomposition of dimethyl disulfide. *Journal of Physical Chemistry A* **114,** 10531–10549 (Oct. 2010).

244. Viculis, L. M., Mack, J. J., Mayer, O. M., Hahn, H. T. & Kaner, R. B. Intercalation and exfoliation routes to graphite nanoplatelets. *Journal of Materials Chemistry* **15,** 974 (2005).

245. Vignolini, S., Yufa, N. A., Cunha, P. S., Guldin, S., Rushkin, I., Stefik, M., Hur, K., Wiesner, U., Baumberg, J. J. & Steiner, U. A 3D optical metamaterial made by self-assembly. *Advanced Materials* **24,** 23–27 (2012).

246. Vincent, J. F. V. *Structural Biomaterials* ISBN: 978-0-333-26126-2 (Macmillan Education UK, London, 1982).

247. Voiry, D., Yang, J. & Chhowalla, M. Recent Strategies for Improving the Catalytic Activity of 2D TMD Nanosheets Toward the Hydrogen Evolution Reaction. *Advanced Materials,* 6197–6206 (2016).

248. Von Freymann, G., Ledermann, A., Thiel, M., Staude, I., Essig, S., Busch, K. & Wegener, M. Three-dimensional nanostructures for photonics. *Advanced Functional Materials* **20,** 1038–1052 (2010).

249. Wang, C., Zhang, C. & Chen, S. The microscopic deformation mechanism of 3D graphene foam materials under uniaxial compression. *Carbon* **109,** 666–672 (2016).

250. Wang, C., Zhang, C. & Chen, S. Micro-mechanism and influencing factors of graphene foam elasticity. *Carbon* **148,** 267–276 (2019).

251. Wang, I., Bouriau, M., Baldeck, P. L., Martineau, C. & Andraud, C. Three-dimensional microfabrication by two-photon-initiated polymerization with a low-cost microlaser. *Optics Letters* **27,** 1348 (2002).

252. Wang, J. & Ellsworth, M. *Graphene Aerogels* in *ECS Transactions* **19** (ECS, 2009), 241–247.

253. Wang, J. K., Xiong, G. M., Zhu, M., Özyilmaz, B., Castro Neto, A. H., Tan, N. S., Choong, C., Barbaros, O., Helio, A., Neto, C., Tan, N. S. & Choong, C. Polymer-Enriched 3D Graphene Foams for Biomedical Applications. *ACS Applied Materials & Interfaces* **7,** 8275–8283 (Apr. 2015).

254. Wang, Q. H., Kalantar-Zadeh, K., Kis, A., Coleman, J. N. & Strano, M. S. Electronics and optoelectronics of two-dimensional transition metal dichalcogenides. *Nature Nanotechnology* **7,** 699–712 (2012).

255. Wang, R., Purdie, D. G., Fan, Y., Massabuau, F. C., Braeuninger-weimer, P., Burton, O. J., Blume, R., Schloegl, R., Lombardo, A., Weatherup, R. S. & Hofmann, S. A peeling approach for integrated manufacturing of large hBN crystals. *ACS Nano* **13,** 2114–2126 (2019).

256. Weatherup, R. S., Bayer, B. C., Blume, R., Baehtz, C., Kidambi, P. R., Fouquet, M., Wirth, C. T., Schlögl, R. & Hofmann, S. On the mechanisms of Ni-catalysed graphene chemical vapour deposition. *ChemPhysChem* **13,** 2544–2549 (July 2012).

257. Weatherup, R. S., Bayer, B. C., Blume, R., Ducati, C., Baehtz, C., Schlögl, R. & Hofmann, S. In situ characterization of alloy catalysts for Low-temperature graphene growth. *Nano Letters* **11,** 4154–4160 (2011).

258. Weatherup, R. S., Dlubak, B. & Hofmann, S. Kinetic Control of Catalytic CVD for High Quality Graphene at Low Temperatures. *ACS Nano* **6,** 9996–10003 (2012).

259. Weatherup, R. S., Shahani, A. J., Wang, Z.-J., Mingard, K., Pollard, A. J., Willinger, M. G., Schloegl, R., Voorhees, P. W. & Hofmann, S. In Situ Graphene Growth Dynamics on Polycrystalline Catalyst Foils. *Nano Letters,* acs.nanolett.6b02459 (2016).

260. Wicklein, M. & Thoma, K. Numerical investigations of the elastic and plastic behaviour of an open-cell aluminium foam. *Materials Science and Engineering A* **397,** 391–399 (2005).

261. Wilson, J. A. & Yoffe, A. D. The transition metal dichalcogenides discussion and interpretation of the observed optical, electrical and structural properties. *Advances in Physics* **18,** 193–335 (1969).

262. Wilson, P. M., Mbah, G. N., Smith, T. G., Schmidt, D., Lai, R. Y., Hofmann, T. & Sinitskii, A. Three-dimensional periodic graphene nanostructures. *Journal of Materials Chemistry C* **2,** 1879–1886 (2014).

263. Worsley, M. A., Kucheyev, S. O., Mason, H. E., Merrill, M. D., Mayer, B. P., Lewicki, J., Valdez, C. A., Suss, M. E., Stadermann, M., Pauzauskie, P. J., Satcher, J. H., Biener, J. & Baumann, T. F. Mechanically robust 3D graphene macroassembly with high surface area. *Chemical Communications* **48,** 8428 (2012).

264. Worsley, M. A., Kucheyev, S. O., Satcher, J. H., Hamza, A. V. & Baumann, T. F. Mechanically robust and electrically conductive carbon nanotube foams. *Applied Physics Letters* **94,** 5–7 (2009).

265. Wu, C., Huang, X., Wu, X., Qian, R. & Jiang, P. Mechanically flexible and multifunctional polymer-based graphene foams for elastic conductors and oil-water separators. *Advanced Materials* **25,** 5658–5662 (2013).

266. Wu, Y., Wang, Z., Liu, X., Shen, X., Zheng, Q., Xue, Q. & Kim, J. K. Ultralight Graphene Foam/Conductive Polymer Composites for Exceptional Electromagnetic Interference Shielding. *ACS Applied Materials and Interfaces* **9,** 9059–9069 (2017).

267. Wu, Y. *et al.* Three-dimensionally bonded spongy graphene material with super compressive elasticity and near-zero Poisson's ratio. *Nature Communications* **6,** 6141 (2015).

268. Wu, Z. S., Winter, A., Chen, L., Sun, Y., Turchanin, A., Feng, X. & Müllen, K. Three-dimensional nitrogen and boron co-doped graphene for high-performance all-solid-state supercapacitors. *Advanced Materials* **24,** 5130–5135 (2012).

269. Xia, M., Su, Z. & Zhang, S. Raman spectra of bilayer graphene covered with Poly(methyl methacrylate) thin film. *AIP Advances* **2,** 032122 (2012).

270. Xia, Z., Zhang, Y. & Ellyin, F. A unified periodical boundary conditions for representative volume elements of composites and applications. *International Journal of Solids and Structures* **40,** 1907–1921 (2003).

271. Xiao, D., Liu, G. B., Feng, W., Xu, X. & Yao, W. Coupled spin and valley physics in monolayers of MoS2and other group-VI dichalcogenides. *Physical Review Letters* **108** (2012).

272. Xiao, X., Beechem, T. E., Brumbach, M. T., Lambert, T. N., Davis, D. J., Michael, J. R., Washburn, C. M., Wang, J., Brozik, S. M., Wheeler, D. R., Burckel, D. B. & Polsky, R. Lithographically Defined Three-Dimensional Graphene Structures. *ACS Nano* **6,** 3573–3579 (2012).

273. Xiao, X., Michael, J. R., Beechem, T., McDonald, A., Rodriguez, M., Brumbach, M. T., Lambert, T. N., Washburn, C. M., Wang, J., Brozik, S. M., Wheeler, D. R., Burckel, D. B. & Polsky, R. Three dimensional nickel-graphene core-shell electrodes. *Journal of Materials Chemistry* **22,** 23749–23754 (2012).

274. Xie, X., Zhou, Y., Bi, H., Yin, K., Wan, S. & Sun, L. Large-range control of the microstructures and properties of three-dimensional porous graphene. *Scientific reports* **3,** 2117 (July 2013).

275. Xu, F., Lin, T., Bi, H. & Huang, F. Graphene-like carbon with three-dimensional periodicity prepared from organic-inorganic templates for energy storage application. *Carbon* **111,** 128–132 (2017).

276. Xu, Y., Sheng, K., Li, C. & Shi, G. Self-Assembled Graphene Hydrogel via a One-Step Hydrothermal Process. *ACS Nano* **4,** 4324–4330 (July 2010).

277. Xu, Z.-Q., Zhang, Y., Lin, S., Zheng, C., Zhong, Y. L., Xia, X., Li, Z., Sophia, P. J., Fuhrer, M. S., Cheng, Y.-B. & Bao, Q. Synthesis and Transfer of Large-Area Monolayer WS2 Crystals: Moving Toward the Recyclable Use of Sapphire Substrates. *ACS Nano* **9,** 6178–6187 (June 2015).

278. Yang, J., Voiry, D., Ahn, S. J., Kang, D., Kim, A. Y., Chhowalla, M. & Shin, H. S. Two-dimensional hybrid nanosheets of tungsten disulfide and reduced graphene oxide as catalysts for enhanced hydrogen evolution. *Angewandte Chemie - International Edition* **52,** 13751–13754 (2013).

279. Yang, Y., Gupta, M. C., Dudley, K. L. & Lawrence, R. W. Novel carbon nanotube - Polystyrene foam composites for electromagnetic interference shielding. *Nano Letters* **5,** 2131–2134 (2005).

280. Yang, Z., Yan, C., Liu, J., Chabi, S., Xia, Y. & Zhu, Y. Designing 3D graphene networks via a 3D-printed Ni template. *RSC Advances* **5,** 29397–29400 (2015).

281. Yavari, F., Chen, Z., Thomas, A. V., Ren, W., Cheng, H.-m. & Koratkar, N. High Sensitivity Gas Detection Using a Macroscopic Three-Dimensional Graphene Foam Network. *Scientific Reports* **1,** 1–5 (Dec. 2011).

282. Yocham, K. M., Scott, C., Fujimoto, K., Brown, R., Tanasse, E., Oxford, J. T., Lujan, T. J. & Estrada, D. Mechanical Properties of Graphene Foam and Graphene Foam-Tissue Composites. *Advanced Engineering Materials* **20,** 1800166 (Sept. 2018).

283. Yoon, J.-C., Lee, J.-S., Kim, S.-I., Kim, K.-H. & Jang, J.-H. Three-dimensional graphene nano-networks with high quality and mass production capability via precursor-assisted chemical vapor deposition. *Scientific reports* **3,** 1788 (2013).

284. Yoon, K.-Y., Lee, J.-S., Kim, K., Bak, C. H., Kim, S.-I., Kim, J.-B. & Jang, J.-h. Hematite-Based Photoelectrochemical Water Splitting Supported by Inverse Opal Structures of Graphene. *ACS Applied Materials & Interfaces* **6,** 22634–22639 (Dec. 2014).

285. Yu, H. *et al.* Wafer-Scale Growth and Transfer of Highly-Oriented Monolayer MoS2 Continuous Films. *ACS Nano* **11,** 12001–12007 (2017).

286. Yuan, J., Márquez, A. G., Reinacher, J., Giordano, C., Janek, J. & Antonietti, M. Nitrogen-doped carbon fibers and membranes by carbonization of electrospun poly(ionic liquid)s. *Polymer Chemistry* **2,** 1654–1657 (2011).

287. Yue, Y., Chen, J. C., Zhang, Y., Ding, S. S., Zhao, F., Wang, Y., Zhang, D., Li, R. J., Dong, H., Hu, W., Feng, Y. & Feng, W. Two-Dimensional High-Quality Monolayered Triangular WS2 Flakes for Field-Effect Transistors. *ACS Applied Materials and Interfaces* **10,** 22435–22444 (2018).

288. Yun, S. J., Chae, S. H., Kim, H., Park, J. H. C., Park, J. H. C., Han, G. H., Lee, J. S., Kim, S. M., Oh, H. M., Seok, J., Jeong, M. S., Kim, K. K. & Lee, Y. H. Synthesis of centimeter-scale monolayer tungsten disulfide film on gold foils. *ACS Nano* **9,** 5510–5519 (2015).

289. Zhan, Y., Liu, Z., Najmaei, S., Ajayan, P. M. & Lou, J. Large-area vapor-phase growth and characterization of MoS2 atomic layers on a SiO2 substrate. *Small* **8,** 966–971 (Apr. 2012).

290. Zhang, B., Zhang, M. & Cui, T. Low-cost shrink lithography with sub-22 nm resolution. *Applied Physics Letters* **100** (2012).

291. Zhang, B., Zhang, M., Song, K., Li, Q. & Cui, T. Shrink induced nanostructures for energy conversion efficiency enhancement in photovoltaic devices. *Applied Physics Letters* **103** (2013).

292. Zhang, C., Kuila, T., Kim, N. H., Lee, S. H. & Lee, J. H. Facile preparation of flower-like NiCo2O4/three dimensional graphene foam hybrid for high performance supercapacitor electrodes. *Carbon* **89,** 328–339 (Aug. 2015).

293. Zhang, L., Alvarez, N. T., Zhang, M., Haase, M., Malik, R., Mast, D. & Shanov, V. Preparation and characterization of graphene paper for electromagnetic interference shielding. *Carbon* **82,** 353–359 (Feb. 2015).

294. Zhang, T., Li, N., Li, K., Gao, R., Gu, W., Wu, C., Su, R., Liu, L., Zhang, Q. & Liu, J. Enhanced proliferation and osteogenic differentiation of human mesenchymal stem cells on biomineralized three-dimensional graphene foams. *Carbon* **105,** 233–243 (Aug. 2016).

295. Zhang, X., Al Balushi, Z. Y., Zhang, F., Choudhury, T. H., Eichfeld, S. M., Alem, N., Jackson, T. N., Robinson, J. A. & Redwing, J. M. Influence of Carbon in Metalorganic Chemical Vapor Deposition of Few-Layer WSe2 Thin Films. *Journal of Electronic Materials* **45,** 6273–6279 (2016).

296. Zhang, X., Vyatskikh, A., Gao, H., Greer, J. R. & Li, X. Lightweight, flaw-tolerant, and ultrastrong nanoarchitected carbon. *Proceedings of the National Academy of Sciences* **116,** 6665–6672 (2019).

297. Zhang, X., Sui, Z., Xu, B., Yue, S., Luo, Y., Zhan, W. & Liu, B. Mechanically strong and highly conductive graphene aerogel and its use as electrodes for electrochemical power sources. *Journal of Materials Chemistry* **21,** 6494 (2011).

298. Zhang, Y., Yang, R., George, S. M. & Lee, Y.-C. C. In-situ inspection of cracking in atomic-layer-deposited barrier films on surface and in buried structures. *Thin Solid Films* **520,** 251–257 (Oct. 2011).

299. Zhang, Y., Qiu, Z., Cheng, X., Xie, H., Wang, H., Xie, X., Yu, Y. & Liu, R. Direct growth of high-quality Al2O3 dielectric on graphene layers by low-temperature H2O-based ALD. *Journal of Physics D: Applied Physics* **47** (2014).

300. Zhang, Y., Zhang, Y., Ji, Q., Ju, J., Yuan, H., Shi, J., Gao, T., Ma, D., Liu, M., Chen, Y., Song, X., Hwang, H. Y., Cui, Y. & Liu, Z. Controlled Growth of High-Quality Monolayer WS2 Layers on Sapphire and Imaging Its Grain Boundary. *ACS Nano* **7,** 8963–8971 (2013).

301. Zhao, H., Min, K. & Aluru, N. R. Size and Chirality Dependent Elastic Properties of Graphene Nanoribbons under Uniaxial Tension. *Nano Letters* **9,** 3012–3015 (Aug. 2009).

302. Zhao, Y., Liu, J., Hu, Y., Cheng, H., Hu, C., Jiang, C., Jiang, L., Cao, A. & Qu, L. Highly Compression-Tolerant Supercapacitor Based on Polypyrrole-mediated Graphene Foam Electrodes. *Advanced Materials* **25,** 591–595 (Jan. 2013).

303. Zheng, X., Lee, H., Weisgraber, T. H., Shusteff, M., DeOtte, J., Duoss, E. B., Kuntz, J. D., Biener, M. M., Ge, Q., Jackson, J. A., Kucheyev, S. O., Fang, N. X. & Spadaccini, C. M. Ultralight, ultrastiff mechanical metamaterials. *Science* **344,** 1373–1377 (June 2014).

304. Zhu, H. X. & Mills, N. J. Modelling the creep of open-cell polymer foams. *Journal of the Mechanics and Physics of Solids* **47,** 1437–1457 (1999).

305. Zhu, H., Knott, J. & Mills, N. Analysis of the elastic properties of open-cell foams with tetrakaidecahedral cells. *Journal of the Mechanics and Physics of Solids* **45,** 319–343 (Mar. 1997).

306. Zhu, H., Hobdell, J. & Windle, A. Effects of cell irregularity on the elastic properties of open-cell foams. *Acta Materialia* **48,** 4893–4900 (Dec. 2000).

307. Zhu, Z. Y., Cheng, Y. C., Schwingenschlögl, U., Schwingenschl, U. & Schwingenschlögl, U. Giant spin-orbit-induced spin splitting in two-dimensional transition-metal dichalcogenide semiconductors. *Physical Review B - Condensed Matter and Materials Physics* **84,** 1–5 (2011).

308. Zou, J., Liu, J., Karakoti, A. S., Kumar, A., Joung, D., Li, Q., Khondaker, S. I., Seal, S. & Zhai, L. Ultralight Multiwalled Carbon Nanotube Aerogel. *ACS Nano* **4,** 7293–7302 (Dec. 2010).

309. Zurutuza, A. & Marinelli, C. Challenges and opportunities in graphene commercialization. *Nature Nanotechnology* **9,** 730–734 (2014).